Investigation of Flexible and Anionic Metal-organic Frameworks and Derived Materials for Energy and Environmental Applications

A Thesis Submitted for the Degree of

Doctor of Philosophy

by

Sohini Bhattacharyya

Chemistry and Physics of Materials Unit (CPMU)
Jawaharlal Nehru Centre for Advanced Scientific Research
(A Deemed University)
Bangalore – 560064

জ্বালাও আলো, আপন আলো,

      জয় করো এই তামসীরে।।

Kindle a light in your soul and win

over this darkness.

—Rabindranath Tagore

Dedicated to
Ma & Baba

DECLARATION

I hereby declare that the matter embodied in the thesis entitled "*Investigation of Flexible and Anionic Metal-organic Frameworks and Derived Materials for Energy and Environmental Applications*" is the result of investigations carried out by me at the Chemistry and Physics of Materials Unit, Jawaharlal Nehru Centre for Advanced Scientific Research, India, under the supervision of Prof. Tapas K. Maji and that it has not been submitted elsewhere for the award of any degree or diploma.

In keeping with the general practice in reporting the scientific observations, due acknowledgement has been made whenever the work described is based on the findings of other investigators. Any omission that might have occurred due to oversight or error in judgement is regretted.

<div align="right">

……………………………

Sohini Bhattacharyya
Date:
Place:

</div>

CERTIFICATE

I hereby certify that the work described in this thesis entitled "***Investigation of Flexible and Anionic Metal-organic Frameworks and Derived Materials for Energy and Environmental Applications***" has been carried out by Sohini Bhattacharyya under my supervision at the Chemistry and Physics of Materials Unit, Jawaharlal Nehru Centre for Advanced Scientific Research, India and that it has not been submitted elsewhere for the award of any degree or diploma.

…………………………….

Prof. Tapas K. Maji

CPMU, JNCASR

(Research Supervisor)

Date:

Place:

Acknowledgements

Majumdar, Gabriel Garcia Marquez, Ernest Hemmingway, Chinua Achebe and Harper Lee are all very close to my heart.

I am deeply indebted to my grandparents, who were very strong individuals, for a wonderful childhood and for inspiring me to always strive harder. Growing up around people who have always fought for their dreams and ideals endows one with a sense of responsibility to go all-out. I might have lost them, but I know they walk beside me every day.

I cannot thank my entire extended family enough -the entire contingent of aunts, uncles and cousins who have always rallied behind me and have always been an immense source of support to my family.

Soumyabrata has been my pillar of strength for a decade now. I hope we continue to grow together, not necessarily older. Together, may we always have our world of books and music, with our windows open and the stars bright.

Lastly, words are insufficient to express my gratitude to my parents who are my source of strength and energy. Ma and Baba have showered me with unconditional love, taken care of my every need and endured all my tantrums and have always encouraged me to go all-out. Their love is precisely the beginning and end of everything.

Preface

This thesis has been divided into five chapters which describe various metal-organic frameworks (MOFs) and their derived materials for multifarious applications in energy and environment. These applications range from gas adsorption and separation to catalysis, sensing, water purification and optoelectronics. Different MOFs have been constructed with different ligands according to which they have diverse structures and properties. The first part of the thesis deals with the development of new flexible MOFs for gas separation, which is extremely relevant industrially, as well as from environmental considerations. The practical applicability of these MOFs as an adsorptive separator of gases has been shown through a breakthrough setup. The latter portion of the thesis deals with anionic MOFs and their derived materials. Careful consideration of stoichiometry has yielded anionic MOFs, where a guest cation resided within the pores to maintain overall charge neutrality of the system. This cation can be replaced by extra-framework cationic species to derive various specific applications like sensing, specific sensitization, chemical fixation and water purification. Moreover the anionic nature of these frameworks has also been exploited to generate MOF derived materials, e.g., nanocarbons and perovskite quantum dot-MOF composites using facile, green synthetic techniques.

Chapter 1 provides an introduction to MOFs in terms of their structure and applications. Flexible MOFs and the origin of flexibility have also been discussed here along with its applications in gas adsorption and separation. Post-synthetic Modification of MOFs has been introduced as an important tool for the synthesis of functionally diverse MOFs. It also discusses the synthesis of anionic MOFs and their various applications by employing post-synthetic modification through guest exchange. Finally it introduces MOF derived nanocarbons and their role as eletrocatalysis.

Chapter 2 comprises the structure property relationships in flexible frameworks and their application in gas separation. **Chapter 2A** describes two novel Cu^{II} based frameworks involving two different tetracarboxylate ligands of varying lengths and flexibility. The first framework is a 2D cage like structure which shows a selective adsorption of CO_2 over N_2 at 195 K. The second framework is a 3D two-fold interpenetrated framework which shows excellent application as an adsorptive separator for CO_2/N_2 as well as C_2H_2/C_2H_4. **Chapter 2B** describes a Mg^{II} based dynamic supramolecular framework which can be converted to a 3D coordination framework at

high temperature. This framework shows excellent performance in the separation of CO_2/N_2 and small hydrocarbons (C_2H_2/C_2H_4 and CH_4/C_2H_6).

Chapter 3 describes a Mg^{II} based anionic MOF (AMOF) and its further conversion into MOF derived nanoporous carbons. **Chapter 3A** discusses the synthesis and structure of the AMOF which contains dimethylammonium (DMA) guest cation within its pores. The anionic nature of the framework has been utilized to selectively capture Cu^{II} and show its turn-off sensing. Moreover, although this framework can capture all lanthanide cations, it specifically sensitizes Eu^{III} via antenna effect to yield a bright red luminescence. In **Chapter 3B**, this AMOF has been pyrolysed at two different temperatures without the use of any external precursor to synthesize two different types of carbon nanomaterials. When pyrolysed at 900°C, a nanoporous carbon is produced, which shows a very high BET surface area of 3690 $m^2.g^{-1}$. The DMA cation acts as a pre-bonded C-N moieties which assists in the generation of carbon nitride dots when pyrolysed at 500°C. These dots show activity as an electrocatalyst for oxygen reduction reaction, which is further enhanced by doping trace amount of Co in the carbon-nitrogen matrix.

Chapter 4 talks about a Zn^{II} based AMOF and its facile green conversion to a perovskite quantum dot-MOF composite. It also discusses the synthesis of inorganic-organic hybrid methylammonium lead bromide perovskites within a perovskite MOF matrix for using the same green mechanochemical synthetic technique. In **Chapter 4A**, the synthesis and structure of the AMOF is discussed, which is water-stable and has large pores. This AMOF is used to sequester Cu^{II} cations and the Cu^{II} incorporated AMOF is used as an efficient heterogeneous catalyst for the synthesis of benzimidazoles. Further this framework shows 99% removal of heavy metals (Hg^{II}, Pb^{II}, Cd^{II}) from their solutions with concentrations as low as 1 ppm. Thus it is extremely relevant in the purification of toxic water from industries. **Chapter 4B** discusses the green mechanochemical conversion of the Pb^{II} loaded MOF into $CsPbX_3$ (X= Cl, Br, I) perovskite quantum dot (PQD)-MOF composite which shows exceptional stability and processibility. Also, the perovskite quantum dots show quantum confinement effect due to size regulation by the pores of the MOF. **Chapter 4C** further extends this mechanochemical synthetic technique of PQD-MOF composites for the synthesis of inorganic-organic hybrid methylammonium halide perovskite quantum dots. This is done by exploiting the methylammonium (MA) cations of an anionic perovskite MOF (MA-M(HCOO)$_3$, M=Co, Mn). This composite

shows the typical optoelectronic properties of the perovskite quantum dot along with exceptional stability owing to the robustness induced by the framework. The composite also shows photoelectrochemical activity.

Chapter 5 summarizes of the entire thesis work. It also contains a discussion about future work that can be done taking the concepts and methods given in the thesis.

Table of Contents

Chapter 1

Introduction

1.1 Metal-organic Frameworks: An Overview

Porous materials, owing to their multifaceted applications, have attracted the attention of materials scientists all over the world since the creation of nanometer sized spaces give rise to many interesting applications, e.g., gas storage, separation, catalysis, sensing, etc. Porous materials can be broadly classified in four different classes, namely inorganic (e.g., zeolites, mesoporous silica), organic (e.g., covalent organic frameworks, conjugated microporous polymers), carbon materials and organic-inorganic hybrid materials, e.g., porous coordination polymers (PCPs), or metal-organic frameworks (MOF) (**Fig. 1**). Zeolites, which are microporous aluminosilicates, are the torchbearers of inorganic porous materials, and have been used extensively as microporous materials for adsorption and separation of industrially important feedstocks, catalysis and ion-exchangers owing to their extra-framework cation.[1, 2] However, zeolites are rather rigid in nature and do not allow functionalization and tuning of the pore surface and hence selective sequestration and signalling is not possible in them.[3] Mesoporous silica is another class of inorganic porous materials which have been used extensively for catalysis and drug delivery. Pure organic porous materials include covalent organic frameworks (COFs) and conjugated microporous polymers (CMP). Although these show large surface areas and good porosity, the synthetic procedures are rather tedious and lack structural control and these materials cannot be tuned easily. The third class of porous materials, activated carbons, have open porous structures with high surface area but the structure is essentially disordered.[4, 5] The salient structural features involve a network of
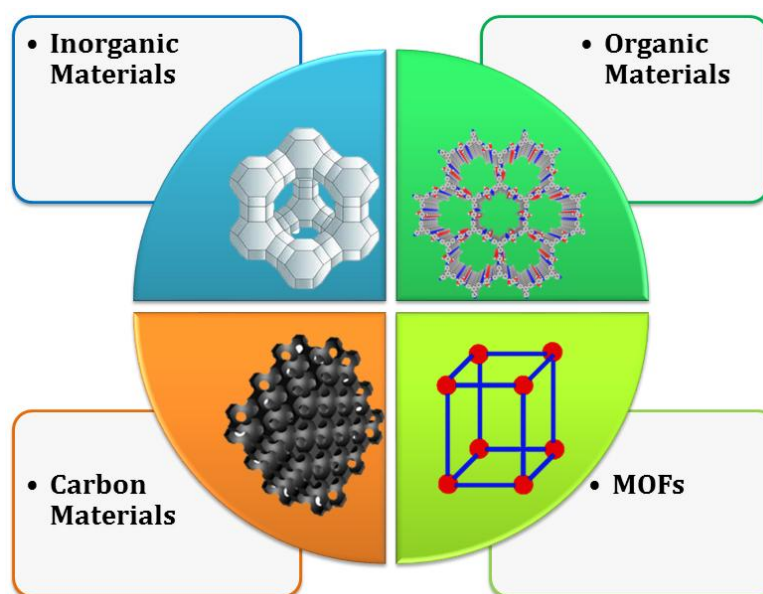
Fig.1 Four classes of porous materials.

defective hexagonal carbon layers, cross-linked by aliphatic bridging groups. These porous carbons have been found to be especially effective in gas storage,[6] catalysis[7] and drug delivery.[8] However, the irregular structure often lowers their porosity and gives a wide pore size distribution, thereby lowering their efficacy in such applications.[9] The last class of porous materials are organic-inorganic hybrid porous materials which comprise metal-organic frameworks or MOFs,[10] which have fascinated chemists for their versatile applications as well as rational crystal structure design.
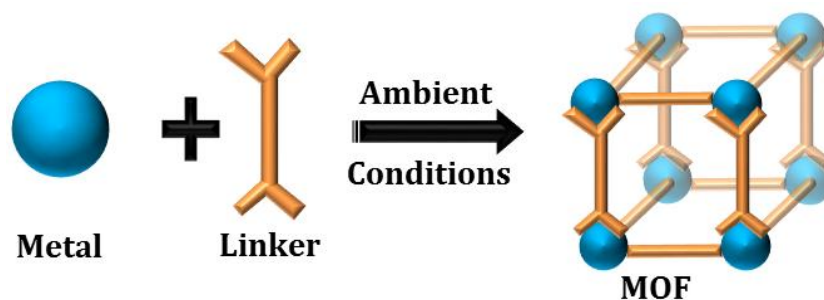
Fig. 2 Formation of MOFs.

In my thesis, I have focussed mainly on the structure-property relationships in different MOF systems. MOFs are porous and polymeric infinite one, two or three dimensional networks held together by the coordination bonds between metal centres and organic ligands (**Fig. 2**).[10, 11] The development of MOFs opened a world of new possibilities, which were beyond the scope of the two earlier classes of materials. MOFs have completely regular structures unique properties, e.g., BET surface areas up to 10,000 $m^2.g^{-1}$, density as low as 0.4 $g.cc^{-1}$, tunable pore sizes up to 5 nm, channels connected in 1-, 2-, or 3-D.[12] Also their internal surfaces can be functionalized easily, *in situ* or by post-synthetic methods.[10, 13, 14] MOFs hold enormous potential as a number of magnetic, electrical, optical, and catalytic applications can be obtained through a wide selection of metal and infinite choice and design of ligands.[15] Unlike zeolites, MOF materials do not require the use of organic/inorganic templates, (e.g., amines, quaternary ammoniums, etc.), as the solvent itself acts as the main template. This is extremely advantageous as it makes most of the MOF materials neutral in nature. In case of zeolites with a cationic framework, the framework often collapses during the extraction of the template owing to strong electrostatic host guest interactions.[3, 16] MOFs, however, have weaker interactions with solvents and therefore the structure evolves easily at low temperatures, keeping the framework intact in most of the cases, thereby providing easily accessible porosity.[17] Also, the existence of both inorganic and organic moieties in the framework allows the coexistence of both hydrophobic and hydrophilic parts within the pores, giving rise to

interesting adsorption properties.[13]

1.2 Metals & Ligands in MOF Geometry

Transition metals are most commonly used as nodes to scaffold MOFs along with organic linkers. Coordination numbers of these transition metals can vary widely, depending on the metal and its oxidation state which gives rise to diverse geometries, which may be linear, T or Y-shaped, tetrahedral, square planar, square pyramidal, trigonal-bipyramidal, octahedral, trigonal-prismatic, pentagonal-bipyramidal, and their corresponding distorted forms.[18] The geometries formed also depend on reaction conditions, solvents, counter anions and organic ligands. The smallest and simplest inorganic linkers used in MOFs are halides, i.e., F, Br, Cl and I. CN^- and SCN^- also have similar coordinating abilities as the halides.[19] Cyanometallate anions manifest several types of geometries, for example, linear, as in $[M(CN)_2]^-$ (M = Au[20] and Ag[21]), trigonal, as in $[Cu(CN)_3]^{2-}$,[22] tetrahedral, as in $[Cd(CN)_4]^{2-}$,[23] square planar, as in $[M(CN)_4]^{2-}$, (M = Ni[24], Pd, and Pt[25]), octahedral, as in $[M(CN)_6]^{3-}$(M = Fe, Co[26], Cr[27], and Mn[28]), and pentagonal bipyramidal, as in $[Mo(CN)_7]$.[29] The octacyanometallates $[M(CN)_8]^{n-}$ (M = Mo and W) also show various coordination geometries like square-antiprism, dodecahedron, or bicapped trigonal-prism.[30] Apart from these, a wide and diverse range of organic ligands are used which may be neutral, cationic or anionic. Di, tri or tetracarboxylate ligands are widely used among the organic linkers due to their multidentate nature.[31-34] Apart from conventional synthetic techniques of MOFs, e.g., solvothermal, slow diffusion and room temperature syntheses, conventional electric heating, microwave heating, electrochemistry, mechanochemistry and ultrasonic methods have also been undertaken over the years.[35] High-throughput methods are also employed in recent times for targeted synthesis of specific compounds. Many of the targeted syntheses are aimed towards achieving specific morphologies of the MOF products. There are numerous reports of thin films, membranes and specific crystal shape and size and all these require the application of different synthetic methods.[36]

1.3 Classification of MOFs

Back in 1998, MOFs were classified as 1st, 2nd and 3rd generation on the basis of their robustness and ability to sustain. The 1st generation compounds possess microporous
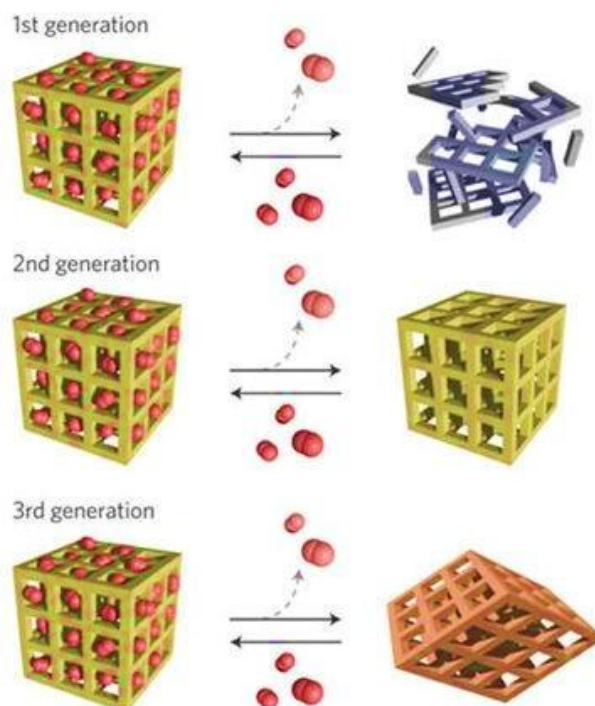
Fig. 3 Classification of MOFs. Reproduced with permission from ref. no. 37. Copyright 2009 Springer Nature.

frameworks that exist only with the guest molecules and the framework collapses irreversibly on the removal of these guest molecules. Thus the first kind is rather ineffective for storage of gas and other applications. The 2nd generation compounds show permanent porosity without any guest molecules in their pores and have stable and robust porous frameworks. Their porosity can be used for a multitude of applications. The 3rd generation compounds have dynamic and flexible structures which respond to external stimuli, e.g., light, electric field, guest molecules and modify their channels or pores reversibly or irreversibly. This class of compounds are not only useful for their porosity, but can also cater to a variety of specific applications owing to their flexibility. Most inorganic porous compounds with covalent bonds are classified under the 2nd generation compounds. However, MOFs are not merely robust 2nd generation compound, they also yield the highly dynamic third generation frameworks.[10, 37]

1.4 Applications of MOFs

The accessible nanospaces within the MOF structure can be exploited for a multitude of applications. Apart from its conventional use in gas storage and separation, it has been used for heterogeneous catalysis,[38] optoelectronics,[39] drug delivery,[40] molecular sensing,[41] etc. (**Fig. 4**) In this thesis, separation of gases, sensing, catalysis and water purification
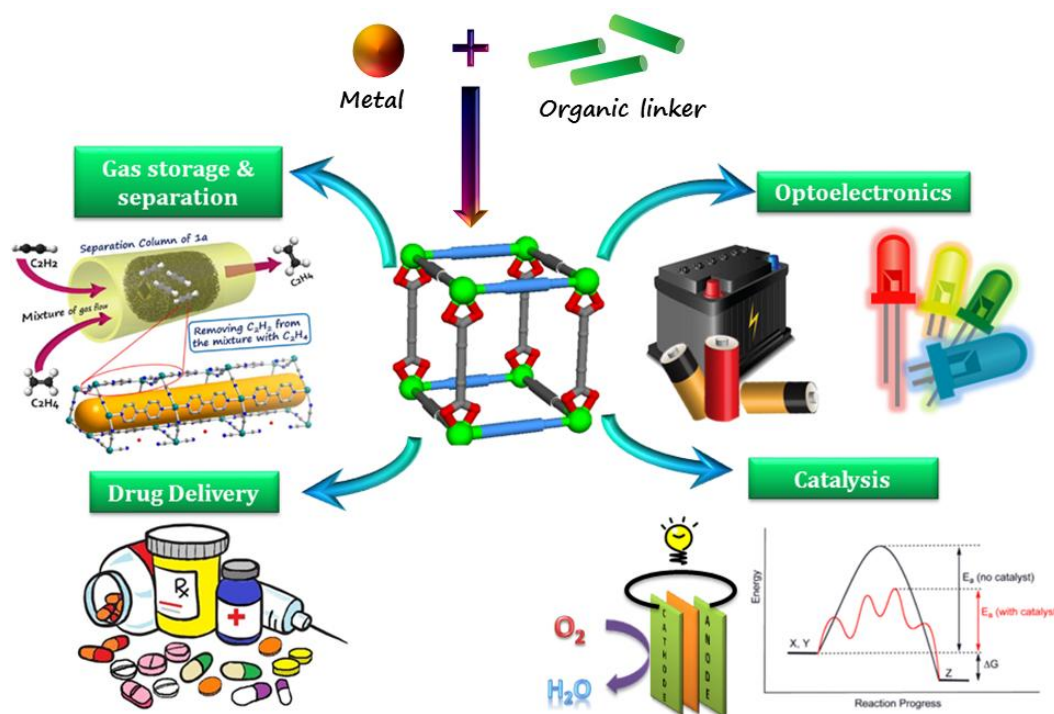
Fig. 4 MOFs and their applications.

are some of the applications that have been attempted using MOFs. The role of MOFs in these applications has been elaborated in the following section.

1.4.1 Gas Adsorption and Separation

MOFs are endowed with a variety of coordination architectures with uniform and dynamic pore structures. They possess crystallographically well defined shapes, e.g., squares, rectangles and triangles, and have exhibited unprecedented adsorption profiles manifesting their uniform microporous nature.[10] The storage and separation of different gas molecules is one of the most important techniques of the modern world, both from industrial as well as environmental considerations. Hydrogen is the most promising candidate to replace the current fossil fuel based energy resources. However, the facile storage of H_2 gas is one of the biggest challenges in this regard. MOFs, with their porous structures, hold great promise to be successful H_2 storage materials.[42] The highest total H_2 storage capacity so far has been exhibited by MOF-210, which has a total capacity of 176 mg.g^{-1} at 77K and 80 bar.[43] The separation of gas mixtures to get the individual components is essential for their use in industry. Some of the conventional methods of gas separation include cryogenic distillation, membrane and adsorption based technologies. Adsorption based technologies have an edge over the other methods owing to less energy expenses, lower carbon footprint and also for being cheaper. Since the
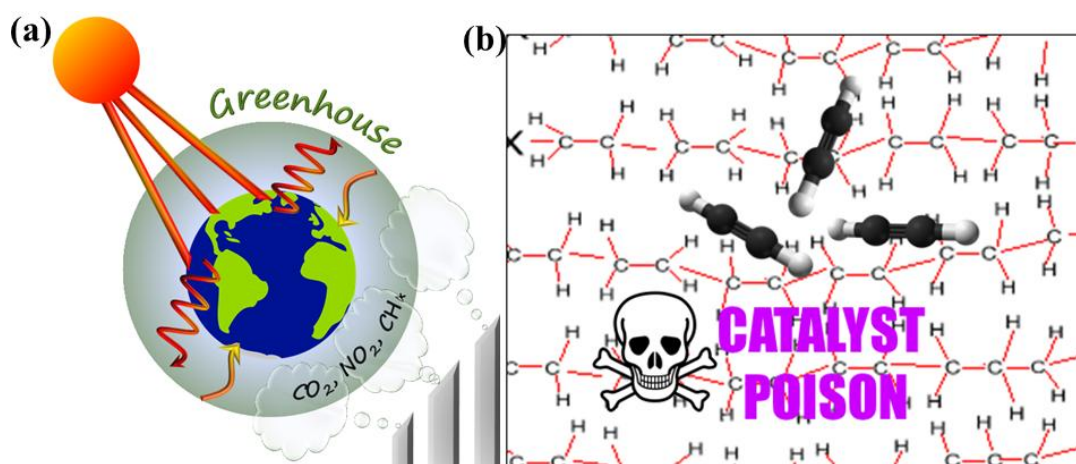
Fig. 5(a) Global warming caused due to greenhouse effects from gases like CO_2. **(b)** C_2H_2 acts as a catalyst poison in the polymerization of C_2H_4.

development of synthetic zeolites in 1940s, adsorption based separation techniques have gained a steady precedence over other separation methods.[44] MOFs have further accelerated this, because they can be tailored and functionalized to selectively adsorb specific gases from a mixture.[45] Moreover, the unique dynamic nature of MOFs is particularly advantageous in separating gases. Some of the most important separation techniques are the separation of CO_2/N_2, CO_2/H_2, CO_2/CH_4, C_2H_4/C_2H_6, C_2H_2/C_2H_4, C_2H_6/CH_4, etc. CO_2 emission from industries is a major problem in the modern era which contributes to the global warming and poses a huge environmental threat (**Fig.5(a)**). Hence, the development of technologies for the effective CO_2 sequestration from the emission sources is vital. MOFs are particularly effective in CO_2 capture and the CO_2 adsorption properties of numerous MOFs have been studied extensively.[46, 47] MOFs are particularly useful in the selective capture of CO_2 from a mixture of gases like flue gas. The capture of CO_2 from industrial flue gas can prevent it from being emitted into the environment and thereby stop its hazardous effects. Moreover, this separated CO_2 can be further reduced to form important value-added products like CO, methanol and methane. MOFs can also store natural gases like CH_4, C_2H_6, etc., and solvent vapours like methanol, ethanol, benzene, etc. Small hydrocarbons like ethane (C_2H_6), methane (CH_4), ethylene (C_2H_4) and acetylene (C_2H_2) are produced as a mixture by the steam cracking of petroleum. Separation of the individual components is extremely important for their efficiency in industrial applications.[48] The separation of CH_4 from a mixture of C_2H_6/CH_4 is essential for the use of the former as a fuel and its calorific upgradation. On the other hand, the presence of even 1% C_2H_2 in C_2H_4 can act as a catalysts poison during the synthesis of polyethylene and hence needs to be removed (**Fig.5(b)**).[49, 50]

Flexible MOFs are particularly effective in gas separation, owing to their dynamic structure because of which they can show increased specificity and unique gas adsorption properties. Such flexible MOFs, also regarded as breathing MOFs are characterized by a drastic change in the unit cell volume upon the application of external stimuli, e.g. temperature, pressure, light, guest adsorption/desorption and are prominent examples of soft porous crystals (SPCs).[51] Soft porous crystals have been described by Horike et al. as porous solids having both a highly ordered network and structural transformability. In interpenetrated MOF, adsorption is often facilitated by the phenomenon of *subnetwork displacement*. In such cases, the two interpenetrated nets are not connected by chemical bonds, but with weak interactions like van der Waals forces. So the subnets can drift, relocate or shift with respect to one another. This can occur in interpenetrated 3D frameworks as well as interdigitated and stacked 2D frameworks.[51]

1.4.1.1 Different Types of Adsorption Based Separation

The porous structure of MOFs in collaboration with surface functionality and chemical tunability shows exceptional potential as an adsorptive separator. The adsorptive separation process in MOFs can be classified into three types based on the nature of selection, as follows:

a) Thermodynamic/ Equilibrium Separation

This type of separation is majorly based on the chemical interaction between the adsorbate molecule and the pore surface of the MOF.[52] This type of separation is known as equilibrium separation since this is related to the equilibrium achieved by the isosteric heat of adsorption.[53] Here, the relative affinity of a specific adsorbate to the framework functionalities is the basis on which one is selectively adsorbed over the other. A common strategy for equilibrium separation is to introduce strong interaction sites on the pore surface to interact selectively with specific gas molecules.[54] For example, unsaturated metal sites or pendent oxygen groups are well known for interacting with CO_2 molecules. Similarly, π-electron clouds from aromatic linkers can interact with small hydrocarbons like C_2H_2 or C_2H_6. An interesting example of thermodynamic separation is observed in case of Fe-MOF-74, where the preferential adsorption of the different hydrocarbons is observed based on the variation in adsorption energy. In this system, it is observed that the unsaturated hydrocarbons acetylene, ethylene and propylene display side-on coordination at iron(II) centers, hence they show higher uptakes. Metal centres have a
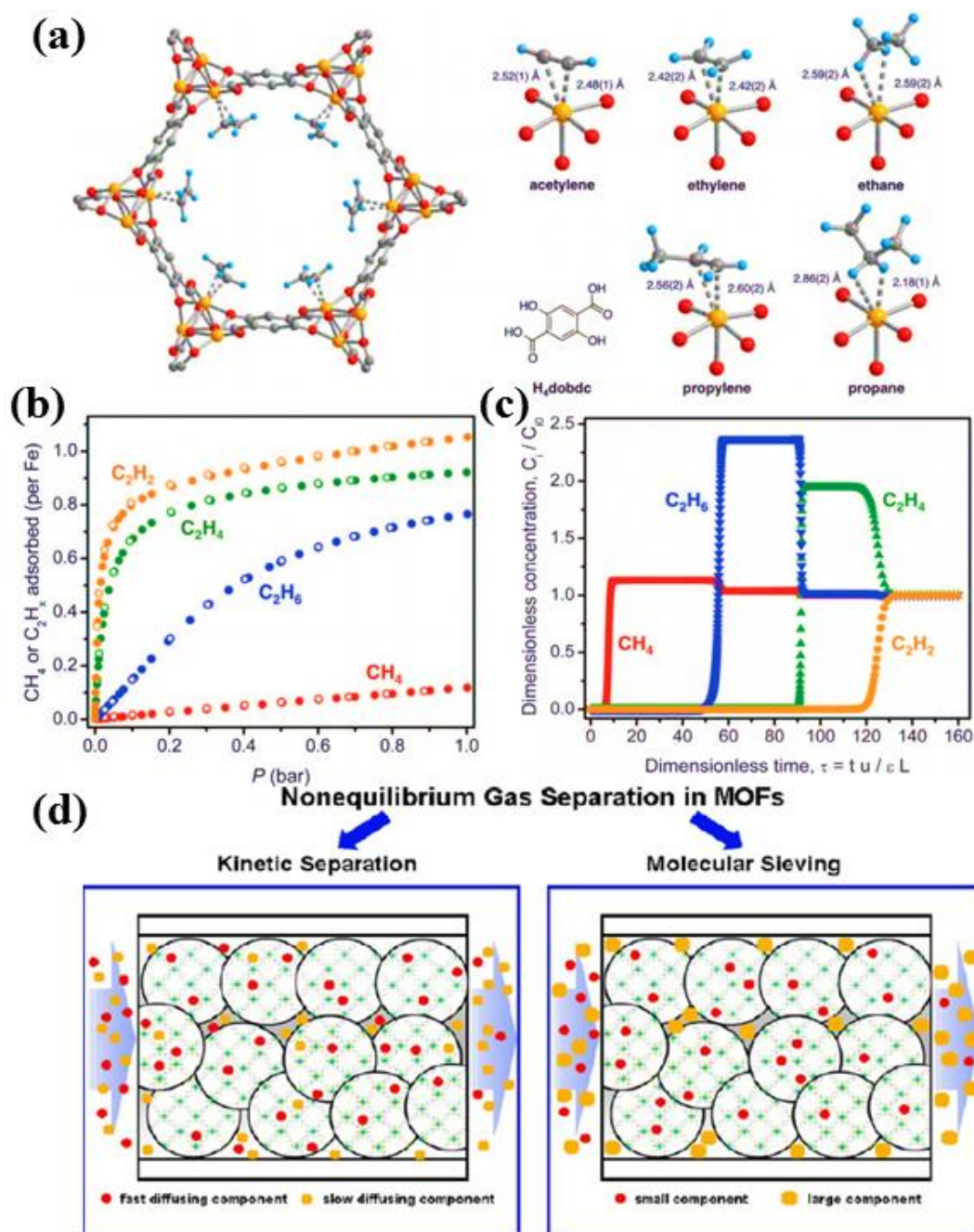
Fig. 6(a) (Left) Pore structure of Fe-MOF-74, showing the attachment of C_2H_4 at the Fe sites. **(Right)** First coordination spheres for the iron centres with the respective adsorbates. **(b)** Gas adsorption isotherms for small hydrocarbons. Reproduced with permission from ref. no. 55. Copyright 2012 Science. **(c)** Breakthrough curves for the hydrocarbons. **(d)** Types of non-equilibrium separation. Reproduced with permission from ref. no 53. Copyright 2017 American Chemical Society.

high-spin electron configuration when binding these gases, hence such weaker interactions can be reversed with little energy penalty. However, in case of ethane and propane, interaction with MOF is very weak, since in these cases Fe-C distances are as long as ~3Å **(Fig. 6(a))**.[55]

b) Non-equilibrium Separation

This type of separation is primarily dependant on the pore size and diffusivity of the gas components in the porous structure. It can be further subdivided into two types: kinetic separation and molecular sieving (**Fig. 6(b)**). While kinetic separation is dependent on the diffusivity of a particular gas component in the porous system, molecular sieving is based on steric separation owing to the size of the adsorbate molecule. Non-equilibrium separation can be easily altered by modifying the pore size. Also, pressure and temperature are of supreme importance in this kind of separation.[53]

1.4.2 Luminescence

MOFs, being a hybrid of organic and inorganic components, are promising multifunctional luminescent materials as both the inorganic and organic parts can contribute to the luminescent property. The most common type of luminescence observed in MOFs originates from aromatic conjugated organic linkers that are used in the constitution of MOFs. In many cases, the fluorescence properties, e.g., maximum emission wavelength and lifetime of organic linkers are different in solid MOFs than those of the free molecules.[56] Conjugated linkers like perylene and pyrene derivatives, phenylenevinylenes and phenyleneethynylenes are well known for the formation of luminescent MOFs. Ligand-to-metal charge transfer (LMCT) and metal-to-ligand charge transfer (MLCT) are commonly prevalent in MOFs by the allowed transition from a charge transfer-excited state to the ground state. LMCT corresponds to the electronic transition from an organic linker-localized orbital to a metal-centred orbital, whereas MLCT involves the electronic transition from a metal-centred orbital to an organic linker localized orbital. Charge transfer luminescence is often observed in d^{10} metal based MOFs.[57,58] Another approach to synthesize luminescent MOFs is with lanthanide ions as the metal node. Lanthanide ions with electronic configurations $[Xe]4f^n$ (n= 0-14) configurations generate a wide variety of electronic energy levels thus producing intricate optical properties. Under normal conditions, Ln^{III} ions are less sensitive to the surrounding chemical environment since the 4f orbitals are well shielded by the filled $5s^2 5p^6$ subshells. In addition, the lanthanide ions are weakly absorbing in nature since f-f transition is forbidden and hence direct excitation of the metal to produce emission is rather futile.[57] However, when a MOF is formed, the organic ligand can itself absorb the energy and transfer it to the Ln^{III} excited state, thereby acting as an antenna.[59] This forms
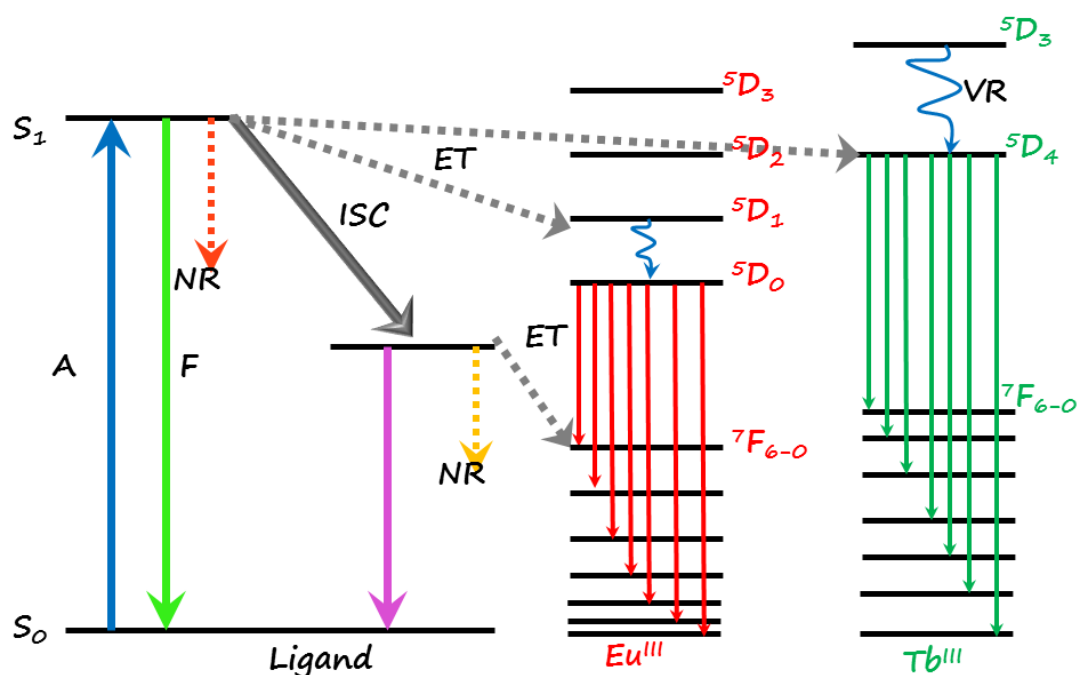
Fig. 7 Schematic representation of Antenna Effect in MOFs. Abbreviations: A = absorption; F = fluorescence; P = phosphorescence; L = lanthanide-centered luminescence; ISC = intersystem crossing; ET = energy transfer; S = singlet; NR= Non-radiative decay; VR= vibrational relaxation.

the basis of the much celebrated "luminescence sensitization" or "antenna effect"(**Fig. 7**).[60, 61] The electronic energy levels in Ln^{III} are well defined and each ion exhibits sharp characteristic 4f-4f transitions. The Eu^{III}, Tb^{III}, Sm^{III}, and Tm^{III} emit red, green, orange, and blue light, respectively, while the Yb^{III}, Nd^{III}, and Er^{III} exhibit near-infrared luminescence. Furthermore, guest molecules within the MOFs can induce or emit luminescence, while metal-ligand charge transfer related luminescence can also be observed within MOFs. In some luminescent MOFs, the permanent porosity has allowed the reversible storage and release of guest substrates and provided the differential recognition of these substrates by acting as sensing species.[57] MOFs can act as rigid or flexible hosts for the encapsulation of the guest luminescence species such as lanthanide ions or fluorescent dyes. The MOF scaffold can sensitize the encapsulated Ln^{III} ions using the antenna effect and also protects them from the outside chemical environment.[57] Using this principle, Luo et al. prepared the Eu^{III} and Tb^{III} doped MOFs which exhibit tunable luminescent properties and can sense metal ions.[62, 63]

The luminescent behaviour of MOFs along with their exceptional tunable structure and properties can be exploited to use them as sensors for the detection of specific species. There is a pressing demand for materials that can selectively and sense gas and vapour phase analytes for a range of applications including industrial process
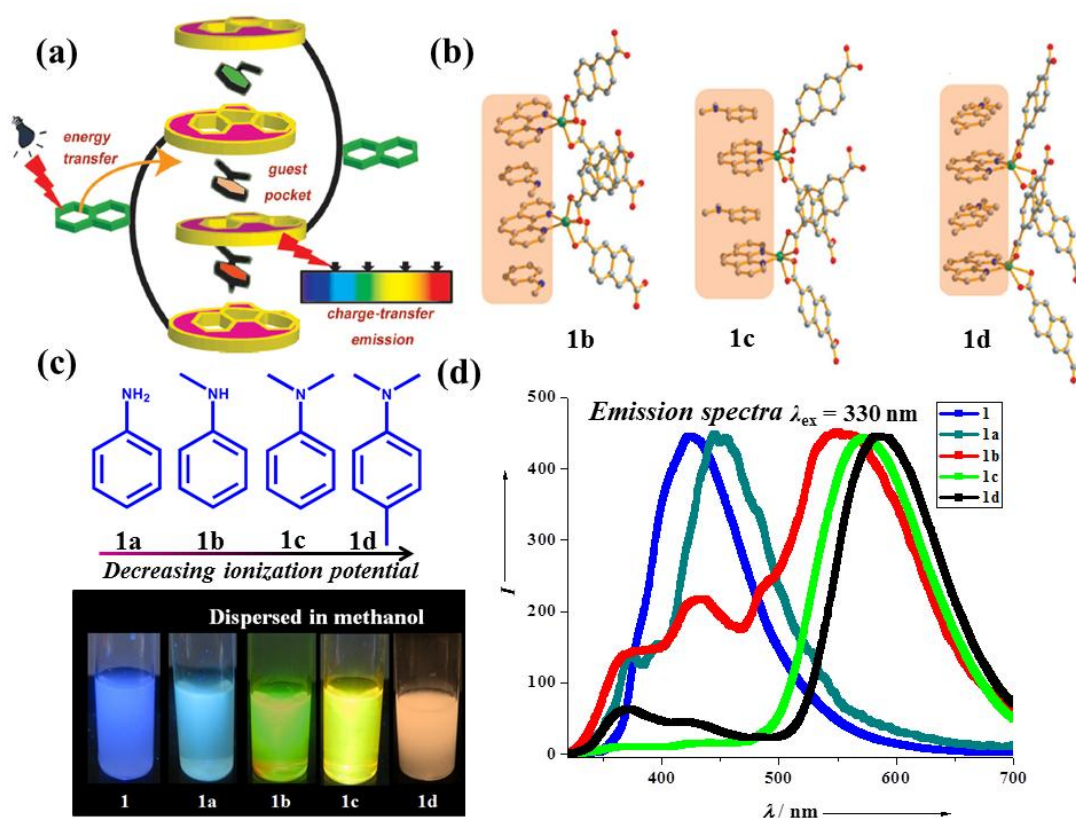
Fig.8(a) Schematic representation of a fluorescent MOF and its adaptable nanospace (guest pocket) suitable for the recognition of aromatic guest molecules through an emission-readout process. **(b)** Columnar stacking of the {Zn(o-phen)} subunit and the guest DMF molecules. **(c)** Photographs of methanolic dispersions of the MOF upon inclusion of different amines under UV lamp. **(d)** Emission spectra of the MOF and amine encapsulated inclusion compounds upon excitation at λ=330 nm. Reprinted with permission from ref. no. 64. Copyright 2014 Wiley VCH.

management, medical diagnostics, environmental monitoring, chemical threat and explosive detection. The advantage of using luminescent MOFs for sensing is the production of a signal that is visible to the eye.[43, 44] Moreover, it can be easily detected through fluorescence spectroscopy up to the single molecular level, without having to fabricate films, directly with the powdered sample. An interesting example of luminescence based sensing can be seen in the flexible 3D supramolecular framework {[Zn(ndc)(*o*-phen)]·DMF}*n* (*o*-phen=1,10-phenanthroline,ndc=2,6-napthalenedicarboxy-late) (**Fig. 8(a)**). This MOF can accommodate different electron donating aromatic amine guests within the confined nanospaces of its structure (**Fig. 8(b)**). These aromatic amines can be detected with selective turn-on emission signalling and the system serves as a molecular recognition platform through an emission readout process (**Fig. 8(c,d)**).This tunable emission signalling with different amines can be attribute to its charge transfer complexation with o-phen linkers.[64]

1.3.4 Catalysis

Porous materials are well suited for catalytic reactions owing to the availability of isolated nanospaces for accommodating the substrate molecules. Zeolites have been extensively used as industrial catalysts for several petrochemical processes.[65, 66] However, in the liquid phase, zeolites are unsuitable for catalysis due the restricted diffusion of substrates within the pores owing to the rigid structures with limited pore volumes.[38] Over the past two decades, there has been a growing interest in the use of MOFs as efficient and eco-friendly heterogeneous catalysts. The high surface areas of MOFs along with tailorable cavities with unique shape and size selectivity render enhanced catalytic activity. Moreover, they have high chemical and thermal stability, making them suitable for a variety of chemical reactions.[67] The metal sites of the MOFs can act as catalytic centres with its linkers helping in attachment of the substrate. Moreover, guest species such as metal nanoparticles hosted within the MOF can also assist in catalysis. Introduction of such catalytically active moieties by *in situ* or post-synthetic functionalization have made MOFs effective as heterogeneous catalysts or catalytic supports for several reaction, e.g., oxidation of CO to CO_2, oxidation of organic substrates, hydrogenation of ethylene, and so on.[68, 69] MOFs have also established themselves as efficient heterogeneous catalysts for C-H bond activation, Knoevenagel Condensation, Suzuki-Miyaura Coupling and hydrogenation reactions. Some of the major advantages of MOFs as catalysts are as follows:

a) Higher selectivity and reactivity than traditional heterogeneous catalysts owing to uniformly distributed catalytically active sites throughout the structure.

b) The porous structure prevents the anchored or encapsulated active sites from leaching or degradation, thereby providing better recyclability.
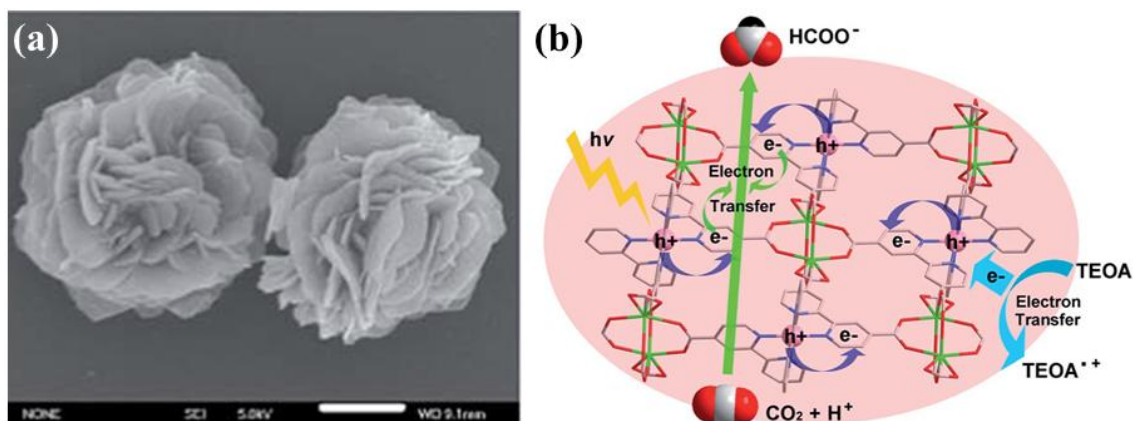
Fig. 9(a) Nanoflowers of Ru-MOF.**(b)** Mechanism of photocatalytic CO_2 reduction in Ru-MOF.Reprinted with permission from ref. no. 71. Copyright Royal Society of Chemistry.

c) MOFs can be post-synthetically modified to functionalize the metal nodes, organic components and pores without damaging the original framework.

d) Crystalline nature of MOF facilitates the molecular level characterization of the catalytically active site and also aids in the mechanistic studies.

e) Cooperative catalysis is easily achieved in MOFs since the distinct isolated active sites can form synergistic interactions with the substrates in a cooperative manner.[67]

Not only heterogeneous catalysis, MOFs can also become extremely effective in photo or electrocatalysis owing to the unique combination of different metal nodes and organic linkers.[70] Nanoflowers of Ru-MOF $(Cd_2[Ru(dcbpy)_3].12H_2O)_n$ (dcbpy= 2,2′-bipyridine-4,4′-dicarboxylate) show excellent activity in photocatalytic CO_2 reduction. Ru ions are formed upon irradiation, where triethanolamine scavenges the holes and electrons are transferred to the pyridine rings of the dcpby ligands. The adsorbed CO_2 then receives two electrons from the pyridine rings to be reduced to formate.[71] (**Fig. 9**).

1.3.5 Water Purification

Contamination of water with hazardous chemical effluents is one of the biggest health hazards brought forth by widespread industrialization. This has left 1 billion people
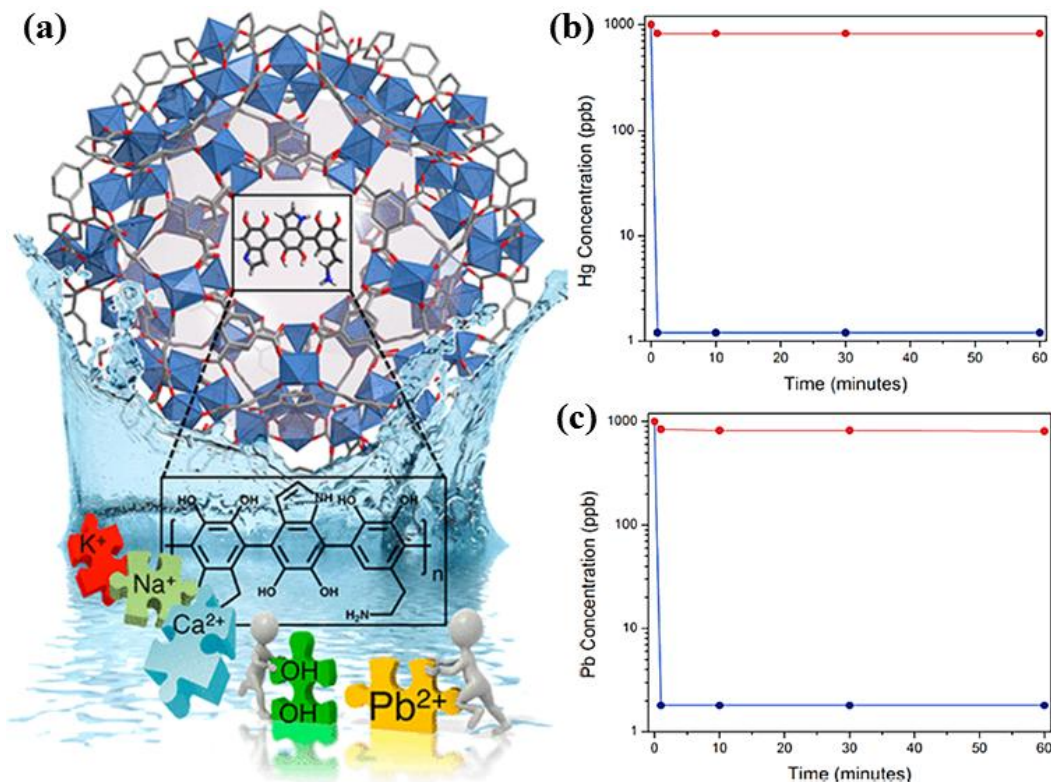
Fig. 10 (a) PDA pinned Fe-BTC MOF for water purification. Metal ion concentrations in 1 ppm solutions of **(b)** Hg[II] and **(c)** Pb[II] after being treated with Fe-BTC/PDA composite (blue) and Fe-BTC (red).Reprinted with permission from ref. no. 73. Copyright 2018 American Chemical Society.

all over the world without access to clean water and at 2 million deaths per year, water contamination continues to be one of the leading causes of death globally. Heavy metal contamination of water from industrial effluents causes deadly diseases like Minamata, Itai-itai, various neurological and gastrointestinal disorders. The conventional methods of water purification are primarily filtration based and have high economic and energy costs, are difficult to regenerate and produce a large amount of chemical sludge. Moreover, such systems have low selectivity and specificity. In contrast, MOF based water purification systems are much more economically and energetically viable and can be regenerated easily. In addition the pore surfaces can be functionalized to trap specific contaminants.[72] In a seminal work, the internal pore surface of Fe-BTC MOF (BTC = 1,3,5-benzenetricaboxylate) is treated to form polydopamine (PDA) within the pores having extrinsic porosity (**Fig 10(a)**). This composite can bind up to 1634 mg of Hg^{II} and 394 mg of Pb^{II} per gram and removes more than 99.8% of these ions from a 1 ppm solution within seconds. It also shows unprecedented selectivity towards Pb^{II} (**Fig 10(b,c)**).[73]

1.5 Postsynthetic Modification in MOFs
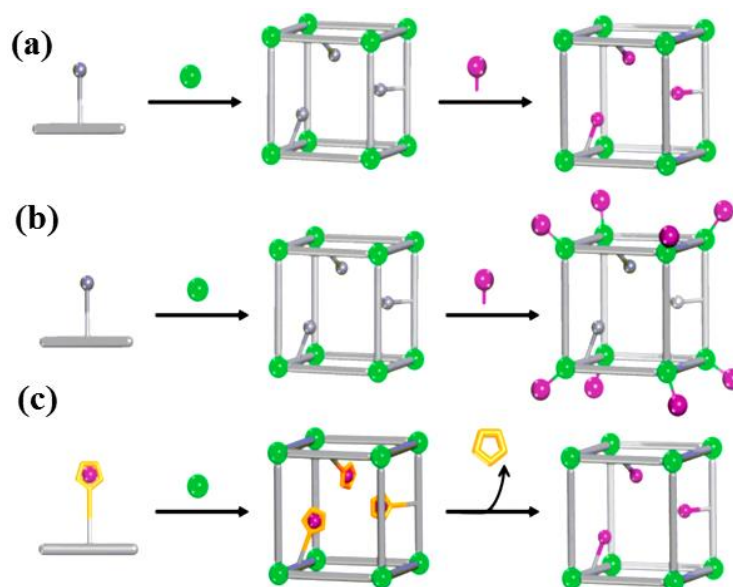
Fig. 11 Different types of post synthetic modifications in MOFs. Reprinted with permission from ref. no.74. Copyright 2012 Royal Society of Chemistry.

Although the traditional usage of MOFs has been for the efficient adsorption and storage of gases, with the development of the field, their applications have also diversified in the fields of catalysis, drug delivery and optoelectronics. The progress of these fields is completely dependent on the development of novel MOFs with specific chemical functionalities. However, it is difficult to retain such functionalities within MOFs
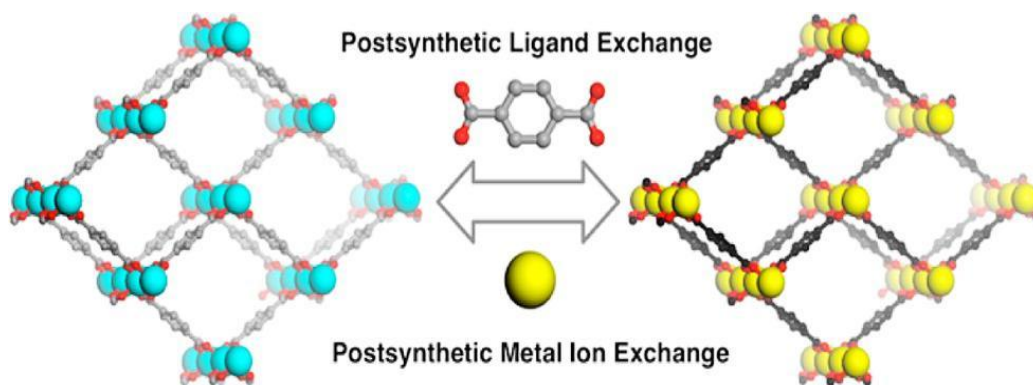
Fig. 12 Post synthetic metal and ligand exchange in MOFs. Reprinted with permission from ref. no. 84. Copyright 2012 American Chemical Society.

synthesized by common solvothermal methods. Ligands generally lose their thermally labile groups during the solvothermal processes either due to problematic solubility or coordination to metal ions.[74] One of the most effective methods of obtaining functionalized MOFs is Post-synthetic Modification of the MOFs, which refers to a series of procedures that may be done to achieve chemical modification on an already synthesized framework, rather than on the molecular precursors. PSM is particularly effective for MOFs since they contain organic ligands which can undergo a vast range of organic transformations. Moreover, since MOFs are highly porous, during PSM, the reagents can act on both the interior and exterior of the material. Using PSM, both the metal as well as the ligand can be functionalized without destabilizing the framework, in turn generating topologically similar frameworks with diversity in functions. The term "Post-synthetic Modification" or PSM was first coined by Cohen, *et al.* back in 2007 when they were describing the modification of IRMOF-3 with acetic anhydride. There are quite a few different ways in which a MOF can be modified physically and chemically on the basis of the type of bond broken or formed during the process of PSM.[74] A few of the common methods are listed below (**Fig. 11**).

(a) covalent PSM[75, 76]

(b) dative PSM[77, 78]

(c) post synthetic deprotection[78]

(d) guest molecule exchange including cation/anion exchange[79-83]

PSM through cation and anion exchange has been observed in several robust MOFs including ZIFs and MILs, which has helped in the development of new applications. PSM can be realized by complete replacement of the metal node, which is regarded as metathesis. By this method, Dinca *et. al.* has exhibited the inclusion of Co^{II} in MOF-5 in this method.[166] Another method of PSM involves the exchange of the linker constructing

the MOF with other linkers. When the process occurs in a solvent medium, it is regarded as SALE (Solvent Assisted Ligand Exchange). In a recent work, the H_4TBPy linker of NU-1000 has been exchanged with tetrakis(4-carboxyphenyl)porphyrin (TCPP) to induce the resultant framework with excellent efficacy in photodynamic theory.[167] Ligand exchange in the solid state under mild conditions was observed in the topologically distinct MOFs MIL-53 (Al) and MIL-68 (In). Metal ion exchange is also observed between intact MOF microcrystalline particles of MIL-53 (Al) and MIL-53 (Fe)[84] (**Fig. 12**). This kind of cation/anion exchange is prevalent mostly in ionic frameworks, where the guest counter cation is replaced by an extra-framework species to achieve specific functionalities.

1.6 Anionic MOFs

Most known MOFs are usually neutral in nature. But in some cases, the framework itself is charged and the overall framework neutrality is maintained by guest counter ions residing within the pores of the MOFs. Likewise, in case of anionic MOFs AMOFs), the
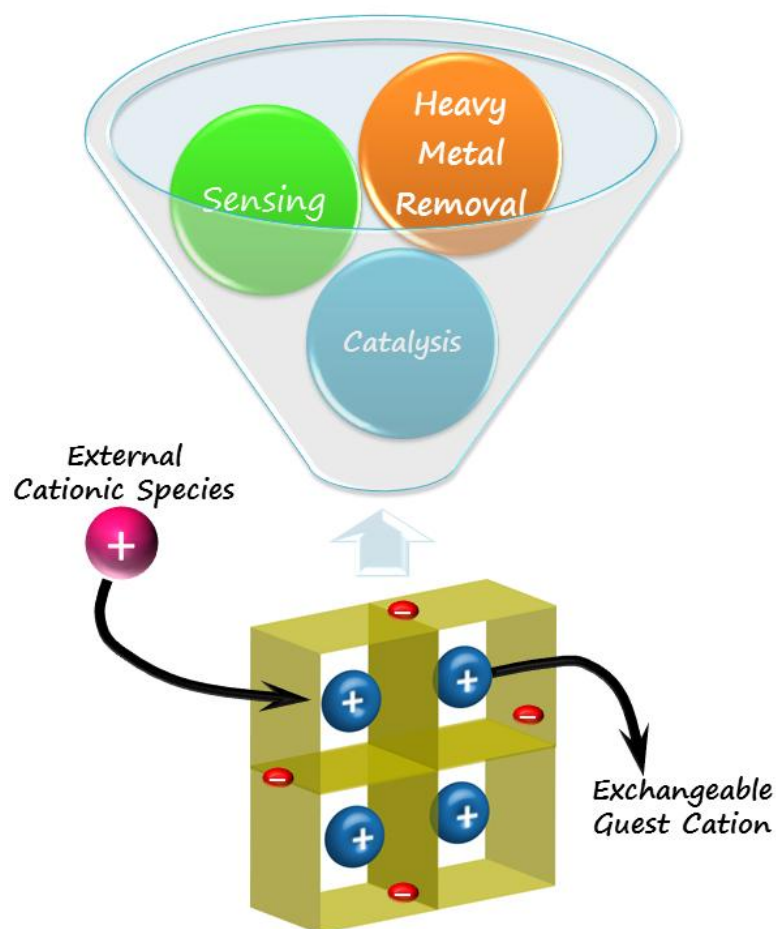
Fig. 13 Various applications achieved by cation exchange in an AMOF.

framework itself is anionic nature, and the structural neutrality is maintained by guest cations present in the pore channels. Many such AMOFs have been reported in recent times and have shown diverse applications by the exchange of the guest cation with other cationic species.[79-83] The nature of the cation species imbibed in the framework determines the application that can be achieved from the AMOF (**Fig. 13**).

An interesting instance of AMOF is bioMOF-1 formulated as $[\{Zn_8(ad)_4(BPDC)_6O \cdot 2Me_2NH_2\}8DMF.11H_2O]$, (ad = adeninate; BPDC = biphenyldicarb-oxylate) reported by Rosi et al. Here, dimethyl amine (NH_2Me_2) (DMA) cations are present within the pores of the framework in order to maintain neutrality. Owing to the stability of bioMOF-1 in PBS (Phosphate Buffered Saline) buffer, its non-toxic and anionic nature, it appears to be an ideal material for the capture and controlled
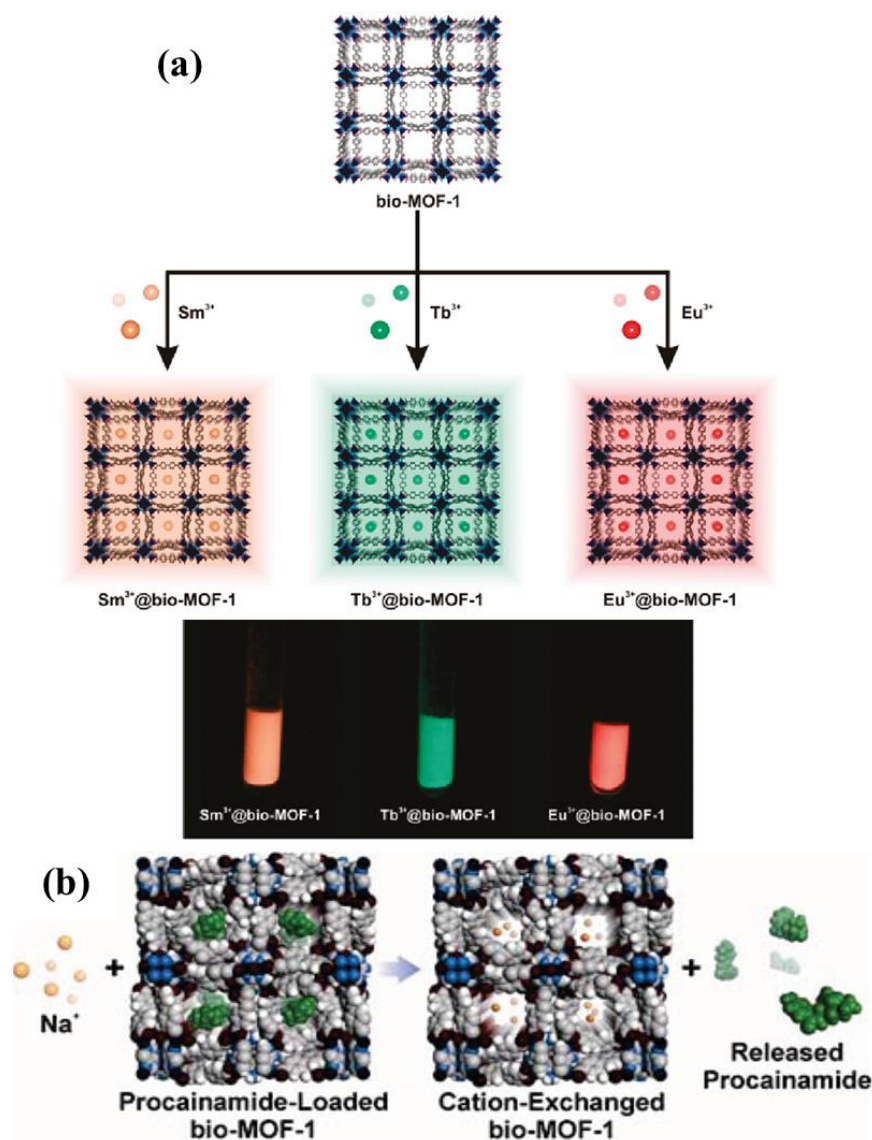
Fig. 14(a) Luminescence through cation exchange in bioMOF-1 **(b)** Cation exchange mediated drug release in bioMOF-1. Reprinted with permission from ref.no.81 and 79. Copyright 2009 and 2011 American Chemical Society.

release of drug. For this purpose the anti- arrhythmia drug procainamide hydrochloride was chosen and bioMOF-1 proved to be an excellent material for its storage and controlled release[79] (**Fig. 14(b)**). The same framework was further used to encapsulate and sensitize several visible and near infrared emitting lanthanide cations in aqueous media to produce luminescence (**Fig. 14(a)**).[81] Furthermore, tunable emission was also achieved using the same framework. Also, cation exchange is performed by introducing tetramethylammonium (TMA), tetraethylammonium (TEA), and tetrabutylammonium (TBA) into the pores to systematically decrease the pore volume and surface area of the material.[80] AMOFs can also be used in catalytic processes, e.g., DMA cation containing ZJU-28 $[(Me_2NH_2)_3\{In_3(BTB)_4\}\cdot12DMF\cdot22H_2O]$ was made to undergo cation exchange with several Rh, Pd, Ir, Fe and Ru complexes. The MOF supported $[Rh(dppe)(COD)]BF_4$ was found to catalyse the hydrogenation of 1-octene to n-octane with better yield and recyclability than the homogenous catalyst.[82] Another interesting application of non-centrosymmetric AMOFs can be seen in second harmonic generation in nonlinear optics. $[(H_2NMe_2)_2Cd_3(C_2O_4)_4]\cdot MeOH\cdot2H_2O$ is an octupolar open 3D framework, which shows high cation exchange rates with NH_4^+, Na^+ and K^+ and shows an unprecedented guest-cation-dependant non-linear optical activity.[83] Thus AMOFs are turning out to be an interesting class of MOFs where different specific applications can be generated by PSM of the framework via facile exchange with a definite cationic species. Ion exchange in anionic MOF has been also used to include Ag^+ cations in the framework and thereby use it for dye enrichment and separation of C_2 hydrocarbons from CH_4.[85]A water stable anionic MOF JXNU-4 has been utilized to separate positively charged ions of Methylene Blue selectively over negatively charged organic dyes like Resorufin. Moreover, the framework also shows a size exclusive sieving of Methylene Blue over other organic dye cations like Janus Green B and Ethyl violet.[86]

1.7 MOF Derived Carbonaceous Materials

The post synthetic treatment of MOFs in different conditions allows the conversion of other porous functional materials for specific applications. The growing interest regarding functional materials associated with molecules, ions and clusters in the nanometer ranges demands the controlled synthesis of nanomaterials with molecular, nanoscopic and mesoscopic structures. The exclusive interactions of such nanomaterials

within confined nanospaces produce unique nanoporous materials with a diverse range of specific applications starting from adsorption[87, 88] and catalysis[89] to electronics[90] and drug delivery[91]. Nanoporous carbon is the most significant in this regard for their great thermal and chemical stability. However, the traditional methods for synthesis of such porous carbon materials involves simple pyrolysis followed by physical or chemical activation of organic precursors, which often gives rise to highly disordered structures with broad pore size distribution. This paved the way for nanocasting or templating approaches, initiated using soft templates, e.g., resols and hard templates, e.g., zeolites.[92, 93] These were again found to be unsuitable for bulk scale production. In an innovative approach, Xu *et al.* first proposed MOFs as self sacrificial templates for effective synthesis of porous carbon.[94] In this work, furfuryl alcohol was impregnated into MOF-5 for this purpose followed by carbonization at 1000°C. The porous carbon material thus synthesized showed a high specific Brunauer-Emmett-Teller (BET) surface area of 2872 $m^2.g^{-1}$. This nanoporous carbon showed a good hydrogen storage capacity as well as exceptional electrochemical
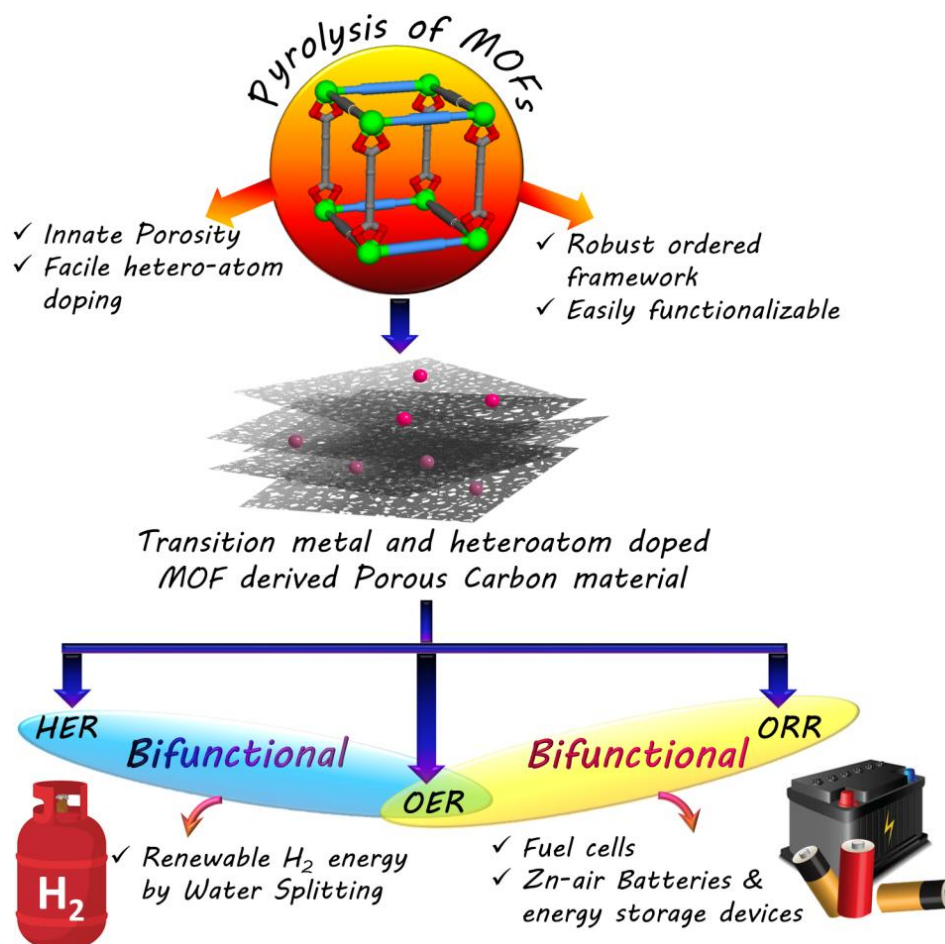
Fig. 15 Development of electrocatalysts from MOF derived carbon materials. Reproduced with permission from ref. no. 9. Copyright 2018 Royal Sciety of Chemistry.

activity as an electrode material for electrochemical double layer capacitor.[94] The inherent porosity of MOF, high surface area, large carbon content and ordered structure makes them ideal candidates as templates for carbon materials. They also ensure facile heteroatom and metal doping in the carbon matrix, thereby producing novel materials with enhanced properties (**Fig. 15**). Apart from furfuryl alcohol, glycerol[95], carbon tetrachloride, ethylenediamine and phenolic resin[96] have been used as carbon sources with MOF-5. Extremely high surface area nanoporous carbons have also been achieved by the carbonization of sucrose impregnated IRMOF-3[97] and the direct carbonization of pristine Al-PCP.[98] Quite a few MOFs have been employed in order to synthesize nanoporous carbons with ordered structure, narrow pore size distribution and higher surface areas.[87, 93, 96] A few very well-known MOFs, e.g., IRMOF-3,[99] MOF-5,[100] Al-PCP[101] and ZIF-8[102] have efficiently played the role of a promising precursor material, resulting in highly nanoporous carbons showing exceptional adsorption,[103] electrochemical capacitance,[94] drug delivery[91] and catalytic properties.[103] However, it is also possible to make such materials without the use of any external precursor and the original MOF linker is treated as a source for carbon as well as heteroatoms like N or S.[9] Porous carbon when doped with heteroatoms, e.g., N, S or B, have been reported to show enhanced electrocatalytic activities, comparable to some of the noble metal-based benchmark catalysts. In addition, if the original electroactive metal atom of the MOF is retained in the form of metal or metal oxide nanoparticles, the electrochemical activity can be further enhanced. Also, non-precious metal and metal oxide nanoparticles (NPs) supported on carbon matrix (MNPC) with high porosity offer numerous exposed and easily accessible active sites,
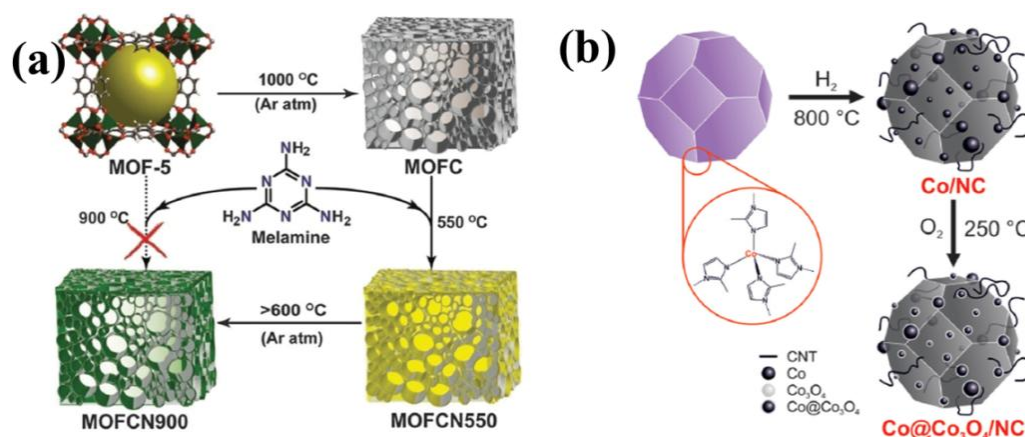
Fig. 16(a) Schematic representation of generation of graphitic carbon nitride from MOF 5 using melamine as a percursor. Reproduced with permission from Ref. no. 92. Copyright 2014 American Chemical Society. **(b)** Synthesis of Co@Co$_3$O$_4$/NC from ZIF-67 by tuning the annealing temperature and atmosphere. Reproduced with permission from Ref. no. 129. Copyright 2016 Wiley VCH.

thereby improving overall electrocatalytic activity.[104-109] To put it in layman's terms, electronic properties of a particular material dictates its efficiency as an electrocatalyst.[110-111] A pure graphitic carbon matrix consisting of sp^2 bonded carbon atoms with an uniformly delocalized electron cloud lacks polarization and consequently cannot afford to accomodate a foreign electronic cloud of intermediates.[112] Heteroatoms, e.g., N, B, P or S, with different electronegativities when introduced into this graphitic matrix, a redistribution of the elctronic cloud takes place, thereby creating a polarization which can now accommodate the foreign invasion of intermediates.[113, 114] The most commonly doped heteroatom is nitrogen which is more electronegative and hence these doping sites are potent for metal/functional group coordination and act as active sites for the electrocatalysis.[110, 111] The heteroatom doped carbon matrix have the potential to act as efficient metal free electrocatalysts.[115-122] One of the primary reasons to choose MOFs as templates for carbonization is the ease of including heteroatoms in the carbon matrix, by simply selecting a MOF with a heteroatom containing linker. For example, MOFs with imidazolate framework are often pyrolyzed at inert atmosphere to get N-doped carbon matrix with large surface area.[123-128]

Highly potent MOF-derived carbon-based electrocatalysts can be synthesized by carefully considering the following points:

1) Careful selection of the MOF is supremely important since ligand composition provides the carbon template with heteroatoms like N, P and S. Similarly, redox-active metal ion from the MOF provides the metal or metal oxide nanoparticles.

2) Morphology, size and shape of the as-synthesized MOF is also crucial as it determines the morphology and corresponding textural parameter of the resultant carbonaceous material.

3) Pyrolysis temperature and condition are also important parameters which plays a crucial role in determining the morphology and composition of the resultant carbon nanocomposite.

Muhler *et al.* showed the formation of coreshell $Co@Co_3O_4$ nanoparticles embedded in carbon nanotubes (CNTs) by the direct carbonization of ZIF-67, a Co imidazolate framework (**Fig. 16(b)**).[129] We showed the formation for Co doped carbon nanotubes (Co-CNTs) by the pyrolysis of dicyanamide based nitrogen rich MOF $\{[Co(bpe)_2(N(CN)_2)]\cdot(N(CN)_2)\cdot(5H_2O)\}_n$ [Co-MOF-1, bpe=1,2-bis(4-pyridyl)ethane, $N(CN)_2^-$ =dicyanamide].[130] However, in most cases, scientists opt for external N-sources like urea, melamine, etc. to generate N containing C materials. Kurungot *et al.* performed

the pyrolysis MOF5 in the presence of nitrogen rich melamine to generate g-C_3N_4 for electrocatalytic ORR (**Fig. 16(a)**).[92] Guest molecules impregnated within the MOF pores may also be used as a source of heteroatom.[131-135,123–128] Also, co-doping two or more elements with reverse electronegativity results in greater number of defects, generating more number of active sites for an elevated electrocatalytic activity. Thus, compared to single heteroatom doping, multiple heteroatom doping could be beneficial. For this, either the ligand must be selected such that it has the choice of heteroatoms or the MOF can be impregnated with heteroatom containing moieties.[9] Methodically developed MOF derived materials having favourable electronic structure with heteroatom doped carbon matrix loaded with metal or metal oxide NPs, can show excellent electrochemical activity. Moreover, suitable morphologies and pore structure that facilitate electron and mass transport are instrumental in developing highly potent electrocatalyst for OER, ORR and HER.[9] Targeted design and synthesis of tailored MOFs has the potential to develop next-generation materials with superior activity for the commercialization of energy devices like fuel cells and metal-air batteries.[9]

1.8 MOFs as Templates

As mentioned in the previous section, MOFs owing to their regular porous structures acts as an excellent self-sacrificial template for the synthesis of nanoporous carbons. In addition, MOFs can act as efficient supports or templates for accommodating activated species or nanoparticles (NPs) in order to provide them with extra stability.[136] The resultant composites often show unique properties that are better than the properties of the both starting components. Such species can be housed within the pores of the MOF either by interaction with the pore surface, or simply as guests without any interaction with the framework.[137] Although metal NPs or nanoclusters are well-known for their multifaceted applications in drug delivery and catalysis, they have high surface energy and tend to aggregate together, hindering the long-term storage, processing and application.[138] Their encapsulation within confined nanospaces, e.g., in a MOF pore can effectively prevent their aggregation. These composites have enhanced photo and electrocatalytic properties of the pristine molecules.[139] Kitagawa, *et. al.* have reported the remarkable enhancement in hydrogen storage capacity by coating Pd nanocrystals with
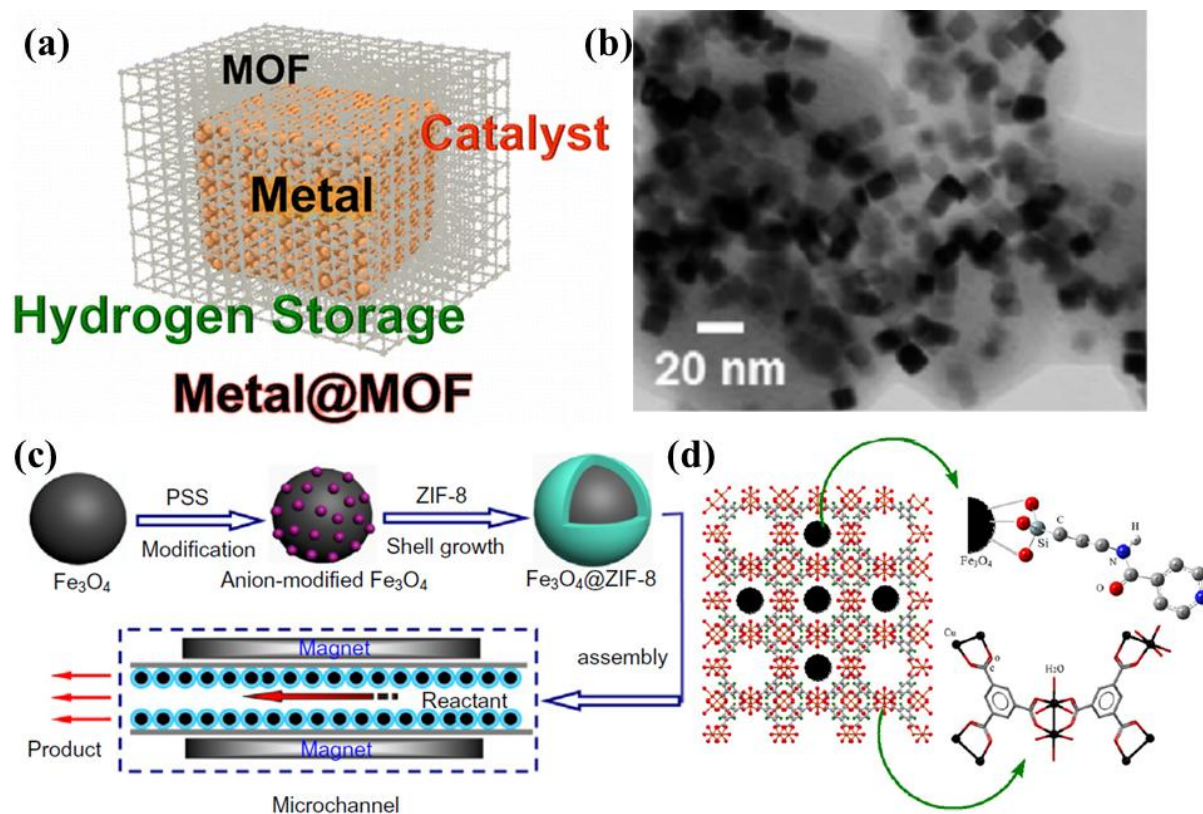
Fig. 17 (a) Multifunctional NP loaded MOFs. **(b)** Pd nanocrystals on HKUST-1 matrix. Reproduced with permission from ref. no. 140. Copyright 2016 American Society of Chemistry.**(c)** Formation of core-shell Fe_3O_4@ZIF-8. Reproduced with permission from ref. no. 143. Copyright 2013 Elsevier. **(d)** Magnetic core of Fe_3O_4@HKUST-1. Reproduced with permission from ref. no. 142. Copyright 2012 Elsevier.

HKUST-1 (Cu^{II} 1,3,5-benzenetricarboxylate) MOF which can be attributed to the charge transfer from Pd NPs to HKUST-1 (**Fig. 17(a)**). Bimetallic Pd-Au NPs have also been incorporated within ZIF-8 framework to show excellent catalytic activity for highly selective alcohol oxidation.[140] *In situ* stabilization of Pd NPs in a tris-aminophenyl amine based MOF with tri-coordinated N-centre enhances the overall H_2 storage of the framework.[141] Similarly, metal oxide nanomaterials which have controllable morphology, size and functionality have found widespread application in optics, electrochemistry, catalysis and photovoltaics. Incorporating them within the cavities of MOF can enhance their durability and their properties. Fe_3O_4 NPs were loaded within both HKUST-1 and ZIF-8 to obtain two magnetic composites. While Fe_3O_4@HKUST-1 can assist in the removal of palladium from environmental samples,[142] Fe_3O_4@ZIF-8 can be easily loaded and unloaded within a capillary microreactor with the help of an external magnetic field (**Fig. 17(b, c)**).[136, 143]

In the world of nanocrystals, perovskite quantum dots (PQDs) have attracted significant attention from materials scientists all over the world owing to their unique set

of properties namely tunable wavelength, narrow emission, and high photoluminescence quantum efficiency (PLQY).[144] In recent times, a wide range of halide PQDs with distinct salient features including cesium lead halide ($CsPbBr_3$) and organic–inorganic mixed cations, e.g. formamidinium ($FAPbBr_3$), methylammonium ($MAPbBr_3$), and also divalent cation doped colloidal $CsPb_{1-x}M_xBr_3$ PQDs (M = Sn^{2+}, Cd^{2+}, Zn^{2+}, Mn^{2+}) PQDs
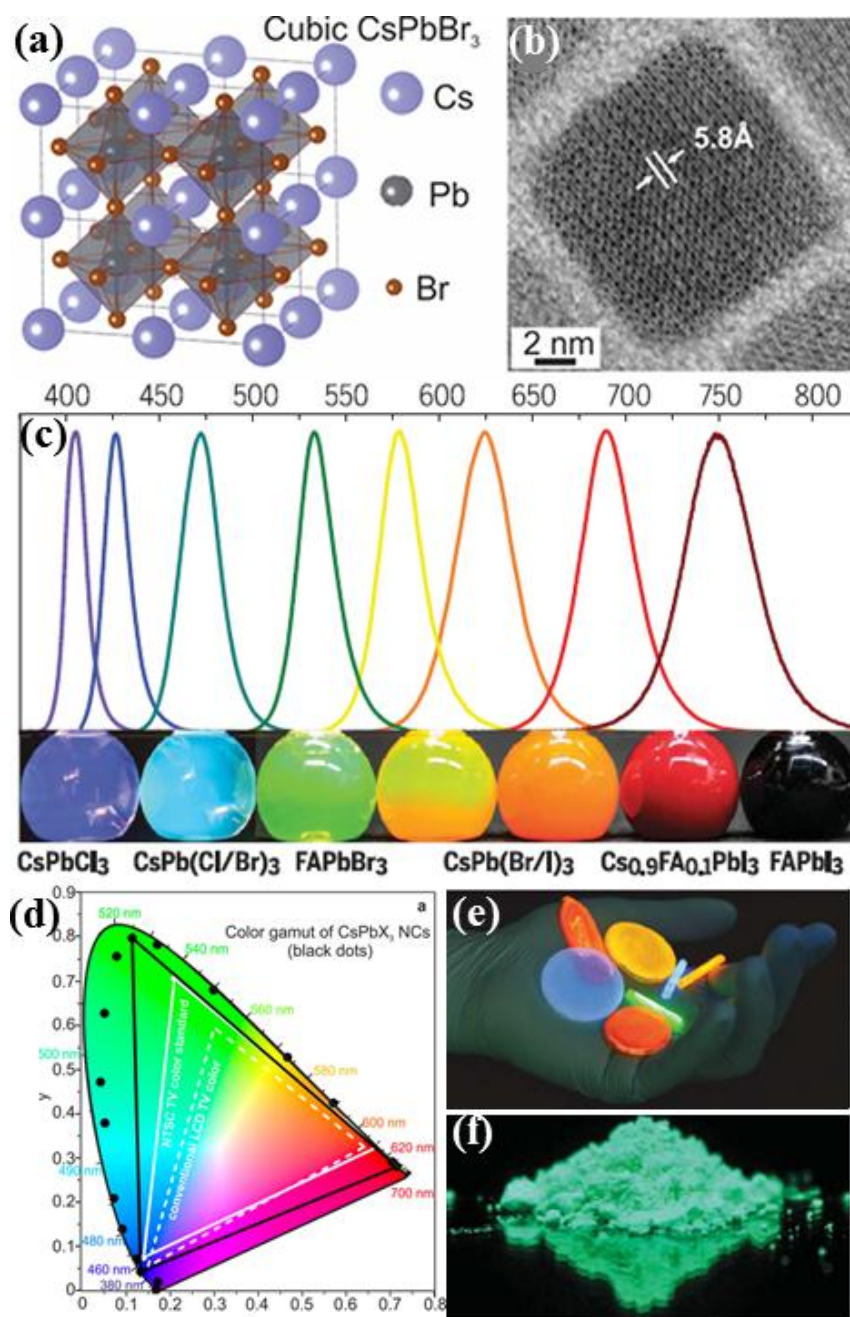
Fig. 18 (a) Schematic representation of the cubic perovskite lattice. **(b)** Typical TEM image of $CsPbBr_3$ NCs. **(c)** Emission of $CsPbX_3$ NCs (black points) plottedon CIE chromaticity coordinates and compared to the color standards of LCD TV(dotted white triangle) and NTSC TV (solidwhite triangle). **(c)** Photograph (λ_{ex} = 365 nm) of highly luminescent $CsPbX_3$NCs-PMMA polymer monoliths obtained with Irgacure 819 asphotoinitiator for polymerization.**(d)** Photograph of mesoporous silica impregnated with $CsPbBr_3$ under UV lamp. Reproduced with permission from ref. no. 144 and 145. Copyright AAAS and American Chemical Society.

have been reported.[145] Such PQDs have opened new avenues for efficient optoelectronic devices for use in lighting and backlight displays, photovoltaics, photocatalysis, sensors, LEDs and security inks.[146, 147] Hybrid organic-inorganic lead halides (MAPbX$_3$, X=Cl, Br or I) based photovoltaic devices have been able to achieve certified power efficiencies upto 20%, which has intrigued scientists globally.[148-151] Such semiconducting nanocrystals often show fascinating features when their radius is reduced than the respective exciton Bohr radius, thereby forming quantum dots with bandgap expansion, enhanced Coulombic attraction of the paired charges, slower electron-photon relaxation and energy level quantization.[152-155] However the properties and applications of colloidal nanoparticles
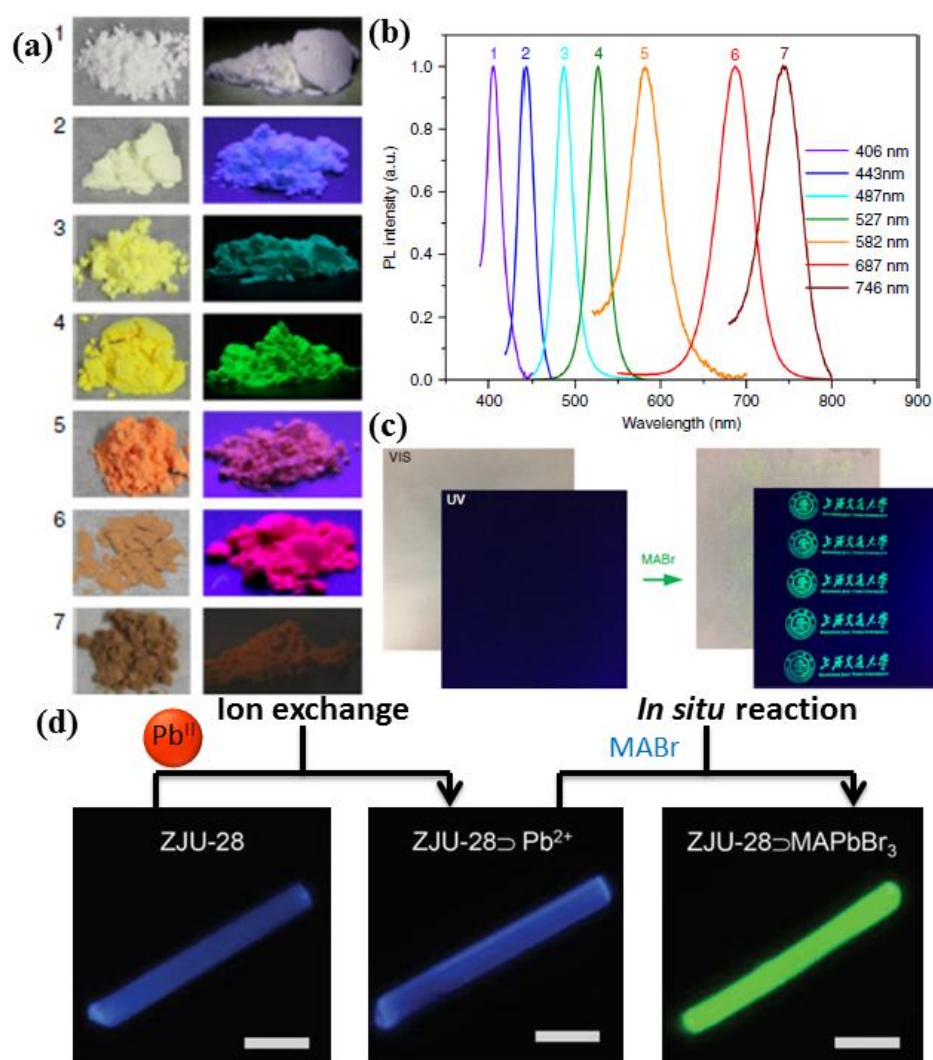
Fig. 19 (a) Optical images of PQDs generated from the Pb-based MOF under ambient light and 365 nm UV lamp. **(b)**Emission spectra of MAPbX$_3$ NCs@Pb-MOF. (1: MAPbCl$_3$, 2: MAPbCl$_2$Br, 3: MAPbClBr$_2$, 4: MAPbBr$_3$, 5: MAPbBr$_2$I, 6:MAPbBrI$_2$, 7: MAPbI$_3$). **(c)** Digital images of the printed logo of a University on a commercial parchment paper before and after MABr loading under ambient light and a 365 nm UV lamp. Reproduced with permission from ref. no. 163. Creative Commons Copyright 2017. **(d)** Optical images of a single crystal of ZJU-28, ZJU-28⊃Pb^{2+}, and ZJU-28⊃MAPbBr$_3$ upon excitation of 365 nm. Reproduced with permission from ref. no. 165. Copyright 2018 Wiley-VCH.

these compounds remain largely unexplored. Colloidal nanocrystal PQDs are easily dispersed in solutions thereby making them useful for procedures like spin-coating and additive manufacturing which helps in coating them over flexible large areas and thus develop inexpensive devices.[147] Also such colloidal nanocrystals can be easily conglomerated with other solution processable materials, e.g., amorphous carbons, fullerenes, carbon nanotubes and polymers in order to generate novel composites with superior optoelectronic, magnetic and catalytic activities. However, the widespread commercialization of such PQDs is hindered by their limited stability in air and other solvents, which lowers their processibility.[156] The ionic character of these PQDs along with their labile surfaces and metastable characters make them extremely unstable in nature and prone to degradation by temperature, oxygen, moisture and light.[144, 145, 157] While oxygen atmosphere and moisture-facilitated ion migration easily etches the unstable PQDs, easy ion migration also results in crystal growth, which lowers the PLQY. The higher stability and quantum confinement effect in these particles can be induced by entrapping them within a porous matrix, which will provide it with extra robustness and also help in the formation of well separated stabilized particles. Porous templates like MOFs, CMPs, zeolites and silica have been used extensively over the decades to stabilize simple inorganic nanoparticles, e.g., metals, oxides, sulphides, carbons or semiconductors for applications in catalysis, magnetism and optoelectronics.[139, 158, 159] Accordingly, Yamauchi, *et al*. were able to grow 0D and 1D $MAPbBr_3$ PQDs within a mesoporous silica template, where the size of the particles and in turn their optical band gap and emission varied according to the pore size of the template.[160] They were also able to synthesize $MAPbBr_3$ PQDs within gyroidal silica template where due to easier solvent accessibility, isolated nanoparticles were formed within the pores.[161] Wang, *et al.* also synthesized a mesoporous PQD nanocomposite with $CsPbX_3$ particles loaded in mesoporous silica which made it possible to mix these particles without anion exchange for backlight displays.[162] Of late, attempts have also been made to incorporate PQDs within MOF structures in order to regulate their size as well as provide them with superior stability.[164] Encryption and decryption based on a security ink was achieved by Zhang, *et al*. by converting a Pb^{II}-based MOF into $CsPbBr_3$ PQDs. But during this process the MOF itself was broken down and the Pb nodes contributed to the formation of the PQDs.[163] In a very interesting approach, the single crystal of an anionic MOF ZJU-28 was used for the facile capture of Pb^{II} by cation exchange with the guest dimethylammonium counter cation. Thereby, it was treated with an ethanolic solution of

MABr to form confined MAPbBr$_3$ PQDs within the single crystal.[165] All these approaches have paved the way for further research on PQDs confined within the MOF matrix, where their size and optical properties can also be modulated by the MOF template, while providing the superior stability. Such PQD@MOF composites with their unique set of properties can be extremely crucial in the fabrication of new devices.

1.9 Scope of the Work

Over the past two decades, MOFs have emerged as a new generation porous material for varied applications like gas storage and separation, heterogeneous catalysis, luminescence, drug delivery and sensing. Besides the traditional rigid porous frameworks, flexible and dynamic frameworks have emerged as efficient systems for specific adsorption and separation of gas molecules. However, like any other material, these systems all have their own drawbacks. The following section summarizes the lacunae existing in the various applicative studies of MOFs and the endeavours made in this thesis to bridge the gap between potential and practical applications. Over the years, several MOFs have been reported for the adsorption of the gases. However the selective adsorption of a particular gas over another and the basis of the selective adsorption are not well studied. Also, the separation of small hydrocarbons using flexible MOFs is rarely studied. Moreover, the role of these materials in practical separation of gases is rarely established. Hence in the first part of this thesis, we have designed and synthesized frameworks which can separate CO_2/N_2 as well as mixtures of small hydrocarbons. In order to establish the practical applicability of these materials in gas separation, we have devised a breakthrough setup involving a gas chromatogram and a mass flow controller. The MOF is packed into a column and it is purged with a gas mixture, which is separated based on the selective adsorption of a particular component and the eluent is detected through gas chromatography. Two tetracarboxylate ligand based Cu^{II} MOFs with very different structural properties have been studied in this thesis. Among these, the flexible tetracarboxylate based interpenetrated framework shows excellent performance as an adsorptive separator of CO_2/N_2 and C_2H_2/C_2H_4 gases. A dynamic Mg^{II} based framework has also been synthesized, which shows structural variations based on the removal of guest molecules and it also shows excellent efficiency for the separation of C_2H_2/C_2H_4 gases in a breakthrough setup.

Part 1: Flexible MOFs for Gas Separation

Part 2: Anionic MOFs & Derived Materials
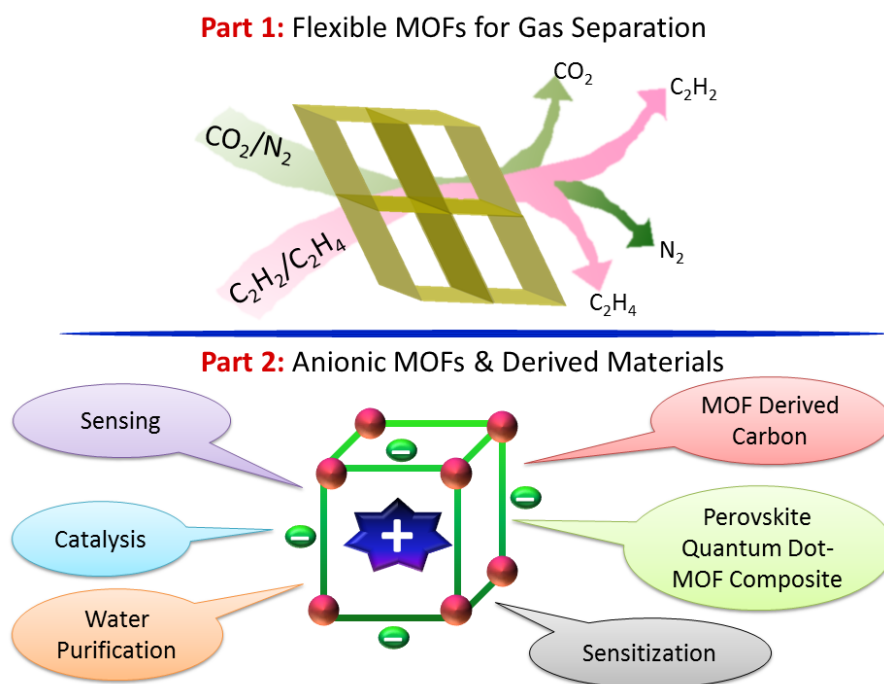
Fig. 20 Topics covered in this thesis.

Apart from gas adsorption and separation, other applications of MOFs, e.g., catalysis, optoelectronics and sensing, requires specific functionalization which can be easily imbibed through post-synthetic modification (PSM). One of the most suitable candidates for such PSM are anionic MOFs which can be tailored to suit diverse specific applications simply by the exchange of the guest counter cation with exogenous cationic species. While neutral MOFs are well reported and studied in literature, ionic MOFs have been rarely explored. Anionic MOFs have frameworks that are negatively charged but the overall structural charge neutrality is maintained by a guest cation. These guest cations can be exchanged with other extra-framework cationic species to get specific applications. But till date, the number of reported anionic MOFs is merely a handful and many interesting applications, e.g., specific sensitization, catalysis or water purification have not been realized. Also, such anioinic MOFs have never been used as templates for the facile synthesis of other derived materials like MOF derived carbons and other nanocomposites. In my thesis, I have focussed extensively on the different applications that can be obtained from anionic MOFs and also tried to demonstrate its facile conversion into other derivatives. I have aimed at the targeted synthesis of such an AMOF which can act as both a selective Cu^{II} sensor and specific Eu^{III} sensitizer. Also this AMOF has been used for the dual synthesis of nanoporous carbon with exceptionally high surface area as well as graphitic carbon nitride using the guest dimethylammonium

cation as a precursor. Another water stable AMOF has been exploited for the capture of hazardous heavy metal cations like Pb^{II}, Cd^{II} and Hg^{II} from solutions of very low concentration. Further the Pb^{II} loaded MOF has been converted to a value-added $CsPbX_3$ perovskite quantum dot@MOF composite via a simple mechanochemical method which shows excellent optoelectronic properties and superior stability. Thus while this thesis shows the practical application of MOFs for gas separation on one hand, on the other it explores very important applications of MOFs like water purification, catalysis and sensitization via anionic MOFs.

1.10 References

1. P. Vanelderen, J. Vancauwenbergh, B. F. Sels and R. A. Schoonheydt, *Coord. Chem. Rev.*, 2013, **257**, 483.

2. Y. Wei, T. E. Parmentier, K. P. de Jong and J. Zečević, *Chem.Soc.Revi.*, 2015, **44**, 7234.

3. M. O'Keeffe, *Philos.Trans. Royal Soc. A*, 2014, **372**, 20120034.

4. L. Wang and X. Hu, *Chem. Asian J.,* 2018, **13**, 1518.

5. B. Sakintuna and Y. Yürüm, *Ind. Eng. Chem. Res.*, 2005, **44**, 2893.

6. Y. Xia, Z. Yang and Y. Zhu, *J. Mater.Chem. A*, 2013, **1**, 9365.

7. J. L. Figueiredo, *J. Mater. Chem. A*, 2013, **1**, 9351.

8. S. Kapri, R. Majee and S. Bhattacharyya, *ACS Sus. Chem. Eng.*, 2018, **6**, 8503.

9. S. Bhattacharyya, C. Das and T. K. Maji, *RSC Adv.s*, 2018, **8**, 26728.

10. S. Kitagawa, R. Kitaura and S.-i. Noro, *Angew. Chem. Int. Ed.*, 2004, **43**, 2334.

11. M. L. Foo, R. Matsuda and S. Kitagawa, *Chem.Mater.*, 2014, **26**, 310.

12. H.-C. Zhou, J. R. Long and O. M. Yaghi, *Chem. Rev.*, 2012, **112**, 673.

13. G. Ferey, *Chem. Soc. Rev.*, 2008, **37**, 191.

14. O. M. Yaghi, M. O'Keeffe, N. W. Ockwig, H. K. Chae, M. Eddaoudi and J. Kim, *Nature*, 2003, **423**, 705.

15. S. L. James, *Chem. Soc. Rev.*, 2003, **32**, 276.

16. S. Yuan, L. Feng, K. Wang, J. Pang, M. Bosch, C. Lollar, Y. Sun, J. Qin, X. Yang, P. Zhang, Q. Wang, L. Zou, Y. Zhang, L. Zhang, Y. Fang, J. Li and H.-C. Zhou, *Adv. Mater.*, 2018, **30**, 1704303.

17. A. Kirchon, L. Feng, H. F. Drake, E. A. Joseph and H.-C. Zhou, *Chem. Soc. Rev.*, 2018, **47**, 8611.

18. R. Haldar, N. Sikdar and T. K. Maji, *Mater. Today*, 2015, **18**, 97.

19. R. Haldar and T. K. Maji, *CrystEngComm*, 2013, **15**, 9276.

20. D. B. Leznoff, B.-Y. Xue, R. J. Batchelor, F. W. B. Einstein and B. O. Patrick, *Inorg. Chem.*, 2001, **40**, 6026.

21. V. Niel, M. C. Muñoz, A. B. Gaspar, A. Galet, G. Levchenko and J. A. Real, *Chem. Eur. J.*, 2002, **8**, 2446.

22. S.-I. Nishikiori, *J. Coord. Chem.*, 1996, **37**, 23.

23. S.-S. Yun, Y.-P. Kim and C.-H. Kim, *Acta Crystallograph. C*, 1999, **55**, 2026.

24. H. Yuge, Y. Noda and T. Iwamoto, *Inorg. Chem.*, 1996, **35**, 1842.

25. D. W. Knoeppel, J. Liu, E. A. Meyers and S. G. Shore, *Inorg. Chem.*, 1998, **37**, 4828.

26. J. O. Eriksen, A. Hazell, A. Jensen, J. Jepsen and R. D. Poulsen, *Acta Crystallograph. C*, 2000, **56**, 551.

27. A. Marvilliers, S. Parsons, E. Rivière, J.-P. Audière, M. Kurmoo and T. Mallah, *Eur. J. Inorg. Chem.*, 2001, **2001**, 1287.

28. M. W. B. Ziegler, M. Schwarten, D. Babel, *Z. Naturforsch. B*, 1999, **54**, 6.

29. J. Larionova, O. Kahn, S. Golhen, L. Ouahab and R. Clérac, *Inorg. Chem.*, 1999, **38**, 3621.

30. A. K. Sra, G. Rombaut, F. Lahitete, S. Golhen, L. Ouahab, C. Mathoniere, J. V. Yakhmi and O. Kahn, *New J. Chem.*, 2000, **24**, 871.

31. Y. Ling, Z.-X. Chen, F.-P. Zhai, Y.-M. Zhou, L.-H. Weng and D.-Y. Zhao, *Chem. Commun.*, 2011, **47**, 7197.

32. X. Lin, J. Jia, X. Zhao, K. M. Thomas, A. J. Blake, G. S. Walker, N. R. Champness, P. Hubberstey and M. Schröder, *Angew. Chem. Int. Ed.*, 2006, **45**, 7358.

33. L. H. Wee, C. Wiktor, S. Turner, W. Vanderlinden, N. Janssens, S. R. Bajpe, K. Houthoofd, G. Van Tendeloo, S. De Feyter, C. E. A. Kirschhock and J. A. Martens, *J. Am. Chem. Soc.*, 2012, **134**, 10911.

34. Z. Pan, H. Zheng, T. Wang, Y. Song, Y. Li, Z. Guo and S. R. Batten, *Inorg. Chem.*, 2008, **47**, 9528.

35. M. Rubio-Martinez, C. Avci-Camur, A. W. Thornton, I. Imaz, D. Maspoch and M. R. Hill, *Chem. Soc. Rev.*, 2017, **46**, 3453.

36. N. Stock and S. Biswas, *Chem. Rev.*, 2012, **112**, 933.

37. S. Horike, S. Shimomura and S. Kitagawa, *Nat Chem*, 2009, **1**, 695.

38. A. Dhakshinamoorthy, M. Opanasenko, J. Čejka and H. Garcia, *Catal. Sci. Technol.*, 2013, **3**, 2509.

39. L. Sun, M. G. Campbell and M. Dincă, *Angew. Chem. Int. Ed.*, 2016, **55**, 3566.

40. M.-X. Wu and Y.-W. Yang, *Adv. Mater.*, 2017, **29**, 1606134.

41. K. Vikrant, V. Kumar, Y. S. Ok, K.-H. Kim and A. Deep, *Trends Anal. Chem.*, 2018, **105**, 263.

42. M. P. Suh, H. J. Park, T. K. Prasad and D.-W. Lim, *Chem. Rev.*, 2012, **112**, 782.

43. H. Furukawa, N. Ko, Y. B. Go, N. Aratani, S. B. Choi, E. Choi, A. Ö. Yazaydin, R. Q. Snurr, M. O'Keeffe, J. Kim and O. M. Yaghi, *Science*, 2010, **329**, 424.

44. N. Kosinov, J. Gascon, F. Kapteijn and E. J. M. Hensen, *J. Membr. Sci.*, 2016, **499**, 65.

45. Z. Kang, L. Fan and D. Sun, *J.Mater. Chem. A*, 2017, **5**, 10073.

46. K. Sumida, D. L. Rogow, J. A. Mason, T. M. McDonald, E. D. Bloch, Z. R. Herm, T.-H. Bae and J. R. Long, *Chem. Rev.*, 2012, **112**, 724.

47. H. Li, K. Wang, Y. Sun, C. T. Lollar, J. Li and H.-C. Zhou, *Mater. Today*, 2018, **21**, 108.

48. Z. Bao, G. Chang, H. Xing, R. Krishna, Q. Ren and B. Chen, *Energy Environ. Sci.*, 2016, **9**, 3612.

49. A. Hazra, S. Jana, S. Bonakala, S. Balasubramanian and T. K. Maji, *Chem. Commun.*, 2017, **53**, 4907.

50. L. Li, R.-B. Lin, R. Krishna, X. Wang, B. Li, H. Wu, J. Li, W. Zhou and B. Chen, *J. Mater. Chem. A*, 2017, **5**, 18984.

51. A. Schneemann, V. Bon, I. Schwedler, I. Senkovska, S. Kaskel and R. A. Fischer, *Chem. Soc. Rev.*, 2014, **43**, 6062.

52. J.-R. Li, R. J. Kuppler and H.-C. Zhou, *Chem. Soc. Rev.*, 2009, **38**, 1477.

53. Y. Wang and D. Zhao, *Cryst. Growth Des.*, 2017, **17**, 2291.

54. S. J. Geier, J. A. Mason, E. D. Bloch, W. L. Queen, M. R. Hudson, C. M. Brown and J. R. Long, *Chem. Sci.*, 2013, **4**, 2054.

55. E. D. Bloch, W. L. Queen, R. Krishna, J. M. Zadrozny, C. M. Brown and J. R. Long, *Science*, 2012, **335**, 1606.

56. X. Li, X.-W. Wang and Y.-H. Zhang, *Inorg. Chem. Commun.*, 2008, **11**, 832.

57. Y. Cui, Y. Yue, G. Qian and B. Chen, *Chem. Rev.*, 2012, **112**, 1126.

58. G.-H. Wang, Z.-G. Li, H.-Q. Jia, N.-H. Hu and J.-W. Xu, *CrystEngComm*, 2009, **11**, 292.

59. S. Roy, A. Chakraborty and T. K. Maji, *Coord. Chem. Rev.*, 2014, **273–274**, 139.

60. E. G. Moore, A. P. S. Samuel and K. N. Raymond, *Acc. Chem. Res.*, 2009, **42**, 542.

61. L. K. Cadman, M. F. Mahon and A. D. Burrows, *Dalton Trans.*, 2018, **47**, 2360.

62. F. Luo and S. R. Batten, *Dalton Trans.*, 2010, **39**, 4485.

63. K. Binnemans, *Chem. Rev.*, 2009, **109**, 4283.

64. R. Haldar, R. Matsuda, S. Kitagawa, S. J. George and T. K. Maji, *Angew. Chem.*, 2014, **126**, 11966.

65. A. Corma, *Chem. Rev.*, 1995, **95**, 559.

66. A. Corma, *Chemical Reviews*, 1997, **97**, 2373.

67. M. Liu, J. Wu and H. Hou, *Chem. Euro. J.*, 2019, **25**, 2935.

68. X.-L. Yang, M.-H. Xie, C. Zou, Y. He, B. Chen, M. O'Keeffe and C.-D. Wu, *J. Am. Chem. Soc.*, 2012, **134**, 10638.

69. M. Zhao, K. Yuan, Y. Wang, G. Li, J. Guo, L. Gu, W. Hu, H. Zhao and Z. Tang, *Nature*, 2016, **539**, 76.

70. Z. Lei, Y. Xue, W. Chen, W. Qiu, Y. Zhang, S. Horike and L. Tang, *Adv. Energy Mater.*, 2018, **8**, 1801587.

71. D. Ma, B. Li, K. Liu, X. Zhang, W. Zou, Y. Yang, G. Li, Z. Shi and S. Feng, *J. Mater. Chem. A*, 2015, **3**, 23136.

72. Z. Gu, W. Song, Z. Yang and R. Zhou, *Phys. Chem. Chem. Phys.*, 2018, **20**, 30384.

73. D. T. Sun, L. Peng, W. S. Reeder, S. M. Moosavi, D. Tiana, D. K. Britt, E. Oveisi and W. L. Queen, *ACS Cent. Sci.*, 2018, **4**, 349.

74. S. M. Cohen, *Chem. Rev.*, 2012, **112**, 970.

75. Z. Wang and S. M. Cohen, *J. Am. Chem. Soc.*, 2007, **129**, 12368.

76. K. K. Tanabe, Z. Wang and S. M. Cohen, *J. Am. Chem. Soc.*, 2008, **130**, 8508.

77. S. S.-Y. Chui, S. M.-F. Lo, J. P. H. Charmant, A. G. Orpen and I. D. Williams, *Science*, 1999, **283**, 1148.

78. T. Yamada and H. Kitagawa, *J. Am. Chem. Soc.*, 2009, **131**, 6312.

79. J. An, S. J. Geib and N. L. Rosi, *J. Am. Chem. Soc.*, 2009, **131**, 8376.

80. J. An and N. L. Rosi, *J. Am. Chem. Soc.*, 2010, **132**, 5578.

81. J. An, C. M. Shade, D. A. Chengelis-Czegan, S. Petoud and N. L. Rosi, *J. Am. Chem. Soc.*, 2011, **133**, 1220.

82. D. T. Genna, A. G. Wong-Foy, A. J. Matzger and M. S. Sanford, *J. Am. Chem. Soc.*, 2013, **135**, 10586.

83. Y. Liu, G. Li, X. Li and Y. Cui, *Angew. Chem.*, 2007, **119**, 6417.

84. M. Kim, J. F. Cahill, H. Fei, K. A. Prather and S. M. Cohen, *J. Am. Chem. Soc.*, 2012, **134**, 18082.

85. Y.-X. Tan, Y. Zhang, Y.-P. He, Y.-J. Zheng and J. Zhang, *Inorg. Chem.*, 2014, **53**, 12973.

86. H.-F. Ma, Q.-Y. Liu, Y.-L. Wang and S.-G. Yin, *Inorg. Chem.*, 2017, **56**, 2919.

87. W. Wang and D. Yuan, *Sci. Rep.*, 2014, **4**, 5711.

88. I. Cabasso, S. Li, X. Wang and Y. Yuan, *RSC Adv.*, 2012, **2**, 4079.

89. M. G. Stevens, K. M. Sellers, H. C. Foley and S. Subramoney, *Chem. Commun.*, 1998, 2679.

90. C. Merlet, B. Rotenberg, P. A. Madden, P.-L. Taberna, P. Simon, Y. Gogotsi and M. Salanne, *Nat Mater*, 2012, **11**, 306.

91. Y. L. Nagy L. Torad, Shinsuke Ishihara, Katsuhiko Ariga, Yuichiro Kamachi, Hong-Yuan Lian, Hicham Hamoudi, Yoshio Sakka, Watcharop Chaikittisilp, Kevin C.-W. Wu and Yusuke Yamauchi, *Chem. Lett.*, 2014, **43**, 2.

92. S. Pandiaraj, H. B. Aiyappa, R. Banerjee and S. Kurungot, *Chem. Commun.*, 2014, **50**, 3363.

93. W. Chaikittisilp, K. Ariga and Y. Yamauchi, *J. Mater. Chem. A*, 2013, **1**, 14.

94. B. Liu, H. Shioyama, T. Akita and Q. Xu, *J. Am. Chem. Soc*, 2008, **130**, 5390.

95. D. Yuan, J. Chen, S. Tan, N. Xia and Y. Liu, *Electrochem. Commun.*, 2009, **11**, 1191.

96. J. Hu, H. Wang, Q. Gao and H. Guo, *Carbon*, 2010, **48**, 3599.

97. K. Jayaramulu, K. K. R. Datta, K. Shiva, A. J. Bhattacharyya, M. Eswaramoorthy and T. K. Maji, *Micropor. Mesopor. Mater.*, 2015, **206**, 127.

98. M. Hu, J. Reboul, S. Furukawa, N. L. Torad, Q. Ji, P. Srinivasu, K. Ariga, S. Kitagawa and Y. Yamauchi, *J. Am. Chem. Soc.*, 2012, **134**, 2864.

99. J. L. C. Rowsell and O. M. Yaghi, *J. Am. Chem. Soc.*, 2006, **128**, 1304.

100. H. Li, M. Eddaoudi, M. O'Keeffe and O. M. Yaghi, *Nature*, 1999, **402**, 276.

101. A. Comotti, S. Bracco, P. Sozzani, S. Horike, R. Matsuda, J. Chen, M. Takata, Y. Kubota and S. Kitagawa, *J. Am. Chem. Soc.*, 2008, **130**, 13664.

102. K. S. Park, Z. Ni, A. P. Côté, J. Y. Choi, R. Huang, F. J. Uribe-Romo, H. K. Chae, M. O'Keeffe and O. M. Yaghi, *Proc. Nat. Acad. Sci.*, 2006, **103**, 10186.

103. A. Aijaz, N. Fujiwara and Q. Xu, *J. Am. Chem. Soc.*, 2014, **136**, 6790.

104. H.-W. Liang, W. Wei, Z.-S. Wu, X. Feng and K. Müllen, *J. Am. Chem. Soc.*, 2013, **135**, 16002.

105. Z.-S. Wu, S. Yang, Y. Sun, K. Parvez, X. Feng and K. Müllen, *J. Am. Chem. Soc.*, 2012, **134**, 9082.

106. D. Guo, R. Shibuya, C. Akiba, S. Saji, T. Kondo and J. Nakamura, *Science*, 2016, **351**, 361.

107. J. Masa, W. Xia, I. Sinev, A. Zhao, Z. Sun, S. Grützke, P. Weide, M. Muhler and W. Schuhmann, *Angew. Chem. Int. Ed.* 2014, **53**, 8508.

108. Q. Liu, J. Tian, W. Cui, P. Jiang, N. Cheng, A. M. Asiri and X. Sun, *Angew. Chem. Int. Ed.*, 2014, **53**, 6710.

109. X. Wang, Y. V. Kolen'ko, X.-Q. Bao, K. Kovnir and L. Liu, *Angew. Chem. Int. Ed.*, 2015, **54**, 8188.

110. J. Duan, S. Chen, M. Jaroniec and S. Z. Qiao, *ACS Catal.*, 2015, **5**, 5207.

111. Y. Zheng, Y. Jiao, M. Jaroniec and S. Z. Qiao, *Angew. Chem. Int. Ed.*, 2015, **54**, 52.

112. L. Zhang and Z. Xia, *J. Phys. Chem. C*, 2011, **115**, 11170.

113. K.-H. Wu, D.-W. Wang, D.-S. Su and I. R. Gentle, *ChemSusChem*, 2015, **8**, 2772.

114. B. D. Mohapatra, S. P. Mantry, N. Behera, B. Behera, S. Rath and K. S. K. Varadwaj, *Chem. Commun.*, 2016, **52**, 10385.

115. J. Zhang, Z. Zhao, Z. Xia and L. Dai, *Nat. Nanotechnol.*, 2015, **10**, 444.

116. C. H. Lee, B. Jun and S. U. Lee, *ACS Sus. Chem. Eng.*, 2018, **6**, 4973.

117. D. K. Singh, R. N. Jenjeti, S. Sampath and M. Eswaramoorthy, *J. Mater. Chem. A*, 2017, **5**, 6025.

118. M. Park, T. Lee and B.-S. Kim, *Nanoscale*, 2013, **5**, 12255.

119. J. Yang, M. Xu, J. Wang, S. Jin and B. Tan, *Sci. Rep.*, 2018, **8**, 4200.

120. J. Zhang and L. Dai, *ACS Catal.*, 2015, **5**, 7244.

121. A. J. Bard, *J. Am. Chem. Soc.*, 2010, **132**, 7559.

122. S. Zhang, Y. Cai, H. He, Y. Zhang, R. Liu, H. Cao, M. Wang, J. Liu, G. Zhang, Y. Li, H. Liu and B. Li, *J. Mater. Chem. A*, 2016, **4**, 4738.

123. D. Zhao, J.-L. Shui, L. R. Grabstanowicz, C. Chen, S. M. Commet, T. Xu, J. Lu and D.-J. Liu, *Adv. Mater.*, 2014, **26**, 1093.

124. B. Chen, R. Li, G. Ma, X. Gou, Y. Zhu and Y. Xia, *Nanoscale*, 2015, **7**, 20674.

125. P. Zhang, F. Sun, Z. Xiang, Z. Shen, J. Yun and D. Cao, *Energy Environ. Sci.*, 2014, **7**, 442.

126. W. Xia, R. Zou, L. An, D. Xia and S. Guo, *Energy Environ. Sci.*, 2015, **8**, 568.

127. W. Zhang, Z.-Y. Wu, H.-L. Jiang and S.-H. Yu, *J. Am. Chem. Soc.*, 2014, **136**, 14385.

128. Q. Lai, Y. Zhao, Y. Liang, J. He and J. Chen, *Adv. Funct. Mater.*, 2016, **26**, 8334.

129. A. Aijaz, J. Masa, C. Rösler, W. Xia, P. Weide, A. J. R. Botz, R. A. Fischer, W. Schuhmann and M. Muhler, *Angew. Chem. Int. Ed.*, 2016, **55**, 4087.

130. S. Roy, A. Bandyopadhyay, M. Das, P. P. Ray, S. K. Pati and T. K. Maji, *J. Mater. Chem. A*, 2018, **6**, 5587.

131. L. Zhang, X. Wang, R. Wang and M. Hong, *Chem. Mater.*, 2015, **27**, 7610.

132. J.-S. Li, Y.-J. Tang, C.-H. Liu, S.-L. Li, R.-H. Li, L.-Z. Dong, Z.-H. Dai, J.-C. Bao and Y.-Q. Lan, *J. Mater. Chem. A*, 2016, **4**, 1202.

133. J. Liu, D. Zhu, C. Guo, A. Vasileff and S.-Z. Qiao, *Adv. Energy Mater.*, 2017, **7**, 1700518.

134. J.-S. Li, S.-L. Li, Y.-J. Tang, M. Han, Z.-H. Dai, J.-C. Bao and Y.-Q. Lan, *Chem. Commun.*, 2015, **51**, 2710.

135. Q. Ren, H. Wang, X.-F. Lu, Y.-X. Tong and G.-R. Li, *Adv. Sci.*, 2018, **5**, 1700515.

136. Q.-L. Zhu and Q. Xu, *Chem. Soc. Rev.*, 2014, **43**, 5468.

137. M.-L. Hu, M. Y. Masoomi and A. Morsali, *Coord. Chem. Rev.*, 2019, **387**, 415.

138. J. Yu, C. Mu, B. Yan, X. Qin, C. Shen, H. Xue and H. Pang, *Mater. Horizons*, 2017, **4**, 557.

139. Q. Yang, Q. Xu and H.-L. Jiang, *Chem. Soc. Rev.*, 2017, **46**, 4774.

140. H. Kobayashi, Y. Mitsuka and H. Kitagawa, *Inorganic Chemistry*, 2016, **55**, 7301.

141. Y. E. Cheon and M. P. Suh, *Angew. Chem. Int. Ed.*, 2009, **48**, 2899.

142. A. Bagheri, M. Taghizadeh, M. Behbahani, A. Akbar Asgharinezhad, M. Salarian, A. Dehghani, H. Ebrahimzadeh and M. M. Amini, *Talanta*, 2012, **99**, 132.

143. T. Zhang, X. Zhang, X. Yan, L. Kong, G. Zhang, H. Liu, J. Qiu and K. L. Yeung, *Chem. Eng. J.*, 2013, **228**, 398.

144. M. V. Kovalenko, L. Protesescu and M. I. Bodnarchuk, *Science*, 2017, **358**, 745.

145. L. Protesescu, S. Yakunin, M. I. Bodnarchuk, F. Krieg, R. Caputo, C. H. Hendon, R. X. Yang, A. Walsh and M. V. Kovalenko, *Nano Lett.*, 2015, **15**, 3692.

146. Y.-H. Ko, M. Jalalah, S.-J. Lee and J.-G. Park, *Sci. Rep.*, 2018, **8**, 12881.

147. H.-C. Wang, Z. Bao, H.-Y. Tsai, A.-C. Tang and R.-S. Liu, *Small*, 2018, **14**, 1702433.

148. I. Chung, B. Lee, J. He, R. P. H. Chang and M. G. Kanatzidis, *Nature*, 2012, **485**, 486.

149. M. Grätzel, *Nat. Mater.*, 2014, **13**, 838.

150. M. A. Green, A. Ho-Baillie and H. J. Snaith, *Nat. Photonics*, 2014, **8**, 506.

151. H. Zhou, Q. Chen, G. Li, S. Luo, T.-b. Song, H.-S. Duan, Z. Hong, J. You, Y. Liu and Y. Yang, *Science*, 2014, **345**, 542.

152. A. J. Nozik, M. C. Beard, J. M. Luther, M. Law, R. J. Ellingson and J. C. Johnson, *Chem. Rev.*, 2010, **110**, 6873.

153. A. D. Yoffe, *Adv. Phys.*, 2001, **50**, 1.

154. M. V. Kovalenko, L. Manna, A. Cabot, Z. Hens, D. V. Talapin, C. R. Kagan, V. I. Klimov, A. L. Rogach, P. Reiss, D. J. Milliron, P. Guyot-Sionnnest, G. Konstantatos, W. J. Parak, T. Hyeon, B. A. Korgel, C. B. Murray and W. Heiss, *ACS Nano*, 2015, **9**, 1012.

155. B. H. Kim, M. J. Hackett, J. Park and T. Hyeon, *Chem. Mater.*, 2014, **26**, 59.

156. F. Krieg, S. T. Ochsenbein, S. Yakunin, S. ten Brinck, P. Aellen, A. Süess, B. Clerc, D. Guggisberg, O. Nazarenko, Y. Shynkarenko, S. Kumar, C.-J. Shih, I. Infante and M. V. Kovalenko, *ACS Energy Lett.*, 2018, **3**, 641.

157. Y. Cai, L. Wang, T. Zhou, P. Zheng, Y. Li and R.-J. Xie, *Nanoscale*, 2018, **10**, 21441.

158. C. Rösler and R. A. Fischer, *CrystEngComm*, 2015, **17**, 199.

159. S. Bhattacharyya, D. Samanta, S. Roy, V. P. Haveri Radhakantha and T. K. Maji, *ACS Appl. Mater. Interfaces*, 2019, **11**, 5455.

160. V. Malgras, S. Tominaka, J. W. Ryan, J. Henzie, T. Takei, K. Ohara and Y. Yamauchi, *J. Am. Chem. Soc.*, 2016, **138**, 13874.

161. V. Malgras, J. Henzie, T. Takei and Y. Yamauchi, *Chem. Commun.*, 2017, **53**, 2359.

162. H.-C. Wang, S.-Y. Lin, A.-C. Tang, B. P. Singh, H.-C. Tong, C.-Y. Chen, Y.-C. Lee, T.-L. Tsai and R.-S. Liu, *Angew. Chem. Int. Ed.*, 2016, **55**, 7924.

163. C. Zhang, B. Wang, W. Li, S. Huang, L. Kong, Z. Li and L. Li, *Nat. Commun.*, 2017, **8**, 1138.

164. Z. Chen, Z.-G. Gu, W.-Q. Fu, F. Wang and J. Zhang, *ACS Appl. Mater. Interfaces*, 2016, **8**, 28737.

165. H. He, Y. Cui, B. Li, B. Wang, C. Jin, J. Yu, L. Yao, Y. Yang, B. Chen and G. Qian, *Adv. Mater.*, 2019, **31**, 1970036.

166. C. K. Brozek, L. Bellarosa, T. Soejima, T. V. Clark, N. Lopez and M. Dinca, *Chem. Eur. J.*, 2014, **20**, 6871.

167. X. Zhao, Z. Zhang, X. Cai, B. Ding, C. Sun, G. Liu, C. Hu, S. Shao and M. Pang, *ACS Appl. Mater. Interfaces*, 2019, **11**, 7884.

Chapter 2A

Tetracarboxylate Linker Based Flexible Cu^{II} Frameworks: Efficient Separation of CO$_2$/N$_2$ and C$_2$H$_2$/C$_2$H$_4$ Mixtures
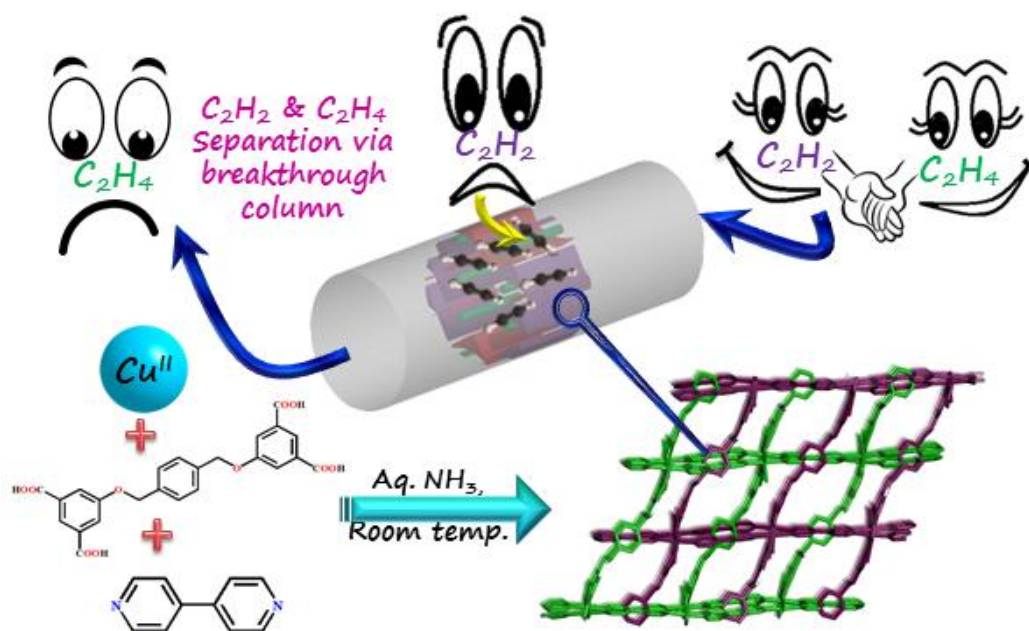
Abstract

This chapter comprises the synthesis, structure and adsorption properties of two new metal-organic frameworks (MOFs) {[Cu_2(bpp)$_3$(**L1**)]·(bpp)·($4H_2O$)} (**1**) and {[Cu_2(bipy)$_2$(**L2**)(H_2O)$_2$]·(bipy)·($5H_2O$)} (**2**) [bpp = 1,3-bis(4-pyridyl) propane; bipy = 4,4'-bipyridine] obtained from two different flexible tetracarboxylate linkers (**L1** and **L2**) of variable lengths and flexibility. While **1** comprising Cu^{II}, **L1** and bpp is a 2D MOF with a cage-type structure, **2** consists of Cu^{II}, **L2** and bipy has a 3D two-fold interpenetrated structure. Both frameworks manifest permanent porosity, as realized from CO_2 adsorption at 195 K. **2** shows excellent CO_2/N_2 and C_2H_2/C_2H_4 adsorption selectivity at 298 K. This has been established by using **2** as a separating medium in a breakthrough column for separating mixtures of CO_2/N_2 (15:85, v/v) and C_2H_2/C_2H_4 (1:99, v/v). The selectivity of **2** towards CO_2 over N_2 and C_2H_2 over C_2H_4 is governed by favourable thermodynamic parameters (ΔH) interactions owing to its structural flexibility and presence of unsaturated metal sites and polar carboxylate groups on the pore surface. Thus **2** prove to be an extremely efficient material for specific gas separation.

2A.1 Introduction

Adsorptive separation[1] of a particular gas from a mixture using porous materials is a technique of supreme importance in recent times, because of its relevance in industrial as well as environmental applications.[2, 3] Different gas molecules are essential to sustain life[4] as well as to cater to our various energy requirements.[5] Thus the effective sieving of the different components of a gas mixture is of paramount importance.[6] Hydrocarbons, particularly ethylene, obtained from natural and shale gases are extremely important in the polymer industry and to produce several other chemicals. During steam cracking for the synthesis of ethylene, acetylene (about 1%) is usually produced as a side product. This trace amount acetylene is a contaminant, which if not removed, acts as a catalyst poison in ethylene polymerization and degrades the quality of the resultant polyethylene.[7] Thus the development of porous materials which can facilitate selective adsorption of acetylene over ethylene is of paramount importance as it can show a cost-effective facile route for the challenging task of gas separation[7-9] thereby helping the polymer industry immensely.

Metal-organic frameworks (MOFs)[10], well known for their multifaceted applications in gas storage[2, 52], catalysis[11], luminescence[12] and sensing properties[13, 14], are extremely relevant in this regard. MOFs are much more efficient, both in terms of energy and cost, than traditional methods for gas separation e.g., cryogenic distillation or partial hydrogenation. Selectivity in MOFs can be achieved by tuning its pore size by modulating the functionalities of the organic linker along with implementation of suitable metal ions with varied geometry.[15-17] By controlling the window dimension or pore size of MOF, kinetic based separation can be achieved.[2, 18, 19] Also, separation can be done on the basis of favourable thermodynamic interaction of the specific adsorbate molecules with the pore surface.[8, 20, 21] Thus it is extremely important to adopt a proper targeted ligand design strategy to synthesize such MOFs with high efficiency. Multidentate flexible linkers, e.g., di, tri and tetra carboxylates[24-27, 51] are the most widely used linkers in MOF chemistry.[22, 23] Such linkers coordinate with metal ions to form a wide range of multinuclear nodes with predictable geometries like binuclear paddle-wheel units, tri or tetranuclear units.[25] In this regard, aromatic tetracarboxylate linkers are particularly utilitarian due to more number of coordinating sites as well as the rich π-electron density.[25, 27] MOFs constructed from such π-electron rich tetracarboxylate linkers have pore surfaces studded with large number of oxygen atoms providing better interaction with gas molecules like CO_2[28, 29] or small hydrocarbon molecules like ethylene and
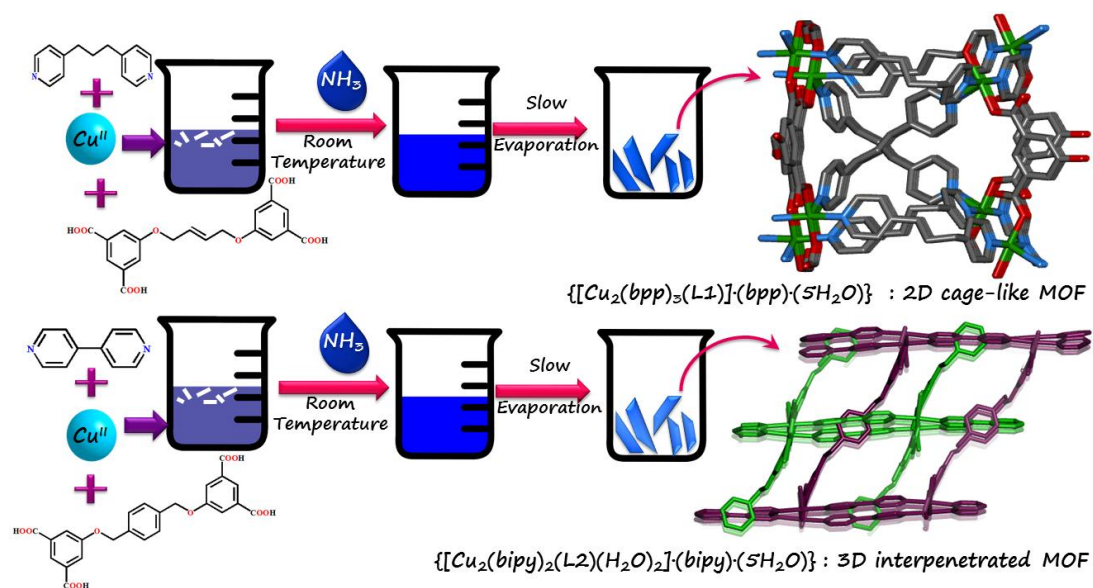
Scheme 1 pH dependent synthesis of compounds **1** and **2** by the self-assembly of Cu^{II} and the respective linkers at room temperature.

acetylene.[30, 31] Furthermore, the flexibility of such ligands contributes in the tunable porosity of MOFs by inducing guest responsive structural dynamicity[23, 31, 32, 50] with ability to respond to external stimuli[33], *e.g.*, temperature, pressure, light, electric fields, chemical inclusion.[32,11] Such dynamic frameworks[34] also manifest stepwise[35] or gated adsorption[36, 37] at a certain pressure of an adsorbate molecule[38, 39] which results in guest selectivity[31, 40] and gas separation.[40-42]

In this chapter, two different flexible π- electron rich tetracarboxylate linkers [5,5'-(1,4-(2-butene)bis(oxy)diisophthalic acid (**L1**) and 5,5'-(1,4-phenylenebis(methylene))bis(oxy)diisophthalic acid (**L2**, **Scheme 1**) of different lengths and flexibility have been used. Self-assembly of **L1** and 1,3-bis(4-pyridyl) propane (bpp) with Cu^{II} at room temperature results in a hydrophobic 2D MOF {[Cu_2(bpp)_3(**L1**)]·(bpp).(4H_2O)}(**1**) with cage[43] type structure. The permanent porosity of the framework has been established by performing CO_2 adsorption at 195 K and different vapour adsorption studies. On the other hand, self-assembly of **L2** and bipyridine (bipy) with Cu^{II} resulted in a 2-fold interpenetrated 3D MOF {[Cu_2(bipy)_2(**L2**)(H_2O)_2]·(bipy)·(5H_2O)}(**2**). The desolvated framework (**2'**) exhibits an excellent selectivity towards C_2H_2 over C_2H_4 at 298 K, and the practical applicability of which has been proven through using a breakthrough column experiment. In addition it is also a selective adsorbent of CO_2 from its mixture with N_2, which makes it a potential separator for industrial flue gas. In both cases, basis of separation is the favourable thermodynamic interaction of the framework with respective adsorbate molecules.

2A.2 Experimental Section

2A.2.1 Materials

All the reagents and solvent were used as obtained from commercial supplies without any further purification. Dimethyl-5-hydroxy isophthalate, α,α'-dibromoparaxylene, Dibenzo-18-crown-6, 1,4-dibromobutene and K_2CO_3 were obtained from Aldrich Co. Ltd.

2A.2.2 Synthesis of 5,5'-(1,4-(2-butene)bis(oxy)diisophthalic acid (L1)

A mixture of dimethyl 5-hydroxy isophthalate (10.0 mmol), 1,4-dibromobutene (5mmol) , dibenzo 18 crown-6 (0.277 mmol) , and K_2CO_3 (16 mmol)were stirred in dry THF (40 ml) under dry atmosphere using a well fitted guard tube at 70°C for 24 hours. After this time 20 ml 10% aqueous Na_2CO_3 solution was added at 0°C under an ice bath. The resulting white solid was filtered and washed with water for several times and finally with diethyl ether and dried under vacuum. A mixture of the residue (2mmol), KOH (20mmol), 40 ml MeOH and 40 ml distilled water were stirred at 80° C in oil bath for 48 hours. The reaction mixture was filtered to remove any unreacted starting materials. 30 ml 6(M) HCl was added dropwise to filtrate at 0°C under stirring. The white precipitate was filtered and washed with distilled water for several times and dried under vacuum. ^{1}H NMR (400 MHz, DMSO-d$_6$): δ= 13.13 (br, 4H), 8.01 (s, 2H), 7.43 (s, 4H), 5.21 (s, 2H), 4.32 (s, 4H). HRMS-EI (m/z) for $[C_{20}H_{16}O_{10} + H_2O]$ Calcd. 434.0849, found 434.1084 (**Fig. 1**).
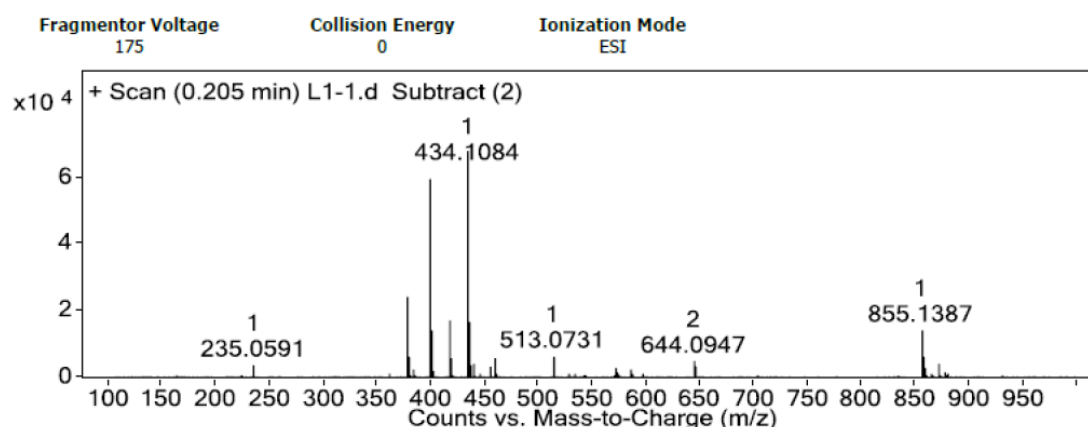
Fig. 1 HRMS spectrum of **L1** showing the peak at 434, owing to the addition of a water molecule (Calcd. 18.0153) to the ligand L1 (Calcd. 416.0743).

44

2A.2.3 Synthesis of 5,5'-(1,4-phenylenebis(methylene))bis(oxy)diiso-phthalic acid (L2)

The synthetic procedure of **L2** is similar to that of **L1**, where 1,4-Bis-bromomethyl-benzene is used instead of 1,4-dibromobutene. ^{1}H NMR (400 MHz, DMSO-d$_6$): δ= 13.29 (br, 4H), 8.05 (s, 2H), 7.69 (s, 4H), 7.47 (s, 4H), 5.21 (s, 4H). HRMS-EI (*m/z*) for [C$_{24}$H$_{18}$O$_{10}$ + H$_2$O] Calcd. 484.1006, found 484.1234 (**Fig. 2**).
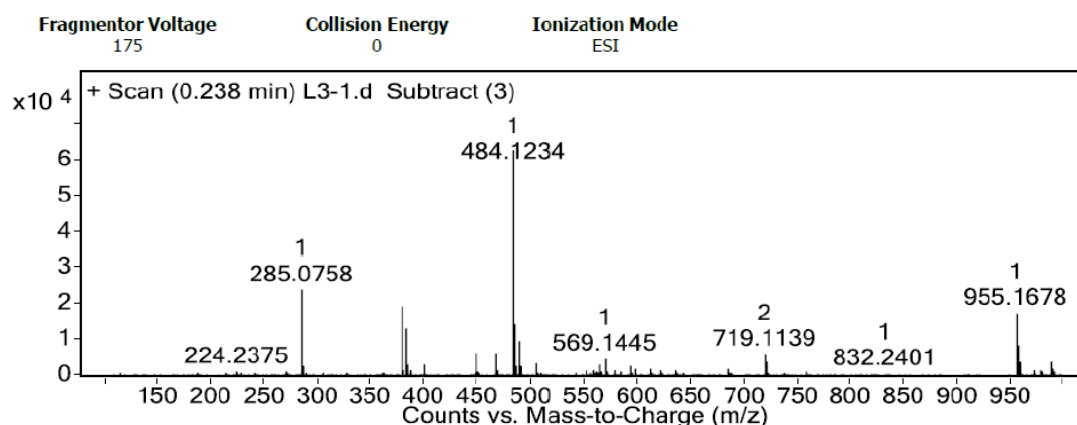
Fig. 2 HRMS spectrum of **L2** showing the peak at 484.1084, owing to the addition of a water adduct (Calcd. 18.0153) to the ligand **L2** (Calcd. 466.3937).

2A.2.4 Synthesis of {[Cu$_2$(bpp)$_3$(L1)]·(bpp)·(4H$_2$O)} (1)

CuCl$_2$·2H$_2$O (0.2 mmol, 0.034 g) and solid **L1** (0·1 mmol, 0.047 g) were mixed with 10 ml water and stirred for 10 mins. Aqueous ammonia (20%) was added dropwise to this mixture till the solution becomes clear. To this 10 ml methanolic solution of 1,3-bis(4-pyridyl)propane (0·5 mmol, 0.099 g) was added and the resulting solution was stirred for 1 hour. The solution was kept undisturbed at room temperature. After 3-4 days, dark blue needle shaped crystals appear. Yield: 60% relative to Cu[II]. Anal. calcd. For C$_{12}$H$_{17}$Cu$_2$N$_{17}$: C 61·051; H 5·123; N 7·910%. Found: C 60·99; H 5·43; N 7·72%. FT-IR (4000-400 cm^{-1}) 1568 (s), 1618 (s), 1358 (s), 778 (s) cm^{-1}.
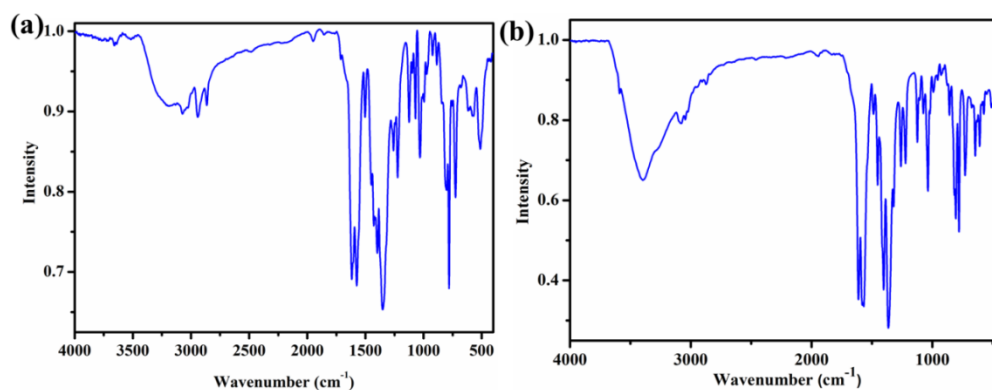
Fig. 3 IR spectra of **(a) 1** and **(b) 2**.

Table 1 Principal Peaks in IR of **1** (**Fig. 3(a)**).

Peak Position	Nature	Vibration
1568, 1618cm^{-1}	strong	C=O stretch
778cm^{-1}	strong	Aromatic C-H stretch
1358cm^{-1}	strong	C-N stretch

2A.2.5 Synthesis of {[Cu$_2$(bipy)$_2$(L2)(H$_2$O)$_2$]·(bipy)·(5H$_2$O)} (2)

CuCl$_2$.2H$_2$O (0·2 mmol, 0.034 g) and solid **L1** (0·1 mmol, 0.047 g) were mixed with 20 ml water and stirred for 10 mins. Aqueous ammonia (20%) was added dropwise to this reaction mixture, till the solid residues dissolve and the solution becomes clear. Subsequently, a 10 ml methanolic solution of 4,4'-bipyridine (0·5 mmol, 78 mg) was added to the previous reaction mixture and the solution was stirred overnight. The solution was kept undisturbed at room temperature. Light blue crystals are formed after 3-4 days. Yield: 72% relative to Cu^{II}. Anal. calcd. for C$_{54}$H$_{46}$Cu$_2$N$_6$O : C 55·054; H 3·935; N 7·133%. Found: C, 55·26; H 3·45; N 7·27%. FT-IR (4000-400 cm^{-1}) 782 (s), 1265 (s), 1354 (s), 1570 (s), 1616 (s), 3900 (w) cm-1. For characterization and adsorption studies, phase pure single crystals were used.

Table 2 Principal peaks in the IR spectrum of **2** (**Fig. 3(b)**)

Peak Position	Nature	Vibration
1570, 1616 cm^{-1}	strong	C=O stretch
782 cm^{-1}	strong	Aromatic C-H stretch
1265, 1354 cm^{-1}	strong	C-N stretch
3900 cm^{-1}	medium, broad	water

2A.2.6 Physical measurements

The elemental analyses were carried out using a Thermo Fischer Flash 2000 Elemental Analyzer. IR spectra were recorded with a Bruker IFS 66v/S spectrophotometer using KBr pellets in the region 4000–400 cm^{-1}. Thermogravimetric analysis (TGA) were carried out (Mettler Toledo) in a nitrogen atmosphere (flow rate = 50 ml min^{-1}) in the temperature range 30–500°C (heating rate = 3°C min^{-1}). Powder X-ray Diffraction patterns of the compounds in different states were recorded by using Cu-Kα radiation (Bruker D8 Discover; 40 kV, 30 mA).

2A.2.7 X-ray Crystallography

X-ray single crystal structural data for **1** and **2** were collected using a Bruker

Smart-CCD diffractometer equipped with a normal focus, 2.4 kW sealed tube X-ray source with graphite monochromated Mo-Kα radiation (λ = 0·71073 Å) operating at 50 kV and 30 mA. The program SAINT[14] was used for integration of diffraction profiles and absorption correction was made using the SADABS[15] program. All of the structures were solved using SHELXLT[47] and refined by a full matrix least square method using SHELXL-2017.[46] All of the hydrogen atoms were geometrically fixed and placed in ideal positions. The potential solvent accessible area or void space was calculated using the PLATON multipurpose crystallographic software.[18] All crystallographic and structure refinement data for **1** and **2** are summarized in **Table 3**. Selected bond lengths and angles for **1** and **2** are given in **Tables 4–9**, respectively.

2A.2.8 Adsorption Study

The adsorption isotherms of CO_2 (195 K), N_2 (77 K, 273 K and 298 K), other gases (C_2H_2, C_2H_4 at 273 K and 298 K) using the desolvated sample of **1 (1')** and **2 (2')** were measured by using a QUANTACHROME AUTOSORB IQ2 analyzer. In the sample tube adsorbent samples **1** and **2** (~100–150 mg) were placed which had been prepared at 353 and 433 K, respectively, under a 1×10^{-1} Pa vacuum for about 6 h prior to measurement of the isotherms. Helium gas (99.999% purity) at a certain pressure was introduced in the gas chamber and allowed to diffuse into the sample chamber by opening the valve. The amount of gas adsorbed was calculated readily from the pressure difference ($P_{cal} - P_e$), where P_{cal} is the calculated pressure with no gas adsorption and P_e is the observed equilibrium pressure. All operations were computer-controlled and automatic. The adsorption of different solvents like MeOH at 293 K and H_2O and EtOH at 298 K was measured in the desolvated sample of **1** and **2** in the vapour state by using a BELSORP Aqua-3 analyzer. The samples of about ~100–150 mg were activated under similar conditions as mentioned earlier. The different solvent molecules used to generate the vapour were degassed fully by repeated evacuation. The dead volume was measured with helium gas. The adsorbate was placed into the sample tube, then the change of pressure was monitored and the degree of adsorption was determined by the decrease in pressure at the equilibrium state. All operations were computer controlled and automatic.

2A.2.9 IAST Selectivity

The ideal adsorbed solution theory (IAST) was used to predict the selectivity in binary mixture adsorption of CO_2/N_2 and C_2H_2/C_2H_4 from the experimental pure-gas isotherms. The single-component isotherms were fit to a single-site Langmuir-Freundlich equation (equation 3). IAST assumes the adsorbed phase to be in a two-dimensional phase in equilibrium with the bulk phase. The binary adsorption of A and B, according to IAST these two equations are to be followed:

$$yP_t = xP_a \text{ -----------(1)}$$
$$(1 - y)P_t = (1 - x)P_b \text{ ---------(2)}$$

where x and y denote the molar fraction of A in the adsorbed phase and the molar fraction of A in the bulk phase, respectively. P_t is the total gas pressure; P_a and P_b are the pressure of component A and B at the same spreading pressure as that of the mixture, respectively. The equation used to fit the single component gas mixture is as follows.

$$Y = Y_0 \left(\ln \frac{BP^n}{(1+BP^n)}\right)\text{-------(3)}$$

The molar fraction of A in the adsorbed phase can be obtained from the following equation:

$$Y_{0,a} \ln\left(1 + \frac{B_a P_t^{n1} y}{x}\right) - Y_{0,b} \ln\left(1 + \frac{B_b P_t^{n2}(1-y)}{(1-x)}\right) = 0\text{------(4)}$$

Where $Y_{0,a}$, B_a and $n1$ are the Langmuir-Freundlich fitting parameters of adsorption equilibrium of pure A, $Y_{0,b}$, B_b and $n2$ are Langmuir-Freundlich parameters of adsorption equilibrium of pure B. The unknown x in Eq. (4) has been solved by Matlab (Version 7.8 (R2009a), The MathWorks, Inc.) for fixed Pt and y values. Then calculated the predicted adsorption selectivity, which is defined as

$$S = \frac{x_1/y_1}{x_2/y_2} \text{ ------(5)}$$

Where x_i and y_i are the mole fractions of component i (i = 1, 2; A, B) in the adsorbed and bulk phases, respectively. The IAST calculations were carried out for equimolar gas-phase mixtures.

2A.2.10 Heat of Adsorption Calculation

The Virial type expression of the following type has been used to fit the combined isotherms data collected at 273 and 293 K.

$$\ln(P) = \ln(A) + \frac{1}{T}\sum_{i=0}^{m} a_i A_i + \sum_{i=0}^{n} b_i B_i$$

Here, P is the pressure expressed in torr, A is the amount adsorbed in mmol/g, T is the temperature in K, a_i and b_i are virial coefficients, and m, n represent the number of coefficients required to describe the isotherms. The values of m and n are gradually increased until the contribution of extra added a and b coefficients were negligible for the overall final fit. The values of the virial coefficient a_i were taken to calculate the isosteric heat of adsorption using the following expression.

$$Q_{st} = -R \sum_{i=0}^{m} a_i A_i$$

Qst is the coverage dependent isosteric heat of adsorption and R is the universal gas constant.

2A.2.11 Breakthrough Measurements

Breakthrough experiments were performed using a column (packed with about 400 mg of powdered **2'**), 4 cm long in length and 0.3 cm diameter. The sample was first activated at 160°C for 12 h prior to loading in column. After loading the sample was again activated with the He flow for 30 mins. CO_2 /N_2 (v/v 15:85 mixture) and C_2H_2/C_2H_4
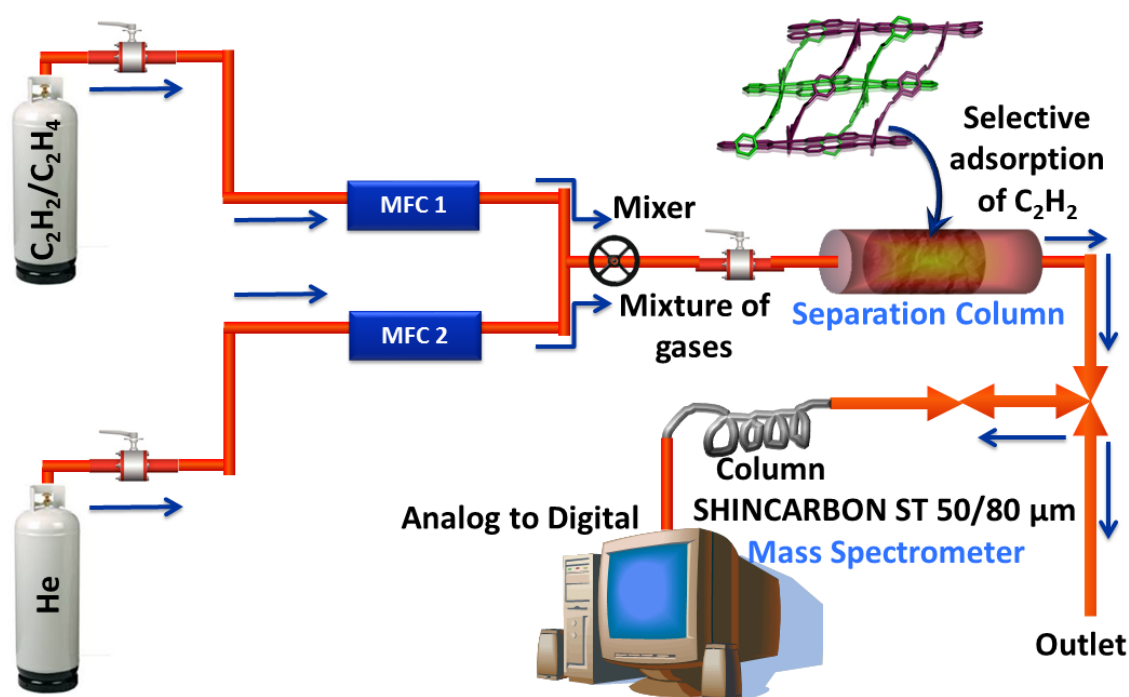
Scheme 2. Schematic representation of the setup for breakthrough experiment.

(v/v: 1:99 mixture) streams were passed through the column with He. The flow was continuous and the flow rate was regulated by MFC. The partial pressure of the gas mixture was kept at p = 5 kPa. The gas stream at the outlet of the column was analyzed on-line with a GC. The space velocity was kept at 4.71 min^{-1} (**Scheme 2**).

2A.3 Results and Discussions

2A.3.1 Single Crystal Structure of Compound 1

Single crystal X-ray diffraction data reveals that compound **1** crystallizes in monoclinic *P*2$_1$/*c* space group. The asymmetric unit contains two crystallographically independent penta-coordinated Cu^{II} centres, which have a (4+1) square pyramidal geometry. The degree of deviation from ideal square pyramidal geometry has been calculated in terms of Addison parameter (τ),[44] the value of which is merely 0·019 for Cu1, suggesting a square pyramidal geometry rather than trigonal bipyramid. The basal plane of Cu1 is occupied by N3 and N6 from two different bpp linkers along with two carboxylate oxygen atoms O1 and O4 from two different **L1** linkers. The apical position is occupied by N1 atom from another bpp linker (**Fig. 4(a)**). The Cu1-O1 bond length at the basal plane is 1.93(8) Å, while that for Cu1-O4 is 1.97(8) Å. The bond lengths for Cu1-N3 and Cu1-N6 are 2.03(10) Å and 2.04(14) Å, respectively. However, the Cu1-N1 bond at the apical position is much longer with a bond length of 2.32 (10) Å, implying a
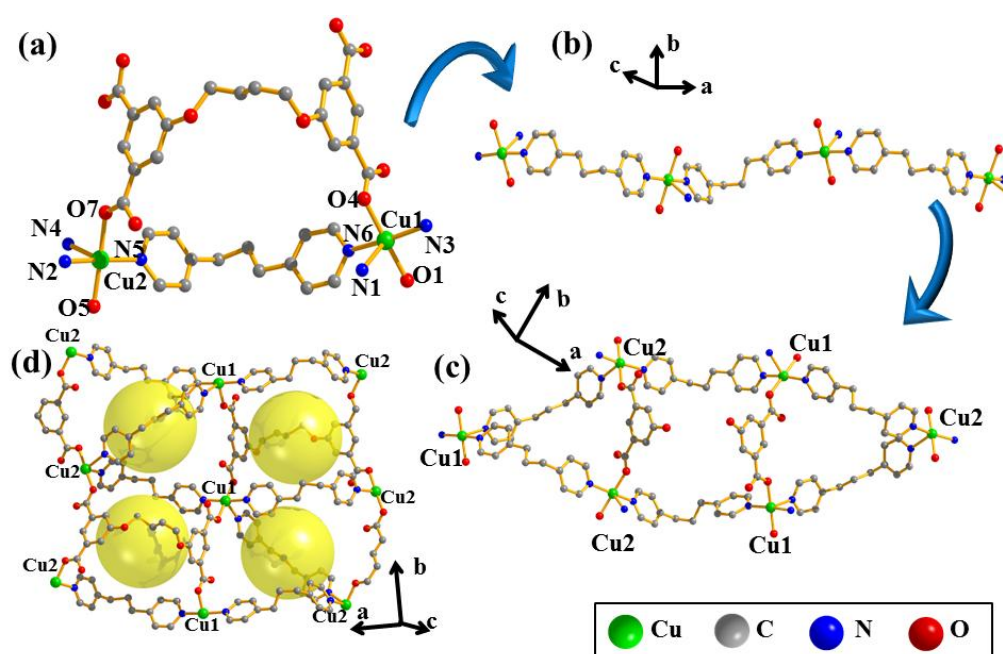
Fig. 4 (a) Coordination sphere of Cu1 and Cu2 in compound **1**. **(b)** 1D wave in **1** formed by Cu centres linked with bpp linkers. **(c)** 2D network in **1**. **(d)** Hydrophobic pockets in the network.

(4+1) geometry. Similarly, the penta-coordination of Cu2 is fulfilled by two carboxylate oxygen atoms (O5 and O7) from **L1** and two nitrogen atoms (N4 and N5) from two different bpp linkers at the basal plane and N2 at the apical position (**Fig. 4(a)**). The τ value for Cu2 is 0·13, suggesting a high distortion from ideal square pyramidal geometry. The bond lengths of Cu2-O5 and Cu2-O7 are 1.97(10) Å and 1.94(9) Å, whereas that of Cu2-N4 and Cu2-N5 are 2.03(12) Å and 2.04(12) Å, respectively. The apical Cu2-N2 is much longer, with a bond length of 2.36(13) Å. Cu1 and Cu2 are connected together by a bpp linker to form a wavy chain (**Fig. 4(b)**). Two such parallel chains are connected by a **L1** linker, where the two carboxylates at one terminal of **L1** connects two Cu1 atoms and the two carboxylates at the other terminal connect two Cu2 atoms (**Fig. 4(d)**). Adjacent to this, the Cu1 centre is further diagonally connected to a Cu2 atom in the other chain by a bpp linker. Thus a 2D network with a cage like structure is formed containing a hydrophobic pocket along *b* direction (**Fig. 4(d)**), which is lined by the π-electron rich aromatic **L1** on one side and bpp linker on the other. This hydrophobic pocket houses a guest bpp molecule which forms a π-π interaction with the pyridyl ring of the bpp linker on the wall of the pocket (cg-cg distance 4·6 Å). The central C3 alkyl moiety in case of both L1 as well as bpp, imparts flexibilty to the pockets, thereby ensuring uptake of adsorbate molecules, in spite of the small pore size. All the guest water molecules present in the framework, except for O5w, are hydrogen bonded with the framework. The hydrogen bonding parameters of **1** have been summarized in **Table 6**. The solvent accessible void space in the framework is 2943·3 Å^3 (39·6% of the total cell volume), which has been calculated using PLATON after removing the guest bpp and the water molecules.

2A.3.2 Single Crystal Structure of Compound 2

Compound **2** crystallizes in the *C*2/*c* monoclinic space group. Each asymmetric unit comprises two crystallographically independent penta-coordinated Cu^{II} centres, each of which assumes a distorted square pyramidal geometry, the degree of distortion being as low as 0·007 for Cu1 and 0·037 for Cu2. The penta coordination of Cu1 is fulfilled by two nitrogen atoms (N1 and N2) from two different bipy molecules, two oxygen atoms (O1 and O3) from tetracarboxylate linker **L2**, and one coordinated water molecule (O7w). Similarly, the penta coordination of Cu2 is satisfied by two nitrogen atoms (N3 and N6) from two different bipy linkers, two oxygen atoms (O5 and O12) from **L2**, and one oxygen atom (O5w) from a coordinated water molecule. The bipy linker (containing N6
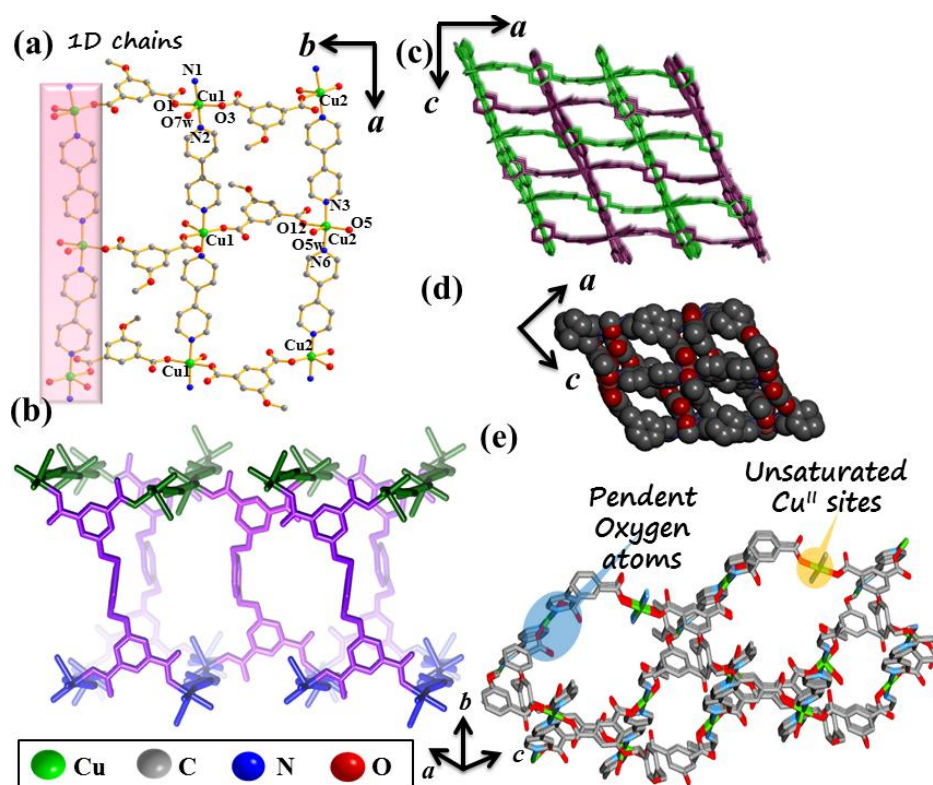
Fig. 5 (a) 1D chain along crystallographic *a* direction in **2**. **(b)** 2D sheet along *ab* plane in **2**. **(c)** Two-fold interpenetrated 3D framework in **2**. **(d)** Pore structure in **2**. **(e)** Pendent oxygen atoms and unsaturated Cu^{II} sites on the pore surface of **2**.

and N7 atom), connecting two adjacent Cu2 centers, is disordered over two positions with 50-50 equal occupancy (**Fig. 5(a)**). Cu1 centres connected by bipy form a 1D chain along the *a* direction and a similar 1D chain is formed by the bridging of Cu2 centres by bipy along the crystallographic *a* direction (**Fig. 5(a)**). The two carboxylates on one terminal of a **L2** linker (marked in violet in **Fig. 5(b)**) connect two of these parallel chains on one plane (marked in dark green in **Fig. 5(b)**). The two carboxylates on the other terminal of the **L2** connect two other such parallel 1D chains on a different plane (marked in blue in **Fig. 5(b)**) to form the 3D framework (**Fig. 5(c)**). Two 3D frameworks interpenetrate each other resulting in a 2-fold interpenetrated 3D framework (**Fig. 5(d)**). Along crystallographic *b* direction, the single net of the 3D framework contain an 1D channel with pore dimension 4.45×5.46 Å^2, which upon 2-fold interpenetration (**Fig. 5(c)**) reduces to smaller channel having pore dimension 2.93×5.14 Å^2 and the channel is occupied by guest bipy and guest water molecules. Detailed analysis with TOPOS[48-49] reveals that compound **2** is 5-nodal (2-c)(4-c)$_2$(4-c)$_2$ periodic net connected by two 4 connected (4-C) Cu center, by two 4 connected (4-C) **L2** linker one 2 connected (2-C) bipy linker. Further analysis shows that compound **2** adopts an unprecedented network
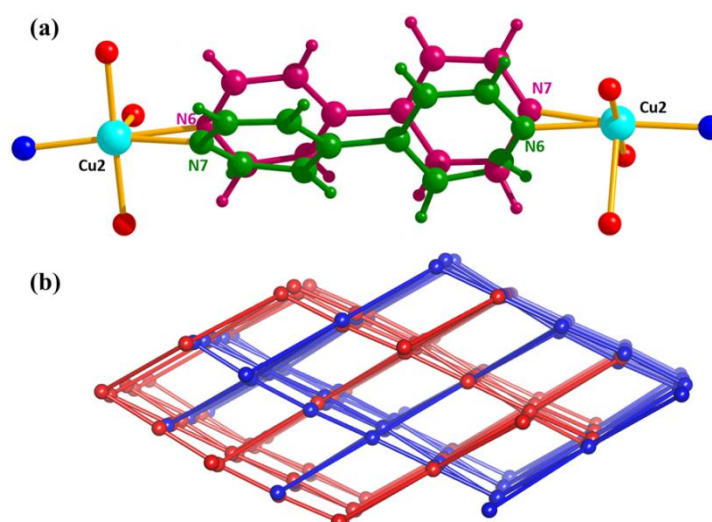
Fig. 6 (a) The coordination sphere of Cu2 in **2** showing the positional disorder in the structure **(b)** TOPOS analysis displaying the interpenetrated net in **2**.

topology with the Schläfli symbol $\{6^2.7^2.8.9\}_2\{6^3.7.8^2\}\{6^4.8.9\}\{6^4.8^2\}^2\{7\}$ (**Fig. 6(b)**). All the water molecules except O4w, are hydrogen bonded to the framework and the hydrogen bonding parameters have been summarized in **Table 8**. The pyridyl ring (containing N4 atom) of guest bipy molecules shares a π- π interaction (cg-cg distance 3·76 Å) with the pyridyl ring (containing N1 atom) of bipy linkers along the pore wall. As we have discussed earlier, both Cu1 and Cu2 are coordinated to water molecules and thus unsaturated metal site (UMS) could be generated after desolvation. The solvent accessible void is 5826.1 $Å^3$ (47.5% of the total cell volume) has been calculated using PLATON after removing the coordinated and as well as guest water and guest bipy molecules.

Table 3 Crystal data and structure refinement for compounds **1** and **2**

Parameter	1	2
Empirical Formula	$C_{72}H_{72}Cu_2N_8O_{15}$	$C_{54}H_{46}Cu_2N_6O_{17}$
Formula Weight	1398.4	1177.9
Crystal System	Monoclinic	Monoclinic
Space Group	$P2_1/c$ (No.14)	$C2/c$ (No.15)
a, Å	23.6727(17)	44.8511(10)
b, Å	18.9130(13)	19.0460(4)
c, Å	17.6128(13)	14.7115(3)
β, deg	109.696(3)	102.380(1)
V, $Å^3$	7424.6	12274.8
Z	4	8
T, K	293	293
μ, mm^{-1}	0.638	0.766
D_{calcd},g/cm^3	1.249	1.331
F (000)	2904	5072

Reflections [*I>2σ(I)*]	3751	6004
unique reflections	8042	9461
measured reflections	94274	81471
R_{int}	0.171	0.085
GOF on F^2	0.96	1.03
$R_1[I>2σ(I)]$[a]	0.1040	0.068
$R_w[I>2σ(I)]$[b]	0.2956	0.2170

$(R = \sum ||F_o|-|F_c||/\sum |F_o| , R_w= [\sum \{w(F_o^2-F_c^2)^2\}/\sum \{w(F_o^2)^2\}]^{1/2})$

Table 4 Selected bond distances (Å) for **1**.

Cu1 -O1	1.931(8)	Cu1-N1	2.319(10)
Cu1-N3	2.030(10)	Cu1-N6	2.042(14)
Cu2-O5	1.973(10)	Cu2-N5	2.043(12)
Cu2-N4	2.035(12)	Cu2-O7	1.936(9)
Cu1-O4	1.968(8)	Cu1 –N2	2.355(17)

Table 5 Selected bond angles (°) for **1**.

O1 -Cu1-N1	90.1(4)	O1 -Cu1-N3	90.2(4)
O1-Cu1 -N6	89.9(5)	O1-Cu1-O4	179.7(2)
N1-Cu1-N6	90.5(4)	N4-Cu2-N5	90.6(5)
O5-Cu2-N4	90.6(4)	O7-Cu2-N4	95.6(5)
O5-Cu2-N5	90.6(5)	N2-Cu2-N5	95.7(5)

Table 6 Hydrogen bond parameters (Å) for **1**.

D–H···A	D–H (Å)	H···A (Å)	D ···A (Å)	∠D–H···A (°)
C1–H1···O1	0.9300	2.5700	3.137(17)	120.00
C5–H5···O4	0.9300	2.5900	3.151(16)	120.00
C14–H14···O52	0.9300	2.4400	3.294(15)	152.00
C16–H16···O3	0.9300	2.5000	3.211(18)	133.00
C25–H25···O8	0.9300	2.4600	3.338(18)	157.00
C26–H26···O6	0.9300	2.4900	3.269(18)	141.00
C27–H27···O7	0.9300	2.5500	3.00(2)	110.00
C31–H31···O6	0.9300	2.4700	3.26(2)	143.00
C37–H37···O3	0.9300	2.5000	3.31(2)	147.00
C54–H54···O52	0.9300	2.4600	2.81(2)	102.00
C70–H70···O1	0.9300	2.4100	2.727(14)	100.00

Table 7 Selected bond distances (Å) for **2**.

Cu1-O1	1.939(4)	Cu2-O5	1.910(4)
Cu1-O3	1.944(4)	Cu2-O5w	2.347(6)
Cu1-O7	2.250(4)	Cu2-N7	1.99(3)
Cu1-N2	2.038(5)	Cu2-O12	1.925(4)
Cu1-N1	2.028(5)	Cu2-N6	2.07(3)

Table 8 Selected bond angles (°) for **2**.

O1-Cu1-O3	176.46(18)	O1-Cu1-O7W	88.22(16)
O1-Cu1 –N1	87.31(17)	O1-Cu1-N2	88.9(2)
O3-Cu1-O7w	93.84(16)	O5-Cu2-O5W	91.21(19)
O5-Cu2-N7	94.0(5)	O5-Cu2-O12	177.94(19)
O12-Cu2-N6	91.7(5)	N3-Cu2-N6	174.6(7)

Table 9 Hydrogen bond parameters (Å) for **2**.

D–H···A	D–H (Å)	H···A (Å)	D ···A (Å)	∠D–H···A (°)
O1W–H1O1···O4	0.9200	1.7800	2.668(7)	162.00
O1W–H2O1···O2	0.9600	1.8800	2.808(7)	161.00
O7W–H1O7···O2W	1.0000	1.7900	2.758(9)	163.00
O5W–H1O5···O13	0.9900	1.9400	2.897(8)	162.00
O5W–H2O5···O6W	0.9600	2.0000	2.949(11)	167.00
O7W–H2O7···O2	0.9200	1.9100	2.767(6)	152.00
O3W–H1O3···O6	0.9900	1.8100	2.787(8)	169.00
O3W–H2O3···O13	1.0300	1.7500	2.781(7)	174.00
O6W–H1O6···O3W	1.0000	1.9000	2.789(13)	147.00
O6W–H2O6···O4	1.0000	2.1000	3.068(11)	163.00
O2W–H2O2···O1W	0.9500	1.8400	2.706(9)	149.00
O2W–H1O2···O6	0.9400	1.9700	2.871(9)	158.00
C5–H5···O1	0.9300	2.4600	2.890(8)	109.00
C7–H7···N5	0.9300	2.6100	3.543(10)	179.00
C26–H26···O4	0.9300	2.5000	3.310(8)	145.00

2A.3.3 Framework Stability of Compounds 1 and 2
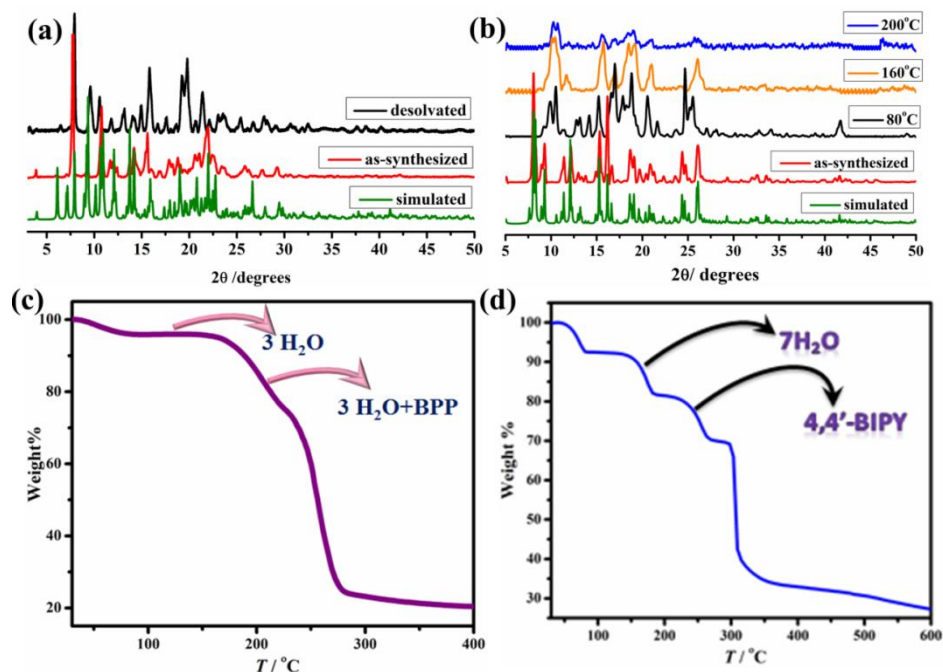
Fig. 7 (a) Change in the PXRD pattern of **1** on being heated to 135°C. **(b)** PXRD pattern of **2** at different temperatures. **(c)** TGA of **1**. **(d)** TGA of **2**.

55

The PXRD pattern of the as-synthesized compound **1** matches perfectly with the simulated pattern, suggesting the phase purity (**Fig. 7(a)**). The framework on being desolvated undergoes structural changes, as evident from the PXRD pattern of the rearrangement in the Bragg's reflections, along with peak broadening and appearance of new peaks, suggesting a structural transformation.

The thermogravimetric analysis (TGA) of compound **1** shows an initial loss of ~4% corresponding to three guest water molecules (**Fig. 7(c)**). Subsequently there is a continuous weight loss beyond ~150°C which may be attributed to the loss of the remaining two guest water molecules and the guest bpp molecule, which can be explained on the basis of SCXRD analysis. Two of the guest water molecules are released at higher temperature. Beyond 200°C, the framework degrades continuously.

PXRD pattern of the as-synthesized compound **2** is in accordance with the simulated pattern. The structure of compound **2** shows changes with increasing the temperature, as evident from the desolvated PXRD pattern (**Fig. 7(b)**). This can be attributed to the removal of the coordinated water molecules and the guest bipy molecules, which interact with the framework via π-π stacking. The removal of the bipy molecule gives rise to another structural phase. In this framework, along with guest water molecules, there are coordinated water molecules and their removal results in UMS. Such change in the coordination sphere of Cu^{II} centre ensue structural change, as reflected from the PXRD pattern.

The thermogravimetric analysis (TGA) of **2** shows an initial loss of ~9% up to 100°C owing to the loss of all 5 guest water molecules and one of the coordinated water molecules. (**Fig. 7(d)**). The subsequent ~13% loss starting at 140°C can be attributed to the loss of the second coordinated water molecule and guest bipyridine molecules. The desolvated framework degrades almost continuously beyond this.

2A.3.4 Gas and Solvent Adsorption

Although compound **1** does not have a definite pore in any direction, the presence of a pocket lined by aromatic moieties and electron rich aromatic benzene and pyridine rings along the crystallographic *b* direction prompted us to check the adsorption behavior of the desolvated compound (**1'**). At 195 K, the adsorption isotherm of **1'** shows an uptake 35 ml.g^{-1} of CO_2, with a steep uptake in the low pressure region. This can be attributed to the interaction of the CO_2 molecules with the free pendant carboxylate oxygen atoms flanking the pore surface and the π-electron density on the pore surface
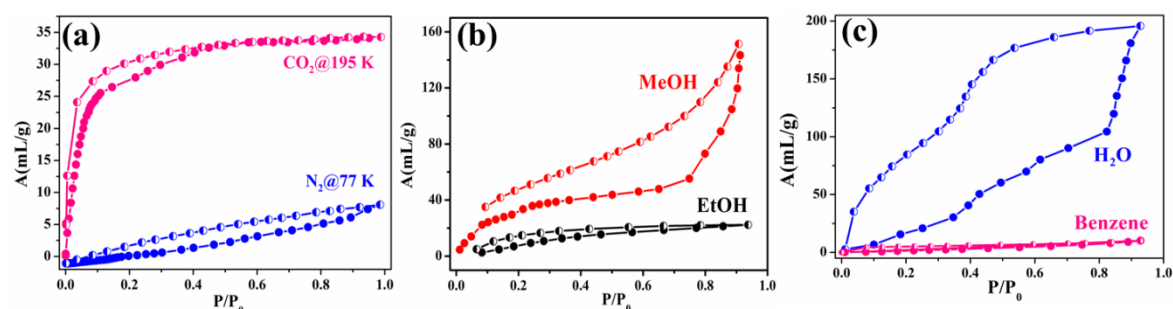
Fig. 8 (a) Adsorption isotherms of CO_2 at 195 K and N_2 at 77 K for compound **1**. **(b, c)** Solvent adsorption isotherms of compound **1** at 298 K.

from the aromatic rings of the linkers (**Fig. 8(a)**). The water adsorption curve (**Fig. 8(c)**) confirms the hydrophobic nature of the framework exhibiting poor uptake at lower pressures, which is also reiterated in the MeOH and EtOH adsorption isotherms (**Fig. 8(b)**). The net adsorption amount decreases from water (2.7 Å) to methanol (3.6 Å) to ethanol (4.5 Å) as the kinetic diameter of the solvent molecules increase in that order. The lower polarity of MeOH ensures a steeper uptake at low pressures, as compared to water, but the net uptake of water is much higher owing to its smaller size. Although the hydrophobic MOF is expected to show a good adsorption of non-polar solvents like benzene, the small pore dimensions of **1** restrict the adsorption of benzene (kinetic diameter of benzene being 5.9 Å) (**Fig. 8(c)**).

In order to check the porous properties of compound **2**, N_2 adsorption isotherm of the desolvated framework (**2'**) was measured at 77 K. **2'** does not adsorb N_2, which is attributed to the high diffusion barrier of the inert N_2 gas (kinetic diameter: 3.64 Å) in the narrow channel of **2'** (2.93×5.14 Å^2 along *b* direction) (**Fig. 5(d)**). Moreover, the accessible void space in this framework is very small due to the two-fold interpenetration. However, the framework **2'** manifests an appreciable amount of CO_2 uptake at 195 K, 273 K as well as at 298 K. At 195 K, **2'** records the adsorption of 127 mL.g^{-1} CO_2, with a steep uptake in the low pressure region, indicating towards its microporous nature (**Fig. 9(a)**). Steps are observed at various stages of adsorption which manifest that the framework is flexible in nature and there are different adsorption sites for CO_2. The desorption does not follow the same path as adsorption initially and we observe a hysteresis till $P/P_0 = 0.55$, below which both the curves converge. The adsorption amount of CO_2 is 85 mL.g^{-1} at 273 K and 65 mL.g^{-1} at 298 K. **2'** shows a type-I adsorption at 298 K where the adsorption and desorption curves do not coincide, exhibiting a narrow hysteretic profile (**Fig. 9(a)**). Besides the pendant oxygen atoms on the pore surface, the presence of unsaturated metal
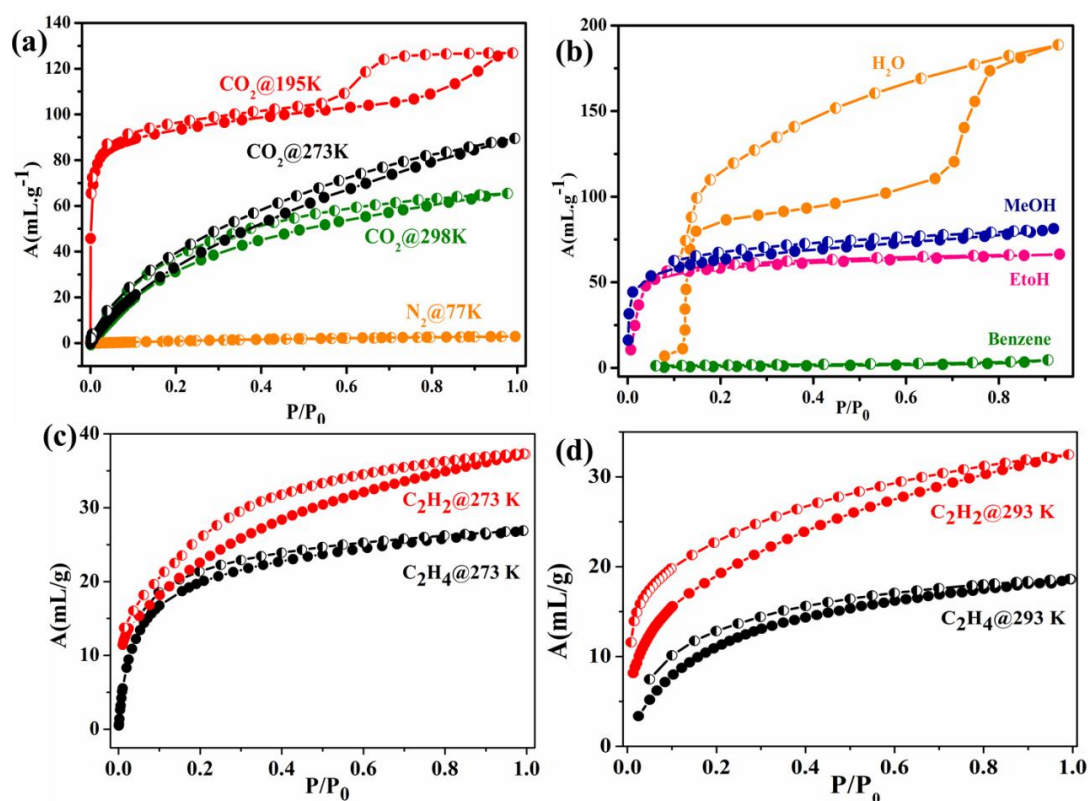
Fig. 9 (a) CO_2 and N_2 adsorption isotherms of **2'** at different temperatures. **(b)** Solvent adsorption isotherms of **2'**. C_2H_2 and C_2H_4 adsorption isotherms of **2'** at **(c)** 273 K and **(d)** 293 K.

sites (UMS), i.e., penta co-ordinated Cu^{II} centres, along the pore further contributes to the enhanced adsorption (**Fig. 5(e)**). Also, the kinetic diameter of CO_2 is smaller (3.3 Å) and its high quadruple moment interacts with the π electron cloud of the aromatic rings on the pore surface. The polar hydrophilic nature of the pore surface of **2'** is manifested by the solvent adsorption profiles (**Fig. 9(b)**). The adsorption isotherms of CO_2 at 273 K and 298 K were fitted in the virial equation, from which the isosteric heat of adsorption ($Q_{st,f}$) for **2'** was calculated to be ~18.9 kJ.mol^{-1} at zero coverage (**Fig. 10 (a,b)**).[8] Intrigued by this, we proceeded to predict the selectivity of **2'** towards CO_2 over N_2 at 298 K using Clausius-Clapeyron equation. At 298 K for **2'**, the predicted IAST (Ideal Adsorbed Solution Theory)[45] selectivities of CO_2 over N_2 for a bimolar (15:85) mixture of CO_2-N_2 is 13. Also here, the selectivity increases with increasing pressure. At pressure 101 kPa, the CO_2-N_2 selectivity is 94 (**Fig. 11(a)**). Such a good theoretical value prompted us to check the actual separation ability of **2** for CO_2 gas from a binary CO_2/N_2 (0.15:0.85) mixture at room temperature (293 K) by breakthrough column experiment. Tightly packed column of **2'** (400 mg, column length 4 cm) were prepared with a gas flow rate of 1 mL/min (carrier He gas). The breakthrough curve of the binary mixture of CO_2/N_2 (0.15:0.85) for **2'** is represented in **Fig. 11(c)**, where it exhibits a CO_2 retention time of 11
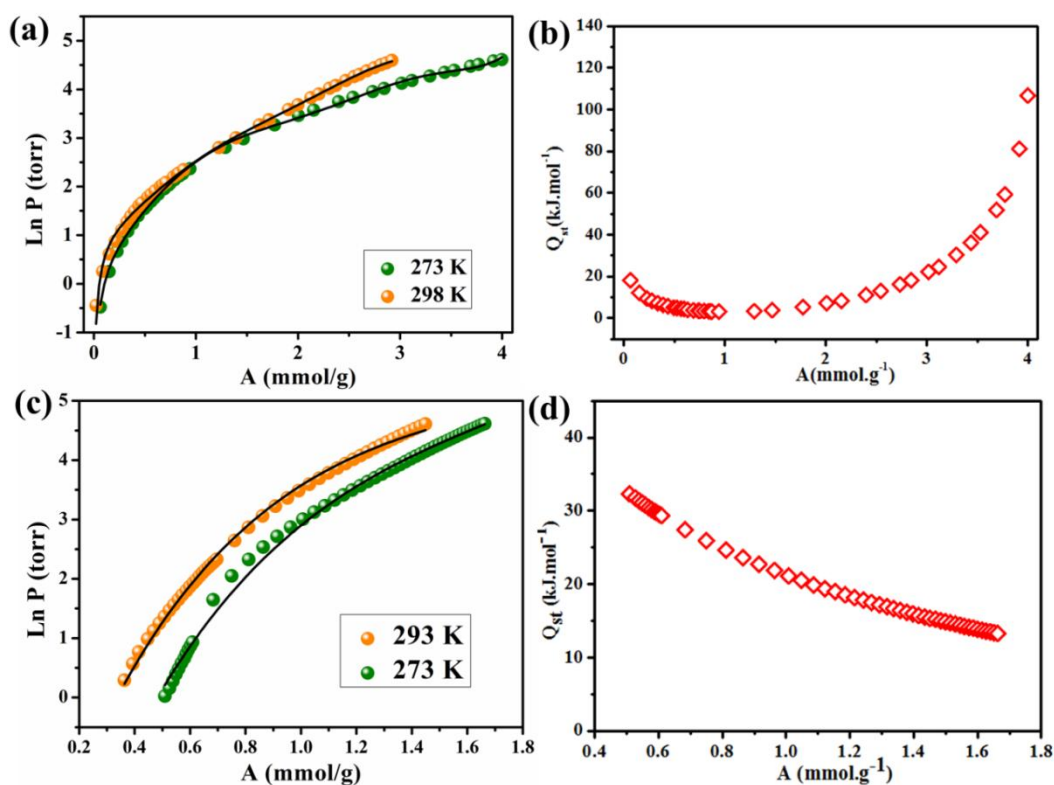
Fig. 10 (a) Adsorption isotherms for CO_2 at 273 and 298 K fitted in the virial Equation for **2'**. **(b)** Change in the heat of enthalpy with loading of CO_2 in **2'** calculated from the Virial fitting of the adsorption isotherms at 273 and 298 K. **(c)** Adsorption isotherms for C_2H_2 at 273 and 293 K fitted in the Virial Equation for **2'**. **(d)** Change in the heat of enthalpy with loading of C_2H_2 in **2'** calculated from the Virial fitting of the adsorption isotherms at 273 and 293 K.

min. This high retention time indicates that **2'** holds immense potential for practical use as a medium for separating CO_2 from other gases. Inspired by such efficiency of **2'** in separating CO_2 and N_2, we were further interested in exploiting the flexible structure and UMS for C2 [acetylene (C_2H_2) and ethylene (C_2H_4)] hydrocarbon storage and separation. Thus **2'** was checked for C_2H_2 and C_2H_4 adsorption and it was found that **2'** can adsorb 38 ml.g^{-1} C_2H_2 at 273 K, whereas the adsorption amount for C_2H_4 is 27 ml.g^{-1} at 273 K (**Fig. 9(c)**). **2'** shows a steeper uptake of C_2H_2 at lower pressure, as compared to C_2H_4. At P/P_0 = 0.01, the adsorbed amount of C_2H_2 per gram of **2'** is 11.5 ml when the adsorbate is C_2H_2 whereas that for C_2H_4 is merely 5ml. The desorption curve for C_2H_2 takes a different route than the adsorption isotherm, thereby forming a hysteresis, indicating towards a strong interaction between the framework and C_2H_2. At 293 K, the adsorption amounts are 33 ml.g^{-1} for C_2H_2 (**Fig. 9(d)**) and 16 ml.g^{-1} for C_2H_4. The isosteric heat of adsorption calculated for C_2H_2 is 32 kJ.mol^{-1} at zero coverage region (**Fig. 10(c,d)**). Thus due to a higher Q_{st} value, C_2H_2 attains more accessibility to the pore surface and interacts with the UMS, unlike C_2H_4. At 293K, the predicted selectivity of C_2H_2 over C_2H_4 for a (1:99)
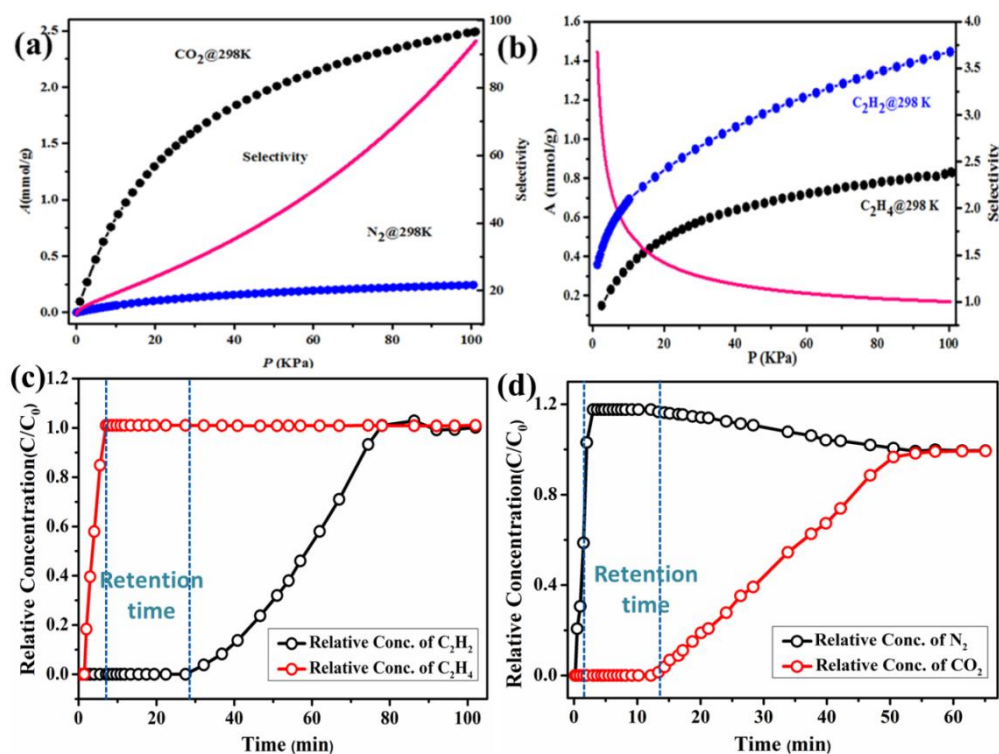
Fig. 11 Calculated selectivities for **(a)** CO_2 and N_2 and **(b)** C_2H_2 and C_2H_4 at 298 K for **2'**. Breakthrough curves for binary mixture of **(c)** N_2/ CO_2 (v/v 85:15) and **(d)** C_2H_2/C_2H_4 (v/v 1:99) for 2'.

mixture of the two gases is calculated in a similar manner as for CO_2-N_2, using IAST,[45] which is 3.7 initially, and the selectivity decreases gradually with increasing pressure (**Fig. 11(b)**). Thus the easy accessibility to UMS coupled with good IAST selectivity, high room temperature uptake and relatively low heat of adsorption certifies that **2'** is an ideal material for C_2H_2-C_2H_4 separation.

In order to establish the practical applicability of **2'** in separating a trace amount of C_2H_2 from C_2H_4, we performed an actual breakthrough experiment where we fed a column of 2 with a (1:99, v/v) mixture of C_2H_2 and C_2H_4 at 298 K. Interestingly, C_2H_4 appears within a few seconds of starting the gas flow. The breakthrough time for C_2H_2 is 27 mins (**Fig. 11(d)**). This is a rather unique feat achieved by any MOF at room temperature and aptly upholds the efficiency of **2** in real-time applications.

2A.4 Conclusion

In conclusion, two different flexible tetracarboxylate linkers **L1** and **L2** have been successfully implemented in two different frameworks **1** and **2** along with exo-bidentate pyridyl based linkers. The variable flexibility and the aromatic π-electron rich nature of the linkers impart very interesting properties within the framework. The presence of

hydrophobic pockets, lined by aromatic rings from the linker in compound **1** enables it to adsorb a reasonable amount of CO_2 at 195 K. On the other hand, compound **2** with a 3D framework with two-fold interpenetration, is a promising material owing to the presence of polar carboxylate groups, UMS and flexible structure. It shows a good IAST selectivity towards C_2H_2 over C_2H_4, which is culminated in practical application using a breakthrough column. **2'** can retain C_2H_2 for a very long time within the breakthrough column, releasing pure C_2H_4. Moreover, **2'** also manifests excellent CO_2-N_2 separation. The selectivity of CO_2 over N_2 and C_2H_2 over C_2H_4 is attributed to more favourable thermodynamic interactions. Thus frameworks constructed from such tetracarboxylate linkers can be used as effective materials for specific gas sequestration and separation by tuning flexibility and functionalities.

2A.5 References

1. L. Chen, P. S. Reiss, S. Y. Chong, D. Holden, K. E. Jelfs, T. Hasell, M. A. Little, A. Kewley, M. E. Briggs, A. Stephenson, K. M. Thomas, J. A. Armstrong, J. Bell, J. Busto, R. Noel, J. Liu, D. M. Strachan, P. K. Thallapally and A. I. Cooper, *Nat. Mater.*, 2014, **13**, 954.

2. J.-R. Li, R. J. Kuppler and H.-C. Zhou, *Chem. Soc. Rev.*, 2009, **38**, 1477.

3. Z. Kang, L. Fan and D. Sun, *J. Mater. Chem. A*, 2017, **5**, 10073.

4. W. Zhang, D. Banerjee, J. Liu, H. T. Schaef, J. V. Crum, C. A. Fernandez, R. K. Kukkadapu, Z. Nie, S. K. Nune, R. K. Motkuri, K. W. Chapman, M. H. Engelhard, J. C. Hayes, K. L. Silvers, R. Krishna, B. P. McGrail, J. Liu and P. K. Thallapally, *Adv. Mater.*, 2016, **28**, 3572.

5. B. Li, H. Wang and B. Chen, *Chem. Asian J.*, 2014, **9**, 1474.

6. D. Banerjee, S. K. Elsaidi and P. K. Thallapally, *J. Mater. Chem. A*, 2017, **5**, 16611.

7. A. Hazra, S. Jana, S. Bonakala, S. Balasubramanian and T. K. Maji, *Chem. Commun.*, 2017, **53**, 4907.

8. L. Li, R.-B. Lin, R. Krishna, X. Wang, B. Li, H. Wu, J. Li, W. Zhou, and B. Chen, *J. Mater. Chem. A*, 2017, **5**, 18984.

9. T.-L. Hu, H. Wang, B. Li, R. Krishna, H. Wu, W. Zhou, Y. Zhao, Y. Han, X. Wang, W. Zhu, Z. Yao, S. Xiang and B. Chen, *Nat. Commun.*, 2015, **6**, 7328.

10. S. Kitagawa, R. Kitaura and S.-i. Noro, *Angew. Chem. Int. Ed.*, 2004, **43**, 2334.

11. J. Liu, L. Chen, H. Cui, J. Zhang, L. Zhang and C.-Y. Su, *Chem. Soc. Rev.*, 2014, **43**, 6011.

12. S. Roy, A. Chakraborty and T. K. Maji, *Coord. Chem. Rev.*, 2014, **273**, 139.

13. Z. Hu, B. J. Deibert and J. Li, *Chem. Soc. Rev.*, 2014, **43**, 5815.

14. S. Horike, S. Shimomura and S. Kitagawa, *Nat. Chem.*, 2009, **1**, 695.

15. A. L. Dzubak, L.-C. Lin, J. Kim, J. A. Swisher, R. Poloni, S. N. Maximoff, B. Smit and L. Gagliardi, *Nat. Chem.*, 2012, **4,** 810.

16. A. S. Duke, E. A. Dolgopolova, R. P. Galhenage, S. C. Ammal, A. Heyden, M. D. Smith, D. A. Chen and N. B. Shustova, *J. Phys. Chem. C*, 2015, **119**, 27457.

17. T. L. Easun, F. Moreau, Y. Yan, S. Yang and M. Schroder, *Chem. Soc. Rev.*, 2017, **46**, 239.

18. H. J. Park and M. P. Suh, *Chem. Commun.*, 2010, **46**, 610.

19. S. Yang, X. Lin, W. Lewis, M. Suyetin, E. Bichoutskaia, J. E. Parker, C. C. Tang, D. R. Allan, P. J. Rizkallah, P. Hubberstey, N. R. Champness, K.M. Thomas, A. J. Blake and M. A Schröder, *Nat. Mater.*, 2012, **11**, 710.

20. A. Hazra, S. Bonakala, K. K. Bejagam, S. Balasubramanian and T. K. Maji, *Chem. Eur. J.*, 2016, **22**, 7792.

21. S. Xiang, Y. He, Z. Zhang, H. Wu, W. Zhou, R. Krishna and B. Chen, *Nat. Commun.*, 2012, **3**, 954.

22. Z.-J. Lin, J. Lu, M. Hong and R. Cao, *Chem. Soc. Rev.*, 2014, **43**, 5867.

23. Z. Chang, D.-H. Yang, J. Xu, T.-L. Hu and X.-H. Bu, *Adv. Mater.*, 2015, **27**, 5432.

24. Y. Ling, Z.-X. Chen, F.-P. Zhai, Y.-M. Zhou, L.-H. Weng and D.-Y. Zhao, *Chem. Commun.*, 2011, **47**, 7197.

25. X. Lin, J. Jia, X. Zhao, K. M. Thomas, A. J. Blake, G. S. Walker, N. R. Champness, P. Hubberstey and M. Schröder, *Angew. Chem. Int. Ed.*, 2006, **45**, 7358.

26. L. H. Wee, C. Wiktor, S. Turner, W. Vanderlinden, N. Janssens, S. R. Bajpe, K. Houthoofd, G. Van Tendeloo, S. De Feyter, C. E. A. Kirschhock and J. A. Martens, *J. Am. Chem. Soc.*, 2012, **134**, 10911.

27. Z. Pan, H. Zheng, T. Wang, Y. Song, Y. Li and Z. Guo, *Inorg. Chem.*, 2008, **47**, 9528.

28. J. Liu, P. K. Thallapally, B. P. McGrail, D. R. Brown and J. Liu, *Chem. Soc. Rev.*, 2012, **41**, 2308.

29. M. Y. Masoomi, K. C. Stylianou, A. Morsali, P. Retailleau and D. Maspoch, *Cryst. Growth Des.*, 2014, **14**, 2092.

30. S. Wu, L. Ma, L.-S. Long, L.-S. Zheng, W. Lin, *Inorg. Chem.*, 2009, **48**, 2436.

31. S. Mukherjee, B. Joarder, A. V. Desai, B. Manna, R. Krishna and S. K. Ghosh, *Inorg. Chem.*, 2015, **54**, 4403.

32. A. Schneemann, V. Bon, I. Schwedler, I. Senkovska, S. Kaskel and R. A. Fischer, *Chem. Soc. Rev.*, 2014, **43**, 6062.

33. P. Kanoo, R. Haldar, S. K. Reddy, A. Hazra, S. Bonakala, R. Matsuda, S. Kitagawa, S. Balasubramanian and T. K. Maji, *Chem. Eur. J.*, 2016, **22**, 15864.

34. A. Schneemann, Y. Takahashi, R. Rudolf, S.-i. Noro, R. A. Fischer, *J. Mater. Chem. A*, 2016, **4**, 12963.

35. S. Sakaida, K. Otsubo, O. Sakata, C. Song, A. Fujiwara, M. Takata and H. Kitagawa, *Nat. Chem.*, 2016, **8**, 377.

36. K. Bärwinkel, M. M. Herling, M. Rieß, H. Sato, L. Li, Y. S. Avadhut, T. W. Kemnitzer, H. Kalo, J. Senker, R. Matsuda, S. Kitagawa and J. Breu, *J. Am. Chem. Soc.*, 2017, **139**, 904.

37. L. Li, R. Krishna, Y. Wang, J. Yang, X. Wang and J. Li, *J. Mater. Chem. A*, 2016, **4**, 751.

38. P. Kanoo, R. Sambhu and T. K. Maji, *Inorg. Chem.*, 2010, **50**, 400.

39. B. Liu, Y. Li, L. Hou, G. Yang, Y.-Y. Wang and Q.-Z. Shi, *J. Mater. Chem. A*, 2013, **1**, 6535.

40. S. Mukherjee, B. Joarder, B. Manna, A. V. Desai, A. K. Chaudhari and S. K. Ghosh, *Sci. Rep.*, 2014, **4**, 5761.

41. R. Haldar, S. K. Reddy, V. M. Suresh, S. Mohapatra, S. Balasubramanian and T. K. Maji, *Chem. Eur. J.*, 2014, **20**, 4347.

42. M. L. Foo, R. Matsuda, Y. Hijikata, R. Krishna, H. Sato, S. Horike, A. Hori, J. Duan, Y. Sato, Y. Kubota, M. Takata and S. Kitagawa, *J. Am. Chem. Soc.*, 2016, **138**, 3022.

43. Y.-Q. Lan, H.-L. Jiang, S.-L. Li and Q. Xu, *Adv. Mater.*, 2011, **23**, 5015.

44. A. W. Addison, T. N. Rao, J. Reedijk, J. van Rijn and G. C. Verschoor, *J. Chem. Soc., Dalton Trans.*, 1984, 1349.

45. A. L. Myers and J. M. Prausnitz, *AlChE J.*, 1965, **11**, 121.

46. G. M. Sheldrick, SHELXL 97, University of Göttingen, Germany, 1997.

47. S. V. a. SMART (V 5.628), XPREP, SHELXTL; Bruker AXS Inc. Madison, Wisconsin, USA, 2004.

48. V. A. Blatov, L. Carlucci, G. Ciani and D. M. Proserpio, *CrystEngComm*, 2004, **6**, 377.

49. V. A. Blatov, A. P. Shevchenko and V. N. Serezhkin, *J. Appl. Crystallogr.*, 2000, **33**, 1193.

50. P. Vishnoi, D. Kaleeswaran, A. Ch. Kalita and R. Murugavel, *CrystEngComm*, 2016, **18**, 9130.

51. A. Halder, B. Bhattacharya, F. Haque and D. Ghoshal, *Cryst. Growth Des.*, 2017, **17**, 6613.

52. V. Sharma, D. De, R. Saha, R. Das, P. K. Chattaraj and P. K. Bharadwaj, *Chem. Commun.*, 2017, **53**, 13371.

Chapter 2B

Crystal-to-Crystal Transformation in a 3D Dynamic Supramolecular Porous Framework of Mg^{II}: Tunable Porosity & Efficient Gas Separation
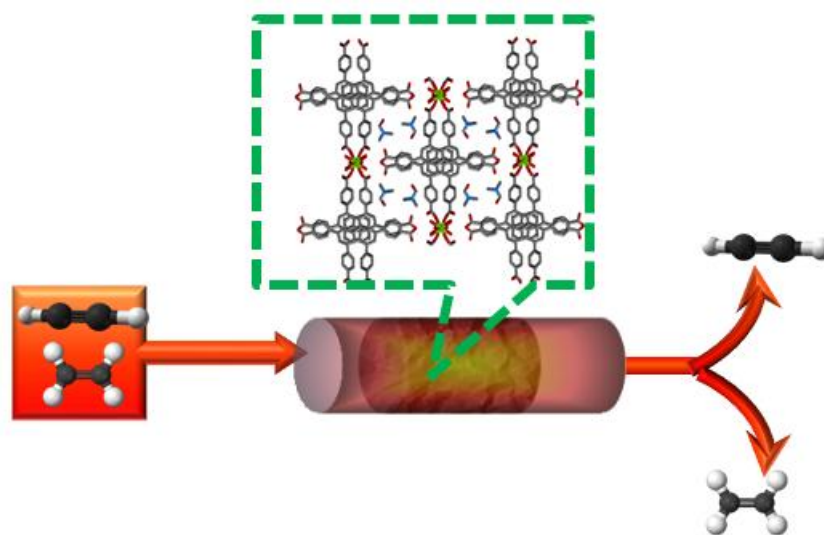
Abstract

This chapter comprises the synthesis, structure and adsorption properties of a new 3D supramolecular porous framework $[Mg(PyTBH_2)(\mu-H_2O)(H_2O)_2].2(DMF)$ (**1**) [(PyTB=1,3,6,8-tetrakis(p-benzoic acid)pyrene] formed by the H-bonding interaction between 2D networks of Mg^{II}, $[Mg(PyTBH_2)(\mu-H_2O)(H_2O)_2]$ [(PyTB=1,3,6,8-tetrakis(p-benzoic acid)pyrene]. These 2D networks are formed by the cross-linking of 1D $\{Mg(\mu-OH_2)\}_n$ chains by the $PyTBH_2$ linkers. $PyTBH_2$ acts as a bidentate bridging linker keeping two –COOH groups non-coordinated. The compound **1** shows interesting crystal-to-crystal structural transformation based on dehydration at different temperatures and also guest exchange. MeOH exchanged single crystals of **1** produces guest free 3D supramolecular framework $[Mg(PyTBH_2)(\mu-H_2O)(H_2O)_2]$ (**2**) under vacuum. Interestingly, when **2** is heated at 80°C, we observe a single-crystal-to-single-crystal transformation which produces $[Mg(PyTBH_2)(H_2O)_2]$ (**3**). Here two coordinated water molecules are replaced by the carboxylate oxygens forming 1D chain of $\{Mg(\mu-OCO)_2\}_n$ and the 3D supramolecular framework remains intact. When compound **3** is heated at high temperature (200°C), all the water molecules are removed and we obtain a 3D MOF $[Mg(PyTBH_2)]$ (**4**) by the coordination of the pendant carboxylate oxygens to the Mg centres. This has been supported by temperature dependant IR spectroscopy and theoretical calculations. **4** shows high surface area (526 $m^2.g^{-1}$) as compared to **3** (202 $m^2.g^{-1}$) and good uptake of CO_2 and other small hydrocarbons (C_2H_2, C_2H_6) both at 273 K and at room temperature. The practical applicability of **4** in gas separation has been demonstrated using a breakthrough setup, where it can separate bimolecular mixtures of CO_2/N_2, CH_4/C_2H_6 and C_2H_2/C_2H_4 with good efficiency.

2B.1 Introduction

The rapid industrialization worldwide has rendered adsorptive separation as one of the most important tools, relevant both industrially as well as environmentally.[1-3] In order to counter global warming, it is of utmost importance that CO_2 is separated from the industrial flue gas and reduced to other value-added product. [4-7] Similarly, the purification of small hydrocarbons, e.g., ethylene, ethane, acetylene, etc., produced by steam-cracking of petroleum is of utmost importance for the polymer industry.[7-10] The presence of even 1% acetylene contamination in ethylene acts as catalyst poison hindering the formation of defect-free polyethylene.[11, 12] Hence, for the advancement of carbon based energy technologies as well as the polymer industry, it is of utmost importance to develop inexpensive and efficient porous materials for adsorptive separation of gases.[13, 14] In this context, metal-organic frameworks (MOFs)[14, 15] are extremely relevant because of their innate porosity, large surface areas and facile tunability.[16, 17] MOF surpasses its purely inorganic counterparts, e.g., zeolites and silica, as an adsorptive separator of gases owing to its flexibility and easy functionalization of the pore surfaces.[18] Moreover, adsorptive separation using MOFs is much more efficient in terms of cost and energy rather than conventional gas separation techniques, e.g., partial hydrogenation or cryogenic distillation.[19, 20]

The basis of gas separation using MOFs lies in the preferential adsorption of a particular gas by the framework.[21-23] Such selectivity can be achieved not only by modulating the pore size (kinetic separation),[24-26] but also by introducing specific sites of interaction with the adsorbate molecules on the pore surface and modulating the heat of adsorption (thermodynamic separation).[27-30] Hence, it is indispensible to assume a targeted ligand design strategy for the synthesis of highly efficient MOFs for selective adsorption of specific adsorbate molecules.[31-35] Multi-dentate aromatic linkers are particularly interesting in this context since they provide a large number of coordinating sites along with high π-electron density on the pore surface.[14, 36-39] The presence of π-electron cloud as well as oxygen atoms from these ligands on the pore surface allows strong interaction of the framework with polar gas molecules like CO_2 or small hydrocarbons like ethylene and acetylene, etc.[40-43] These linkers can give rise to a host of multinuclear nodes with various geometries and also impart flexibility to the framework leading to tunable porosity and guest-responsive structural dynamicity in the framework.[44, 45]

With these considerations in mind, we have synthesized a Mg^{II} based dynamic supramolecular framework by assembling it with a pyrene-based tetracarboxylic acid [1,3,6,8-tetrakis(p-benzoic acid)pyrene] (PyTBH$_4$). The resultant framework {[Mg(PyTBH$_2$)(H$_2$O)$_3$]}$_n$ (**1**) is a 3D supramolecular framework[46, 47] held together by H-bonding between the 2D networks of [Mg(PyTBH$_2$)(H$_2$O)$_3$]. The framework contains dimethyformamide (DMF) guest present within the pores. Based on the partial and complete removal of the guest and coordinated water molecules, three different intermediate states have been isolated, two of which have been structurally characterized. Compounds [Mg(PyTBH$_2$)(H$_2$O)$_2$]$_n$ (**3**) and [Mg(PyTBH$_2$)]$_n$ (**4**) show surface areas of 202 and 526 $m^2.g^{-1}$, respectively. The completely desolvated state **4** shows excellent affinity towards small hydrocarbons and CO_2. Moreover, upon performing breakthrough measurements, we have found out that the framework shows excellent performance in the separation of CO_2/N_2, CH_4/C_2H_6 and C_2H_2/C_2H_4 from their mixtures at 293 K.

2B.2 Experimental Section

2B.2.1 Materials

All the reagents and solvent were used as obtained from commercial supplies without any further purification. $MgNO_3.6H_2O$ and 1,4-Dioxane were obtained from Aldrich Co. Ltd. Dimethylformamide was obtained from Spectrochem Co.

2B.2.2 Synthesis of PyTBH$_4$ [1,3,6,8-tetrakis(p-benzoic acid)pyrene]

Pyrene (5 g, 24 mmol) was taken in 100 mL of nitrobenzene and was reacted with excess bromine (5.6 mL, 109 mmol) for 14 h at 120 °C to give 1,3,6,8-tetrabromopyrene. Further, (4-(methoxycarbonyl)phenyl)boronic acid (5 g, 32.9 mmol), 1,3,6,8-tetrabromopyrene (2.85 g, 5.5 mmol), palladium tetrakis(triphenylphosphine) (0.1 g, 0.09 mmol) and potassium carbonate (6 g, 44 mmol) were taken in dry dioxane (50 mL) and was stirred under nitrogen for 72 h at 85 °C. The reaction mixture was poured into an ice-cold solution of concentrated hydrochloric acid (3:1). The organic phase of the mixture was extracted with chloroform, dried over sodium sulfate, and the solvent was evaporated in a rotatory evaporator to yield 1,3,6,8-tetrakis(4-(methoxycarbonyl)phenyl)pyrene. A 20 mL 1 M NaOH solution was added to the mixture of 1 g 1,3,6,8-tetrakis(4-

(methoxycarbonyl)phenyl) pyrene in 100 mL of THF/dioxane/H_2O (ratio 5:2:2) and the mixture was stirred under reflux at 85 °C overnight. The solvent was removed under vacuum, and then H_2O was added to the residue. The solution was stirred at room temperature for 2 h and conc. HCl was added. The resulting yellow solid was collected by filtration, washed with water, HCl (1 M), and diethyl ether, and then dried under vacuum. ^{1}H NMR (DMSO-*d*6): δ 7.73 (d, *J*) 8.2 Hz, (s, 8H), 8.05 (s, 2H), 8.12 (d, *J*) 8.2 Hz,(s, 8H), 8.3 (s, 4H), 13.3 (s, 4H).

2B.2.3 Synthesis of [Mg(PyTBH$_2$)(H$_2$O)$_3$].2(DMF) (1)

MgNO$_3$.6H$_2$O (10 mg) and solid PyTBH$_4$ (10 mg) were taken in a glass vial. A total 4 ml of solvent containing DMF, 1,4- dioxane and H_2O in the ratio (2:1:1) was added to the vial. The mixture is sonicated for 10 mins and then kept undisturbed at 85°C for 4 days. Yellow needle shaped crystals appear after 4 days which are collected. Yield: 70% relative to Mg^{II}. Anal. calcd. for $C_{50}H_{44}MgO_{13}N_2$: C 67·54; H 4·99; N 3·15%. Found: C 66·99; H 4·76; N 2.87%. The IR data has been summarized in **Table 1**.
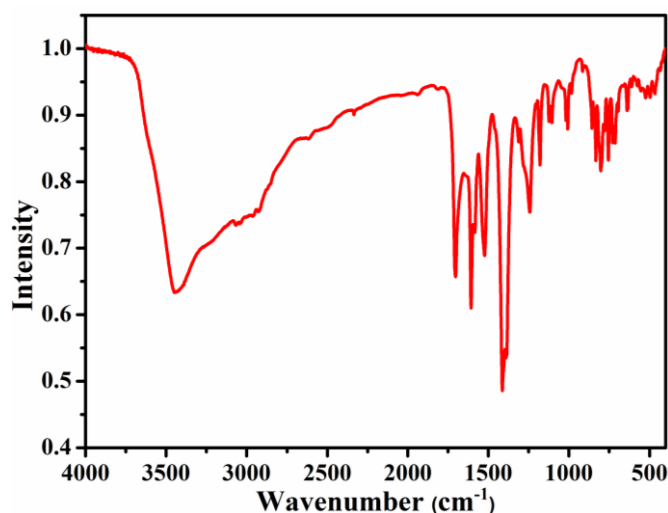
Fig. 1 IR spectrum of **1**.

Table 1 Principal peaks in IR of **1** (**Fig. 1**).

Peak Position (cm^{-1})	Nature	Vibration
3435	sharp	N-H stretch
3230-3460	broad	O-H stretch
1704	sharp	C=O stretch
1607	sharp	C=C stretch
1518	sharp	Aromatic C=C stretch

2B.2.4 Physical measurements

The elemental analyses were carried out using a Thermo Fischer Flash 2000 Elemental Analyzer. IR spectra were recorded with a Bruker IFS 66v/S spectrophotometer using KBr pellets in the region 4000–400 cm^{-1}. Thermogravimetric analysis (TGA) were carried out (Mettler Toledo) in a nitrogen atmosphere (flow rate = 50 ml min^{-1}) in the temperature range 30–500 °C (heating rate = 3 °C min^{-1}). Powder XRD patterns of the compounds in different states were recorded by using Cu-Kα radiation (Bruker D8 Discover; 40 kV, 30 mA).

2B.2.5 X-ray Crystallography

X-ray single crystal structural data for compounds **1**, **2**, and **3** were collected using a Bruker Smart-CCD diffractometer equipped with a normal focus, 2.4 kW sealed tube X-ray source with graphite monochromated Mo-Kα radiation (λ = 0·71073 Å) operating at 50 kV and 30 mA. The program SAINT[14] was used for integration of diffraction profiles and absorption correction was made using the SADABS[15] program. All the structures were solved using SHELXL[47] and refined by a full matrix least square method using SHELXL-2017.[46] All of the hydrogen atoms were geometrically fixed and placed in ideal positions. The potential solvent accessible area or void space was calculated using the PLATON multipurpose crystallographic software.[18]

2B.2.6 Adsorption Study

The adsorption isotherms of CO_2 (195 K), N_2 (77 K, 273 K and 298 K), other gases (CH_4, C_2H_6, C_2H_2, C_2H_4 at 273 K and 298 K) for the compounds **3** and **4** are measured by using a QUANTACHROME AUTOSORB IQ2 analyzer. In the sample tube adsorbent samples **3** and **4** (~100–150 mg) were placed which had been prepared at 353 and 433 K, respectively, under a 1×10^{-1} Pa vacuum for about 6 h prior to measurement of the isotherms. Helium gas (99.999% purity) at a certain pressure was introduced in the gas chamber and allowed to diffuse into the sample chamber by opening the valve. The amount of gas adsorbed was calculated readily from the pressure difference ($P_{cal} - P_e$), where P_{cal} is the calculated pressure with no gas adsorption and P_e is the observed equilibrium pressure. All operations were computer-controlled and automatic. The adsorption isotherms of different solvents like MeOH at 293 K and H_2O and EtOH at 298

K were recorded with compounds **3** and **4** in the vapour state by using a BELSORP Aqua-3 analyzer. The samples of about ~100–150 mg were activated under similar conditions as mentioned earlier. The different solvent molecules used to generate vapour were degassed fully by repeated evacuation. The dead volume was measured with helium gas. The adsorbate was placed into the sample tube, then the change of pressure was monitored and the degree of adsorption was determined by the decrease in pressure at the equilibrium state. All operations were computer controlled and automatic.

2B.2.7 Heat of Adsorption Calculation

The virial type expression of the following type has been used to fit the combined isotherms data collected at 273 and 293 K.

$$\ln(P) = \ln(A) + \frac{1}{T} \sum_{i=0}^{m} a_i A_i + \sum_{i=0}^{n} b_i B_i$$

Here, P is the pressure expressed in torr, A is the amount adsorbed in mmol/g, T is the temperature in K, a_i and b_i are virial coefficients, and m, n represent the number of coefficients required to describe the isotherms. The values of m and n are gradually increased until the contribution of extra added a and b coefficients were negligible for the overall final fit. The values of the virial coefficient a_i were taken to calculate the isosteric heat of adsorption using the following expression.

$$Q_{st} = -R \sum_{i=0}^{m} a_i A_i$$

Q_{st} is the coverage dependent isosteric heat of adsorption and **R** is the universal gas constant.

2B.2.8 Breakthrough Measurements

Breakthrough experiments were performed using a column (packed with about 150 mg of powdered **4**), 1.5 cm long in length and 0.3 cm diameter. The sample was first activated at 200°C for 12 h prior to loading in column. After loading the sample was again activated with the He flow for 30 mins. CO_2 /N_2 (v/v 15:85 mixture), CH_4/C_2H_6 (v/v 50:50) and C_2H_2 /C_2H_4 (V/V: 1:99 mixture) streams were passed through the column with He. The flow was continuous and the flow rate was regulated by MFC. The partial pressure of the gas mixture was kept at P = 5 kPa. The gas stream at the outlet of the column was analyzed on-line with a GC. The space velocity was kept at 4.71 min^{-1}.

2B.3 Results and Discussions

2B.3.1 Single Crystal Structure of Compound 1

Single crystal X-ray diffraction analysis reveals that **1** crystallizes in monoclinic $C2/c$ space group. The asymmetric unit consists of one Mg^{II} cation, one dianionic $PyTBH_2$, one bridging and two terminal water molecules and two guest DMF molecules (**Fig. 2(a)**). Each Mg (Mg1) centre is connected to its adjacent one on both sides by bridging water molecules (O1w, O1w*) resulting in a 1D chain of $\{Mg(\mu\text{-}H_2O)\}_n$ along the crystallographic c direction (**Fig. 2(b)**). These 1D chains are cross-linked by the $PyTBH_2$ linkers through monodentate oxygen atom from the opposite side of the carboxylate groups of the linkers, resulting in a 2D network lying in the crystallographic ac plane (**Fig. 2(c)**). Other two coordination sites of Mg centre are occupied by the water molecules (O2w, O2w*). The other two carboxylic acid groups remain uncoordinated and the two benzoic acid moieties stayed in an orthogonal orientation with the pyrene core. Interestingly, these 2D networks stack over one another in an ABAB fashion in the ab plane, when viewed along the c-axis. This is reinforced by the H-bonding interaction between the free carboxylic groups of one network and the coordinated water molecules
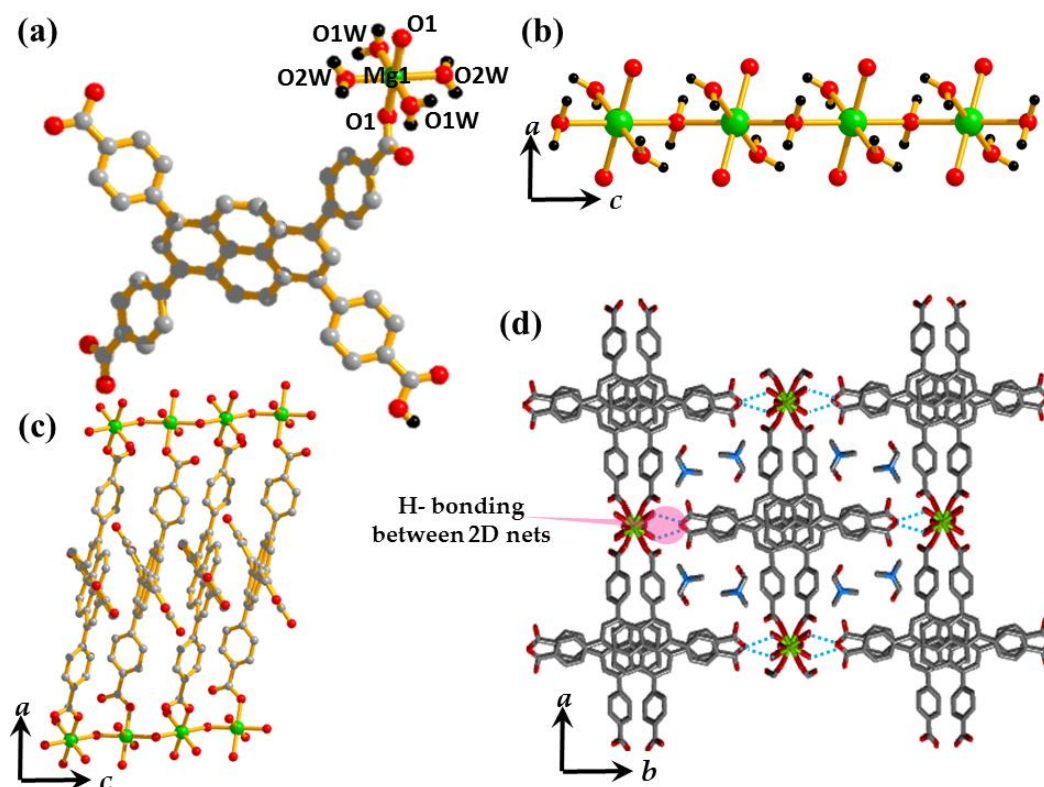
Fig.2 (a) Assymmetric unit of MOF **1** showing the coordination sphere of Mg1. **(b)** 1D chain formed by the bridging of Mg-O clusters by H_2O in the c direction. **(c)** 2D sheet in MOF **1**. **(d)** 3D supramolecular framework formed by H-bonding between the 2D sheets.

of another network (**Fig. 2(d)**). The H- bonding parameters have been tabulated in **Table 5**. The resulting 3D supramolecular framework enclosed 1D square shaped channels with dimensions of 4.136×5.046 Å^2, that house the DMF guest molecules. The solvent accessible void space in the framework after removing the DMF guests is 31.3% of the total cell volume, which has been calculated using PLATON after removing the guest DMF molecules. The crystallographic parameters of **1** and selected bond distance and angles have been tabulated in **Tables 2, 3** and **4**.

Table 2 Crystal data and structure refinement for compound **1**

Parameter	1
Empirical Formula	$C_{50}H_{44}MgN_2O_{13}$
Formula Weight	905.18
Crystal System	Monoclinic
Space Group	*C2/c* (No.15)
***a*, Å**	21.8425(14)
***b*, Å**	27.1568(18)
***c*, Å**	7.6389(5)
***ß*, deg**	99.565(2)
***V*, Å^3**	4468.2(5)
Z	4
***T*, K**	200
***μ*, mm^{-1}**	0.110
***D*$_{calcd}$,g/cm^3**	1.346
***F* (000)**	1896
Reflections [*I>2σ(I)*]	2827
Unique reflections	4197
Measured reflections	12282
***R*$_{int}$**	0.073
GOF on *F*^{2}	0.97
***R*$_1$[*I>2σ(I)*][a]**	0.1040
***R*$_w$[I>2σ(I)][b]**	0.2348

$(R = \sum||F_o|-|F_c||/\sum|F_o| , R_w = [\sum\{w(F_o{}^2-F_c{}^2)^2\}/\sum\{w(F_o{}^2)^2\}]^{1/2})$

Table 3 Selected bond distances (Å) for **1**.

Mg1-O1	2.046(3)	Mg1-O2W_b	2.1372(17)
Mg1-O1W	2.061(3)	O1-C1	1.268(5)
Mg1-O2W	2.1372(17)	O2-C1	1.259(5)
Mg1-O1_b	2.046(3)	O3-C16	1.214(6)
Mg1-O1W_b	2.061(3)	O4-C16	1.323(6)

Table 4 Selected bond angles (°) for **1**.

O1-Mg1-O1W	91.66(11)	O1W-Mg1-O2W	88.25(11)
O1-Mg1-O2W	91.02(9)	O1_b -Mg1-O1W	88.34(11)
O1-Mg1-O1_b	180.00	O1W-Mg1-O1W_b	180.00
O1-Mg1-O1W_b	88.34(11)	O1W-Mg1-O2W_b	91.75(11)
O1-Mg1-O2W_b	88.98(9)	O1_b -Mg1 -O2W	88.98(9)

Table 5 Hydrogen bond parameters for **1**.

D–H···A	D–H (Å)	H···A (Å)	D ···A (Å)	∠D–H···A (°)
O1W–H1O1···O1	0.8300	2.0100	2.807(4)	161.00
O2W–H1O2···O1	0.9100	2.5000	2.985(3)	114.00
O2W–H1O2···O2	0.9100	1.7300	2.628(3)	168.00
O1W–H2O1···O3	0.9400	1.8500	2.753(5)	161.00
O4–H4O4···O2	0.8400	1.8300	2.665(4)	172.00

2B.3.2 Framework Stability of Compound 1
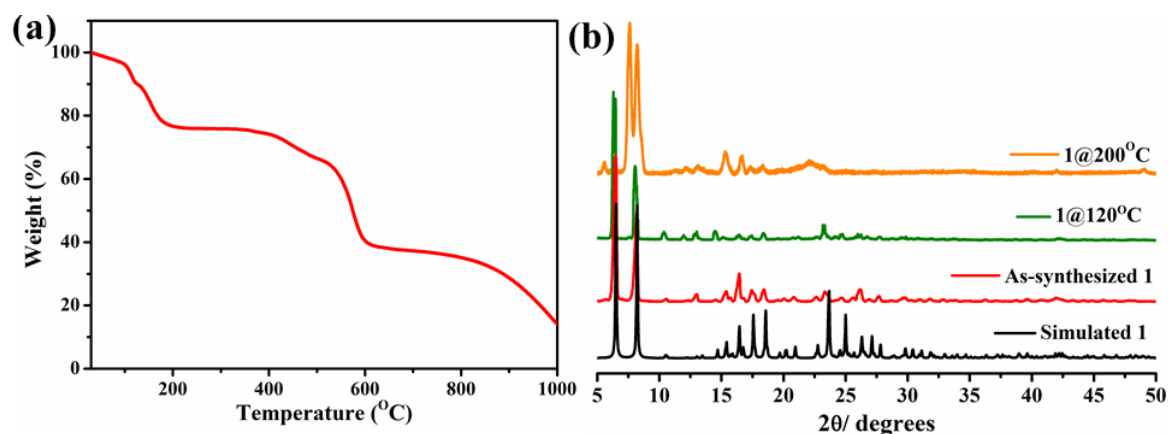
Fig. 3(a) TGA of **1**. **(b)** Temperature dependant PXRD of MOF **1**.

The thermogravimetric analysis (TGA) of **1** shows a stepwise loss of 21 wt% till 185°C which corresponds to the loss of three water and two DMF molecules present in the unit cell (theoretically calculated 22%). The framework is stable thereafter till 400°C, beyond which it degrades continuously (**Fig. 3(a)**). Phase purity of the compound **1** was characterized by PXRD pattern as shown in **Fig. 1(b)**. As the compound **1** contains guest DMF, coordinated/bridging water molecules, PXRD patterns were collected by heating the compound at different temperatures. PXRD pattern at 120°C did not show significant change, suggesting framework remains intact without reorganization. However, PXRD pattern of the compound obtained by heating **1** at 200°C, i.e., the completely desolvated state showed significant change, with appearance of new peaks and shifting of Bragg's

reflection, suggesting significant reorganization in the 3D framework (**Fig. 3(b)**). The presence of H-bonding, guest and bridging water molecules upholds the probability of structural reorganization in the framework of **1** with the change in temperature.

2B.3.3 Crystal-to- Crystal Structural Transformation in 1
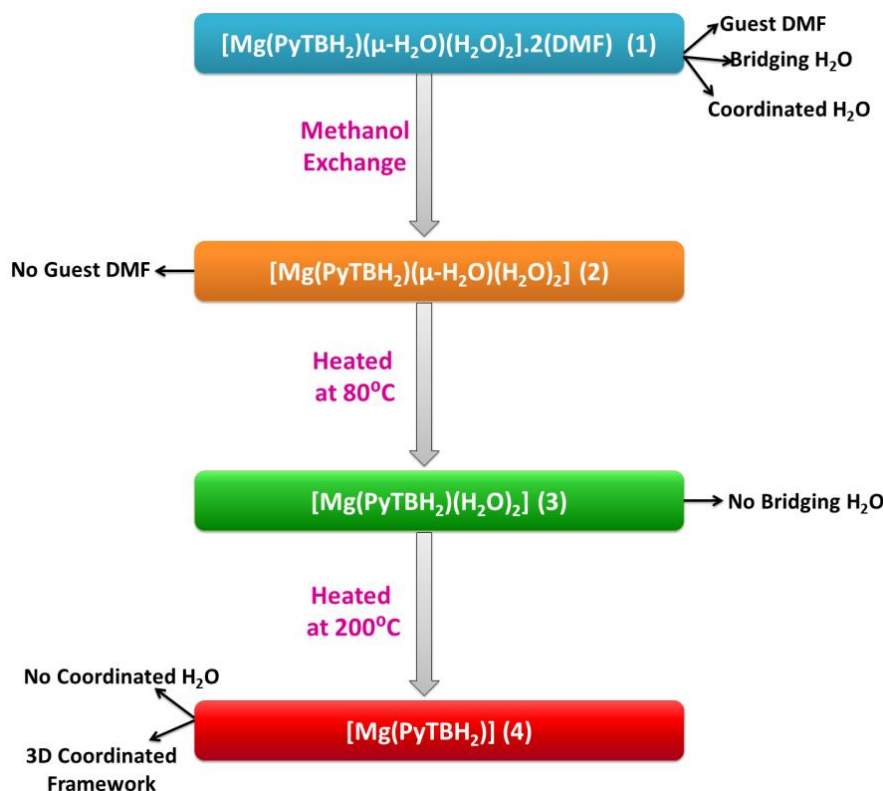
Scheme 1 Schematic representation of the temperature dependant structural changes in **1**.

In order to check the gas adsorption properties, it is essential to desolvate the framework in order to generate empty pore channels by removing the DMF guests. However, as simple as it might appear, H-bonded supramolecular systems often collapse upon being exposed to high temperatures. Hence, we attempted to remove the DMF solvent by exchanging it initially with the low-boiling methanol, and thereafter heating it under vacuum at different temperatures. During MeOH exchange and subsequent vacuum drying and heating, we were able to discern two more crystal structures under different conditions, where changes in the coordination sphere of Mg1 start appearing under varying conditions (**Scheme 1**). Initially, in order to remove the guest DMF molecules, we immersed the crystals of **1** in MeOH for 2 days and then the crystals were dried under high vacuum and single crystal structure determination showed a structure similar to **1** with formula $[Mg(PyTBH_2)(\mu-H_2O)(H_2O)_2]$ (**2**). The atom connectivities in the SBU remain the same as in **1** and the only difference here is the absence of any guest
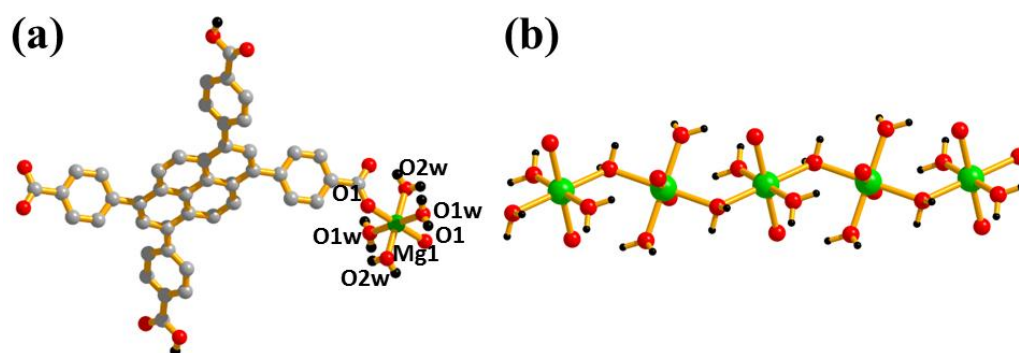
Fig. 4(a) Asymmetric unit of **2**. **(b)** 1D chain in **2**.

molecules in the 1D supramolecular channels. The overall structure is identical to that of **1**, where hexa-coordinated Mg centres (**Fig. 4(a)**) bridged by water molecules form 1D chains (**Fig. 4(b)**) that are connected by the PyTBH$_2$ linker molecule to form 2D networks. The overall 3D supramolecular framework is built by the H-bonding between the 2D networks involving the coordinated water molecules and the free carboxylate terminals. H-bonding parameters have been summarized in **Table 9**.

When **2** is heated at 80°C under high vacuum, we found the single crystals remain intact. The resultant incompletely desolvated compound shows slight changes in cell parameter and has the formula [Mg(PyTBH$_2$)$_2$(H$_2$O)$_2$] (**3**). Single crystal structure determination shows significant change in the binding modes of carboxylate groups in **3**. Here, each Mg^{II} centre is hexa-coordinated to 6 oxygen atoms, where four of the O atoms
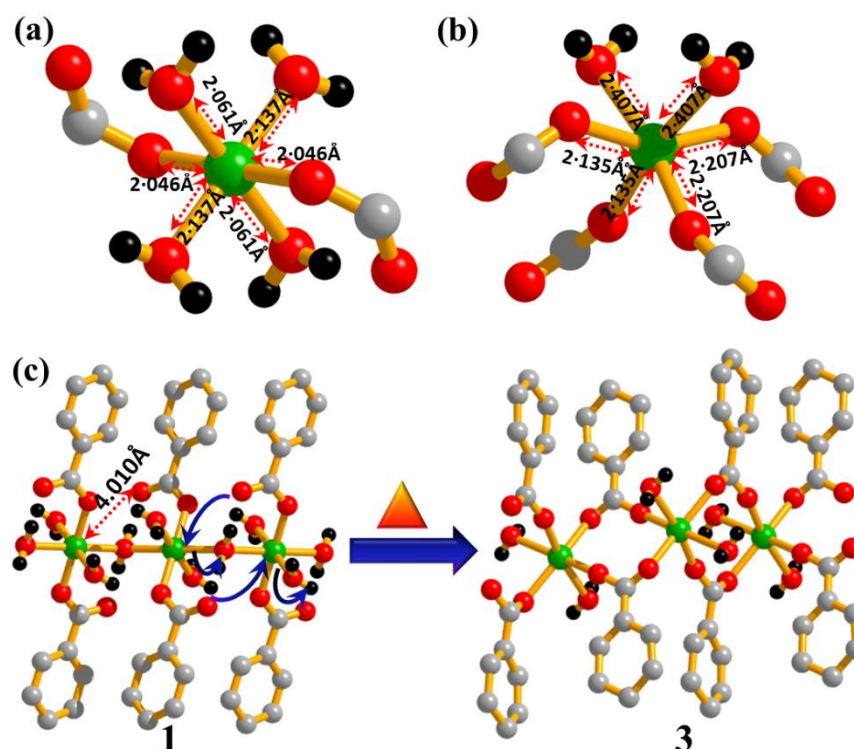
Fig. 5(a) Coordination environment of Mg in **1**. **(b)** Coordination environment of Mg in **2**. **(c)** The probable conversion pathway from **1** to **3**.

are carboxylate oxygen atoms from two $PyTBH_2$ linker molecules whereas the other two are coordinated water molecules (**Fig. 6(a)**). The most remarkable change in this structure is the absence of bridging water molecules and the 1D chain $\{Mg(\mu\text{-}OCO)_2\}_n$ is formed by bridging bidentate binding from two carboxylate groups of the linkers which are monodentate in compound **1** (**Fig. 6(b)**). In **1**, the coordination environment of Mg contains the two bridging water molecules arranged at *trans* positions. Similarly, the two coordinated water molecules and the two carboxylate oxygens are also in *trans* positions among themselves (**Fig. 5(a)**). However, in **3**, we observe that two coordinated water molecules are arranged in a *cis* fashion. Likewise, the two pairs of carboxylate oxygens are *syn* to each other. From here, we can conjecture that the during dehydration, the pendant carboxylate oxygens that are present in close proximity to the Mg centre (4.010 Å) bind the Mg centre to fulfill the octahedral environment. The environment and the spatial orientation of the non-coordinated carboxylate oxygen atoms drive the release of a bridging and a coordinated water molecule (**Fig. 5(c)**). The 2D networks along the *ac* plane are as usual formed by linking the 1D chains with the $PyTBH_2$ along the *a* direction. Like the other structures, here also the 2D sheets stack over one another in an
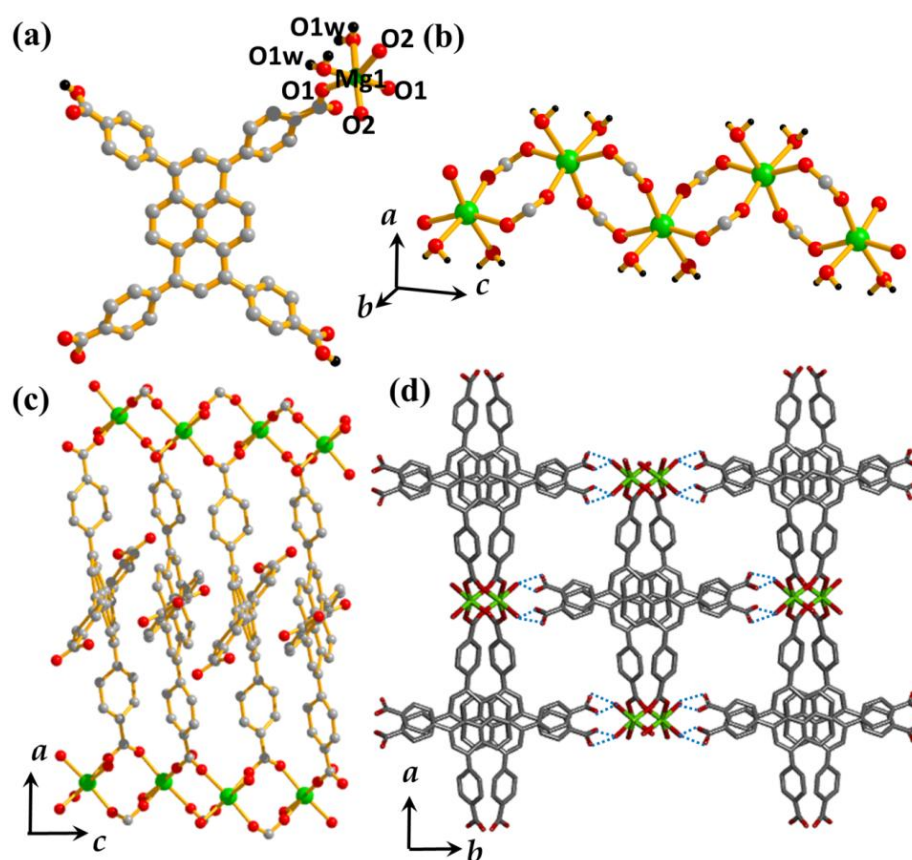
Fig. 6 (a) Assymmetric unit of MOF **4** showing the coordination sphere of Mg1. **(b)** 1D chain in MOF **4**. **(c)** 2D sheet in MOF **4**. **(d)** 3D supramolecular framework formed by H-bonding between the 2D sheets.

ABAB fashion, which then connect by the H- bonding involving the coordinated water molecules (**Fig. 6(d)**). The crystallographic parameters of **2** and **3** have been summarized in **Table 6**.The bond distances, bond angles and hydrogen bonding parameters of **2** and **3** have been summarized in **Table 7-12**.

Table 6 Crystal data and structure refinement for compounds **2** and **3**.

Parameter	2	3
Empirical Formula	$C_{44}H_{31}MgO_{11}$	$C_{44}H_{28}MgO_{10}$
Formula Weight	758.99	740.97
Crystal System	Monoclinic	Monoclinic
Space Group	*C2/c* (No.15)	*C2/c* (No.15)
a, Å	21.6747(19)	21.11(5)
b, Å	27.080(2)	27.08(7)
c, Å	7.6389(6)	8.05(2)
ß, deg	98.816(3)	100.87(7)
V, Å^3	4430.7(6)	4519(19)
Z	4	4
T, K	120	293
μ, mm^{-1}	0.095	0.090
D$_{calcd}$,g/cm^3	1.138	1.089
F (000)	1576	1536
Reflections [*I*>2σ(*I*)]	3806	1382
Unique reflections	4936	4465
Measured reflections	47852	23953
R$_{int}$	0.060	0.671
GOF on *F*^{2}	1.11	1.73
R$_1$[*I*>2σ(*I*)]$^{[a]}$	0.0553	0.3578
R$_w$[I>2σ(I)]$^{[b]}$	0.1798	0.7029

$(R = \sum ||F_o|-|F_c||/\sum |F_o| , R_w = [\sum \{w(F_o^2-F_c^2)^2\}/\sum \{w(F_o^2)^2\}]^{1/2})$

Table 7 Selected bond distances (Å) for **2**.

Mg1-O1	2.0392(16)	Mg1-O2W	2.0568(16)
Mg1-O1W	2.1354(10)	Mg1-O1_c	2.0392(16)
Mg1-O1W_c	2.1354(10)	Mg1-O2W_c	2.0568(16)
O1-C1	1.267(3)	O2-C1	1.261(3)
O3-C20	1.209(3)	O4-C20	1.322(4)

Table 8 Selected bond angles (°) for **2**.

O1-Mg1-O1W	89.08(5)	O1W-Mg1-O2W	88.31(6)
O1-Mg1-O2W	88.59(6)	O1_c-Mg1-O1W	90.92(5)
O1-Mg1-O1_c	180.00	O1W-Mg1-O1W_c	180.00
O1-Mg1-O1W_c	90.92(5)	O1W-Mg1-O2W_c	91.69(6)
O1-Mg1-O2W_c	91.41(6)	O1_c-Mg1-O2W	91.41(6)

Table 9 Hydrogen bond parameters for **2**.

D–H···A	D–H (Å)	H···A (Å)	D···A (Å)	∠D–H···A (°)
O1W–H1O1···O2W	0.8900	2.4700	2.9209(16)	112.00
O1W–H1O1···O2	0.8900	1.9100	2.6320(18)	136.00
O2W–H1O2···O1	0.9000	1.9400	2.786(2)	156.00
O2W–H2O2···O3	0.8400	1.9300	2.769(3)	175.00
O4–H1O4···O2	0.9100	1.7600	2.651(3)	167.00

Table 10 Selected bond distances (Å) for **3**.

Mg1-O1	2.21(2)	Mg1-O2_d	2.14(2)
Mg1-O1W	2.41(3)	O1 -C1	1.16(3)
Mg1-O1_a	2.21(2)	O2 -C1	1.25(3)
Mg1-O1W_a	2.41(3)	O3-C22	1.27(3)
Mg1-O2_b	2.14(2)	O4-C22	1.29(3)

Table 11 Selected bond angles (°) for **3**.

O1-Mg1-O1W	82.8(11)	O1-Mg1-O1_a	156.3(9)
O1-Mg1-O1W_a	82.4(10)	O1-Mg1-O2_b	103.1(7)
O1-Mg1-O2_d	94.2(7)	O1_a-Mg1-O1W	82.4(10)
O1W-Mg1-O1W_a	102.4(9)	O1W-Mg1-O2_d	85.7(7)
O1W-Mg1-O2_b	170.7(9)	O1_a-Mg1-O1W_a	82.8(10)

Table 12 Hydrogen bond parameters (Å) for **3**.

D–H···A	D–H (Å)	H···A (Å)	D···A (Å)	∠D–H···A (°)
O1W–H1O1···O4	0.8000	2.2000	2.98(4)	165.00
O1W–H1O2···O3	0.7600	2.2300	2.99(3)	176.00
O3–H3A···O1	0.8200	2.1300	2.93(3)	166.00

It is expected that at high temperatures around 200°C, as suggested by the TGA profile, the coordinated water molecules will be released to obtain a completely dehydrated form [Mg(PyTB)$_2$] (**4**). Interestingly, we observed a significant change in the PXRD pattern of **4** as compared to **2** and **3**, suggesting structural reorganization. After removal of the two coordinated water molecules, the 4-coordinated Mg^{II} centre will be stabilized by the coordination of oxygen atoms from the uncoordinated carboxylate groups which were involved in H-bonding with the coordinated water molecules. These uncoordinated carboxylate groups are in close proximity to the Mg^{II} centres (4-5Å) and
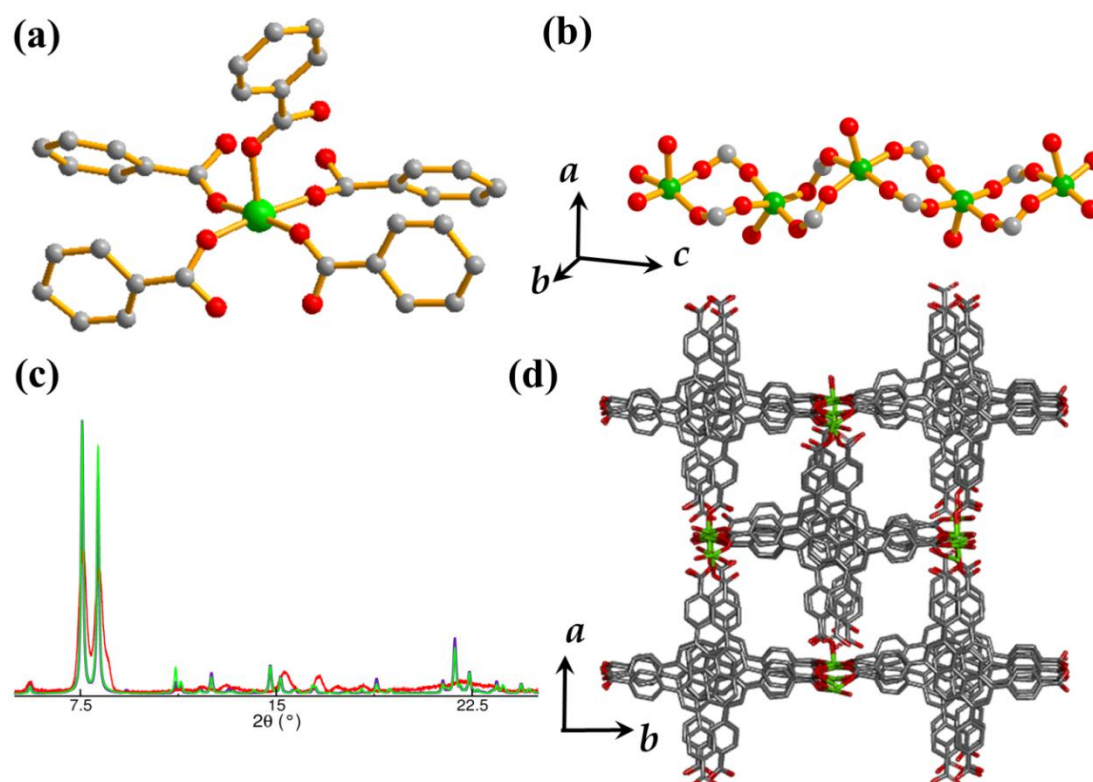
Fig. 7 (a) Assymmetric unit of MOF **4** showing the coordination sphere of Mg1. **(b)** 1D chain formed by the bridging of Mg-O clusters by carboxylate groups in the *c* direction in **4**. **(c)** Experimental and simulated PXRD patterns of **4**. **(d)** 3D coordination polymer **4**.

thus are easily accessible. However, we were not able to isolate the single crystal of **4** and hence, a completely desolvated structure has also been theoretically simulated using the PXRD pattern of **4**. In this case, the framework no longer remains a supramolecular framework based on H-bonding, but instead is transformed to a 3D porous coordination polymer, with rigid structures. Here, each Mg^{II} centre is penta-coordinated and connected to 5 different carboxylate oxygen atoms (**Fig. 7(a)**). Here, 1D chains of $\{Mg(\mu\text{-}OCO)_2\}_n$ are linked by the oxygen atom from the free –COOH groups
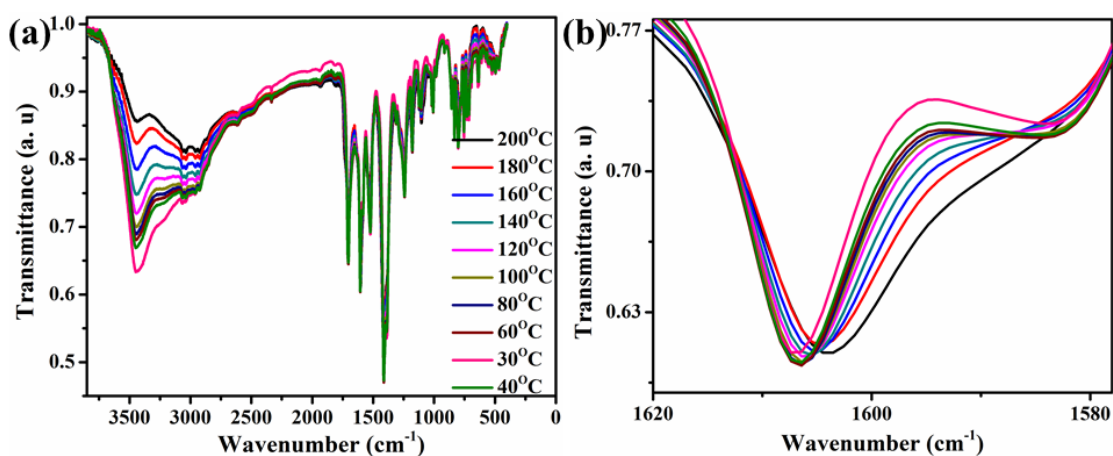
Fig. 8 (a) Temperature dependent IR spectroscopy of **1**. **(b)** Magnified image of shift in band corresponding to C=O stretching with increasing temperature.

81

from 2D networks that were stacked in ABAB fashion, resulting in a 3D framework (**Fig. 7(b, d)**). The proof of this carboxylate bridging in **4** is also evident from the temperature dependant IR spectroscopy of **1**, where the wide peak centred around 3300 cm^{-1} corresponding to the water present in the framework diminishes as the temperature is raised, indicating towards the removal of the bridging and coordinating water molecules (**Fig. 8(a)**). Moreover, the peak at 1601 cm^{-1} corresponding to carboxylate C=O stretching gradually shifts to lower frequencies when the temperature is increased. This hints towards the lowering of C=O bond strength, which may be caused by the attachment of the free carboxylate (COOH) terminals to the Mg^{II} centre after the removal of the bridging and coordinated water molecules (**Fig. 8(b)**). We attempted to discern intermediate structures through SCXRD for the in depth understanding of structural dynamism in **1**.

2B.3.4 Adsorption and Gas Separation in 3 and 4

The large nanochannels, sufficient void space and structural dynamicity in **1** prompted us to check the inherent porosity and surface area of the compound. We also checked the porosity in different stages of dehydration. In order to understand the variation in porosity as a function of the structural dynamicity, we degassed **2** at 80°C to
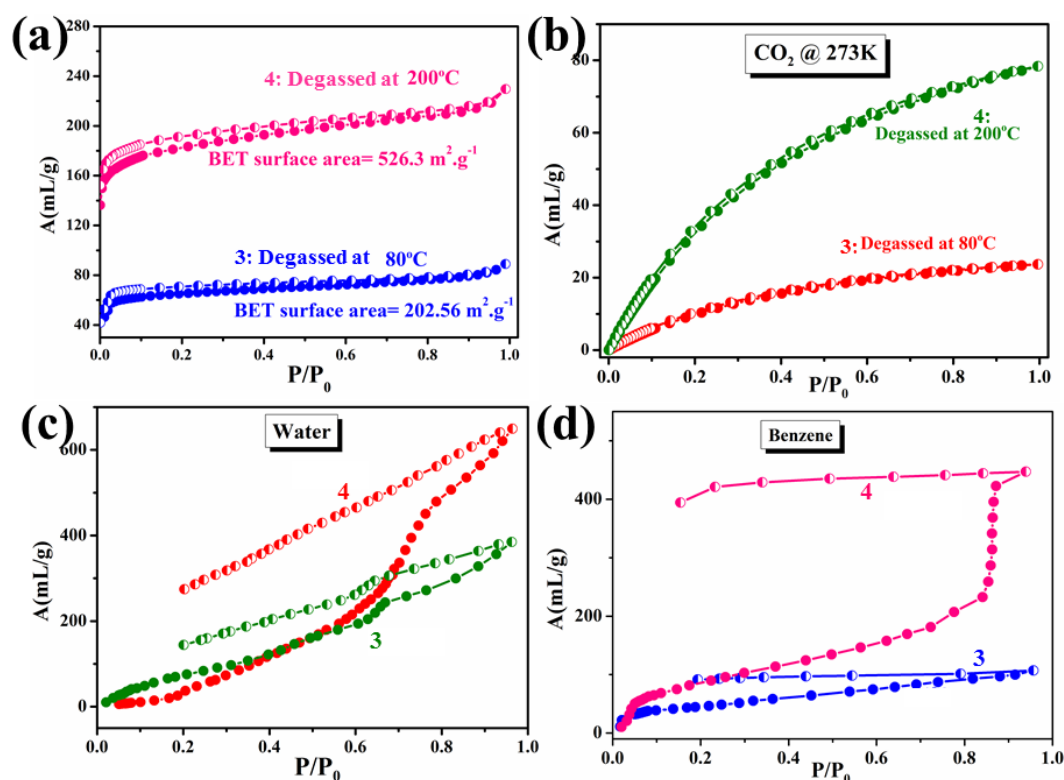
Fig. 9 (a) N_2 adsorption isotherm at 77 K for **3** and **4**. **(b)** CO_2 adsorption isotherm at 273 K for **3** and **4**. **(c)** H_2O adsorption isotherm for **3** and **4**. **(d)** C_6H_6 adsorption isotherm for **3** and **4**.

get **3** and also degassed **2** at 200°C to get **4**. Adsorption was carried out with **3** and **4** to observe the change in porosity and surface area with partial and total removal of the water molecules. The N_2 adsorption at 77 K shows a typical Type-I curve both in case of **3** and **4**, indicating towards a microporous nature, however the uptake amount is 240 ml.g^{-1} in case of **4**, but is merely 85 ml.g^{-1} for **3** (**Fig. 9(a)**). Consequently, the BET surface area of **4** is 526.3 m^2.g^{-1} whereas that for **3** is 202.56 m^2.g^{-1}. This clearly elucidates that upon heating at 80°C, the MOF is not properly desolvated and the presence of bridging water molecules reduce the overall porosity and surface area of the sample. In order to establish the same, CO_2 adsorption at 273 K were carried out for compounds **3** and **4**. In both cases a type I curve is observed, with steep uptake at low pressure ranges, however the total uptake amount is 80 ml.g^{-1} for **4**, but it is merely 28 ml.g^{-1} for **3** (**Fig. 9(b)**). Although **4** shows a total uptake of 650 ml.g^{-1} of water in contrast to 390 ml.g^{-1} for **3**, at the low pressure region, the uptake by **4** is much lesser than that in **3** (**Fig. 9(c)**). At P/P$_0$=0.18, the water uptake for **3** is 71 ml.g^{-1}, but it is only 20 ml.g^{-1} for **4**. This is a clear indication that upon degassing at higher temperature, when **1** forms **4** by the loss of the bridging water molecules, it becomes increasingly hydrophobic. This can be attributed to the pores
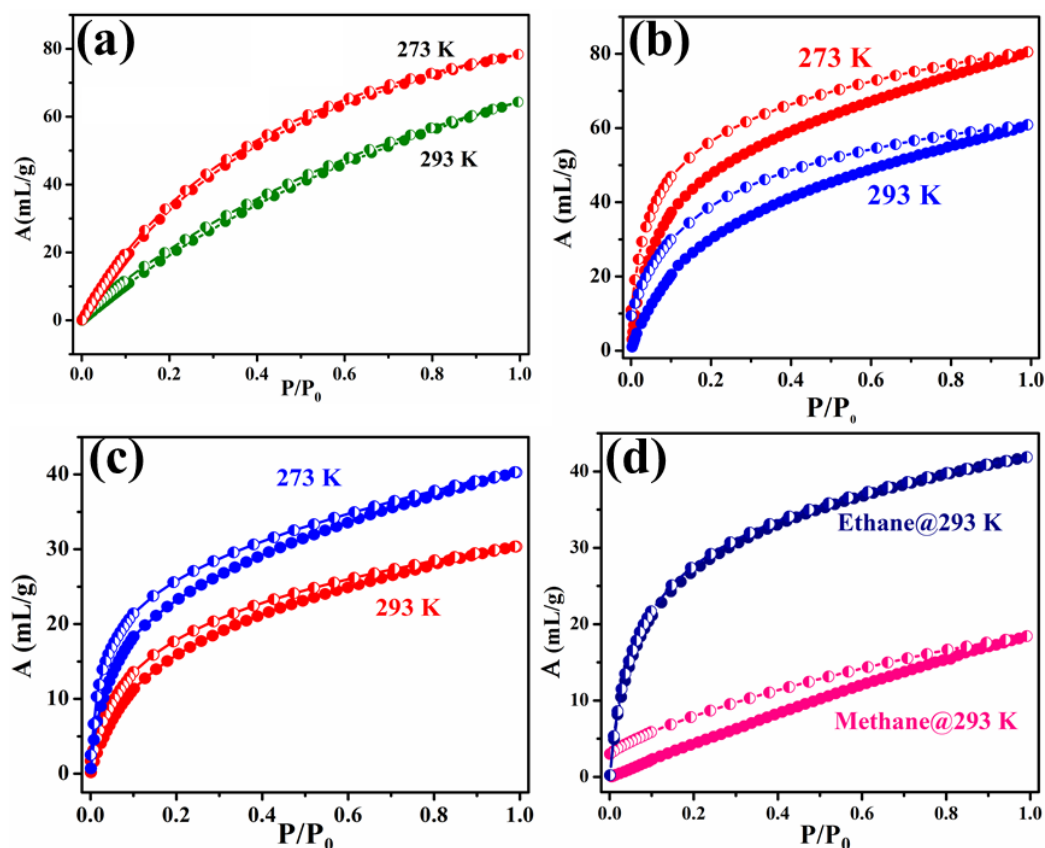
Fig. 10 (a) CO_2 adsorption isotherm at 273 K and 293 K for **4**. **(b)** C_2H_2 adsorption isotherm at 273 K and 293 K for **4**. **(c)** C_2H_4 adsorption isotherm at 273 K and 293 K for **4**. **(d)** CH_4 and C_2H_6 adsorption isotherm at 293 K for **4**.

of the framework lined by the aromatic pyrene cores and because of the removal of the framework water molecules, there is no scope for H-bonding with the adsorbate water molecules. This is further reiterated by the benzene adsorption isotherm, where we observe that **4** shows a higher overall uptake of 430 ml.g^{-1} with a higher uptake at lower pressure regions as well than in **3**, which establishes the non-polar nature of its pore channels (**Fig. 9(d)**). Since **4** shows an overall higher uptake of gases than **3** in all cases,
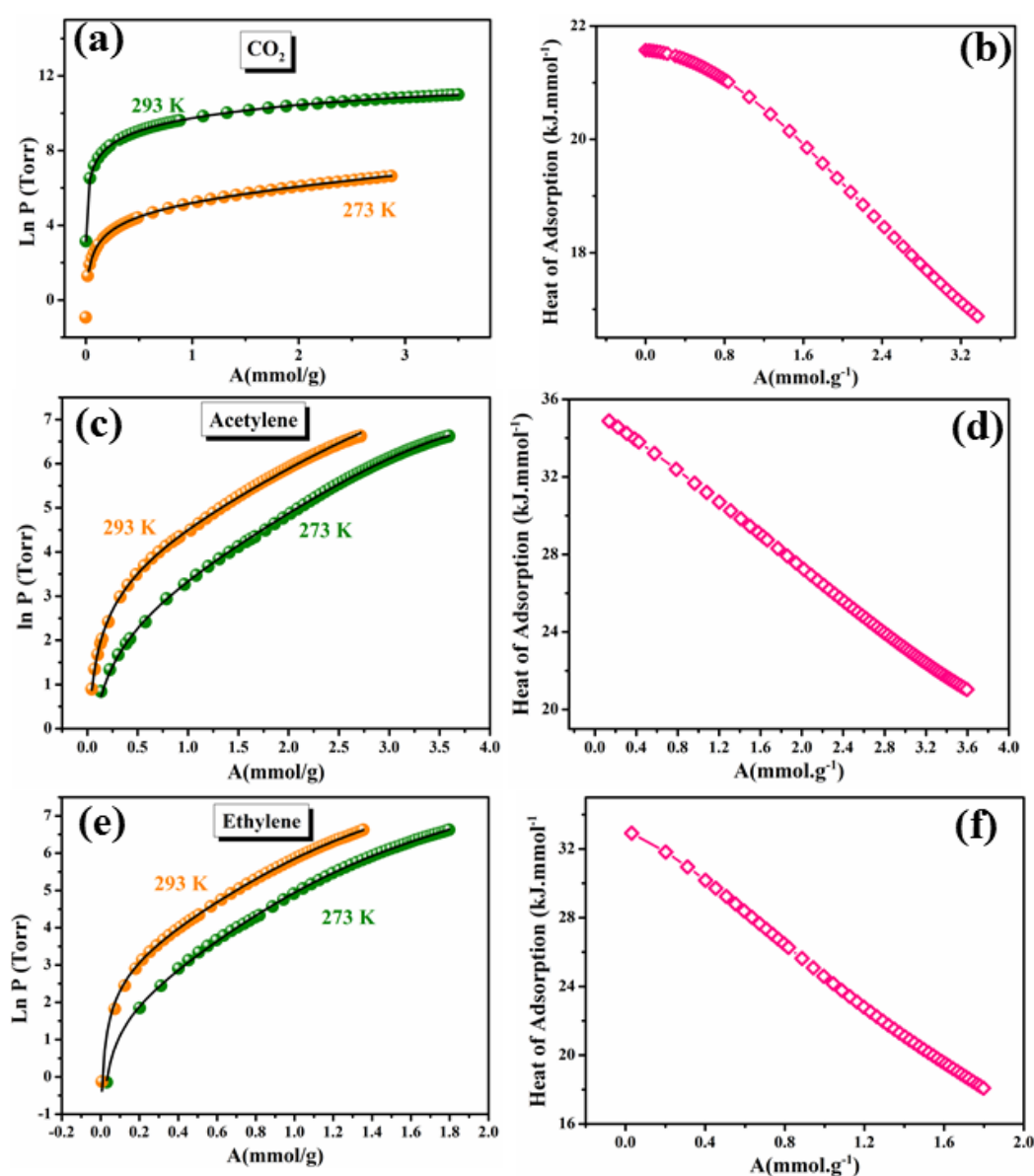
Fig. 11 (a) Adsorption isotherms for CO_2 at 273 and 293 K fitted in the Virial Equation for **4**. **(b)** Change in the heat of enthalpy with loading of CO_2 in **4** calculated from the Virial fitting of the adsorption isotherms at 273 and 293 K. **(c)** Adsorption isotherms for C_2H_2 at 273 and 293 K fitted in the Virial Equation for **4**. **(d)** Change in the heat of enthalpy with loading of C_2H_2 in **4** calculated from the Virial fitting of the adsorption isotherms at 273 and 293 K. **(e)** Adsorption isotherms for C_2H_2 at 273 and 293 K fitted in the Virial Equation for **4**. **(f)** Change in the heat of enthalpy with loading of C_2H_2 in **4** calculated from the Virial fitting of the adsorption isotherms at 273 and 293 K.

further adsorption and separation experiments were all carried out with **4**. For practical applications, CO_2 adsorption is carried out at 293 K, which shows a Type I curve with a total uptake of 60 ml.g^{-1} (**Fig. 10(a)**). The low kinetic diameter of CO_2 (3.3 Å) and its high quadruple moment that interacts with the π-cloud from the pyrene cores contribute towards the high CO_2 uptake of **4**. The adsorption isotherms of CO_2 at 273 K and 293 K were fitted in the virial equation, from which the isosteric heat of adsorption ($Q_{st,f}$) for **4** was calculated to be ~22 kJ.mol^{-1} at zero coverage (**Fig. 11(a, b)**).

The pore channels in **4** are lined by the pyrene cores from the PyTB linker and hence we conjectured that **4** should show a good uptake of small hydrocarbons like methane, ethane, acetylene etc. because of their interaction with the π-cloud of the framework. With this consideration in mind we proceeded to check the hydrocarbon adsorption of **4** both at 293 K as well as 273 K. **4** adsorbs 60 ml.g^{-1} C_2H_2 at 273 K and 80 ml.g^{-1} at 293 K, while for C_2H_4 the adsorption amounts are 40 ml.g^{-1} at 273 K and 30 ml.g^{-1} at 293 K (**Fig. 10(b,c)**). In order to understand the difference in the uptake amounts of C_2H_2 and C_2H_4, we calculated the $Q_{st,f}$ for both after fitting their adsorption isotherms in the virial equation (**Fig. 11(c,d)**). While the $Q_{st,f}$ for C_2H_2 is 35 kJ.mmol^{-1}, that for C_2H_4 is 32 kJ.mmol^{-1}, which explains the lower uptake of ethylene (**Fig. 11(e,f)**). At room temperature, At 293 K, **5** also shows an uptake of 31 ml.g^{-1} of ethane and 18
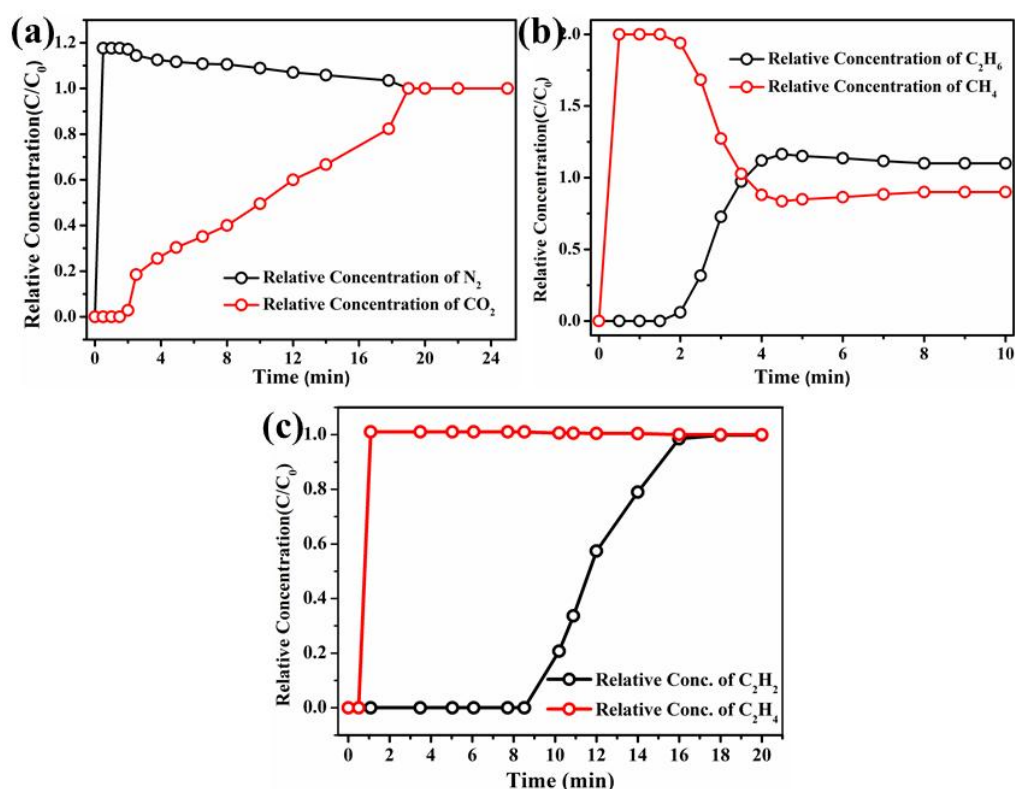
Fig. 12 Breakthrough curves for binary mixture of **(a)** N_2/ CO_2 (0.85:0.15), **(b)** CH_4/C_2H_6 (0.50:0.50) and **(c)** C_2H_2/C_2H_4 (0.1:0.99) for **4**.

ml.g^{-1} of methane (**Fig. 10(d)**).

The difference in the adsorption amounts prompted us to check the potential of **4** for practical applications in gas separation using a breakthrough setup. For this purpose, tightly packed column of **4** (180 mg, column length 1.5 cm) were prepared with a gas flow rate of 1 mL/min (carrier He gas). Through this column, the following binary gas mixtures were purged: CO_2/N_2 (85:15); C_2H_2:C_2H_4 (1:99) and CH_4:C_2H_6 (50:50). The CO_2 retention time by the column was 2 mins, while that for C_2H_6 was also 2mins (**Fig. 12(a,b)**). For C_2H_2, the breakthrough time was rather high and found to be 8 mins, as can be seen in the breakthrough curve (**Fig. 12(c)**). Hence, **4** shows immense potential as a practical separator for C_2H_2 and C_2H_4, which is essential in the polymer industry for purification of ethylene.

2B.4 Conclusions

1 is an interesting supramolecular framework formed by the H-bonding between the coordinated water molecules and uncoordinated carboxylate terminals. The removal and replacement of the coordinated water molecules can give rise to different structures which have been determined. When heated at high temperature, the bridging water molecules are removed. Instead the uncoordinated carboxylate terminals in close proximity to the Mg centres directly chelate with it, giving rise to a 3D coordination polymer **4**. **4** shows high surface area and excellent room temperature adsorption capacity for CO_2, as well as small hydrocarbons like CH_4, C_2H_6, C_2H_2 and C_2H_4. **4** also shows a good adsorptive separation of CO_2/N_2, CH_4/C_2H_6 and C_2H_2/C_2H_4 in a breakthrough measurement. Overall **1** is an extremely intriguing supramolecular framework which shows structural dynamism and one of its derivatives also show great potential in the adsorption and separation of gases.

2B.5 References

1. J.-R. Li, R. J. Kuppler and H.-C. Zhou, *Chem. Soc. Rev.*, 2009, **38**, 1477.

2. B. Van de Voorde, B. Bueken, J. Denayer and D. De Vos, *Chem. Soc. Rev.*, 2014, **43**, 5766.

3. J.-R. Li, J. Sculley and H.-C. Zhou, *Chem. Rev.*, 2012, **112**, 869.

4. H. Yin, J. Wang, Z. Xie, J. Yang, J. Bai, J. Lu, Y. Zhang, D. Yin and J. Y. S. Lin, *Chem. Commun.*, 2014, **50**, 3699-3701.

5. S. C. King, R.-B. Lin, H. Wang, H. D. Arman and B. Chen, *Mater. Chem. Front.*, 2017, **1**, 1514.

6. B. Monteiro, A. R. Nabais, F. A. Almeida Paz, L. Cabrita, L. C. Branco, I. M. Marrucho, L. A. Neves and C. C. L. Pereira, *Energy Technol.*, 2017, **5**, 2158.

7. R. Zhong, Z. Xu, W. Bi, S. Han, X. Yu and R. Zou, *Inorg. Chim. Acta*, 2016, **443**, 299.

8. A. Hazra, S. Jana, S. Bonakala, S. Balasubramanian and T. K. Maji, *Chem. Commun.*, 2017, **53**, 4907.

9. L. Li, R.-B. Lin, R. Krishna, X. Wang, B. Li, H. Wu, J. Li, W. Zhou and B. Chen, *J. Mater. Chem. A*, 2017, **5**, 18984.

10. J. Lee, C. Y. Chuah, J. Kim, Y. Kim, N. Ko, Y. Seo, K. Kim, T. H. Bae and E. Lee, *Angew. Chem. Int. Ed.*, 2018, **57**, 7869.

11. Y. Zhao, J. Wang, Z. Bao, H. Xing, Z. Zhang, B. Su, Q. Yang, Y. Yang and Q. Ren, *Sep. Purif. Technol.*, 2018, **195**, 238.

12. S.-C. Xiang, Z. Zhang, C.-G. Zhao, K. Hong, X. Zhao, D.-R. Ding, M.-H. Xie, C.-D. Wu, M. C. Das, R. Gill, K. M. Thomas and B. Chen, *Nat. Commun.*, 2011, **2**, 204.

13. R.-B. Lin, L. Li, H. Wu, H. Arman, B. Li, R.-G. Lin, W. Zhou and B. Chen, *J. Am. Chem. Soc.*, 2017, **139**, 8022.

14. S. Bhattacharyya, A. Chakraborty, A. Hazra and T. K. Maji, *ACS Omega*, 2018, **3**, 2018.

15. S. Kitagawa, R. Kitaura and S.-i. Noro, *Angew. Chem. Int. Ed.*, 2004, **43**, 2334.

16. M. L. Foo, R. Matsuda and S. Kitagawa, *Chem.Mater.*, 2014, **26**, 310.

17. H.-C. Zhou, J. R. Long and O. M. Yaghi, *Chem. Rev.*, 2012, **112**, 673.

18. R. Haldar and T. K. Maji, *CrystEngComm*, 2013, **15**, 9276.

19. Z. Sumer and S. Keskin, *Ind. Eng. Chem. Res.*, 2016, **55**, 10404.

20. N. Sikdar, S. Bonakala, R. Haldar, S. Balasubramanian and T. K. Maji, *Chem. Euro. J.*, 2016, **22**, 6059.

21. Z. Kang, L. Fan and D. Sun, *J. Mater. Chem. A*, 2017, **5**, 10073-10091.

22. H. Li, K. Wang, Y. Sun, C. T. Lollar, J. Li and H.-C. Zhou, *Mater. Today*, 2018, **21**, 108.

23. Z. Zhao, X. Ma, A. Kasik, Z. Li and Y. S. Lin, *Ind. Eng. Chem. Res.*, 2013, **52**, 1102.

24. K. Tan, S. Zuluaga, E. Fuentes, E. C. Mattson, J.-F. Veyan, H. Wang, J. Li, T. Thonhauser and Y. J. Chabal, *Nat. Commun.*, 2016, **7**, 13871.

25. J. Peng, H. Wang, D. H. Olson, Z. Li and J. Li, *Chem. Commun.*, 2017, **53**, 9332.

26. Y. Wang and D. Zhao, *Crys. Growth Des.*, 2017, **17**, 2291.

27. R. Zacharia, L. F. Gomez, R. Chahine, D. Cossement and P. Benard, *Micropor. Mesopor. Mater.*, 2018, **263**, 165.

28. K. Adil, Y. Belmabkhout, R. S. Pillai, A. Cadiau, P. M. Bhatt, A. H. Assen, G. Maurin and M. Eddaoudi, *Chem. Soc. Rev.*, 2017, **46**, 3402.

29. M. I. H. Mohideen, R. S. Pillai, K. Adil, P. M. Bhatt, Y. Belmabkhout, A. Shkurenko, G. Maurin and M. Eddaoudi, *Chem*, 2017, **3**, 822.

30. M. K. Rana, H. S. Koh, H. Zuberi and D. J. Siegel, *J. Phys. Chem. C*, 2014, **118**, 2929.

31. F. A. Almeida Paz, J. Klinowski, S. M. F. Vilela, J. P. C. Tomé, J. A. S. Cavaleiro and J. Rocha, *Chem. Soc. Rev.*, 2012, **41**, 1088.

32. T. Islamoglu, S. Goswami, Z. Li, A. J. Howarth, O. K. Farha and J. T. Hupp, *Acc. Chem. Res.*, 2017, **50**, 805.

33. Z.-H. Xuan, D.-S. Zhang, Z. Chang, T.-L. Hu and X.-H. Bu, *Inorg. Chem.*, 2014, **53**, 8985.

34. M. Zhang, M. Bosch, T. Gentle Iii and H.-C. Zhou, *CrystEngComm*, 2014, **16**, 4069.

35. D. Zhao, D. J. Timmons, D. Yuan and H.-C. Zhou, *Acc. Chem. Res.*, 2011, **44**, 123.

36. Z. Lu, H. Xing, R. Sun, J. Bai, B. Zheng and Y. Li, *Cryst.Growth Des.*, 2012, **12**, 1081.

37. J. Pang, S. Yuan, J. Qin, C. Liu, C. Lollar, M. Wu, D. Yuan, H.-C. Zhou and M. Hong, *J. Am. Chem. Soc.*, 2017, **139**, 16939.

38. R.-J. Li, M. Li, X.-P. Zhou, D. Li and M. O'Keeffe, *Chem.Commun.*, 2014, **50**, 4047.

39. C. V. McGuire and R. S. Forgan, *Chem. Commun.*, 2015, **51**, 5199.

40. J. M. Seco, E. San Sebastián, J. Cepeda, B. Biel, A. Salinas-Castillo, B. Fernández, D. P. Morales, M. Bobinger, S. Gómez-Ruiz, F. C. Loghin, A. Rivadeneyra and A. Rodríguez-Diéguez, *Sci. Rep.*, 2018, **8**, 14414.

41. B. Li, H. Wang and B. Chen, *Chem. Asian J.*, 2014, **9**, 1474.

42. H. Alawisi, B. Li, Y. He, H. D. Arman, A. M. Asiri, H. Wang and B. Chen, *Cryst. Growth Des.*, 2014, **14**, 2522.

43. N. Zhao, F. Sun, N. Zhang and G. Zhu, *Cryst. Growth Des.*, 2017, **17**, 2453.

44. A. Schneemann, V. Bon, I. Schwedler, I. Senkovska, S. Kaskel and R. A. Fischer, *Chem. Soc. Rev.*, 2014, **43**, 6062.

45. S. Horike, S. Shimomura and S. Kitagawa, *Nat. Chem.*, 2009, **1**, 695.

46. K. Prasad, R. Haldar and T. K. Maji, *RSC Adv.*, 2015, **5**, 74986-74993.

47. Z.-B. Han, Z.-Z. Xiao, M. Hao, D.-Q. Yuan, L. Liu, N. Wei, H.-M. Yao and M. Zhou, *Cryst. Growth Des.*, 2015, **15**, 531.

Chapter 3A

A Bimodal Anionic MOF: Turn-off Sensing for Cu^{II} and Specific Sensitization of Eu^{III}
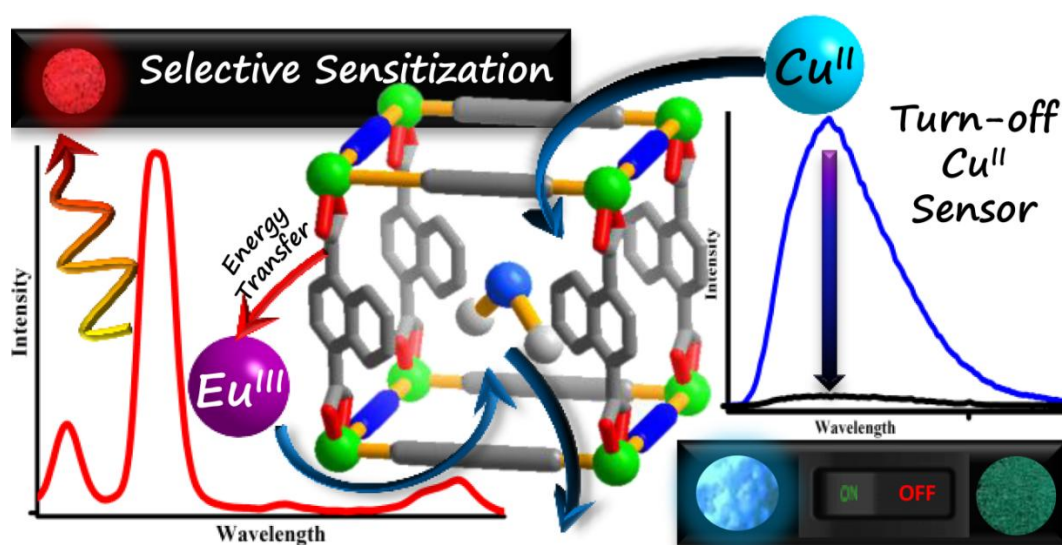
Abstract

This chapter describes the synthesis of a novel porous anionic metal-organic framework (AMOF) $\{[Mg_3(ndc)_{2.5}(HCO_2)_2(H_2O)][NH_2Me_2] \cdot 2H_2O \cdot DMF\}$(**1**) and its metal ion sequestration and sensing properties. In this AMOF, the stoichiometric ratio is such that the framework itself is anionic, however the overall charge neutrality of the framework is maintained by exchangeable dimethyl amine (DMA) cations residing in the 1D channels. These DMA cations can undergo facile exchange with other exogenous cationic species in order to suit specific applications. When **1** is made to undergo cation exchange with Cu^{II}, the characteristic blue emission of **1** is quenched in the Cu^{II} exchanged compound (**Cu^{II}@1'**). Moreover, the colour of **1** changes from white to bright green in **Cu^{II}@1'**. Hence **1** can provide a fast fluorescence read-out for sensing Cu^{II}. Also, the framework is capable of encapsulating several lanthanide cations, e.g., Eu^{III}, Tb^{III}, Sm^{III} and Dy^{III}. However, it can selectively sensitize Eu^{III} resulting in a bright red luminescent framework. Through cation exchange, **1** manifests bimodal functionality, being a turn-off sensor of Cu^{II} on one hand, and a selective sensitizer of Eu^{III} emitting intense pure red emission on the other.

3A.1 Introduction

Zeolites, the much studied microporous aluminosilicates, are established ion exchangers owing to the presence of extra framework cations.[1-2] However, zeolites do not allow the functionalization of pore surfaces and thus selective sequestration and read-out signalling of a specific metal cation is not possible. This drawback has been overcome in metal-organic frameworks (MOFs), which are tunable porous materials with modifiable pore surfaces and functionalities.[3-4] The efficiency of MOFs in gas storage and separation,[5] catalysis, drug delivery and optoelectronic devices are well documented.[4] However, unlike zeolites, ion exchange is infrequent in MOFs,[6] which are generally neutral in nature. Applying proper synthetic strategies, it is possible to get anionic MOFs (AMOFs),[7-13] where the cationic guest molecules can undergo facile exchange with other exogenous cationic species. Such post-synthetically modified AMOFs have already shown potential in second harmonic generation,[7,9] drug delivery,[10] tunable adsorption,[13] and catalysis.[8,11] However the chemical affinity of the coordination spaces determines the selective capture of a specific metal ion, therefore proper functionalization of pore surface is crucial.[14] Furthermore flexible cation exchangeable nano-spaces constructed from chromophoric linkers would provide a fast fluorescence read-out of the recognition process through change in emission intensity for a particular metal ion leading to sensory MOFs. Hence, it should have correct pore window dimensions and proper stabilization environment, preferably the presence of Lewis basic sites for better interaction with the specific metal cation. Selective uptake of Cu^{II} ion by such AMOFs would be particularly interesting as this strategy would ensue a novel route for Cu^{II} sensing,[15] which is of paramount importance for biological applications. The study of prognosis of copper imbalance related diseases, e.g., Menkes, Wilson and Alzheimer's diseases, prion disorders, and amyotrophic lateral sclerosis demand effective sensing and removal of copper[16] in biological systems. Also, by exploiting the cation exchange in AMOFs, new luminescent materials can be designed by inclusion of lanthanide (Ln) ions. The role of the AMOF as a light harvesting antenna for sensitizing Ln^{III} cations to furnish novel Ln-doped luminescent materials and new Ln sensors has been studied previously.[17-18] However, selective Eu^{III} sensitization by an AMOF is very unusual and finds its application in low-energy driven pure red emitters in optoelectronic devices and also for biological labelling.[19]

This chapter describes the synthesis and structural characterization of a 3D
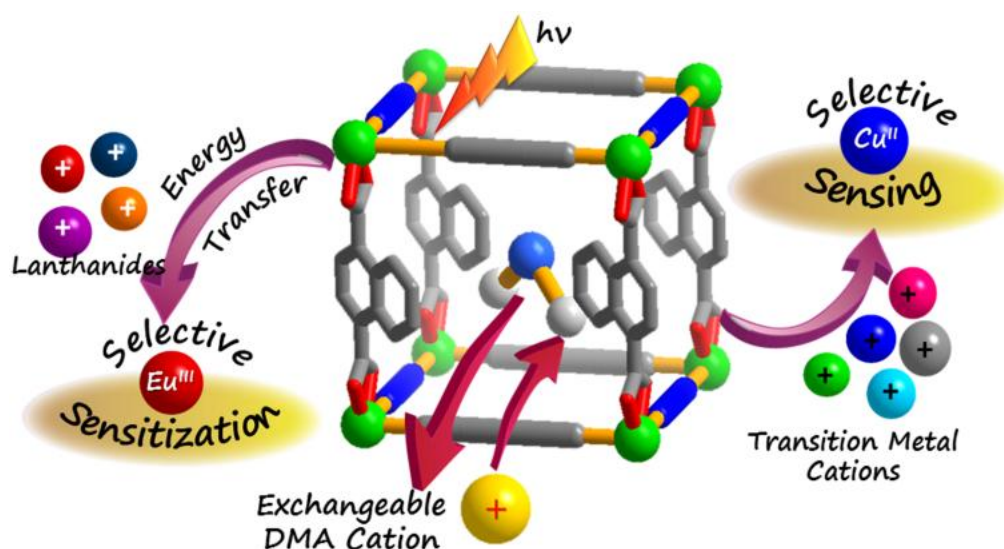
Scheme 1: Schematic representation of the bimodal functionalities in **1** through cation exchange.

anionic MOF, {[Mg$_3$(ndc)$_{2.5}$(HCO$_2$)$_2$(H$_2$O)][NH$_2$Me$_2$]·2H$_2$O·DMF} (**1**) [ndc: 1,4-naphthalenedicarboxylate] and its metal ion sequestration and sensing properties. The framework contains 1D channels occupied by the cationic guest **NH$_2$Me$_2$$^+$** [dimethyl ammonium (**DMA**)] which can be selectively replaced by Cu^{II} ions among other transition metal cations. Moreover the framework can encapsulate several lanthanide metal ions but selectively sensitize Eu^{III} resulting in a bright red luminescent framework (**Scheme 1**). Such bimodal functionalities of specific sensing[20-21] and removal of a transition metal (Cu^{II}) and selective sensitization of a lanthanide metal (Eu^{III}) based on luminescence quenching and enhancing respectively using a single framework system is really unique.

3A.2 Experimental Section

3A.2.1 Materials

All the reagents and solvent were used as obtained from commercial supplies without any further purification. 1,4-Naphthalene dicarboxylic acid(ndc) and the metal salts used were procured from Alfa Aesar and Aldrich Chemical Co. Ltd. respectively.

3A.2.2 Synthesis of [Mg$_3$(ndc)$_{2.5}$(HCO$_2$)$_2$(H$_2$O)(NH$_2$Me$_2$)]·2H$_2$O·DMF (1)

Mg(NO$_3$)$_2$·6H$_2$O(1mmol, 256mg) and 1,4-ndc(1 mmol, 216 mg) were mixed well in 20 mL DMF. Then a few drops of water were added and the mixture was sonicated for

10 mins. The resulting mixture was transferred into a Teflon sealed autoclave and the system was kept at 120 ºC for two days. On cooling colourless single crystals of **1** were obtained. Yield: 76% relative to Mg^{II}. Anal. Calculated for $C_{37}H_{37}Mg_3O_{18}N_2$: H: 4.28 C: 51.04 N: 3.22% Found: H: 4.12 C: 51.63 N: 3.27%

3A.2.3 Preparation of $M^{II}@1'$ and $Ln^{III}@1'$

For preparing the different metal ion exchanged compounds, **1** is activated at 110 °C under high vacuum overnight before immersing it in the respective metal ion solutions. 50 mg of activated **1**(**1'**) is immersed in 30 mL 0.01 (M) M^{II} (where M is any transition metal) solutions in ethanol for 7 days and the solution is changed daily within these 7 days. For Stern-Volmer plots, **1'** is dipped in standard solutions for 7 days as mentioned in the main text. Then it is washed repeatedly with ethanol. For **$Ln^{III}@1'$**, 0.01 (M) solutions of nitrates of Eu^{III}, Dy^{III}, Tb^{III} and Sm^{III} are used in the same way.

3A.2.4 Physical Measurements

The elemental analysis was carried out using a Thermo Fischer Flash 2000 Elemental Analyzer. Thermogravimetric analysis (TGA) was carried out (Mettler Toledo) in nitrogen atmosphere (flow rate = 50 mL min^{-1}) in the temperature range 30 – 550 °C (heating rate = 3°C min^{-1}). Powder XRD pattern was recorded by using Cu-Kα radiation (Bruker D8 Discover; 40 kV, 30 MA). Electronic absorption spectra were recorded on a Perkin Elmer Lambda 750 UV-VIS-NIR Spectrometer and emission spectra were recorded on Perkin Elmer Ls 55 Luminescence Spectrometer. Solid state UV spectrum was recorded in reflectance mode. IR spectra of the compounds were recorded on a Bruker IFS 66v/S spectrophotometer using the KBr pellets in the region 4000−400 cm^{-1}. Inductively Coupled Plasma-Optical Emission Spectroscopy (ICP-OES) measurements were recorded on Perkin Elmer Optima 7000dv ICP-OES.

3A.2.5 Crystallography

A suitable single crystal of compound **1** was mounted on a thin glass fibre with commercially available super glue. X-ray single crystal structural data were collected on a Bruker Smart-CCD diffractometer equipped with a normal focus, 2.4 kW sealed tube X-ray source with graphite monochromated Mo-Kα radiation (λ = 0.71073 Å) operating at 50 kV and 30 mA. The program SAINT[23] was used for the integration of diffraction

profiles and absorption correction was made with SADABS[24] program. All the structures were solved by SIR 92[25] and refined by full matrix least square method using SHELXL.[26] All the hydrogen atoms were fixed by HFIX and placed in ideal positions. Potential solvent accessible area or void space was calculated using the PLATON[27] multipurpose crystallographic software. All crystallographic and structure refinement data of **1** is summarized in Table 1. All calculations were carried out using SHELXL 97,[26] PLATON,[27] SHELXS 97 [26] and WinGX system, Ver 1.80.05.[28]

3A.2.6 Preparation of Sample for Adsorption

Adsorption isotherms of CO_2 at 195 K and N_2 at 77 K were recorded with the dehydrated sample using QUANTACHROME QUADRASORB-SI analyzer. To prepare the dehydrated sample of **1** (**1′**) approximately 100 mg of sample was taken in a sample holder and degassed at 110ºC under 10^{-1} Pa vacuum for about 12 hrs prior to the measurements. Dead volume of the sample cell was measured using helium gas of 99.999% purity. The amount of gas adsorbed was calculated from the pressure difference $(P_{cal} - P_e)$, where P_{cal} is the calculated pressure with no gas adsorption and P_e is the observed equilibrium pressure. All the operations were computer-controlled and automatic.

3A.2.7 Characterization

The phase purity was checked by comparing the PXRD pattern (**Fig. 1**) of the bulk powder sample with the simulated data from single-crystal data. The IR spectrum was also recorded (**Fig. 2(a)**).
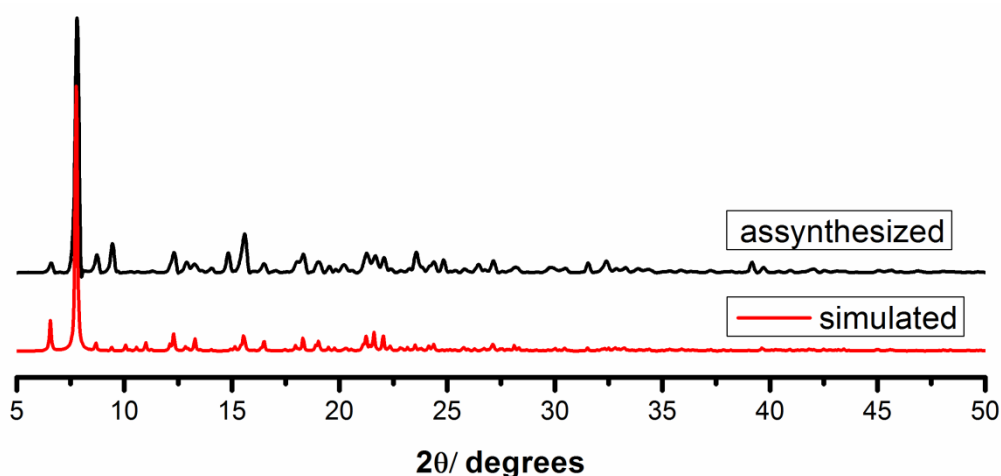
Fig. 1 The simulated and as-synthesized PXRD pattern of **1**.
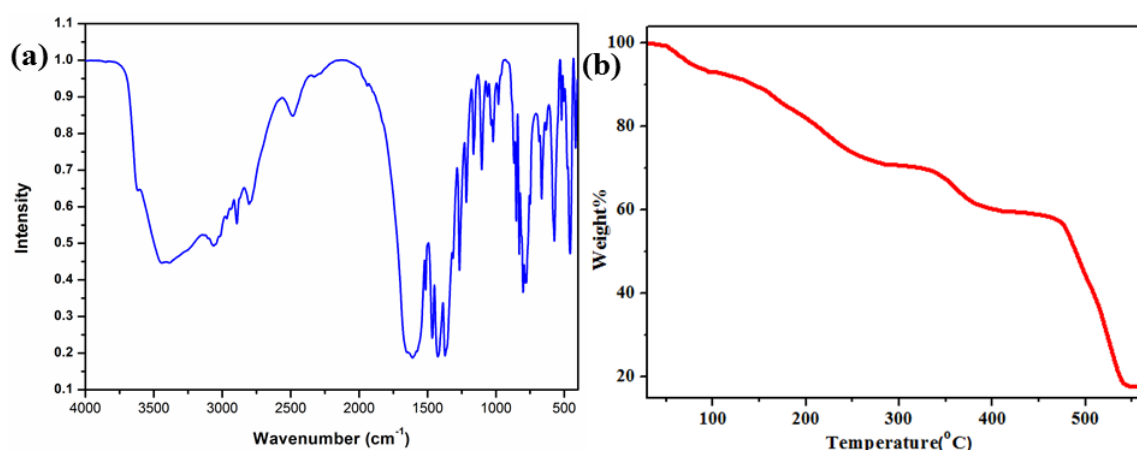
Fig. 2(a) FT-IR spectrum of **1** **(b)** TGA analysis for **1**.

Table 1: Principal Peaks in IR (**Fig. 2(a)**)

Peak Position	Nature	Vibration
1640 cm^{-1}	strong	C=O stretch
795 cm^{-1}	strong	Aromatic C-H stretch
1269, 1374 cm^{-1}	strong	C-N stretch
2809, 3063 cm^{-1}	strong, broad	N-H stretch

The thermogravimetric analysis (TGA) of **1** shows an initial ~6% weight loss corresponding to one coordinated water and two guest water molecules till 100 °C. Next ~ 8% weight loss till 170 °C corresponds to one DMF molecule. Beyond this the framework starts decomposing continuously (**Fig. 2(b)**).

3A.3 Results and Discussion

3A.3.1 Crystal Structure Description

Single crystal X-ray diffraction analysis reveals that compound 1 crystallizes in $P2_1/c$ space group. Each asymmetric unit contains three crystallographically independent hexa-coordinated Mg^{II} centers, all of which are distorted from perfectly octahedral geometry (**Fig. 3(a)**). The hexa-coordination of Mg1 is fulfilled by oxygen atoms (O1, O6, O7 and O10) from three different ndc ligands and two oxygen atoms (O11 and O13) from two different formate ligands. Mg2 adopts a similar coordination environment with O3, O4, O5 and O9 atoms from ndc and O12 and O13 from formate ligands. In case of Mg3, three oxygens from three different ndc moieties (O2, O3, and O8), two oxygen atoms (O11 and O14) from formate and one coordinated water molecule (O1w) ligate to fulfill the hexa-coordination (Fig. 3(a)). Mg1 and Mg3 centers are bridged to each other
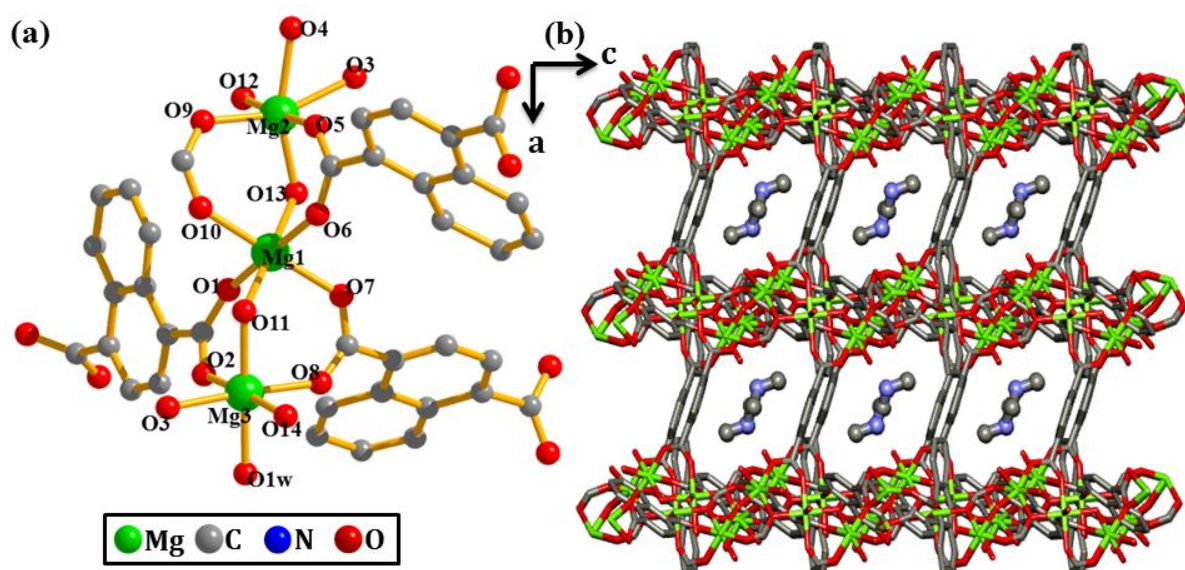
Fig. 3 (a) Coordination environment of Mg^{II} centers in **1**. **(b)** View of 3D framework of **1** along *b* axis showing DMA cations in the pore.

through two ndc and one formate ligands. Mg1 and Mg2 centers are also connected similarly. Thus three Mg^{II} centers are arranged to form a 1D chain along *c* direction (**Fig. 4(a)**). These 1D chains are further connected with each other through ndc_a molecules to generate a 2D network in the crystallographic *ac* plane (**Fig. 4(b)**). These 2D sheets are further cross-linked by ndc_b and ndc_c and repeat themselves along *b* direction to generate the 3D framework (**Fig. 4(c)**) with 1D channels occupied by the guest H_2O,
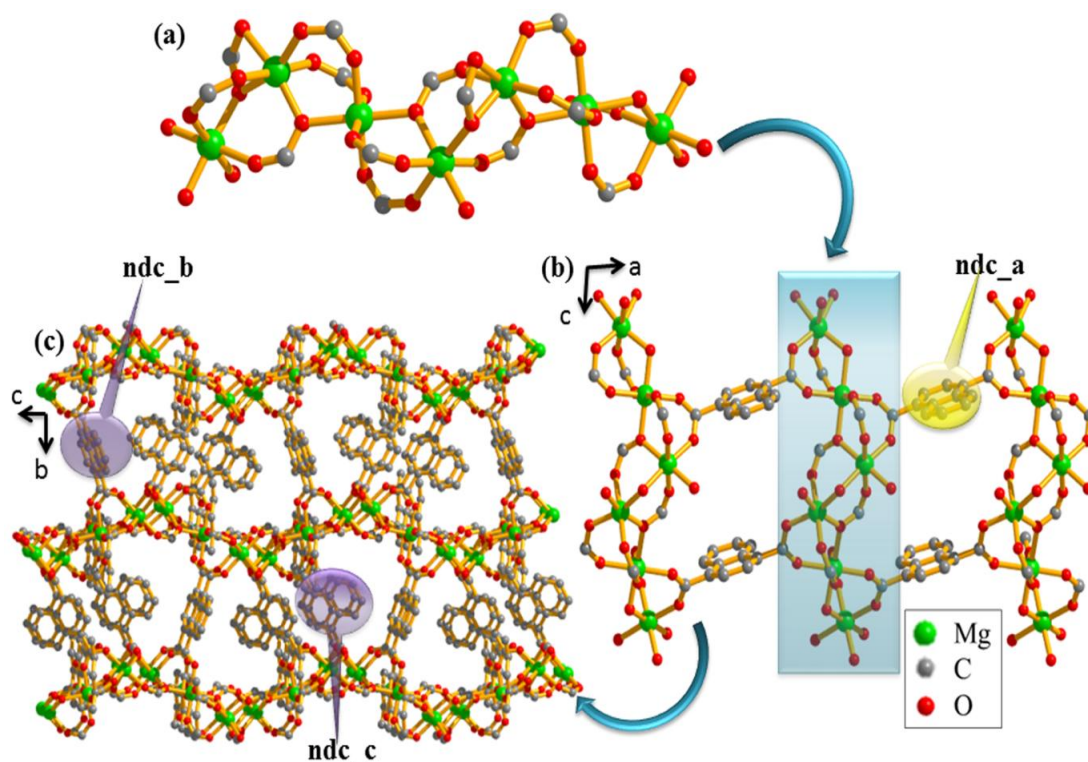
Fig. 4 (a) 1D chain of **1** along crystallographic *c* direction. **(b)** 2D sheet of **1** along the crystallographic *ac* plane. **(c)** View of 3D network of **1** along crystallographic *a* axis.

DMF and extra framework DMA cations (**Fig. 3(b)**). The formate and DMA cations are formed *in situ* from DMF under solvothermal conditions[10, 11]. The solvent accessible void space of the desolvated framework (**1'**) is 28% including the cation.

Table 2. Crystal Data and Structure Refinement for **1**

Parameter	1
Empirical formula	$C_{37}H_{37}Mg_3O_{18}N_2$
Formula weight	870.61
Crystal system	*Monoclinic*
Space group	*P*21/*c* (No.14)
a, Å	11.3593(4)
b, Å	22.5823(8)
c, Å	16.5923(5)
β, deg	92.129(2)
V, Å^3	4253.3(2)
Z	4
T, K	120
μ, mm^{-1}	0.147
D_{calcd}, g/cm^3	1.353
F (000)	1796
reflections [$I>2\sigma(I)$]	3619
unique reflections	7457
measured reflections	57145
R_{int}	0.185
GOF on F^2	1.01
$R_1[I>2\sigma(I)]$[a]	0.0992
$R_w[I>2\sigma(I)]$[b]	0.2988

$(R = \sum||F_o|-|F_c||/\sum|F_o|$, $R_w= [\sum\{w(F_o^2-F_c^2)^2\}/\sum\{w(F_o^2)^2\}]^{1/2})$

Table 3. Selected bond distances (Å) for **1**.

Mg1-O1	2.011(5)	Mg2-O13	2.047(5)
Mg1-O6	2.036(5)	Mg2-O9	2.023(5)
Mg1-O11	2.114(5)	Mg2-O3	2.125(5)
Mg1-O13	2.134(5)	Mg2-O4	2.183(5)
Mg1-O7	2.063(5)	Mg2-O12	2.041(5)

Table 4. Selected bond angles (°) of Compound **1**.

O1-Mg1-O6	176.4(2)	O3-Mg2-O12	90.7(2)
O1-Mg1-O7	90.7(2)	O4-Mg2-O12	91.9(2)
O1w-Mg3-O2	88.8(2)	O3-Mg2-O5	88.1(2)
O1-Mg1-O11	91.3(2)	O6-Mg1-O11	91.3(2)
O2-Mg3-O8	90.9(2)	O4-Mg2-O5	85.0(2)
O1w-Mg3-O11	177.0(2)	O1-Mg1-O10	91.3(2)

3A.3.2 Adsorption Properties
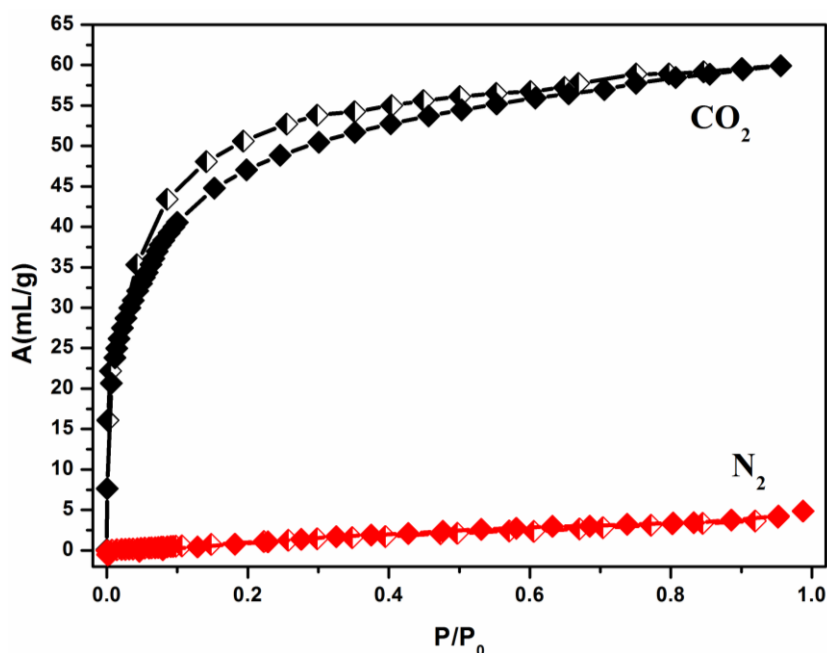
Fig. 5 N_2 (red) and CO_2 (black) adsorption isotherms of **1'.**

To check the adsorption properties, **1** is activated at 110 °C under high vacuum overnight to prepare **1'**. **1'** shows type-1 CO_2 adsorption isotherm at 195 K, while N_2 adsorption reveals only surface adsorption (**Fig. 5**). The typical type I adsorption profile clearly indicates that **1** is microporous in nature. The preferential interaction of CO_2 with **1'** could be attributed to the presence of polar carboxylate groups and unsaturated Mg^{II} sites in **1'**, which can interact well with the quadruple moment of CO_2.[29]

3A.3.3 Cation Exchange

The presence of guest DMA cations and several carboxylate oxygen atoms on the pore surface prompted us to study the exchange properties of **1** with different transition metal cations by immersing **1'** in 0.01M solutions of different metal chlorides. Inductively Coupled Plasma Optical Emission Spectroscopy (ICP-OES) analysis of the exchanging
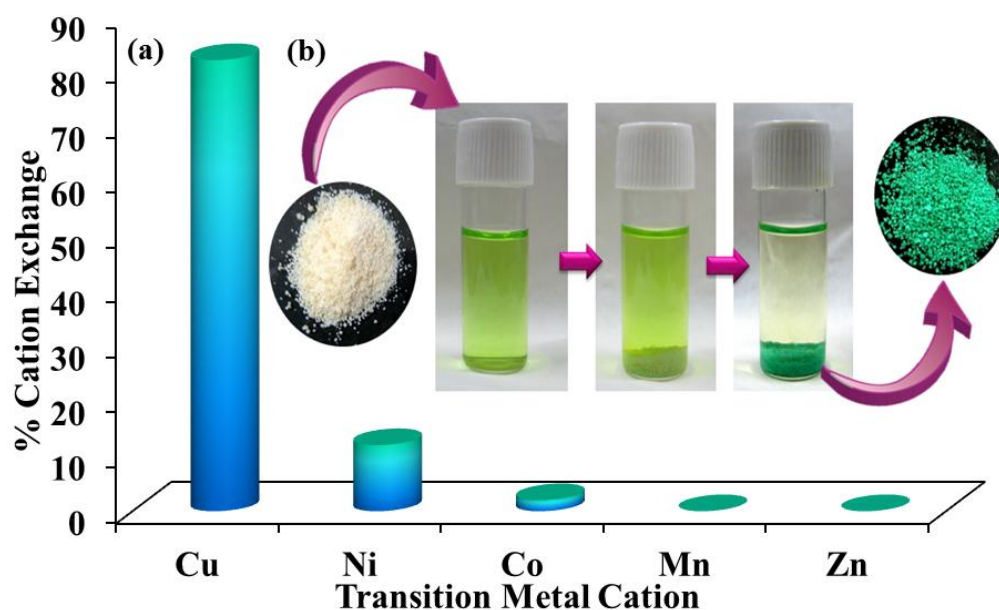
Fig. 6(a) Uptake of different cations by **1'** from an equimolar mixture of all the cations **(b)** Cu^{II} exchange in **1'** in ethanol medium

solution showed the absence of Mg^{II} ions, implying that only the guest DMA cations are exchanged. Also ICP analysis of resulting samples showed that 88% of the DMA guests are exchanged with Cu^{II} ions, while the extent of exchange for Mn^{II}, Co^{II}, Ni^{II} and Zn^{II} are 0, 4, 12 and 0% respectively (**Fig. 6(a), Table 5**). This high percentage of exchange for Cu^{II} is evident as a green solution of Cu^{II} in ethanol becomes colourless on immersing **1'** in it, while the white solid **1'** yields bright green **Cu^{II}@1'** (**Fig. 6(b)**).

Table 5 ICP-MS data for cation exchange in individual cation solutions (0.01M of each metal cation)

Sl. No.	Cation	Number of Cations per Formula Unit	Maximum Number of Cations Possible per Formula Unit	% Exchange of Cation with DMA
1	Mn^{II}	0	0.5	0.0
2	Co^{II}	0.02	0.5	4
3	Ni^{II}	0.06	0.5	12
4	Cu^{II}	0.44	0.5	88
5	Zn^{II}	0	0.5	0.0

3A.3.3.1 Selective Cu^{II} Sensing

As evident from the ICP-OES data, Cu^{II} uptake is more than other transition metal cations. The Cu^{II} uptake amount can also be quantified from the UV spectrum of the Cu^{II} solution used for the exchange process. The decrease in the absorbance intensity of the
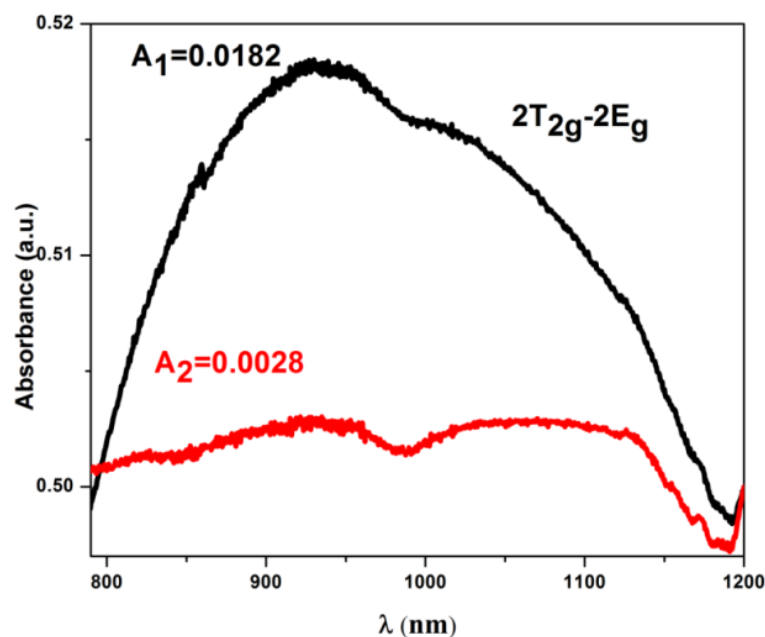
Fig. 7 UV-VIS spectra: (Black) Cu^{II} solution of 6.25×10^{-4} (M) and (Red) Cu^{II} solution obtained after immersing **1'** for 7 days.

UV spectra of the supernatant solution indicates that 84.5% DMA are exchanged with Cu^{II} (**Fig. 7**). Due to d-d transition, a new band appears in the UV spectra of $\mathbf{Cu^{II}@1'}$ at ~720 nm in addition to the band at ~317 nm as observed in **1** (**Fig. 11**). This further supports the coordination of Cu^{II} with the carboxylate oxygens of **1**. Due to structural reorganization after encapsulation of Cu^{II}, there are some changes in the PXRD pattern of $\mathbf{Cu^{II}@1'}$ as well as the appearance of a few new peaks (**Fig. 8**).
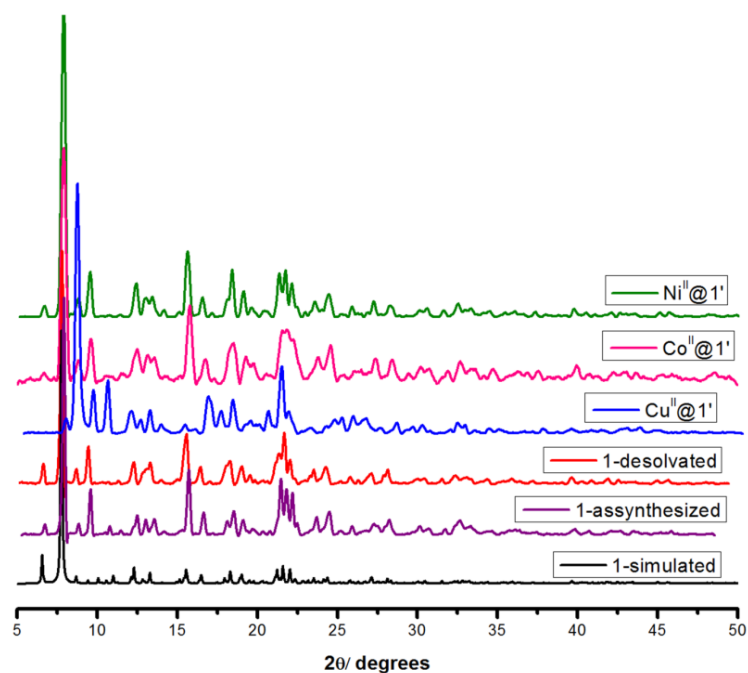
Fig. 8 PXRD patterns of **1** and $\mathbf{M^{II}@1'}$, (where M^{II} is a transition metal cation).
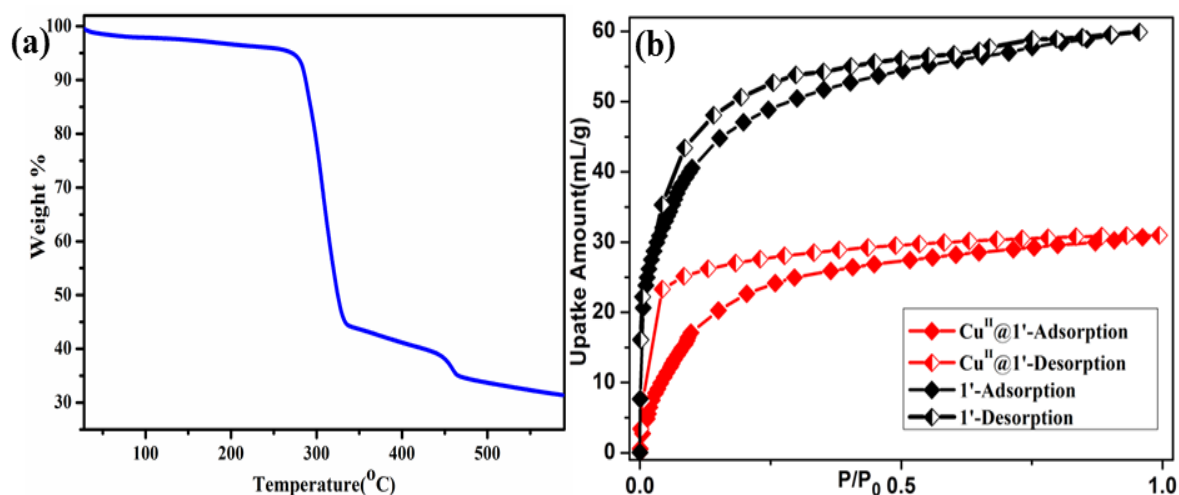
Fig. 9 (a) TGA for **Cu^{II}@1'**. **(b)** Comparison of the adsorption profile of **Cu^{II}@1'** with **1'**.

The thermal stability of **Cu^{II}@1'** was also analysed and it was found that the framework is stable till 250 °C after an initial loss of 2% (**Fig. 9(a)**).

The inclusion of Cu^{II} into the pore of **1** was further confirmed from the CO$_2$ adsorption isotherm (**Fig. 9(b)**) of **Cu^{II}@1'** at 195 K, which shows a 48% decrease in CO$_2$ uptake compared to that of **1**. This decrease in uptake may be attributed to the fact that Cu^{II} ions occupy the pores of **1** randomly, thus inhibiting the diffusion of CO$_2$. Furthermore, the Cu^{II} selectivity of **1** was studied by immersing **1'** in an equimolar solution of a mixture of Mn^{II}, Cu^{II}, Co^{II}, Ni^{II} and Zn^{II} ions. ICP-OES analysis confirmed the exchange of 85% of the DMA cations with Cu^{II}, which is much higher compared to the other metal ions (**Table 6**). This selective capture of Cu^{II} may be explained based on the flexible geometry of Cu^{II} owing to which it can be accommodated in a variety of coordination environments, unlike other transition metal ions. Furthermore, **1** shows ndc linker based emission maximum at ~410 nm when excited at 317 nm in solid state (**Fig. 12(a)**). We anticipated that the emission intensities would be affected by the

Table 6 ICP-MS data for cation exchange in a mixture (0.01 (M) of each metal cation).

Sl. No.	Cation	Number of Cations per Formula Unit	Maximum Number of Cations Possible per Formula Unit	% Exchange of Cation with DMA
1	Mn^{II}	0	0.5	0.0
2	Co^{II}	0.016	0.5	3.2
3	Ni^{II}	0.090	0.5	17.9
4	Cu^{II}	0.423	0.5	84.5
5	Zn^{II}	0	0.5	0.0
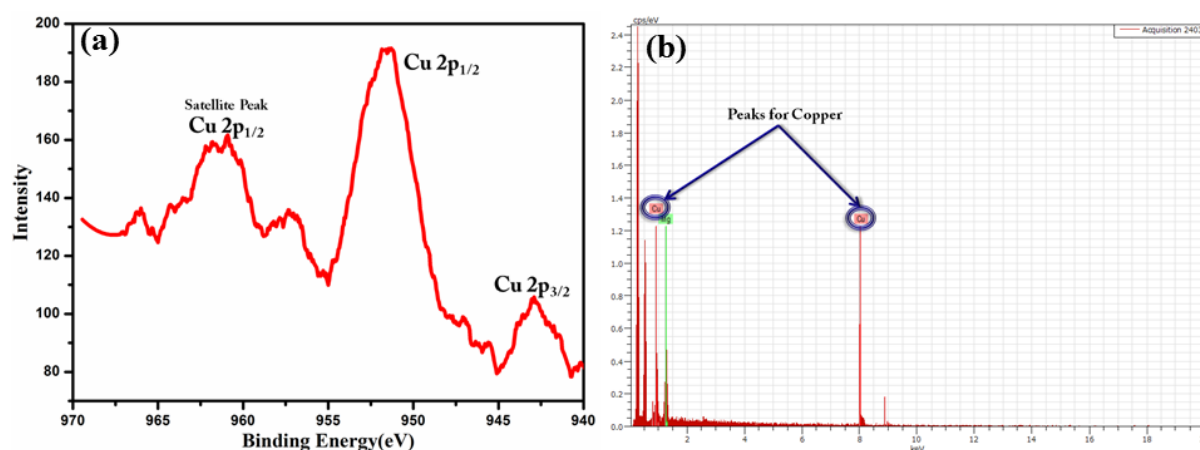
Fig 10(a) XPS data for Cu 2p in **Cu^{II}@1'**. **(b)** EDS analysis of **Cu^{II}@1'**. Peaks for Cu in the EDS analysis plot has been marked.

incorporation of Cu^{II} and this was validated by the significant quenching of emission in **Cu^{II}@1'**. The quenching of emission can be attributed to the ligand field splitting of d-orbitals of Cu^{II} resulting in reabsorption of emission energy by the framework. The XPS analysis clearly shows the different peaks for Cu 2p$_{3/2}$ and 2p$_{1/2}$, implying ligand field splitting of the d-orbitals of Cu in **Cu^{II}@1'** (**Fig. 10(a)**).

In order to check the sensing efficiency, **1'** was immersed in 10^{-3}, 10^{-4}, 10^{-5}, 10^{-6} and 10^{-9} M solutions of Cu^{II} and emission is quenched gradually as the concentration of the Cu^{II} solution increases (**Fig. 12(b)**). To determine the efficiency of **1** as a Cu^{II} sensor, the Stern-Volmer plot at room temperature(~30°C) was constructed and the quenching constant was found to be 1.986×10^3 M^{-1} (**Fig. 12(d)**), which decreased to 3.621×10^2 M^{-1} on repeating the experiment at 80°C (**Fig. 12(c)** and **(d)**). This suggests that the quenching follows a static mechanism, presumably by the complexation of Cu^{II} with **1'**.
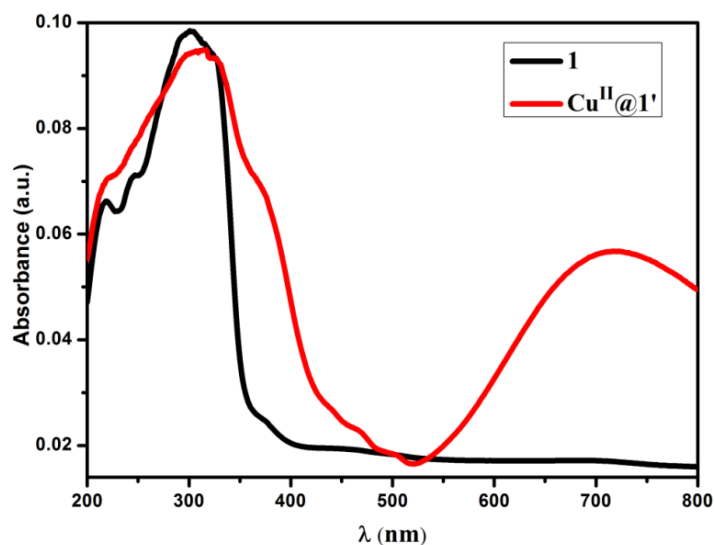
Fig. 11 UV-vis spectra of solid **1** and **Cu^{II}@1'**.

103
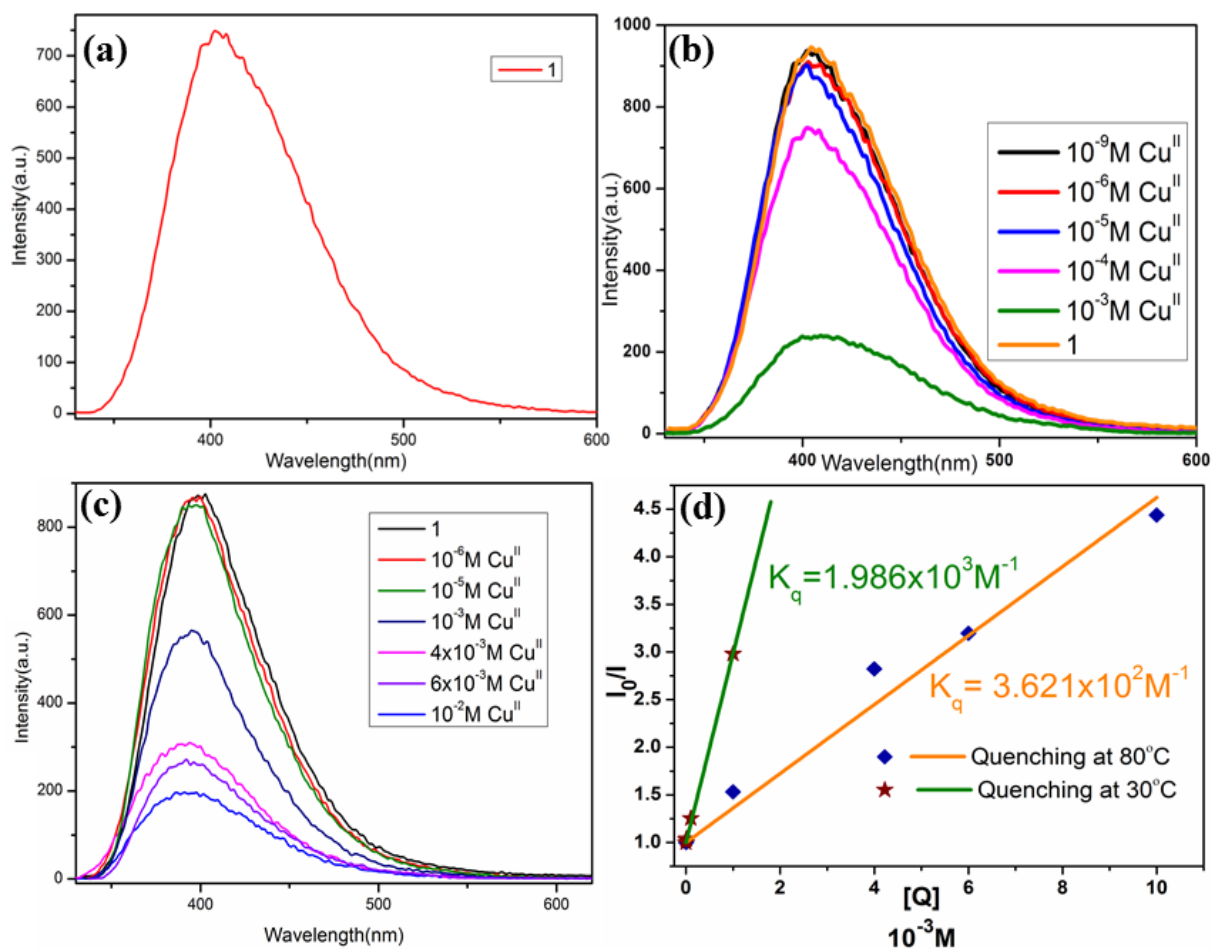
Fig. 12 (a) Characteristic emission spectrum of **1**. (b) Characteristic emission of **1** quenched by different concentration of Cu^{II} solutions at 30 °C. (c) Characteristic emission of **1** quenched by different concentration of Cu^{II} solutions at 80 °C. (d) Stern Volmer plot for quenching by Cu^{II} at 30 °C and 80 °C.

Increase in temperature decreases this complexation promoting the decrease in the quenching constant. The new band in the UV spectra at ~720 nm is also an evidence of the static quenching (**Fig. 11**).

3A.3.3.2 Selective Eu^{III} Sensitization

As the pore surface of **1** is studded with hard oxygen donors, we anticipated the framework to be a potential candidate for encapsulating different hard acid Ln^{III} cations. The Ln^{III} ions are capable of expanding the coordination spheres based on their flexible geometry. **Ln^{III}@1'** samples were prepared by immersing **1** in 0.01M solutions of nitrate salts of Eu^{III}, Tb^{III}, Sm^{III} and Dy^{III}. ICP-OES data suggests that the exchange is about 62% with Sm^{III}, 68% with Eu^{III}, 75% with Tb^{III} and 77% with Dy^{III} in the respective exchanged compounds. After the exchange, structural integrity of **1** is maintained, as evident from the PXRD pattern (**Fig. 13**).
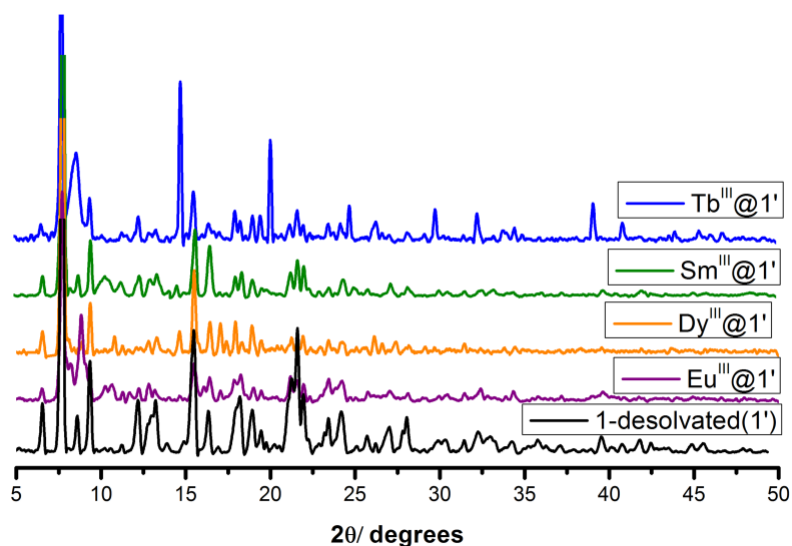
Fig. 13 PXRD patterns of **1** and **Ln^{III}@1'**.

The emission properties of **Ln^{III}@1'** were studied since typically non emissive Ln^{III} ions were expected to furnish new luminescent materials through the antenna effect[30-33] when captured in the pores of **1'**. However, to our surprise, **1** fails to sensitize Dy^{III}, Sm^{III} or Tb^{III} which is evident from the absence of the characteristic peaks of Dy^{III}, Sm^{III} or Tb^{III} from emission spectra of the respective exchanged compounds when excited at 317 nm (**Fig. 14(a)**). Rather **Ln^{III}@1'** [Ln=Dy, Sm, Tb] samples show a blue emission similar to as-synthesized **1** which is observed under UV lamp (**Fig. 14(b)**). The emission spectrum of **Eu^{III}@1'** is rather remarkable, showing the appearance of characteristic emission bands of the Eu^{III} ion centred at 591, 615, 659, 693nm which can be attributed to the $^5D_0 \rightarrow ^7F_{1-4}$ transitions. This is accompanied with concomitant decrease in the emission
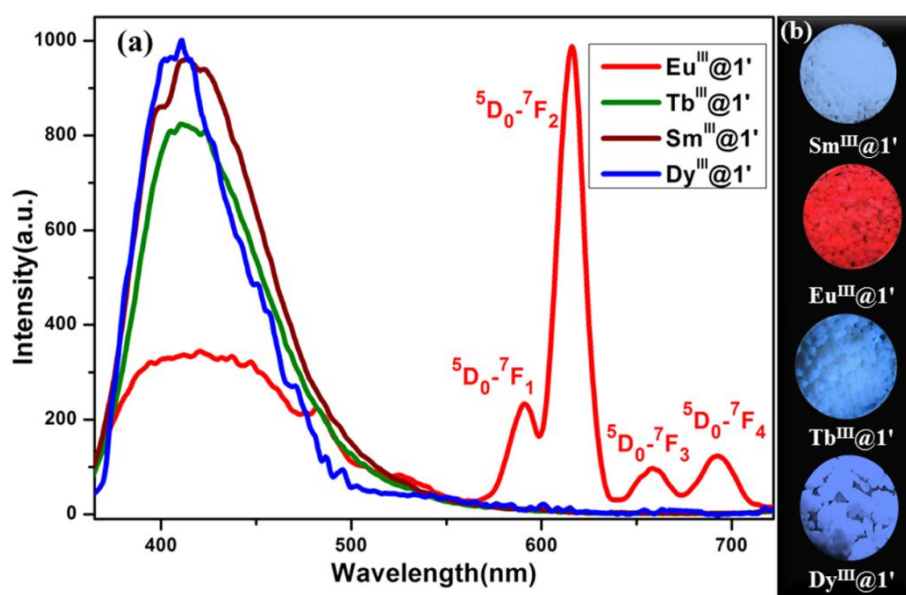
Fig. 14(a) Emission spectra of **Eu^{III}@1'**, **Tb^{III}@1'**, **Sm^{III}@1'** and **Dy^{III}@1'**.**(b)** Photographs of the respective samples under UV lamp.

intensity of the AMOF at ~410 nm (**Fig. 14(a)**). The spectrum is dominated by the $^5D_0 \rightarrow {}^7F_2$ intense band and it is responsible for the brilliant red emission of the **Eu^{III}@1'** hybrid. This confirms that **1** acts as an antenna and selectively sensitizes Eu^{III}, although it takes up other Ln^{III} cations. Probably this unprecedented selective sensitization of Eu^{III} is realized due to the facile energy transfer to the excited $^5D_0$ state of Eu^{III} from the singlet excited states of **1**, which is not favourable in case of the other lanthanides.

3A.4 Conclusion

In conclusion, a new Mg based AMOF (**1**) with 1D cation exchangeable channels has been synthesized that has been exploited for selective sequestration for Cu^{II} ions. The flexible geometry of Cu^{II} allows it to be accommodated in a variety of coordination environments and hence it is captured selectively over other metal cations. This can be realized through fluorescence read out by the turn-off of emission. The AMOF can also encapsulate several hard lanthanide metal ions through preferential binding with the hard oxygen centers. The Ln^{III} exchanged framework exhibits unprecedented specific sensitization for Eu^{III} resulting in a red luminescent material through Post Synthetic Modification. Such bimodal functionalities are accomplished through proper size and functionalities of the cation exchangeable channels in **1**. Inclusion of specific cationic groups in such AMOFs would also facilitate targeted fabrication of smart materials with versatile properties like catalytic activity, adsorption, magnetism, nonlinear optical response etc., which is currently being explored in our laboratory.

3A.5 References

1. P. Vanelderen, J. Vancauwenbergh, B. F. Sels and R. A. Schoonheydt, *Coord. Chem. Rev.*, 2013, **257**, 483.

2. J. Jiang, J. Yu and A. Corma, *Angew. Chem. Int. Ed.*, 2010, **49**, 3120.

3. R. Haldar and T. K. Maji, *CrystEngComm*, 2013, **15**, 9276.

4. *Themed Issue: Metal-organic Frameworks Chem. Rev.*, 2012, **112**, 673.

5. Z. Zhang, Z.-Z. Yao, S. Xiang and B. Chen, *Energy Environ. Sci.*, 2014, **7**, 2868.

6. S. Y. Vyasamudri and T. K. Maji, *Chem. Phys. Lett.*, 2009, **473**, 312.

7. Y. Liu, G. Li, X. Li and Y. Cui, *Angew. Chem.*, 2007, **119**, 6417.

8. E. Quartapelle Procopio, F. Linares, C. Montoro, V. Colombo, A. Maspero, E. Barea and J. A. R. Navarro, *Angew. Chem. Int. Ed.*, 2010, **49**, 7308.

9. J. Yu, Y. Cui, C. Wu, Y. Yang, Z. Wang, M. O'Keeffe, B. Chen and G. Qian, *Angew. Chem. Int. Ed.*, 2012, **51**, 10542.

10. J. An, S. J. Geib and N. L. Rosi, *J. Am. Chem. Soc.*, 2009, **131**, 8376.

11. D. T. Genna, A. G. Wong-Foy, A. J. Matzger and M. S. Sanford, *J. Am. Chem. Soc.*, 2013, **135**, 10586.

12. J. Tian, L. V. Saraf, B. Schwenzer, S. M. Taylor, E. K. Brechin, J. Liu, S. J. Dalgarno and P. K. Thallapally, *J. Am. Chem. Soc.*, 2012, **134**, 9581.

13. S. Yang, X. Lin, A. J. Blake, G. S. Walker, P. Hubberstey, N. R. Champness and M. Schröder, *Nat Chem*, 2009, **1**, 487.

14. S. Yang, G. S. B. Martin, J. J. Titman, A. J. Blake, D. R. Allan, N. R. Champness and M. Schröder, *Inorg. Chem.*, 2011, **50**, 9374.

15. K. Jayaramulu, R. P. Narayanan, S. J. George and T. K. Maji, *Inorg. Chem.*, 2012, **51**, 10089.

16. T. Hirayama, G. C. Van de Bittner, L. W. Gray, S. Lutsenko and C. J. Chang, *Proc. Nat. Acad. Sci.*, 2012, **109**, 2228.

17. J.-S. Qin, S.-J. Bao, P. Li, W. Xie, D.-Y. Du, L. Zhao, Y.-Q. Lan and Z.-M. Su, *Chem. Asian J.*, 2014, **9**, 749.

18. J.-S. Qin, S.-R. Zhang, D.-Y. Du, P. Shen, S.-J. Bao, Y.-Q. Lan and Z.-M. Su, *Chem. Eur. J.*, 2014, **20**, 5625.

19. C. Yang, L.-M. Fu, Y. Wang, J.-P. Zhang, W.-T. Wong, X.-C. Ai, Y.-F. Qiao, B.-S. Zou and L.-L. Gui, *Angew. Chem. Int. Ed.*, 2004, **43**, 5010.

20. Y.-Q. Chen, G.-R. Li, Z. Chang, Y.-K. Qu, Y.-H. Zhang and X.-H. Bu, *Chem. Sci.*, 2013, **4**, 3678.

21. S. Liu, J. Li and F. Luo, *Inorg. Chem. Commun.*, 2010, **13**, 870.

22. Y.-W. Li, J.-R. Li, L.-F. Wang, B.-Y. Zhou, Q. Chen and X.-H. Bu, *J. Mater. Chem. A*, 2013, **1**, 495.

23. S. V. a. SMART (V 5.628), XPREP, SHELXTL; Bruker AXS Inc. Madison, Wisconsin, USA, 2004.

24. G. M. Sheldrick, *SADABS, Empirical Absorption Correction Program, University of Göttingen, Göttingen*, 1997.

25. A. Altomare, G. Cascarano, C. Giacovazzo and A. Guagliardi, *J. Appl. Crystallogr.*, 1993, **26**, 343.

26. G. M. Sheldrick, *SHELXL 97, Program for the Solution of Crystal Structure, University of Göttingen, Germany*, 1997.

27. A. Spek, *J. Appl. Crystallogr.*, 2003, **36**, 7.

28. L. Farrugia, *J. Appl. Crystallogr.*, 1999, **32**, 837.

29. J.-R. Li, R. J. Kuppler and H.-C. Zhou, *Chem. Soc. Rev.*, 2009, **38**, 1477.

30. Y. Cui, Y. Yue, G. Qian and B. Chen, *Chem. Rev.*, 2011, **112**, 1126.

31. S. Roy, A. Chakraborty and T. K. Maji, *Coord. Chem. Rev.*, 2014, **273**, 139.

32. S. Mohapatra, S. Adhikari, H. Riju and T. K. Maji, *Inorg. Chem.*, 2012, **51**, 4891.

33. B. Chen, L. Wang, Y. Xiao, F. R. Fronczek, M. Xue, Y. Cui and G. Qian, *Angew. Chem. Int. Ed.*, 2009, **48**, 500.

Chapter 3B

Synthesis of Nano-porous Carbon and Nitrogen Doped Carbon Dots from an Anionic MOF
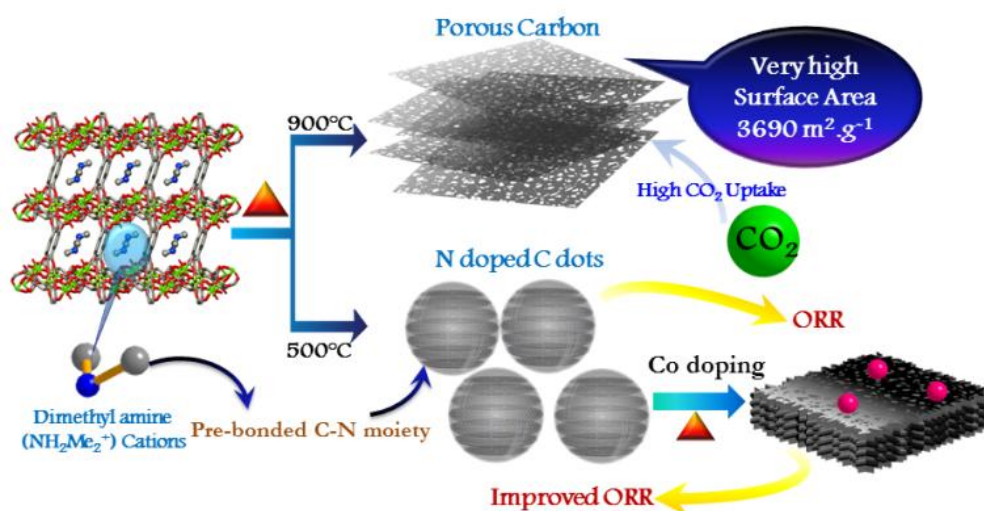
Abstract

Metal-organic frameworks (MOFs) are effective self-sacrificial templates for the synthesis of carbon materials owing to innate porosity, high carbon content and ease of heteroatom doping. A Mg^{II} based anionic MOF $\{[Mg_3(ndc)_{2\cdot5}(HCO_2)_2(H_2O)]\cdot[NH_2Me_2]\cdot2H_2O\cdot DMF\}$ (**1**) has been carbonized as a sacrificial template for the synthesis of high surface area nanoporous carbon as well as nitrogen doped carbon dots, simply by adjusting the carbonization temperature. The nanoporous carbon synthesized from the MOF precursor exhibits an exceptionally high surface area and high CO_2 uptake capacity. The anionic MOF **1** contains dimethyl amine cation in its pores which, owing to its pre-bonded C-N moiety, acts as a precursor for N-doping of the carbon dots. The N-doped carbon dots are held together by graphitic stacking and they show electrocatalytic activity as metal free catalyst for the oxygen reduction reaction (ORR). Trace amount of metallic Co nanoparticles were post-synthetically incorporated into the N-doped carbon dots leading to enhanced electrocatalytic activity and stability for the ORR of the resulting material. The controlled design and synthetic strategy presented here offers a new platform for developing highly active and stable electrocatalysts.

3B.1 Introduction

Porous nanocarbon composite materials have attracted wide spread attention as sustainable oxygen reduction reaction (ORR)[1, 2] catalysts in alkaline media owing to their low cost, high electrical conductivity, good corrosion resistance, high surface area and environmental acceptability.[3-5] Among the many exciting allotropes of carbon, heteroatom (such as N, S, P or B) doped carbon catalysts have been reported as attractive ORR catalysts, with or without additional transition metal content.[6-9] It has also been realized that the presence of a trace amount of transition metals (e.g. Fe, Co, or Ni) can effectively enhance the activity of pristine nitrogen-carbon catalysts for ORR by modifying the electronic properties of the carbon lattice.[9]

Conventional methods for synthesizing porous carbon materials, e.g., chemical vapour deposition (CVD), nitrogen plasma treatment or simple pyrolysis of carbon materials followed by activation of organic precursors often yield unsatisfactory results, thus giving rise to templating or nanocasting approaches.[10] Soft templates, e.g., resols, block- copolymers and hard templates, e.g., zeolites and silica along with suitable carbon precursors were used for this purpose. However, these approaches are rather unfavourable for bulk-scale production.[3] The pioneering work by Xu *et al.*, first upheld metal-organic frameworks (MOFs)[11-13] as self-sacrificial templates for the efficient synthesis of porous carbon materials due to their innate porosity, high surface area and large carbon content.[2, 14, 15] In many cases, precursors like furfuryl alcohol,[14] sucrose[15], glycerol,[16] phenolic resin[17] etc. have been impregnated in MOF templates as a source of carbon. The use of a MOF template also ensures relatively easy heteroatom doping e.g., N, P, S and B, in the porous carbon matrix[18, 19] thereby producing novel materials with different morphologies as well as interesting opto-electronic properties.[18, 20, 21] Owing to their electron rich surfaces these heteroatom doped carbon materials have the potential to manifest photocatalytic[22, 23] and electrocatalytic[2, 19, 24, 25] activity. More recently, carbon nanodots which are nanoscale quasi-spheres, with unique photoluminescence, photo-induced electron transfer, high catalytic activity and electron reservoir properties have gained widespread attention in the fields of energy storage and catalysis.[21, 26, 27, 35, 39] These have been synthesized primarily from organic precursors by many different ways, e.g., electrochemical, microwave

and hydrothermal.[35] Their unique morphology reveals robust chemical stability, easy tunability and intriguing optical properties, which can be further tuned by nitrogen doping,[21, 28-32] making them suitable for metal-free catalysis of oxygen evolution reaction (OER) or oxygen reduction reaction (ORR), e.g., in fuel cells. In order to improve the overall efficiency of ORR activity, trace amounts of non-precious transition metals (Co, Ni or Fe) may be incorporated into the carbon-nitrogen matrix,[8] which is a facile and cost effective method to synthesize suitable stable electrocatalysts. The synthesis of carbon nanodots is often performed by pyrolysis of suitable precursors, although in many cases disordered amorphous structures with a high percentage of sp^3 carbon are formed.[33] This can be easily overcome by the use of a crystalline starting material with a highly ordered structure e.g., a MOF. The synthesis of heteroatom-doped porous carbon materials like graphitic carbon nitride analogues using MOF templates involves the use of a precursor containing pre-bonded C-N moieties such as melamine or dicyandia-mide.[10, 34] However, if the MOF itself contains such a moiety as a guest, it is possible to synthesize N-doped carbon materials *in situ* by simply carbonizing the MOF at an optimum temperature in absence of any additional reagent. This can be
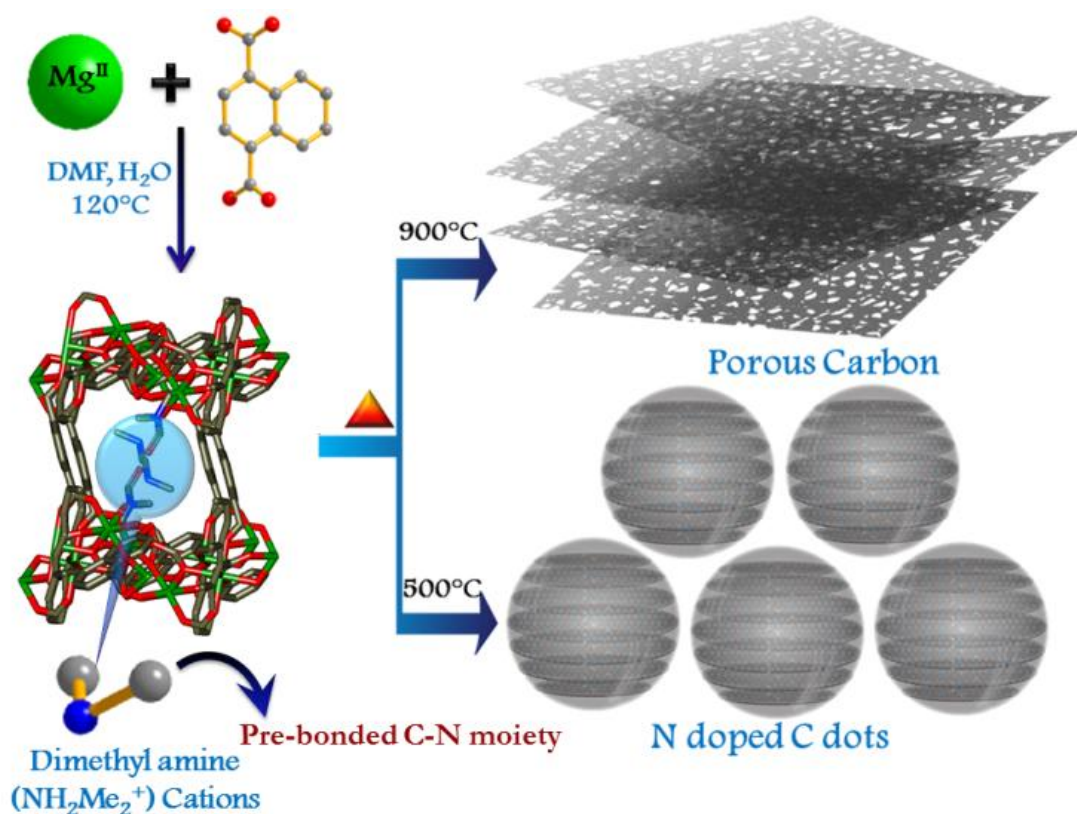
Scheme 1 Schematic representation of the synthesis of nanoporous carbon and N-doped carbon dots from AMOF **1**.

favourably realized in so called anionic MOFs (AMOF)[12, 13, 35, 36] which bear a guest cation in the pores of their anionic frameworks in order to maintain the overall charge neutrality. If this guest cation contains a C-N moiety, it can act as a precursor for N-doped carbon material, while the framework itself acts as a self-sacrificial template. Hence, the synthesis of N-doped carbon dots as well as nanoporous carbon can be achieved from the same AMOF without the use of any external reagent, simply by changing the carbonizing temperature. In this chapter, the synthesis of both N-doped carbon dots (**NCD-1**) as well as nanoporous carbon (**NPC-1**) from AMOF [$Mg_3(ndc)_{2.5}(HCO_2)_2(H_2O)$]·[$NH_2Me_2$]·$2H_2O$·DMF (**1**) (ndc = 1,4-naphthalenedicarboxylate) (**Scheme 1**) has been documented.[12] **NPC-1** exhibits one of the highest surface areas for a porous carbon material obtained from a MOF, whereas **NCD-1** manifests unique emission properties and also acts as an ORR catalyst. In order to improve the overall efficiency of ORR activity, a trace residue of Co (1.5 wt%) was introduced into the **NCD-1** matrix and the enhancement in ORR activity was investigated. The templated synthesis of N-doped carbon dots and nanoporous carbon from the same MOF simply by changing the carbonization temperature without the use of any external precursor is unprecedented. Moreover, enhanced ORR activity is achieved by incorporating traces of non-precious metal, thus opening up the possibility towards a new class of low-cost and earth-abundant electrocatalysts.

3B.2 Experimental Section

3B.2.1 Materials

All reagents and solvents were used as obtained without any further purification. 1,4-naphthalenedicarboxylic acid (H_2ndc) and 5,10,15,20-tetrakis(4-methoxyphenyl)-21H,23H-porphine cobalt(II) were procured from Alfa Aesar. $Mg(NO_3)_2.6H_2O$ was obtained from Sigma Aldrich.

3B.2.2 Synthesis of NPC-1 and NCD-1

{[$Mg_3(ndc)_{2.5}(HCO_2)_2(H_2O)$]·[$NH_2Me_2$]·$2H_2O$·DMF} (**1**) was synthesized following the method reported in the previous chapter.[12] The crystals of **1** were finely ground in a mortar with a pestle for 15 min. The powder **1** was then carbonized at 900 °C and 500 °C under Ar atmosphere for 6 h to obtain **NPC-1** and

NCD-1, respectively. Both samples were washed meticulously with a concentrated acid mixture [HCl:HNO$_3$=1:1 (v/v)] to remove residual metal oxides and then repeatedly with water. Afterwards the products were dried in air.

3B.2.3 Incorporation of Co into NCD-1

17.0 mg of **NCD-1** was mixed with 3.0 mg of the corresponding 5,10,15,20-tetrakis(4-methoxyphenyl)-21H,23H-porphine cobalt(II) complex. This mixture was ground and dried in air and subsequently pyrolyzed at 800 °C under N$_2$ atmosphere (50 sccm, 2 h).

3B.2.4 Materials Characterization

The carbonization was carried out in an Elite programmable tube furnace (Model TSH15/50/180/2416) in a porcelain boat within a quartz tube. The elemental analysis was carried out using a Thermo Fischer Flash 2000 Elemental Analyzer. Powder X-ray diffraction (PXRD) was recorded by using Cu-Kα radiation (Bruker D8 Discover; 40 kV, 30 mA). Absorption and emission spectra were recorded using a Perkin Elmer Lambda 750 UV-VIS-NIR spectrometer and Perkin Elmer Ls 55 Luminescence Spectrometer, respectively. Solid state UV spectra were recorded in reflectance mode. IR spectra of the compounds were recorded with a Bruker IFS 66v/S spectrophotometer using the KBr pellets in the region 4000−400 cm^{-1}. Transmission electron microscopy (TEM) analysis has been performed using a JEOL JEM-3010 with an accelerating voltage at 300 kV or a FEI TECNAI G2 20 STWIN TEM operating at 200 kV. One drop of the samples dispersed in ethanol solution was taken in a holey carbon coated Cu grid for TEM imaging. Atomic force microscopy was done with Bruker Innova Atomic Force Microscope. Height profiles of the nanostructures were acquired with a JPKSPM data processing software.

3B.2.5 Adsorption Study

The adsorption isotherms of CO$_2$ (195 K), N$_2$ (77 K, 273 K and 298 K), other gases (C$_2$H$_2$, C$_2$H$_4$ at 273 K and 298 K) using the desolvated sample of **NPC-1** and **NCD-1** were measured by using a QUANTACHROME AUTOSORB IQ2 analyzer. In the sample tube adsorbent samples **NPC-1** and **NCD-1** (~100–150 mg) were placed which

had been prepared at 353 and 433 K, respectively, under a 1×10^{-1} Pa vacuum for about 6 h prior to measurement of the isotherms. Helium gas (99.999% purity) at a certain pressure was introduced in the gas chamber and allowed to diffuse into the sample chamber by opening the valve. The amount of gas adsorbed was calculated readily from the pressure difference ($P_{cal} - P_e$), where P_{cal} is the calculated pressure with no gas adsorption and P_e is the observed equilibrium pressure. All operations were computer-controlled and automatic.

3B.2.6 Electrochemical Measurements

All electrochemical measurements were performed using an Autolab potentiostat/galvanostat (PGSTAT12) in a conventional three-electrode cell in combination with a Metrohm RDE-2 rotator. A glassy carbon electrode of geometric area of 0.126 cm^2 modified with the catalysts was used as the working electrode, a Ag/AgCl/3M KCl as reference electrode and a Pt mesh as counter electrode. The reference electrode was calibrated with respect to the reversible hydrogen electrode (RHE). Prior to experiments, the glassy carbon electrode was polished on a polishing cloth using different alumina pastes (grain size from 3.0 to 0.05 μm) to obtain a mirror-like surface, followed by ultrasonic cleaning in water. For electrochemical measurements a catalyst ink was prepared by dispersing 5.0 mg mL^{-1} of the catalyst in water under ultrasonication for 30 min. 5.0 μL of the catalyst suspension was drop-coated onto the polished glassy carbon electrode and dried in air at room temperature. The catalyst loading for each electrode was 0.198 mg cm^{-2}. Before the ORR measurements, the modified electrodes were subjected to continuous potential cycling in the potential window from -0.5 V to 0.2 V until reproducible voltammograms were obtained. All current densities were calculated using the geometric surface area of the electrode. All potentials were rescaled to the pH-independent reversible hydrogen electrode (RHE). The long-term stability was evaluated by means of chronopotentiometry at a constant potential vs RHE on catalyst-modified graphite rotating disk electrodes (5 mm diameter) in 0.1 M KOH solution. During the measurements, the electrode was maintained at a rotation of 1600 rpm to avoid accumulation of gas bubbles on the electrode surface. The electrolyte was purged for ~20 min with O_2 prior to measurements and an O_2 stream was maintained over the electrolyte throughout the time of the experiment. All measurements were carried out at room temperature.

3B.2.6.1 Koutecky-Levich Plot

The kinetic parameters can be calculated on the basis of Koutecky-Levich equations:

$$\frac{1}{j} = \frac{1}{j_L} + \frac{1}{j_K} = \frac{1}{B\omega^{1/2}} + \frac{1}{j_K}$$

$B = 0.62nFC_0(D_0)^{2/3}\ v^{-1/6}$

$j_K = nFkC_0$

where j_K and j_L are the kinetic and diffusion-limiting current densities, ω is the angular velocity in rad s^{-1}, n is the number of the transferred electrons, C_0 (1.26×10^{-6} mol cc^{-1}) and D_0 (1.93×10^{-5} cc s^{-1}) are the bulk concentration and diffusion coefficient of O_2 in electrolyte, v (1.01×10^{-2} cm^2 s^{-1}) is the kinematic viscosity of the electrolyte, and k is the electron-transfer rate constant.[19] n and j_K can be determined from the slope and the intercept of the plots respectively.

3B.3 Results and Discussions

$\{[Mg_3(ndc)_{2.5}(HCO_2)_2(H_2O)]\cdot[NH_2Me_2]\cdot2H_2O\cdot DMF\}$ (**1**) is a 3D anionic framework in which the charge neutrality is maintained by dimethyl amine ($NH_2Me_2^+$) (DMA) cations residing in its pores as mentioned in the previous chapter.[12] In AMOF **1**, three Mg^{II} centres are connected together by carboxylate groups of ndc and formate ligands to form 1D chains. These 1D chains are further coordinated by ndc linkers in all three directions to form a 3D framework with 1D channels along the *b* direction that contains the DMA cations. N-doped C-dots are synthesised by heating the AMOF **1** at 500°C under Ar atmosphere for 6 h. The general synthetic procedure of N doped carbon materials like g-C$_3$N$_4$ involves the pyrolysis of pre-bonded C-N moieties like dicyanamide or melamine. Upon heating the AMOF, the dimethyl amine cations provide the necessary C-N-C moiety for developing a N-doped C-matrix. The dimethyl amines fuse together to form matrix of N-doped carbon, that stack up to form nanodots. Next, nanoporous carbon (**NPC-1**) is synthesized from AMOF **1** by heating it in a tube furnace at 900°C for 6 h under Ar atmosphere, and the material obtained after acid treatment was characterized by PXRD, FTIR, Raman Spectroscopy and XPS analysis. On

being heated at a higher temperature, i.e., 900° C, most of the nitrogen leaves the material as NH_3, thereby forming sheets of nanoporous carbon (**NPC-1**).

3B.3.1 Characterization of NPC-1

NPC-1 shows diffraction peaks at $2\theta = 24.2°$ and $42.8°$, which are characteristic of graphitic carbon (**Fig. 1(a)**). The Raman spectrum of **NPC-1** shows the well distinguished D and G bands (**Fig. 1(b)**) of graphitic carbon implying the presence of a disordered sp^2 hybridized C-structure, with the intensity ratio of D and G bands (I_D/I_G) being equal to 0.96. FT-IR spectra confirmed the presence of aromatic in-ring C=C stretch vibrations (1550 cm^{-1}), along with C=O (1715 cm^{-1}), C-O (1160 cm^{-1}) and O-H (3290 cm^{-1}) groups (**Fig. 1(c)**) indicating the presence of oxygen in the carbon matrix. In order to determine the configuration of C and O in the matrix of **NPC-1**, C 1s and O 1s XPS spectra were analysed. The XPS C 1s spectrum can be deconvoluted into five components which can be attributed to sp^2 C=C (284.5 eV), sp^3 C-C/C-H (285.5 eV), C-O (286.4 eV), C=O (288.9 eV) and COOH (291.5 eV) (**Fig. 1(d)**). The presence of oxygen is further ascertained by the three deconvoluted components of the O 1s spectrum in the XPS, which can be attributed to C=O, C-O and C-O-H bonds (**Fig. 1(e)**). From the XPS peak area analysis, the composition of the sample surface can be calculated as 92.03% C and 7.97% O. Additionally, TEM analysis of **NPC-1**
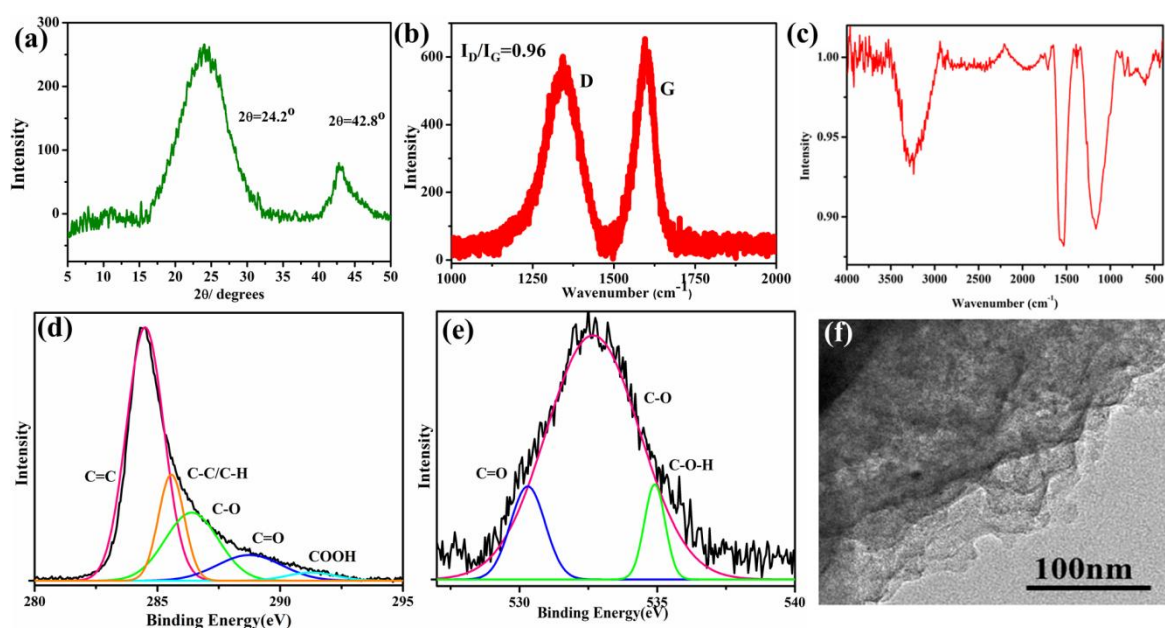
Fig. 1(a) PXRD pattern of **NPC-1**. **(b)** Raman spectrum of **NPC-1**. **(c)** IR spectra of **NPC-1**. **(d)** C1s spectrum in the XPS analysis of **NPC-1**. **(e)** O1s spectrum in the XPS analysis of **NPC-1**. **(f)** TEM image of **NPC-1**.

was performed, which showed a structural morphology comprising multiple layers of disordered graphitic carbon arranged one upon another (**Fig. 1(f)**). This layered morphology is indicative of a porous structure and hence the porosity and surface area of the sample was evaluated. **NPC-1** shows a total uptake of 3042 ml g^{-1} N_2 at 77 K with a mixture of type-I and type-IV sorption behaviour. The calculated BET surface area is 3690 m^2 g^{-1}, which is one of the highest surface area for a porous carbon obtained from directly carbonizing a MOF, without the use of any external precursor.[37] The pore size distribution shows an accumulation of both micro- and mesopores, with most of the pores being around 1.08 nm, and a few around 3.46 nm and 4.8 nm (**Fig. 2(a)**). Hence, **NPC-1** is a very promising material for gas storage and it shows a steady CO_2 uptake of 47 ml g^{-1} and 35 ml g^{-1} at 273 K and 293 K, respectively (at P ~1 bar) (**Fig. 2(b)**).

3B.3.2 Characterization of NCD-1

Graphitic N-doped carbon dots (**NCD-1**) were obtained by carbonizing finely powdered **1** at 500°C under Ar atmosphere. The DMA cations of **1** act as precursors providing pre-bonded C-N moieties for the synthesis of N-doped carbon dots. The PXRD of **NCD-1** shows a split peak at around 2θ = 12.8° and a broad one around 2θ = 24.5° (**Fig. 3(a)**), similar to the diffraction peaks obtained for graphitic carbon nitride (g-C_3N_4).[38] The peak at 12.8° corresponds to a *d* spacing of 0.708 nm, which can be attributed to an in-plane structural packing motif, similar to the size of a tris-*s*-triazine unit (0.73 nm).[39] The peak at 2θ = 24.5° is indicative of the graphitic stacking with an interlayer distance of 0.362 nm. The Raman spectrum of **NCD-1** also shows both D and G bands (**Fig. 3(b)**), with $I_D/I_G = 0.64$, which is predictably lower than in the case of **NPC-1**, indicating more ordered
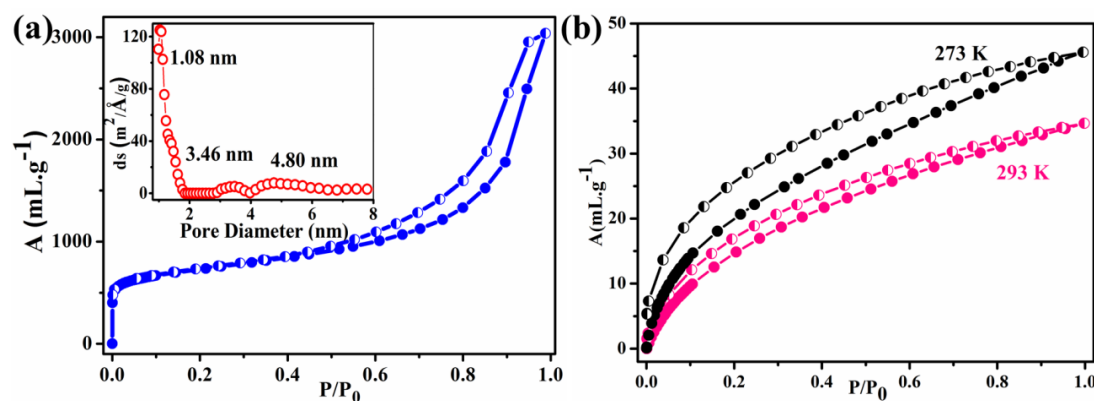
Fig. 2(a) N_2 adsorption isotherm of **NPC-1** at 77K. Inset shows pore size distribution of **NPC-1**. **(b)** CO_2 adsorption isotherms of **NPC-1** at 273 K (**black**) and 293 K (**pink**).

graphitic stacking. The IR spectrum of **NCD-1** confirms the presence of the C=N and C-N stretching vibrations in C-N heterocycles with characteristic peaks between 1200-1650 cm^{-1} (1280, 1337, 1377, 1528 cm^{-1}).[40] The peak at 1700 cm^{-1} is attributed to the C=O vibration which implies that some oxygen is also present in the carbon nitride matrix (**Fig. 3(c)**). The XPS analysis of the C 1s spectrum of **NCD-1** indicates the presence of C-N and C=N functionalities, in addition to C=C, C-O and C=O bonds. The N 1s spectrum can be deconvoluted into four peaks corresponding to C=N (397.5 eV), NH_2 (399 eV), C-N-C (406.1 eV) and N-C_3 (413 eV), whereas the O 1s spectrum shows the components for C=O, C-O and C-O-H at 530, 532.5 and 535.5 eV, respectively (**Fig. 3(e)**). From the peak area
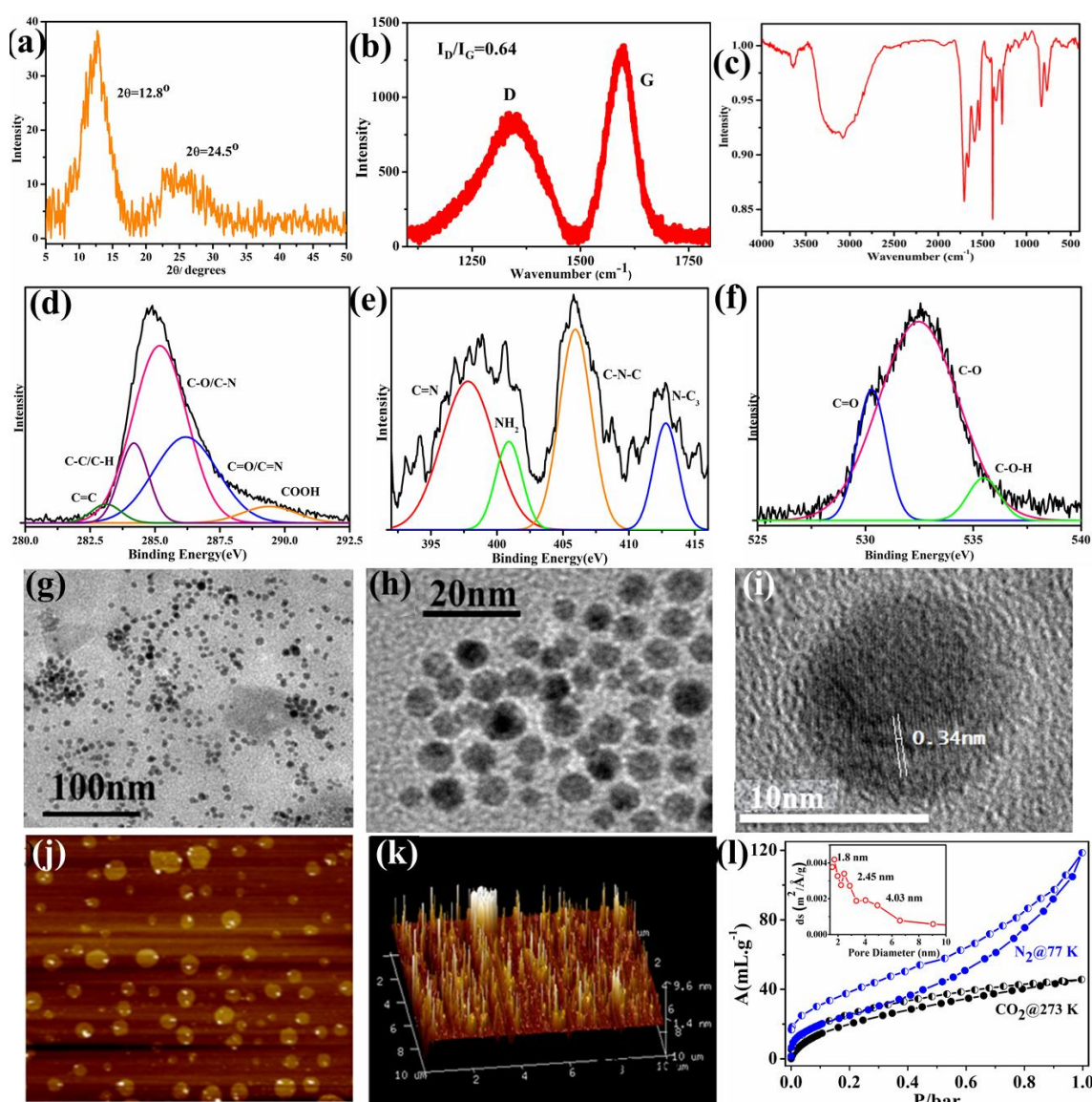

Fig. 3(a) PXRD pattern of **NCD-1**. **(b)** Raman spectrum of **NCD-1**. **(c)** IR spectrum of **NCD-1**. **(d)** C1s, **(e)** N1s and **(f)** O1s spectra in the XPS analysis of **NCD-1**. **(g,h,i)** HRTEM images of **NCD-1**. **(j,k)** AFM images of **NCD-1**. **(l)** N_2 adsorption isotherm at 77 K and CO_2 adsorption isotherm at 273 K for **NCD-1**. **(inset)** Pore size distribution of **NCD-1**.

integration of the XPS spectra, we arrive at the molecular formula $C_{6.3}N_{0.84}O_{1.6}$, with the percentage of C = 75.4%, N = 11.74% and O = 12.85%. As-synthesized **NCD-1** forms a stable dispersion in water owing to the solvation of the polar oxygen functional groups (C=O and –OH) present on the surface. The TEM images of **NCD-1** provide rather remarkable images with a uniform distribution of spherical N-doped carbon dots throughout the sample (**Fig. 3(g, h, i)**). The diameter of each dot measured is well below 10 nm. HRTEM of **NCD-1** shows the graphitic lattice fringes with an inter-planar distance of 0.34 nm (**Fig. 3(i)**). This is in accordance with the graphitic peak observed in the related PXRD measurement with the inter-planar distance of 0.362 nm (**Fig. 3(a)**). Moreover, AFM shows that the average height of the particles is about ~10 nm (**Fig. 3 (j,k)**), implying that each particle comprises ~30 graphitic planes stacked together. The porous properties of **NCD-1** were also investigated. **NCD-1** adsorbs 120 mL g^{-1} of N_2 at 77 K and the BET surface area is calculated to be 95 $m^2.g^{-1}$ (**Fig. 3(l)**). The relatively low surface area of **NCD-1** can be attributed to the graphitic stacking.[38,39] The pore size distribution shows that the sample comprises both meso- and micropores and most of the pores have diameters of 1.8, 2.5 and 4 nm (**Fig. 3(l) inset**). The CO_2 adsorption capacity of **NCD-1** was measured and it shows a CO_2 uptake of 46 mL g^{-1} at 273 K (**Fig. 3(l)**). Nitrogen doping to the carbon matrix facilitates the formation of interesting electron rich surfaces leading to remarkable optical and catalytic properties. With this in mind, we measured the optical band gap of **NCD-1** from the reflectance spectrum using the Kubelka-Munk function, which is 1.95 eV, and hence lower than the optical band gap of conventionally synthesized g-C_3N_4 (2.7 eV) (**Fig. S10**).[38] This implies that theoretically **NCD-1** can utilize all light with a wavelength below 640 nm. Hence, **NCD-1** may be an interesting material for photocatalytic applications. The aqueous dispersion of **NCD-1** shows an absorbance band at ~205 nm (**Fig. 4(a)**), attributed to the $\pi \rightarrow \pi^*$ transition of the conjugated C=C of the aromatic core. The absorption band has a long tail that extends up to ~260 nm owing to the multiple functional groups (e.g., C=O, C=N, etc.) that absorb over a wide range of wavelengths. The aqueous dispersion of **NCD-1** exhibits a bright blue luminescence under an UV lamp (**Fig. 4(a) inset**). Upon excitation at 240 nm, the emission band is centred at 402 nm. By gradually increasing the excitation wavelength, the emission peak is red shifted as

reported for most N-doped carbon dots.[29-31] The unusual excitation wavelength-dependent emission behaviour of **NCD-1** manifests a spectrally broad fluorescence emission (**Fig. 4(b)**). We conjecture that the wide range of functional groups present on the surface of **NCD-1** (e.g., C=O, C=N, NH$_2$, etc.) are responsible for this excitation-dependent emission, since these moieties form multiple emissive traps each of which control the emission at different excitation wavelengths.[29-31]

3B.3.3 NCD-1 and Co doped NCD-1 in ORR Catalysis

Due to the structural and compositional features of **NCD-1** and its analogy with g-C$_3$N$_4$, which is known to show good activity as a catalyst for oxygen reduction reaction (ORR),[10, 41] we expected **NCD-1** to act as metal free electrocatalyst for ORR. The electrocatalytic activity of **NCD-1** towards ORR was investigated by cyclic voltammetry in 0.1 M KOH solution with a catalyst loading of 198 µg cm^{-2}. As shown in **Fig. 4(d)**, a cathodic peak at 0.53 V was observed in Ar-saturated KOH solution. In contrast, when the electrolyte was saturated with O$_2$, the cathodic peak potential shifted to 0.58 V, with significantly enhanced peak currents. Linear sweep voltammetry at different rotation speeds is shown in **Fig. 4(e)**. **NCD-1** exhibits moderate catalytic performance for ORR. It has been shown previously that the incorporation of transition-metal residues into nitrogen-doped carbon (CN)
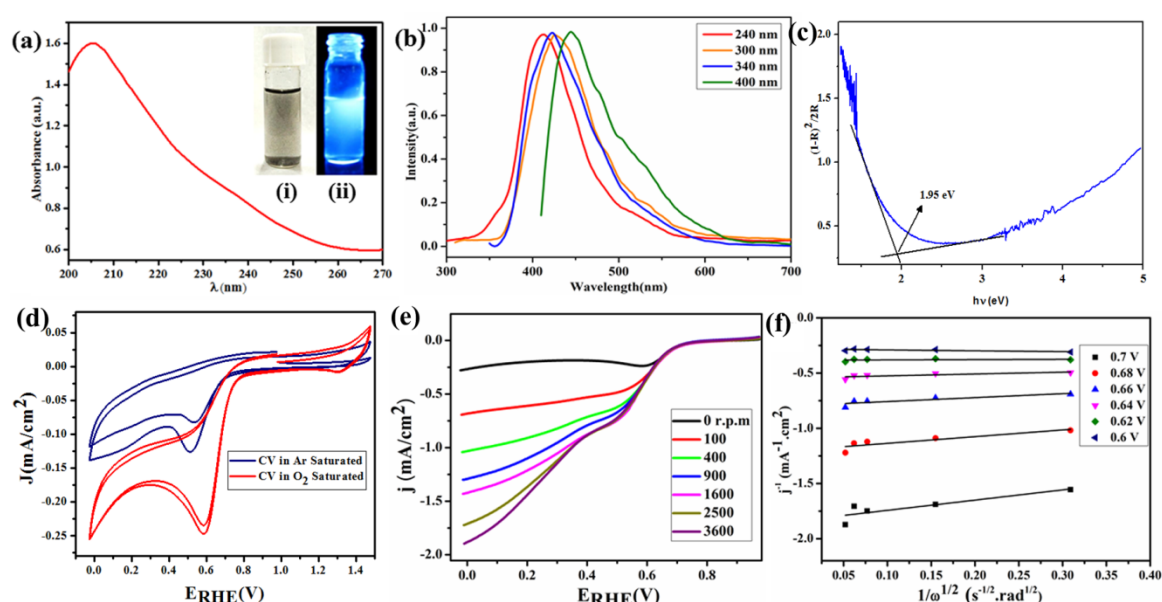
Fig. 4(a) UV-vis spectrum of **NCD-1** (**inset**) Dispersion of **NCD-1** in water. (**i**) Under normal light and (**ii**) under a UV lamp. (**b**) Emission spectrum of **NCD-1** excited at different wavelengths. (**c**) Band gap calculation of **NCD-1** from Kubelka-Munk function. (**d**) CV of **NCD-1**. (**e**) LSV of NCD-1. (**f**) Koutecky–Levich plot derived from the LSV measurements of **NCD-1**.

catalysts largely influences the ORR activity[42-44] owing to the electronic interaction between the metal nanoparticles and graphitic carbon,[8] which accelerates the kinetics of the ORR. Considering this, Co-metal residues were doped into **NCD-1** by mixing it with Co-porphyrin and pyrolyzing the mixture at 800° C to produce **Co@CN**. The PXRD pattern of the obtained **Co@CN** shows a broad and intense characteristic graphitic peak at $2\theta = 25°$ along with a small peak at $2\theta = 43.5°$,
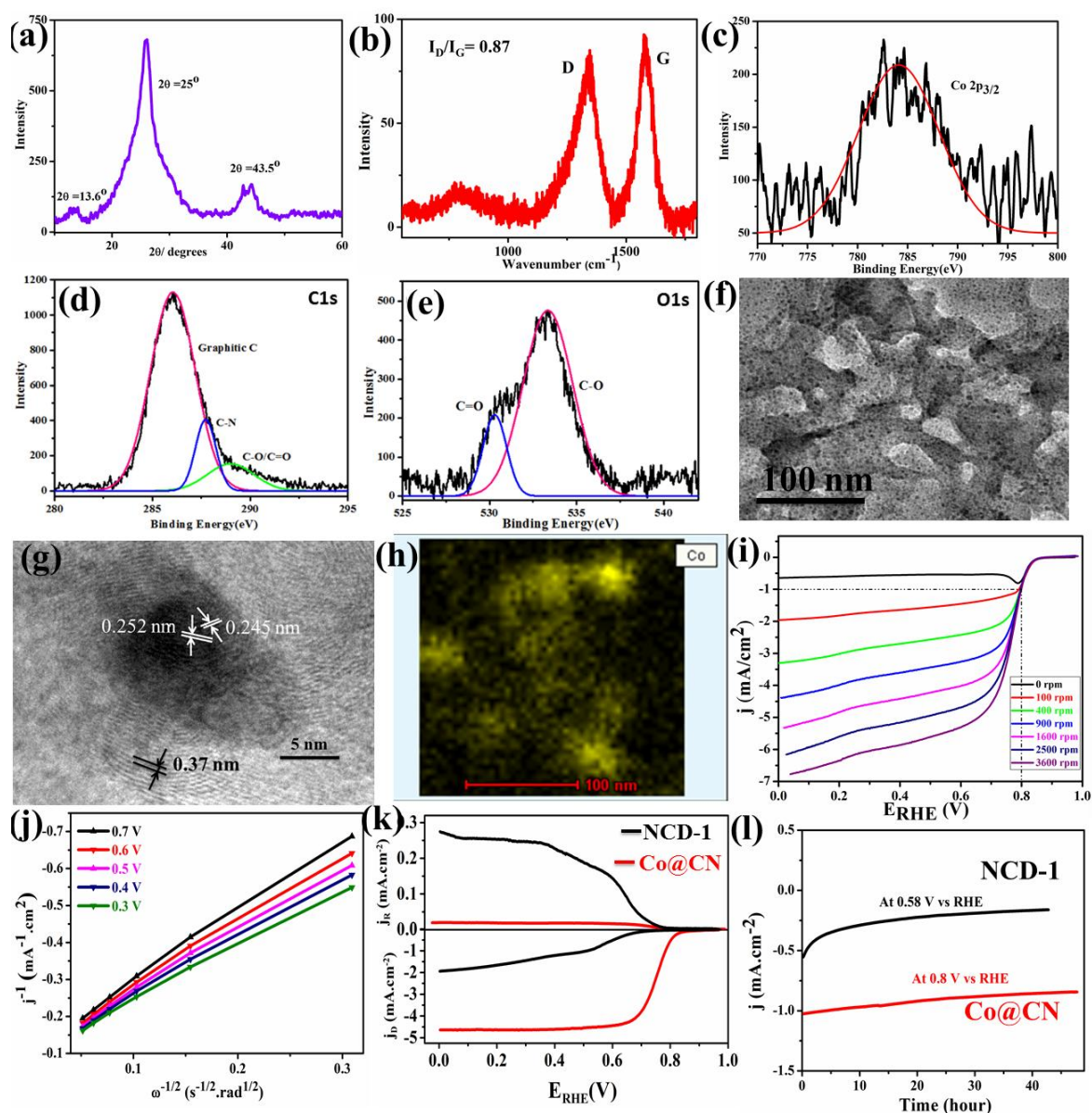
Fig. 5(a) PXRD pattern of **Co@CN**. **(b)** Raman spectrum of **Co@CN**. **(c)** Co2p, **(d)** C1s and **(e)** O1s spectra in the XPS analysis of **Co@CN**. **(f,g)** TEM images of **Co@CN**. **(h)** Co in the elemental colour mapping of **Co@CN**. **(i)** ORR RDE voltammograms recorded at 5 mV/s with **Co@CN** at different rotation speeds. **(j)** Koutecky-Levich plots, ω is the angular rotation speed. **(k)** RRDE voltammograms collected at 5 mV/s and 1600 rpm showing the ORR in 0.1 M KOH at the disk (i_D) and the oxidation of H_2O_2 at the ring (i_R) polarized at 0.4 V for **NCD-1** and **Co@CN**. **(l)** Chronoamperometric response for **NCD-1** at 0.58 V and **for Co@CN** at 0.8 V during durability test.

indicative of the *fcc* phase of Co. A small peak at $2\theta = 13.6°$ is suggestive of the arrangement of the tris-*s*-triazine units in carbon nitride (**Fig. 5(a)**) which remains intact after Co doping. However, it is much weaker than in the case of **NCD-1**, which is an indication of increased disorder. Furthermore, Raman spectroscopy shows the typical graphitic D and G bands at 1343 and 1580 cm^{-1} (I_D/I_G ratio = 0.87) along with a peak at 794 cm^{-1} corresponding to metallic Co nanoparticles (**Fig. 5(b)**). The XPS analysis of the Co 2p spectrum of **Co@CN** shows a peak centred at 783 eV, corresponding to the binding energy of Co 2p$_{3/2}$ (**Fig.5(c)**). The C1s spectrum shows peaks for graphitic carbon (286 eV), C=N (287 eV) and C-O/C=O (289 eV) (**Fig. 5(d)**), suggesting that metallic Co nanoparticles are embedded in a matrix of graphitic carbon nitride. This has been further ascertained from TEM analysis, which displays Co nanoparticles with diameters of less than 5 nm embedded in a carbon matrix (**Fig. 5(f)**). The lattice spacing of the nanoparticles is ~0.24 nm, which corresponds to *fcc* Co, whereas the background carbon showed a *d* spacing of 0.37 nm, characteristic of a graphitic material (**Fig.5(f,g)**). The elemental colour mapping shows Co particles uniformly distributed within a matrix of carbon and nitrogen (**Fig. S13**). ICP analysis reveals that **Co@CN** contains about 1.5 wt% of Co.

Notably, a considerable difference is observed between the ORR activity of **NCD-1** and **Co@CN**. LSV clearly indicates a significantly enhanced cathodic current as a function of rotation rate. Most remarkably, the ORR current density of **Co@CN** was enhanced at all potentials as compared to that of **NCD-1** (**Fig. 5(f)** and **Fig. 4(c)**). **Co@CN** exhibited remarkable catalytic performance for ORR affording a current density of -1 mA cm^{-2} at low overpotentials (~0.8 V) as compared to **NCD-1** (~0.36 V). Furthermore, upon comparing the catalytic activity of **Co@CN** with commercial Pt/C as reference catalyst, a close ORR activity was observed (**Fig 6(c)**) In fact, our results are well consistent with previously reported studies on metal residues that can significantly affect the electrocatalytic properties of the NC catalysts[45, 46], thus highlighting the role of Co on the ORR activity of nitrogen-modified carbon catalysts.[50-53] The activities of different amounts of Co doped CN are shown in **Fig. 6(d)**, which suggests that further increase in the amount of Co would not help in improving the catalytic activity. The Tafel plot was constructed by polarising the electrode at a low scan rate of 1 mV s^{-1} and at a

rotation speed of 1600 rpm. At lower current densities a Tafel slope of 63 mV dec^{-1} was measured, while a higher Tafel slope of 141 mV dec^{-1} is observed at higher current densities, indicating that the electrocatalytic activity is enhanced in the presence of Co nanoparticles as compared to **NCD-1**, which exhibits overall higher Tafel slopes (**Fig. 6(a.b)**). The corresponding Koutecky-Levich plot (j^{-1} vs ω$^{-1/2}$) showed linear nature and the calculated number of electrons transferred during the ORR is ~3.87 (**Fig. 5(g)**). Additionally, the influence of Co nanoparticles on the ORR activity was investigated with respect to the generation of H$_2$O$_2$ using RRDE voltammetry (**Fig. 5(h)**). The amount of H$_2$O$_2$ decreased from 40.8% for **NCD-1** to 2.3% for **Co@CN**. Evidently, the metallic Co nanoparticles encapsulated by the N-doped carbon matrix play an important role in promoting the ORR and significantly influence the selectivity of the ORR reaction. The metallic cobalt sites can participate in the electrocatalytic process actively, or may also have indirect involvement. In the present study we believed that the N-modified carbon moieties catalyze the reduction of O$_2$ to H$_2$O$_2$ while metallic cobalt particles catalyze the decomposition of the formed H$_2$O$_2$.[49] To assess the catalytic stability, the catalysts
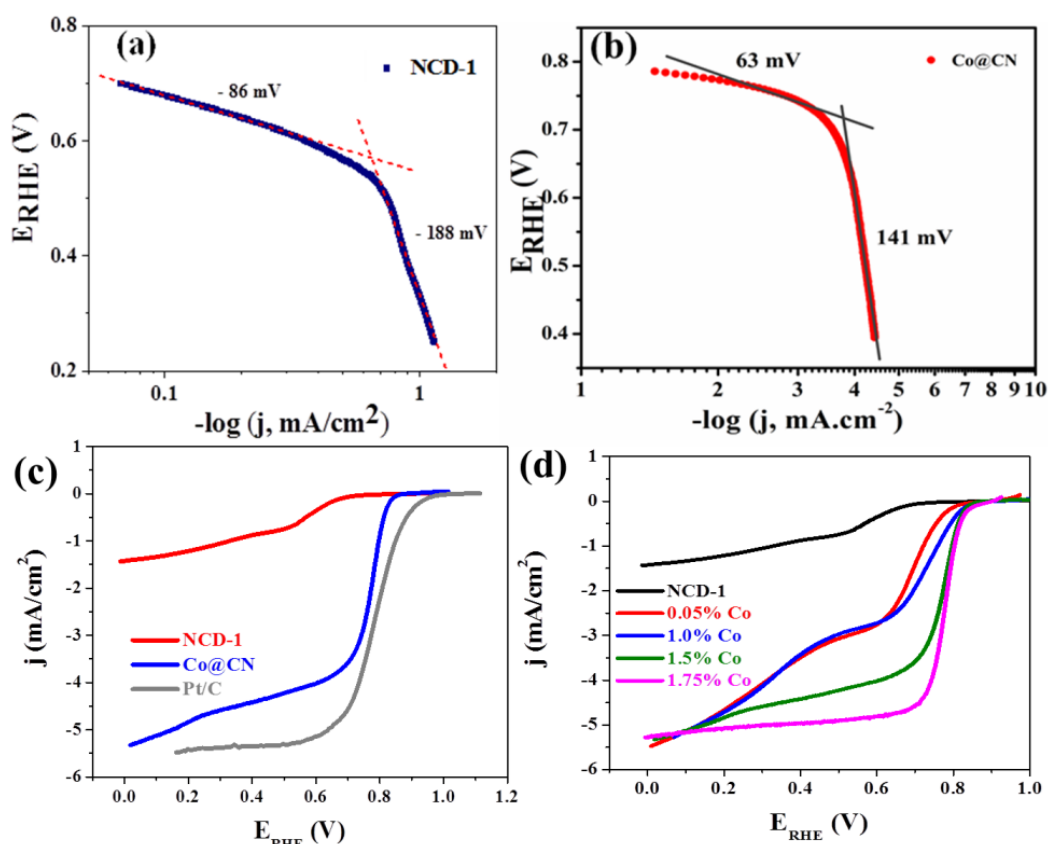
Fig. 6 Tafel plots for **(a) NCD-1** and **(b) Co@CN**. **(c)** Comparison of ORR activity of **Co@CN** with Pt/C. **(d)** ORR voltammograms recorded at 5 mV/s with **Co@CN** at different Co residues with 1600 rpm.

were compared by means of chronopotentiometric electrolysis at a constant voltage (vs RHE), 0.58V for **NCD-1** and 0.8V for **Co@CN** for at least 48 h at a rotation speed of 1600 rpm. **Fig 5(i)** demonstrates the excellent stability of **NCD-1** and **Co@CN** in alkaline solution during the ORR. Catalytic ORR activity of **Co@CN** is comparable with other N-doped carbon materials (**Table 1**) and can be further improved by doping different metals or by specific functionalization, which is currently being investigated in our lab.

Table 1 Comparison of ORR activity of different Co doped N doped C materials in alkaline media

Material	Co doping %	Over-potential values at -1 mA/cm^2 (V vs RHE)	Reference
Co@CN	1.5 wt%	~0.8 V	
Co₃O₄/rmGO	20 wt%	~0.85 V	50
Co-N-C800	5 wt%	~0.82 V	51
Co-N-C900	0.68 wt%	~0.8 V	52
MnCo₂O₄/N-rmGO	65-80 wt% of MnCo₂O₄	~0.81 V	53

3B.4 Conclusions

Both nanoporous carbon and N-doped carbon dots have been synthesized from a single AMOF using a simple and unique synthetic procedure exploiting its extra-framework guest cation without the use of any external precursor. **NPC-1** exhibits a very high surface area of 3690 m^2 g^{-1} with a high CO_2 uptake. **NCD-1** not only manifests a remarkable spherical morphology with unique optical properties, but also acts as an electrocatalyst for ORR with reasonable activity. Moreover, incorporation of metallic Co nanoparticles (1.5 wt%) in the N-doped carbon matrix of **NCD-1** revealed excellent electrocatalytic ORR activity as well as stability. The higher activity can be attributed mainly to the improved electronic interaction between metallic Co and the N-doped graphitic carbon matrix. The facile and dual strategy demonstrated here to prepare two different nanoporous materials from a single MOF-template without using any precursors is unprecedented and opens up a new platform for developing highly active MOF-derived electrocatalysts.

3B.5 References

1. S. Chatterjee, K. Sengupta, S. Hematian, K. D. Karlin and A. Dey, *J. Am. Chem. Soc.*, 2015, **137**, 12897.

2. B. Y. Xia, Y. Yan, N. Li, H. B. Wu, X. W. Lou and X. Wang, *Nat. Energy*, 2016, **1**, 15006.

3. W. Chaikittisilp, K. Ariga and Y. Yamauchi, *J. Mater. Chem. A*, 2013, **1**, 14.

4. S. M. Saufi and A. F. Ismail, *Carbon*, 2004, **42**, 241.

5. S. J. Yang, H. Jung, T. Kim and C. R. Park, *Prog. Nat. Sci. Mater. Int.*, 2012, **22**, 631.

6. P. Pachfule, V. M. Dhavale, S. Kandambeth, S. Kurungot and R. Banerjee, *Chem. Eur. J.*, 2013, **19**, 974.

7. R. Silva, D. Voiry, M. Chhowalla and T. Asefa, *J. Am. Chem. Soc.*, 2013, **135**, 7823.

8. L. Wang, A. Ambrosi and M. Pumera, *Angew. Chem. Int. Ed.*, 2013, **52**, 13818.

9. Y. Liu, H. Jiang, Y. Zhu, X. Yang and C. Li, *J. Mater. Chem. A*, 2016, **4**, 1694.

10. S. Pandiaraj, H. B. Aiyappa, R. Banerjee and S. Kurungot, *Chem. Commun.*, 2014, **50**, 3363.

11. G. Kumar and S. K. Das, *Inorg. Chem. Front.*, 2017, **4**, 202.

12. S. Bhattacharyya, A. Chakraborty, K. Jayaramulu, A. Hazra and T. K. Maji, *Chem. Commun.*, 2014, **50**, 13567.

13. A. Chakraborty, S. Bhattacharyya, A. Hazra, A. C. Ghosh and T. K. Maji, *Chem. Commun.*, 2016, **52**, 2831.

14. B. Liu, H. Shioyama, T. Akita and Q. Xu, *J. Am. Chem. Soc.*, 2008, **130**, 5390.

15. K. Jayaramulu, K. K. R. Datta, K. Shiva, A. J. Bhattacharyya, M. Eswaramoorthy and T. K. Maji, *Micropor. Mesopor. Mater.*, 2015, **206**, 127.

16. D. Yuan, J. Chen, S. Tan, N. Xia and Y. Liu, *Electrochem. Commun.*, 2009, **11**, 1191.

17. J. Hu, H. Wang, Q. Gao and H. Guo, *Carbon*, 2010, **48**, 3599.

18. K. Jayaramulu, N. Kumar, A. Hazra, T. K. Maji and C. N. R. Rao, *Chem. Eur. J.*, 2013, **19**, 6966.

19. P. Zhang, F. Sun, Z. Xiang, Z. Shen, J. Yun and D. Cao, *Energy Environ. Sci.*, 2014, **7**, 442.

20. A. Aijaz, N. Fujiwara and Q. Xu, *J. Am. Chem. Soc.*, 2014, **136**, 6790.

21. A.-M. Alexander and J. S. J. Hargreaves, *Chem. Soc. Rev.*, 2010, **39**, 4388.

22. J. Liu, Y. Liu, N. Liu, Y. Han, X. Zhang, H. Huang, Y. Lifshitz, S.-T. Lee, J. Zhong and Z. Kang, *Science*, 2015, **347**, 970.

23. X. Wang, K. Maeda, A. Thomas, K. Takanabe, G. Xin, J. M. Carlsson, K. Domen and M. Antonietti, *Nat. Mater.*, 2009, **8**, 76.

24. V. W.-h. Lau, I. Moudrakovski, T. Botari, S. Weinberger, M. B. Mesch, V. Duppel, J. Senker, V. Blum and B. V. Lotsch, *Nat. Commun.*, 2016, **7**, 12165.

25. L. Feng, L. Yang, Z. Huang, J. Luo, M. Li, D. Wang and Y. Chen, *Sci. Rep.*, 2013, **3**, 3306.

26. K. Qiu and Z. X. Guo, *J. Mater. Chem. A*, 2014, **2**, 3209.

27. S. Khan, N. C. Verma, A. Gupta and C. K. Nandi, *Sci. Rep.*, 2015, **5**, 11423.

28. H. Li, Z. Kang, Y. Liu and S.-T. Lee, *J. Mater. Chem.*, 2012, **22**, 24230.

29. A. J. Amali, H. Hoshino, C. Wu, M. Ando and Q. Xu, *Chem. Eur. J.*, 2014, **20**, 8279.

30. Y.-F. Kang, Y.-W. Fang, Y.-H. Li, W. Li and X.-B. Yin, *Chem. Commun.*, 2015, **51**, 16956.

31. F. Arcudi, L. Đorđević and M. Prato, *Angew. Chem. Int. Ed.*, 2016, **55**, 2107.

32. Y. Xu, M. Wu, Y. Liu, X.-Z. Feng, X.-B. Yin, X.-W. He and Y.-K. Zhang, *Chem. Eur. J.*, 2013, **19**, 2276.

33. L. Wang and H. S. Zhou, *Anal. Chem.*, 2014, **86**, 8902.

34. Z. Yang, M. Xu, Y. Liu, F. He, F. Gao, Y. Su, H. Wei and Y. Zhang, *Nanoscale*, 2014, **6**, 1890.

35. B. J. Moon, Y. Oh, D. H. Shin, S. J. Kim, S. H. Lee, T.-W. Kim, M. Park and S. Bae, *Chem. Mater.*, 2016, **28**, 1481.

36. M. Hu, J. Reboul, S. Furukawa, L. Radhakrishnan, Y. Zhang, P. Srinivasu, H. Iwai, H. Wang, Y. Nemoto, N. Suzuki, S. Kitagawa and Y. Yamauchi, *Chem. Commun.*, 2011, **47**, 8124.

37. Y. Liu, G. Li, X. Li and Y. Cui, *Angew. Chem.*, 2007, **119**, 6417.

38. J. An, S. J. Geib and N. L. Rosi, *J. Am. Chem. Soc.*, 2009, **131**, 8376.

39. M. Hu, J. Reboul, S. Furukawa, N. L. Torad, Q. Ji, P. Srinivasu, K. Ariga, S. Kitagawa and Y. Yamauchi, *J. Am. Chem. Soc.*, 2012, **134**, 2864.

40. J. Zhu, P. Xiao, H. Li and S. A. C. Carabineiro, *ACS Appl. Mater. Interfaces*, 2014, **6**, 16449.

41. A. Thomas, A. Fischer, F. Goettmann, M. Antonietti, J.-O. Muller, R. Schlogl and J. M. Carlsson, *J. Mater. Chem.*, 2008, **18**, 4893.

42. H. Xu, J. Yan, X. She, L. Xu, J. Xia, Y. Xu, Y. Song, L. Huang and H. Li, *Nanoscale*, 2014, **6**, 1406.

43. Q. Liu and J. Zhang, *Langmuir*, 2013, **29**, 3821.

44. J. Masa, A. Zhao, W. Xia, Z. Sun, B. Mei, M. Muhler and W. Schuhmann, *Electrochem. Commun.*, 2013, **34**, 113.

45. B. Šljukić, C. E. Banks and R. G. Compton, *Nano Lett.*, 2006, **6**, 1556.

46. C. E. Banks, A. Crossley, C. Salter, S. J. Wilkins and R. G. Compton, *Angew. Chem. Int. Ed.*, 2006, **45**, 2533.

47. Y. Li, W. Zhou, H. Wang, L. Xie, Y. Liang, F. Wei, J.-C. Idrobo, S. J. Pennycook and H. Dai, *Nat. Nano*, 2012, **7**, 394.

48. J.-S. Lee, G. S. Park, S. T. Kim, M. Liu and J. Cho, *Angew. Chem. Int. Ed.*, 2013, **52**, 1026.

49. T. S. Olson, S. Pylypenko, J. E. Fulghum and P. Atanassov, *J. Electrochem. Soc.*, 2010, **157**, B54.

50. Y. Liang, Y. Li, H. Wang, J. Zhou, J. Wang, T. Regier, H. Dai, Nat. Mater., 2014, 10, 780.

51. Y. Qian, Z. Liu, H. Zhang, P. Wu, C. Cai, C., *ACS Appl. Mater. Interfaces,* 2016, **8**, 32875.

52. C. Guo, Y. Wu, Z. Li, W. Liao, L. Sun, C. Wang, B. Wen, Y. Li. C. Chen, *Nanoscale Res. Lett.*, 2017, **12**, 1.

53. Y. Liang, H. Wang, J. Zhou, Y. Li, J. Wang, T. Regier, H. Dai, *J. Am. Chem. Soc.*, 2012, **134**, 3517.

Chapter 4A

Post-synthetic Metalation in an Anionic MOF for Efficient Catalysis and Heavy Metal Removal
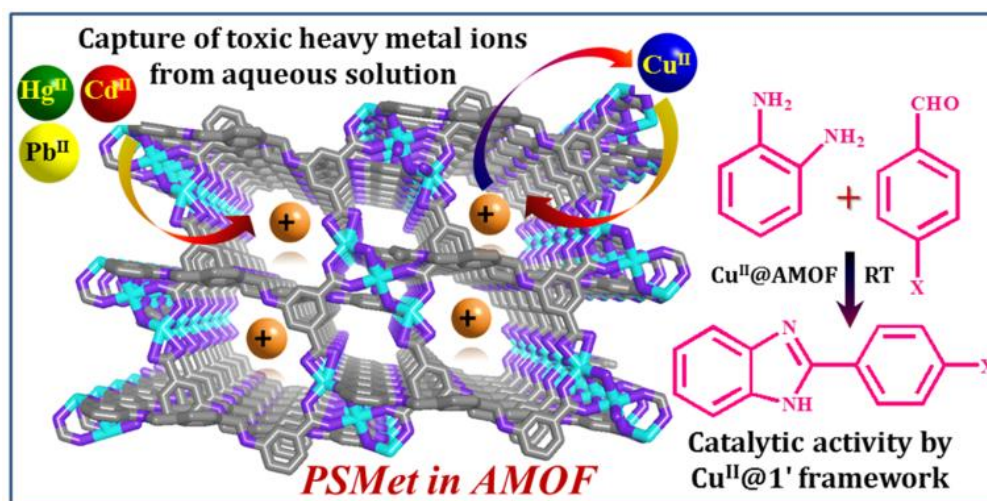
Abstract

This chapter describes the synthesis of a 3D flexible anionic metal-organic framework (AMOF) $\{[(NH_2Me_2)_2][Zn_3(L)_2]\cdot 9H_2O\}$ (**AMOF-1**) utilizing Zn^{II} and a flexible aromatic tetracarboxylic acid ligand (L). Exceptional water stability and the large pores of **AMOF-1** prompted us to check its heavy metal ions removal capacity from water. **AMOF-1** showed exceptional potential for capture and removal of toxic metal ions like Pb^{II}, Cd^{II} and Hg^{II} from aqueous solution with a detection limit in the ppm level. Similarly, Cu^{II} is sequestered within **AMOF-1** by immersing it in a solution of Cu^{II}. The **Cu^{II}@AMOF-1** hybrid thus obtained by post-synthetic metalation showed excellent activity as a heterogeneous catalyst for the synthesis of various benzimidazole derivatives.

4A.1 Introduction

The extraordinary modular nature of metal–organic frameworks (MOFs)[1] allows post-synthetic modification (PSM) of the pristine framework to furnish novel properties.[2-7] In this regard, anionic MOFs (AMOFs)[8-14] are particularly interesting since their nanopores can be modified using a simple ion-exchange process. However, their tunability gives them an edge over conventional ion-exchangers like zeolites.[15] Through post-synthetic metalation[16] (PSMet, a subset of the PSM approach), AMOFs can be functionalized suitably for targeted actions via the encapsulation of exogenous metal ions, e.g. sensitization of lanthanide ions,[17] capture of toxic heavy metal pollutants from liquid phase waste[18-19] or immobilization of highly Lewis acidic metal sites for catalysis. The focus of this study is to exploit an AMOF for such applications (**Scheme 1**). Environmental pollution by heavy metals like Pb^{II}, Cd^{II} and Hg^{II} is a major threat to human health which continues to increase with rapid industrialization. Thus effective capture and removal of these heavy metal ions from water is of utmost importance.[20-23] Although porous solids like activated carbon have been traditionally used to adsorb heavy metal ions, the higher flexibility and structural diversity in MOFs led us to envisage that a suitable AMOF will be much more effective for this purpose. Water stability along with a good detection limit, preferably in the parts per million (ppm) level,[23] should be the desired features of the AMOF for the efficient capture of heavy metal ions from their aqueous solution. To realize Lewis acidic catalytic activity in AMOFs, PSMet could be a promising approach where the resulting hybrid would contain unsaturated metal sites (UMSs)[24-28] in the desolvated state, as in general the pristine AMOF will not fulfil all the coordination sites of the encapsulated metal ions. Furthermore, based on the favourable interactions with the AMOF, the metal ions will be precisely positioned in the framework, thus they would not suffer from leaching during catalysis. The exchanged solid MOF being a heterogeneous catalyst also offers easy separation of catalyst from the reaction mixture.

In this context, the Cu^{II} exchanged AMOF as a Lewis acid catalyst was exploited as a heterogeneous for the synthesis of benzimidazole derivatives, which are important intermediates in different organic reactions[29] and are also essential for various medicinal applications including antiviral, antiulcer, antifungal, antihypertensive, anticancer and antihistamine activity.[30-32] In this chapter, the synthesis and structural characterization of a 3D flexible AMOF {[(NH$_2$Me$_2$)$_2$][Zn$_3$(L)$_2$]·9H$_2$O} (**AMOF-1**; L = 5,5'-(1,4- phenylene-
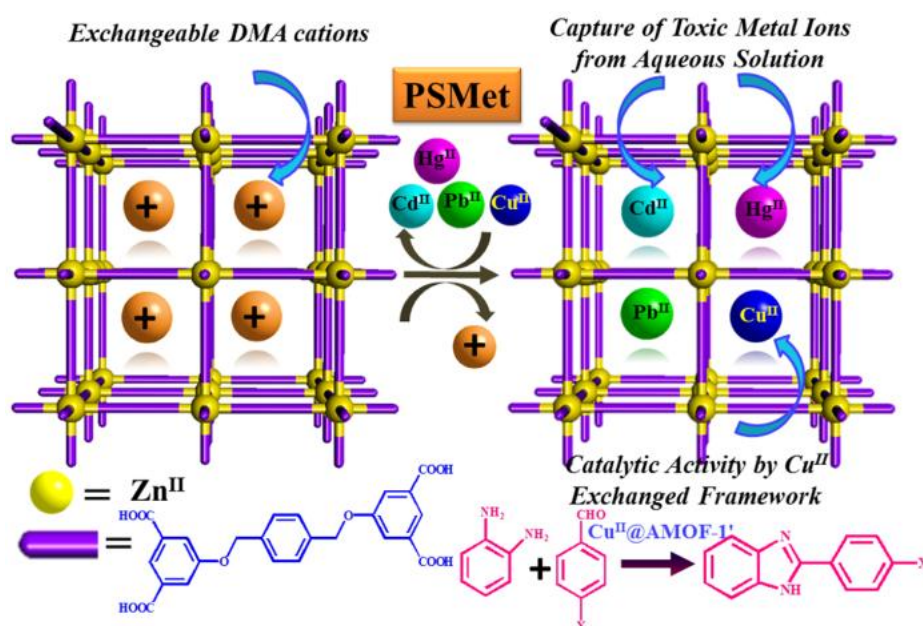
Scheme 1 Schematic representation of the **AMOF-1** and its applications to capture toxic heavy metal ions and Lewis acidic catalytic activity through PSMet.

bis(methylene))bis(oxy)diisophthalic acid) has been reported. **AMOF-1** has been exploited for capture and removal of toxic heavy metal ions from water with a detection limit in the ppm level. To the best of our knowledge, capture of toxic metal ions in the ppm level by an AMOF is unprecedented. Moreover, PSMet of **AMOF-1'** (desolvated **AMOF-1**) with Cu^{II} results in a **Cu^{II}@AMOF-1'** hybrid which is studied as a catalyst for the synthesis of benzimidazole derivatives.

4A.2 Experimental Section

4A.2.1 Materials

All the reagents and solvents employed were commercially available and used as supplied without further purification. Dimethyl-5-hydroxy isophthalate, α,α'-dibromoparaxylene, dibenzo-18-crown-6, and $Zn(NO_3)_2 \cdot 6H_2O$ were obtained from Aldrich Chemical Co.

4A.2.2 Synthesis of 5,5'-(1,4-phenylenebis(methylene))bis(oxy)diiso-phthalate

A mixture of dimethyl-5-hydroxy isophthalate (2.1 g, 10.0 mmol), α,α' dibromo paraxylene (1.31 g, 4.96 mmol), Dibenzo-18-crown-6 (0.277 mmol) and K_2CO_3 (2.21g, 16 mmol) were stirred in dry THF (40 ml) at 70 °C for 24 hours. After this stirring, 20 ml

of 10 % aqueous Na$_2$CO$_3$ solution was added at 0 °C under an ice bath. The resulting white solid was filtered and washed with water for several times and finally with diethyl ether and dried under vacuum. Yield: 97% relative to dibromo paraxylene. ^{1}H NMR (400 MHz, CDCl$_3$): δ (in ppm): 8.29 (s, 2H), 7.83 (s, 4H), 7.48 (s, 4H), 5.16 (s, 4H), 3.93 (s, 12H).

4A.2.3 Synthesis of 5,5'-(1,4-phenylenebis(methylene))bis(oxy)diiso-phthalic acid (L)

A mixture of 5,5′-(1,4-phenylenebis(methylene))bis(oxy)diisophthalate (2mmol), KOH (20 mmol), 40 ml MeOH and 40 ml distilled water were stirred at 80 °C in oil bath for 24 hours. The reaction mixture was filtered to remove any unreacted starting materials and 30 ml 6 M HCl was added dropwise to filtrate at 0 °C under stirring. The white precipitate was filtered and washed with distilled water for several times and dried under vacuum. ^{1}H NMR (400 MHz, DMSO-d_6): δ = 13.29 (br, 4H), 8.05 (s, 2H), 7.69 (s, 4H), 7.47 (s, 4H), 5.21 (s, 4H).
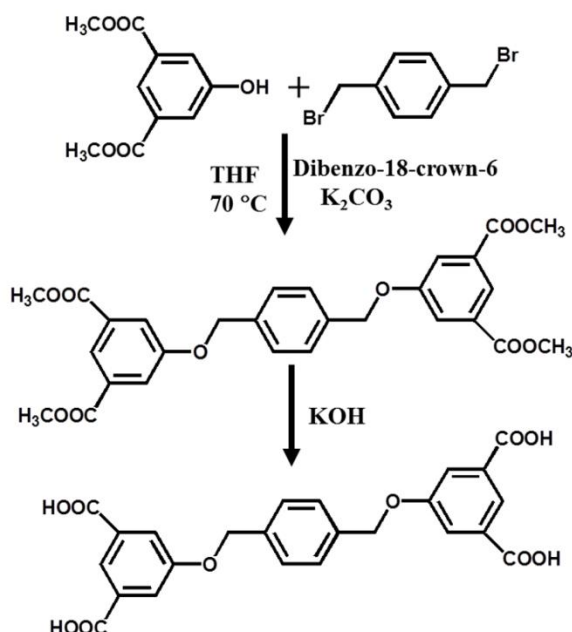
Scheme 2 Reaction scheme for the ligand (L) synthesis.

4A.2.4 Synthesis of {[(NH$_2$Me$_2$)$_2$][Zn$_3$(L)$_2$].9H$_2$O} (AMOF-1)

Zn(NO$_3$)$_2$.6H$_2$O (0.2 mmol) and L (0.1 mmol) were dissolved in DMF (6 ml), ethanol (3 ml) and distilled water (5 ml) in a 23 mL Teflon-lined stainless steel autoclave and was stirred for 30 minutes. The autoclave was sealed and was kept in an oven at 80 °C for 96 h. After completion of the reaction, the reactor was cooled at RT for 12 h.

Colourless crystalline product was collected by filtration. Elemental analysis shows the following result: C, 45.52; H, 3.89; N, 2.13. Indeed, the observed values are close for $\{[(NH_2Me_2)_2][Zn_3(L)_2].9H_2O\}$ (cald: C, 45.68; H, 3.98; N, 2.04). Yield: 60 %, relative to Zn^{II}. The sample was characterised using IR spectroscopy (**Fig. 1**).
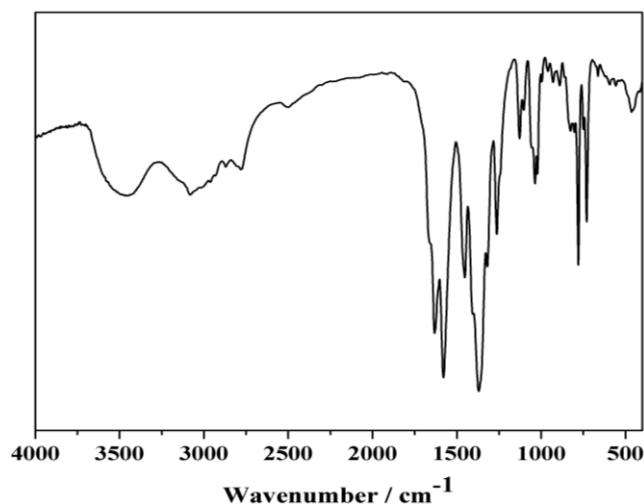
Fig. 1 FT-IR spectrum of **1**.

Table 1: Principal Peaks in IR (**Fig. 1(a)**)

Peak Position	Nature	Vibration
3460 cm^{-1}	broad	O-H stretch
1632 cm^{-1}	sharp	C=O stretch
1580 cm^{-1}	very sharp	C=C stretch
1036 cm^{-1}	medium	C-O stretch

4A.2.5 Physical measurements

^{1}H NMR data were measured on a Bruker AV-400 spectrometer with chemical shifts reported as ppm (TMS as internal standard). FTIR spectra were recorded on a Bruker IFS 66v/S spectrophotometer using KBr pellets in the region 4000-400 cm^{-1}. The elemental analysis was carried out using a Flash 2000 Organic Elemental Analyzer. Thermogravimetric analysis (TGA) was carried out on METTLER TOLEDO TGA850 instrument in the temperature range of 30 - 600 °C under nitrogen atmosphere (flow rate of 50 mL/min) at a heating rate of 5 °C/min. Powder X-ray diffraction (PXRD) patterns were recorded on a Bruker D8 Discover instrument using Cu-Kα radiation. Inductively Coupled Plasma-Optical Emission Spectroscopy (ICP-OES) measurements were recorded on Perkin Elmer Optima 7000dv ICP-OES instrument.

4A.2.6 Adsorption measurements

Adsorption isotherms of CO_2 and N_2 were recorded at 195 K and 77 K respectively with the dehydrated samples using QUANTACHROME QUADRASORB-SI analyser. To prepare the desolvated samples of **AMOF-1** (**AMOF-1′**) approximately 70 mg of sample was taken in a sample holder and degassed at 160 ℃ under 10^{-1} pa vacuum for about 8 hours prior to the measurements. Dead volume of the sample cell was measured with helium gas of 99.999% purity. The H_2O adsorption isotherms were measured at 298 K in the gaseous state by using BELSORP-aqua-3 analyzer. The different solvent molecules used to generate the vapour were degassed fully by repeated evacuation. All operations were computer controlled and automatic.

4A.2.7 Single Crystal X-ray Diffraction

A suitable single crystal of compound **AMOF-1** was mounted on a thin glass fiber with commercially available super glue. X-ray single crystal structural data were collected on a Bruker Smart-CCD diffractometer equipped with a normal focus, 2.4 kW sealed tube X-ray source with graphite monochromated Mo-Kα radiation (λ = 0.71073 Å) operating at 50 kV and 30 mA. The program SAINT[37] was used for the integration of diffraction profiles and absorption correction was made with SADABS[38] program. All the structures were solved by SIR 92[39] and refined by full matrix least square method using SHELXL.[40] All the hydrogen atoms were fixed by HFIX and placed in ideal positions. The solvent water molecules were highly disordered and hence could not be located. We have employed PLATON/SQUEEZE[41] to produce a set of solvent-free diffraction intensities; the structures were then refined again using the data generated. Potential solvent accessible area or void space was calculated using the PLATON[41] multipurpose crystallographic software. All crystallographic and structure refinement data of **1** is summarized in Table S1. All calculations were carried out using SHELXL 97,[40] PLATON,[41] SHELXS 97[40] and WinGX system, Ver 1.80.05.[42] Selected bond lengths and angles are displayed in Tables 3 and 4.

4A.2.8 Preparation of M^{II}@AMOF-1'

For preparing the different metal ion exchanged compounds, **AMOF-1** is activated at 160℃ under high vacuum overnight before immersing it in the respective metal ion solutions. 50 mg of activated **AMOF-1** (**AMOF-1'**) is immersed in 20 ml

0.01M M^{II} (where M is any transition metal/heavy metal cation) solutions in water and the solution is stirred for 24 hours and the solution is changed every 8 hours within these 24 hours. Then it is washed repeatedly with water to remove any unreacted metal solution. The exchanged solids thus obtained were then dried and Inductively Coupled Plasma Optical Emission Spectroscopy (ICP-OES) analyses were performed with the solids after decomposing them with acid. The % of inclusion of the exogenous metal ions (M^{II}) were calculated based on the relative ratio of Zn^{II} and M^{II}.

To know the maximum possible uptake capacity of the heavy metal ions by the desolvated AMOF, we have also carried out exchange for prolonged time (7 days). 50 mg of activated **AMOF-1** (**AMOF-1'**) is immersed in 20 ml 0.01M M^{II} (where M is the heavy metal cations) solutions in water and the solution is stirred for 7 days and the solution is changed daily (to ensure maximum uptake of the heavy metal ions). The exchanged solids thus obtained were then dried and ICP-OES analyses were performed with the solids after decomposing them with acid (Table S4). For Cu^{II} ion also, exchange experiment was carried out for 7 days. To understand the kinetics of heavy metal removal efficiency, we have immersed 20 mg of **AMOF-1'** in 20 ml aq. Hg^{II} (1 ppm) and the changes in conc. of Hg was measured over a period of time by using ICP-OES. The maximum heavy metal ion uptake capacity by **AMOF-1'** is calculated from the ICP-OES data analysis of metal exchanged solids obtained after 7 days of exchange experiments.

4A.2.9 Detection of dimethylammonium (DMA) cation released into solution by metal ion exchange

In order to verify that the metal inclusion in the AMOF occurs by cation exchange, we have performed cation exchange experiment in DMSO-d_6. For this **AMOF-1'** is suspended in a DMSO-d_6 solution of Cd^{II} for 10 days and the exchanged solution was analysed for DMA using NMR spectroscopy (diamagnetic and does not interfere in the NMR spectrum).

4A.2.10 Catalysis Study

The catalytic activity of the **Cu^{II}@AMOF-1'** was investigated in one-pot condensation reactions for the synthesis of benzimidazole derivatives by the reaction between *o*-phenylenediamine and different *p*-substituted benzaldehydes. A mixture of *o*-phenylenediamine (1 equivalent) and benzaldehyde (1 equivalent) and activated Cu^{II}@**1'** catalyst (0.05 mol%; the molecular weight of dehydrated Cu^{II}@AMOF-**1'** catalyst is

calculated based on the ICP data of Cu^{II}@**1'** while the activation is carried out at 120 °C under 10^{-1} pa vacuum for 8 hours) were taken in EtOH at RT and stirred for fixed time (monitored by TLC). After the reaction was completed, the solid catalyst was removed by filtration and the quantitative analysis of product conversion is monitored by GC-MS analyser. Time-dependant product formation was also monitored; in case of benzaldehyde (X= H) nearly 62% conversion was observed after 3 h, while after 6 h it is increased to 97%, suggesting that the conversion takes almost 6 h to complete. Catalytic recycling efficiency test of the **Cu^{II}@AMOF-1'** catalyst was carried out using *o*-phenylenediamine and benzaldehyde (X= H). After the 1st cycle of reaction, the catalyst was separated by filtration and the recovered catalyst was washed with EtOH thoroughly to remove any unreacted reagent. The recovered catalyst was dried in air and then activated at 120 °C under 10^{-1} pa vacuum for 8 hours to perform further reactions under identical conditions. The PXRD patterns of **Cu^{II}@AMOF-1'** samples after each cycle were recorded, which suggest that the structural integrity of the framework is maintained after each cycle.

4A.3 Results and Discussions

4A.3.1 Crystal Structure of AMOF-1

Single–crystal X–ray diffraction experiment reveals that **AMOF-1** crystallizes in the triclinic $P\bar{1}$ space group and the asymmetric unit contains three crystallographically independent hexa-coordinated Zn(II) centers, two linkers (L1
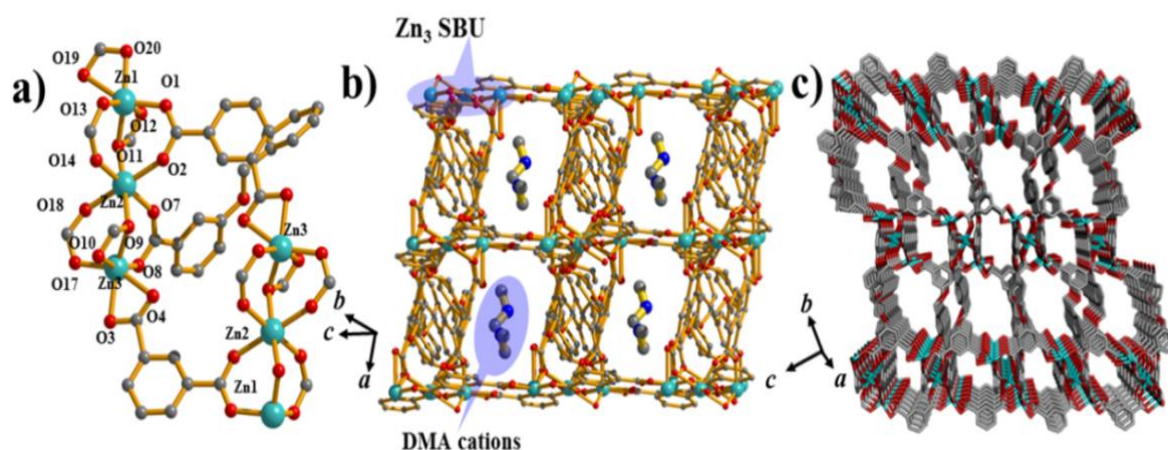
Fig. 2 (a) View of the coordination environment around Zn^{II} centers and the trinuclear SBU. Color Code: C: grey; Zn: cyan; O: red. **(b)** 3D framework with rectangular channel containing DMA cations. **(c)** View along crystallographic *a* direction showing biporous 3D framework with interconnected channels.

and L2) and two different dimethyl ammonium (DMA) cations. Three Zn^{II} centers in the anionic framework $[Zn_3(L)_2]$ are linked to each other through the carboxylate groups of the linker L. Zn1 and Zn2 are connected through different bridging bidentate carboxylate groups (O1, O2; and O13, O14 oxygen atoms) in *syn-syn* fashion. Zn1 and Zn2 are also bridged by μ_2-oxo bridging (O11 atom) from another carboxylate group. Zn2 and Zn3 are connected similarly (**Fig. 2(a)**). Such connections result in the formation of a trinuclear $[Zn_3(CO_2)_8]$ secondary building unit (SBU). Each of the linkers (L1 and L2) is connected to four $[Zn_3(CO_2)_8]$ SBUs and the dihedral angles between two terminal benzene rings of L1 and L2 are 79.8° and 73.9°, respectively (**Fig. 3(a)**). Such spatial orientation of the terminal benzene rings containing carboxylate groups eventually extends the SBUs along the crystallographic *ac* plane. The 2D networks lying in the *ac* plane are further bridged through two crystallographically different L linkers along the *b* direction resulting in a complex 3D framework structure (**Fig. 3(b)**). The framework along crystallographic *a* direction, two different channels can be seen which are circumvented by the phenyl rings (**Fig. 2(c)**). The smaller and the larger channels
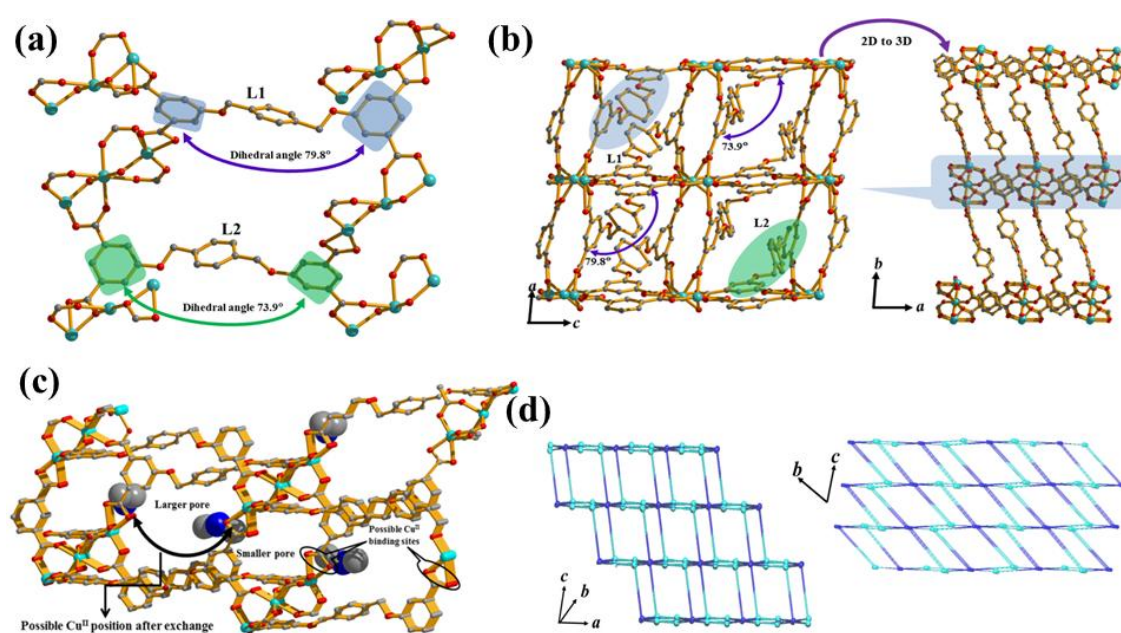
Fig. 3 (a) Connectivity of the four $[Zn_3(CO_2)_8]$ SBUs through L linkers. The spatial orientation of the terminal benzene rings of L1 and L2 are highlighted (dihedral angles between the terminal benzene rings of L1 and L2 are 79.8° and 73.5° respectively). **(b)** (**Left**) 2D network containing the $[Zn_3(CO_2)_8]$ SBUs connected through L linkers. (**Right**) Formation of the 3D framework from the 2D nets connected through L linkers along *b* direction. **(c)** View of the crystallographically different DMA cations residing near the junctions of the different channels. **(d)** Topology of the 2-nodal net of **AMOF-1**. Color Code: Ligand (L): cyan; trinuclear Zn_3 SBU: blue.

(pore dimensions are 2.7×2.2 Å^2 and 4.1×3.6 Å^2, respectively) are interconnected by the DMA cations containing channels (**Fig. 3(c)**). Topological analysis shows that **AMOF-1** is a 2-nodal net and has fluorite type topology with stoichiometry (4-c)2(8-c). The Schläfli symbol of the net is determined as $\{4^{12}.6^{12}.8^4\}\{4^6\}\{2\}$ (**Fig. 3(d)**). The solvent water molecules are highly disordered and hence could not be located crystallographically. The solvent accessible void space of the framework including the DMA cations is 27% of the total cell volume.

Table 2 Crystal Data and Structure Refinement for **AMOF**-1

Parameter	AMOF-1
Empirical formula	$C_{52}H_{44}Zn_3O_{20}N_2$
Formula weight	1213.06
Crystal system	*Triclinic*
Space group	$P\bar{1}$ (No.2) 9.4533(19)
a, Å	18.614(4)
b, Å	19.976(4)
c, Å	9.4533(19)
α, deg	18.614(4)
β, deg	19.976(4)
γ, deg	3223.2(13)
V, Å^3	2
Z	100
T, K	1.172
μ,mm^{-1}	0.147
*D*calcd,g/cm^3	1240
F (000)	5987
reflections [*I>2σ(I)*]	11141
unique reflections	21940
measured reflections	0.090
*R*int	1.06
GOF	0.1105
R$_1$[*I>2σ(I)*][a]	0.3304

$(R = \sum||F_o|-|F_c||/\sum|F_o|$,$R_w= [\sum\{w(F_o^2-F_c^2)^2\}/\sum\{w(F_o^2)^2\}]^{1/2})$

Table 3 Selected bond distances (Å) for **AMOF-1**.

Zn1-O12	2.563(8)	Zn1-O19	2.332(8)
Zn1-O13	1.983(7)	Zn1-O20_c	2.041(8)
Zn1-O1	1.977(8)	Zn1 -O11	2.004(8)
Zn2-O2	2.149(8)	Zn2-O9	2.254(8)
Zn2-O14	1.986(8)	Zn2-O11	2.151(8)
Zn2-O18	2.083(5)	Zn2-O7	2.000(8)
Zn3-O10	2.559(8)	Zn3-O9	2.051(8)

Table 4 Selected bond angles (°) of Compound **AMOF-1**.

O1 -Zn1-O11	100.6(3)	O11-Zn2-O18	90.9(3)
O1-Zn1-O12	86.6(3)	O9-Zn3-O10	55.6(3)
O11-Zn1-O19	94.9(3)	O11-Zn1-O13	109.1(3)
O7-Zn2-O18	97.8(3)	O11-Zn1-O12	55.8(3)
O7-Zn2-O9	84.5(3)	O1-Zn1-C48	125.0(3)

4A.3.2 Framework stability and adsorption
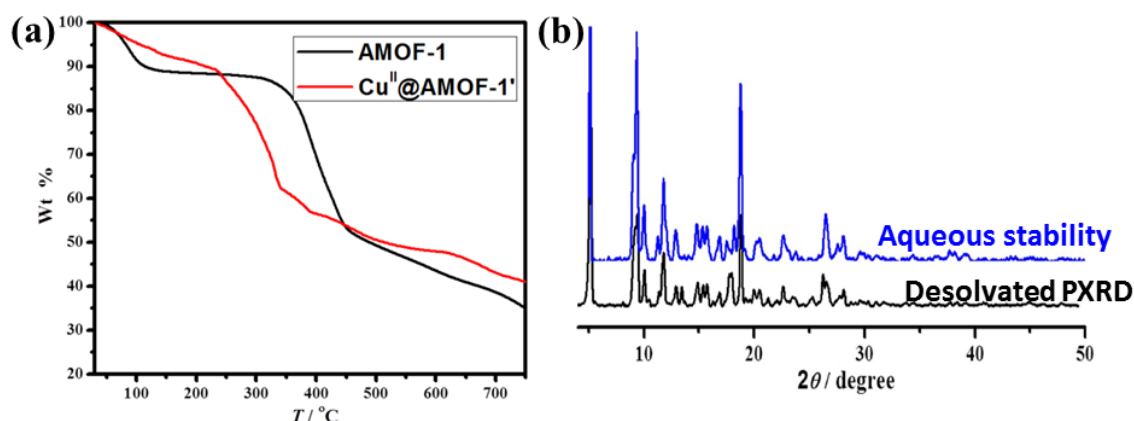
Fig. 4(a) TGA of **AMOF-1** and **Cu^{II}@AMOF-1**. (**b**) PXRD of pristine **AMOF-1** and after immersing it in water for 7 days.

Thermogravimetric analysis (TGA) shows a loss of 11% up to 120 °C, which corresponds to loss of nine guest water molecules and the desolvated framework is stable up to 300 °C (**Fig. 4(a)**). PXRD pattern of **AMOF-1'** reveals that the PXRD pattern becomes slightly broadened upon desolvation but the structural integrity is maintained (**Fig. 5(a)**). When solid sample of **AMOF-1** was immersed in water for 7 days and the dried sample shows similar PXRD pattern to **AMOF-1** suggesting its stability in water (**Fig. 4(b)**).

AMOF-1' does not adsorb N$_2$ at 77 K probably due to the high diffusion barrier for N$_2$ into the framework. CO$_2$ adsorption at 195 K reveals an initial type I uptake of 30 ml/g up to $P = 0.65$ bar followed by a step with a final uptake of 145 ml/g at 1 bar (**Fig. 5(c)**). The desorption curve does not retrace the adsorption profile and shows a large
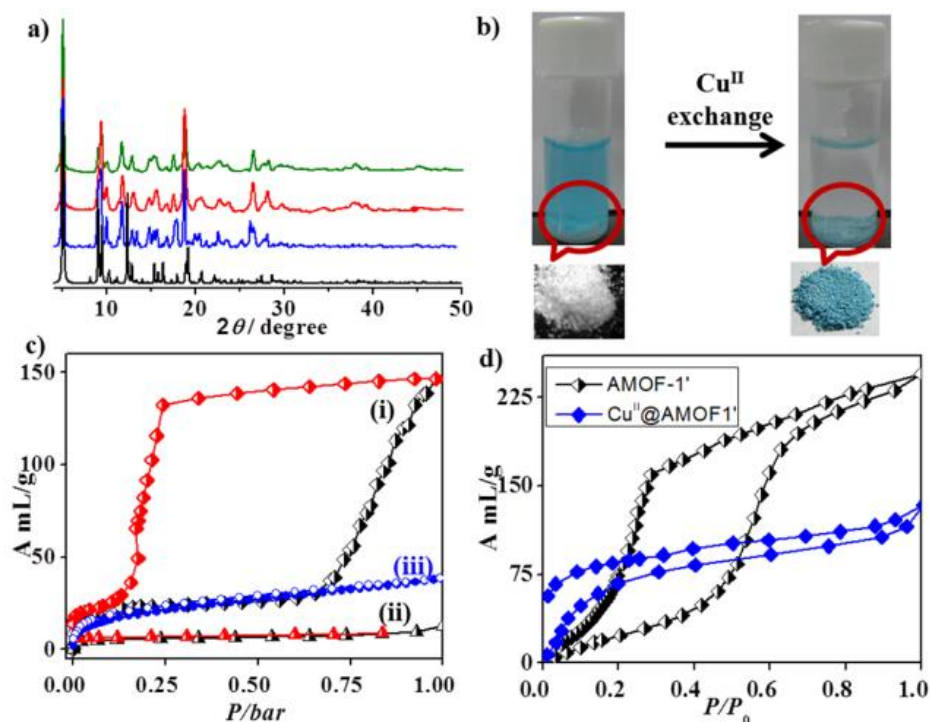
Fig. 5 (a) PXRD patterns; **black**: simulated; **blue**: as-synthesized **AMOF-1**, **red**: **AMOF-1'**, **green: Cu^{II}@AMOF-1' (b)** Visible colour change during Cu^{II} exchange in aqueous solution **(c)** Adsorption isotherms **(i)** CO_2 of **AMOF-1′** at 195 K, **(ii)** N_2 of **AMOF-1′** at 77 K and **(iii)** CO_2 of Cu^{II}@AMOF-1'at 195 K, **(d)** Water vapour adsorption isotherms for **AMOF-1′** and **Cu^{II}@AMOF-**1' at 298 K, P_0 is the saturated vapour pressure of the adsorbates at respective temperature.

hysteretic sorption profile. We conjecture that CO_2 molecules first diffuse into the larger pore resulting in the initial uptake. The interaction between polar DMA cations and CO_2 molecules probably induce diffusion through the interconnected channels thus resulting in stepwise adsorption.

4A.3.3 Heavy Metal Capture in AMOF-1

The anionic nature and water stability of the framework motivated us to study the capture and removal of toxic heavy metal ions from their aqueous solution. To check the ability to capture in a very low concentration, we have performed cation exchange by immersing 20 mg **AMOF-1'** in 20 ml 1 ppm M^{II} solutions. The initial and residual metal ion concentrations were measured through Inductively Coupled Plasma Optical Emission Spectroscopy (ICP-OES) analysis, which showed that after 24 hours almost complete removal of heavy metal ions
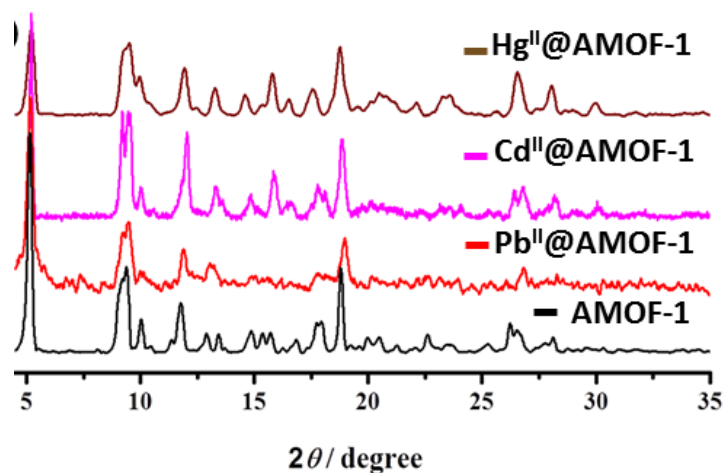
Fig. 6 PXRD patterns of heavy metal ion exchanged samples.

occur (**Table 5**). Thus **AMOF**-**1** can be used for effective removal of heavy metal ions from waste water with detection limit in ppm level. Time-dependent measurements were performed for Hg^{II} ion which shows within 24 hours almost complete removal (98.7%) occur. To know the uptake capacity of different ions, **AMOF**-**1'** was immersed in 0.01 M solutions of Pb^{II}, Cd^{II} and Hg^{II} and the solutions were stirred for 24 hours. Exchange experiments were also carried out for prolonged time (7 days) to check the maximum uptake capacity. ICP-OES analyses of the exchanged solids suggest that number of Hg^{II}, Pb^{II} and Cd^{II} cations per formula unit are 0.31, 0.26 and 0.29, respectively after 24 hours of exchange reaction, which increases to 0.48, 0.42 and 0.45 after 7 days of exchange. The maximum uptake capacity for Hg^{II}, Pb^{II} and Cd^{II} are 78 mg, 71 mg and 41 mg per g of **AMOF**-**1'**, respectively (**Table 6**). PXRD pattern shows that the framework integrity is maintained even after the incorporation of the heavy metal cation (**Fig. 6**). ICP-OES
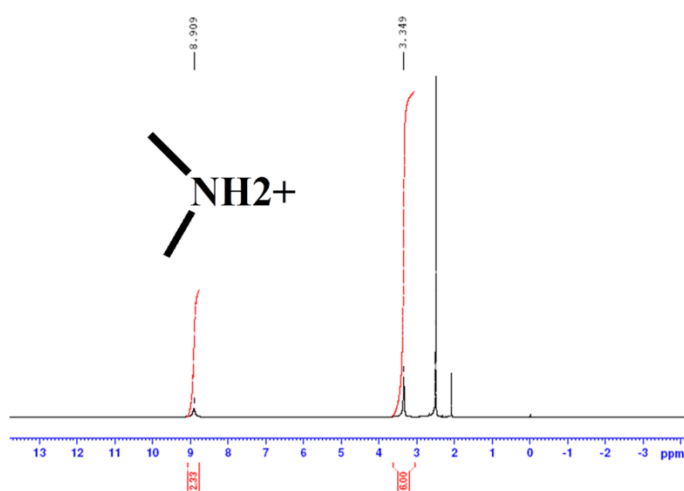
Fig. 7 ^{1}H-NMR spectra (in DMSO-d$_6$) of the exchanging solution showing peaks corresponds to DMA cation.

145

analysis of the exchanging solution does not show presence of Zn^{II} ions which indicate that Zn^{II} ions do not leach out from the framework and do not exchange with the heavy metal cations. On the other hand, NMR analysis of exchanging solution shows presence of DMA cation, clearly advocating that the metal inclusion in the AMOF occurs by cation exchange (**Fig. 7**).

Table 5 Results for the heavy metal ion exchange from **1** ppm aqueous solution

Heavy metal (M^{II})	Exchange time (hour)	Initial concentration of M^{II} ions (ppm)	Concentration of M^{II} ions after exchange(ppm)	Removal efficiency (%)
Hg^{II}	2	1	0.579	42.1
	6	1	0.326	67.4
	12	1	0.109	89.1
	18	1	0.059	94.1
	24	1	0.013	98.7
Pb^{II}	24	1	0.024	97.6
Cd^{II}	24	1	0.018	98.2

Table 6 Results for the heavy metal ion exchange from 1 M aqueous solutions

Heavy metal (M^{II})	Time of exchange	No. of M^{II} per formula of the exchanged framework	Maximum number of M^{II} possible per formula unit	% exchange of M^{II} with DMA
Hg^{II}	24 hours	0.31	1	31
	7 days	0.48	1	48
Pb^{II}	24 hours	0.26	1	26
	7 days	0.42	1	42
Cd^{II}	24 hours	0.29	1	29
	7 days	0.45	1	45

4A.3.4 Transition Metal Cation Sequestration in AMOF-1

Next, we have checked encapsulation of different transition metal ions (M^{II}) ions by immersing **AMOF-1'** into 0.01(M) solutions of M^{II} for 24 hours. ICP data suggest that Cu^{II} ions are exchanged with 49% of the DMA guests, while the extent of exchange for Mn^{II}, Co^{II}, and Ni^{II} are 24, 25, 27%, respectively. The higher percentage of Cu^{II} exchange is attributed to the flexible geometry of Cu^{II} which helps Cu^{II} ions to be accommodated in diverse coordination environments in the nanospace.[6] Such exchange is also evident as a blue solution of Cu^{II} in water becomes colourless on dipping **AMOF-1'** in it, while the white solid of **AMOF-1'** transform into blue coloured **Cu^{II}@AMOF-1'** (**Fig. 5(b)**). It is noteworthy that

extent of Cu^{II} exchange does not increase after 7 days of exchange. The structural integrity is maintained upon Cu^{II} inclusion as evident from the PXRD patterns (**Fig. 5(a)**). We conjecture that the Cu^{II} ions replace the DMA cations and would reside near the carboxylate oxygen atoms which can serve as coordination sites for Cu^{II}. The TGA profile of **Cu^{II}@AMOF-1'** shows continuous weight loss at higher temperature (>150 °C) suggesting the presence of Cu^{II} bound water molecules.

The Cu^{II} inclusion was further validated from the CO_2 adsorption isotherm which shows a type I (**Fig. 5(c)**) profile without any step. We propose that once Cu^{II} ions replace the DMA cations, the accessibility of the interconnected channels would be restricted resulting in a type I profile without any step/hysteresis. To further investigate the impact of Cu^{II} exchange on the polarity of the pore surfaces, water adsorption measurements were carried out at 298 K for **AMOF-1'** and **Cu^{II}@AMOF-1'**. A type IV profile is observed for **AMOF-1'** which suggests hydrophobic nature of the pore surface (**Fig. 5(d)**). In **Cu^{II}@AMOF-1'**, the steeper uptake at low pressure regions compared to that of **AMOF-1'** (**Fig. 5(d)**) suggest strong affinity of water molecules to the pore surface, which can be attributed to the presence of open Cu^{II} Lewis acidic sites in **Cu^{II}@AMOF-1'**.

4A.3.5 Catalysis using Cu^{II}@AMOF-1
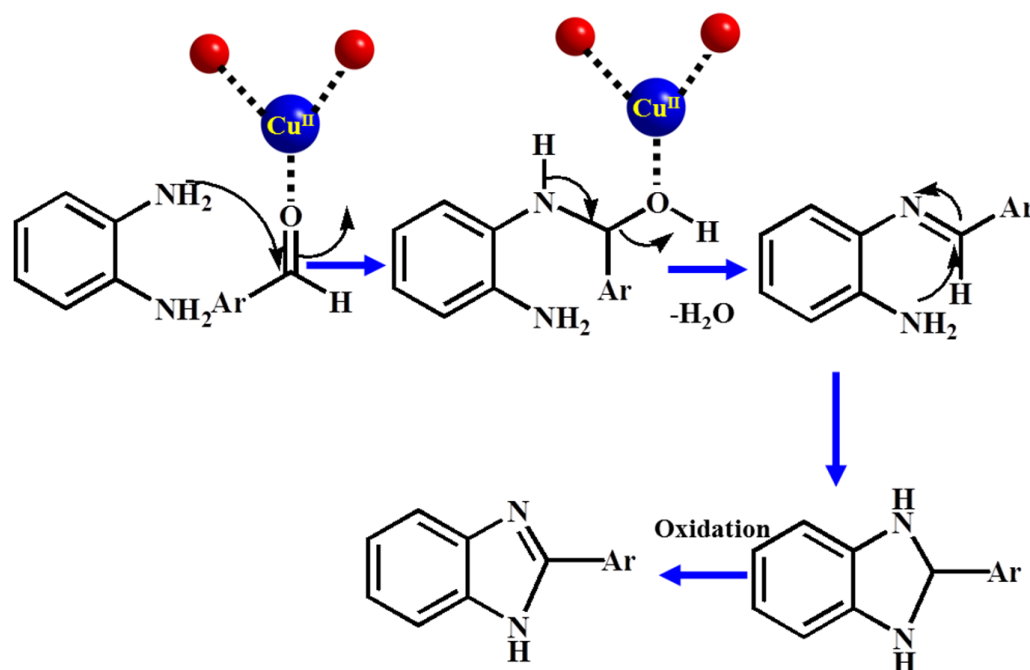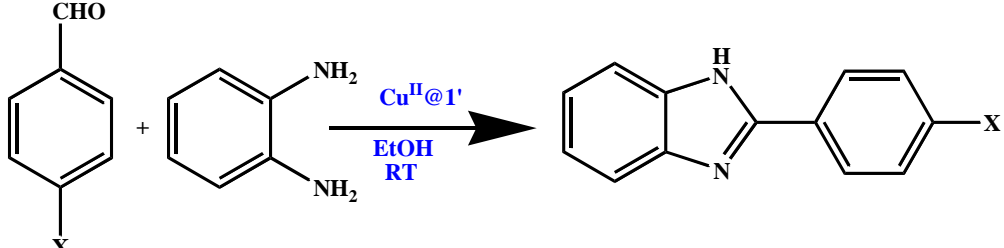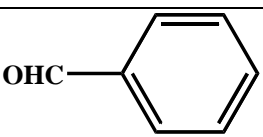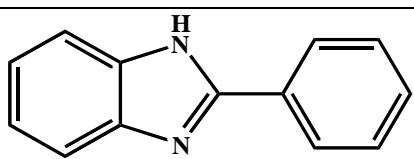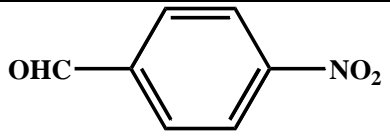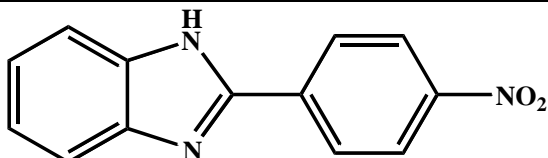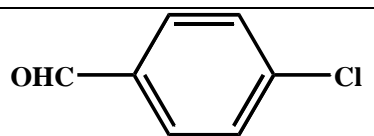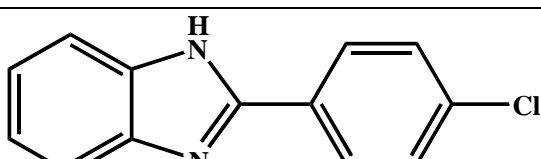
Fig. 8 The plausible mechanism of benzimidazole formation in presence of **Cu^{II}@AMOF-1'** catalyst. Colour code: Cu: blue; O (from carboxylate of L3 ligand): red.

The permanent porosity and presence of UMS in the activated **Cu^{II}@AMOF-1'** inspired us to use this hybrid as a Lewis acid catalyst for the synthesis of chemically important benzimidazole compounds (**Fig. 8**).[33-36] We have carried out reaction of *o*-phenylenediamine with different *p*-substituted benzaldehyde (X = H, NO$_2$, Cl, CH$_3$ and OCH$_3$) at room temperature.[14] The quantitative analysis of product conversion is monitored by GC-MS analyser at regular intervals of times. The conversion of products with benzaldehyde (X= H) is 62% after 3 h, after 6 h the product conversion is increased to 97%, suggesting that the conversion is almost complete within 6 h (for X= H). It is noteworthy that homogeneous Cu^{II} catalyst, dehydrated cupric acetate does not show any conversion under similar conditions as employed for **Cu^{II}@AMOF-1'**, which reflects the heterogeneous **Cu^{II}@AMOF-1'** is a superior catalyst than the homogeneous Cu^{II} catalyst. We have carried out reaction of *o*-phenylenediamine and benzaldehyde in the presence of only **AMOF-1'**, which shows no conversion of product even after 12 hours. This suggests that **AMOF-1'** could not act as a catalyst. In another reaction using **Cu^{II}@AMOF-1'** catalyst, we have removed the catalyst after a time period of 3 h by filtration and the reaction mixture was further stirred for additional 3 h. After 6 h, there was no increase in the yield (62%), suggesting that Cu^{II} sites indeed act as the catalytic sites. ICP analysis of the filtrate obtained after removing the solid catalyst from the reaction mixture shows no detectable Cu^{II} ions suggesting that no leaching of Cu^{II} ions occurs during the catalysis. This result indicates that the substituents with reaction time of 6 h (**Table 7**). Although the conversion of the products are significant for X= H, NO$_2$ and Cl, the yield is significantly reduced for X= CH$_3$ and OCH$_3$ group (the purity of the products is verified through the ^{1}H NMR measurements). T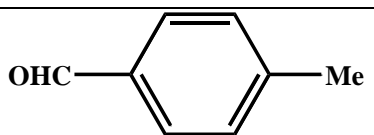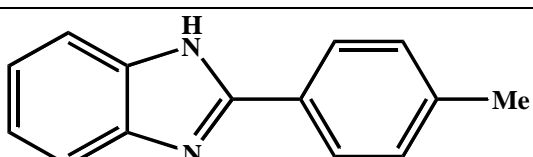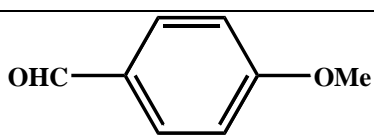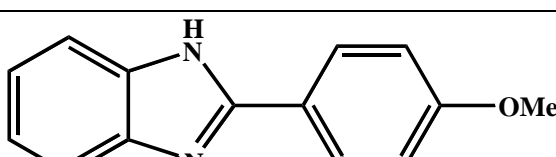his suggests that an electron withdrawing group at *para* position of aldehyde enhance electrophilic nature of the carbonyl carbon thereby increasing its reactivity, while electron donating methoxy and methyl groups exhibit lesser yield (**Table 7**). The recyclability experiment was studied with benzaldehyde (X = H), which suggest that the solid catalyst could be reused for at least 3 cycles.

To compare the catalytic activity of **Cu^{II}@AMOF-1'** with homogeneous Cu^{II} catalyst, we have carried out reaction of *o*-phenylenediamine (1 equivalent) and benzaldehyde (1 equivalent) using dehydrated cupric acetate (0.05 mol%) as a

catalyst in ethanol and GC-MS data show that there is no conversion of product after 6 hours, which reflects the heterogeneous **Cu^{II}@AMOF-1'** is a superior catalyst than the homogeneous Cu^{II} catalyst.

Table 7 The catalytic reactions and the results with varying substituent on the aldehydes.

Aromatic Aldehyde	Benzimidazole (product)	Conversion (%)
		97
		88
		82
		60
		23

4A.4 Conclusions

In conclusion, we have synthesized a new porous AMOF that allows easy access of desired exogeneous cations and offers a unique way to post-synthetically modify the AMOF. The AMOF effectively capture toxic metal ions from their aqueous solutions. The large pores of the AMOF coupled with its water stability

are particularly effective for heavy metal removal. The Cu^{II} exchanged AMOF shows good catalytic activity towards the synthesis of benzimidazole derivatives at room temperature. Such PSMet in water stable AMOFs will ensue a new route to capture toxic metal ions from industrial waste water. Suitable AMOF would also act as the platform to immobilize different cationic groups to obtain versatile targeted functions.

4A.5 References

1. Themed Issue: Metal-organic Frameworks, *Chem. Rev.*, 2012, **112**, 673.

2. S. M. Cohen, *Chem. Rev.*, 2012, **112**, 970.

3. W. M. Bloch, R. Babarao, M.R. Hill, C. J. Dooan and C. J. Sumby, *J. Am. Chem. Soc.*, 2013, **135**, 10441.

4. C. K. Brozek and M. Dinca, *J. Am. Chem. Soc.*, 2013, **135**, 12866.

5. D. Sun, F. Sun, X. Deng and Z. Li, *Inorg. Chem.*, 2015, **54**, 8639.

6. D. Sun, W. Liu, M. Qiu, Y. Zhang and Z. Li, *Chem. Commun.*, 2015, **51**, 2056.

7. J. S. Costa, P. Gamez, C. A. Black, O. Roubeau, S. J. Teat and J. Reedijk, *Eur. J. Inorg. Chem.*, 2008, 1551.

8. E. Quartapelle Procopio, F. Linares, C. Montoro, V. Colombo, A. Maspero, E. Barea and J. A. R. Navarro, *Angew. Chem. Int. Ed.*, 2010, **49**, 7308.

9. J. Yu, Y. Cui, C. Wu, Y. Yang, Z. Wang, M. O'Keeffe, B. Chen and G. Qian, *Angew. Chem. Int. Ed.*, 2012, **51**, 10542.

10. J. An, S. J. Geib and N. L. Rosi, *J. Am. Chem. Soc.*, 2009, **131**, 8376.

11. D. T. Genna, A. G. Wong-Foy, A. J. Matzger and M. S. Sanford, *J. Am. Chem. Soc.*, 2013, **135**, 10586.

12. J. Tian, L. V. Saraf, B. Schwenzer, S. M. Taylor, E. K. Brechin, J. Liu, S. J. Dalgarno and P. K. Thallapally, *J. Am. Chem. Soc.*, 2012, **134**, 9581.

13. S. Yang, G. S. B. Martin, J. J. Titman, A. J. Blake, D. R. Allan, N. R. Champness and M. Schröder, *Inorg. Chem.*, 2011, **50**, 9374.

14. J. Yu, Y. Cui, H. Xu, Y. Yang, Z. Wang, B. Chen and G. Qian, *Nat. Chem.*, 2013, **4**, 2719.

15. P. Vanelderen, J. Vancauwenbergh, B. F. Sels and R. A. Schoonheydt, *Coord. Chem. Rev.*, 2013, **257**, 483.

16. J.D. Evans, C. J. Sumby and C. J. Doonan, *Chem. Soc. Rev.*, 2014, 43, 5933.

17. S. Bhattacharyya, A. Chakraborty, K. Jayaramalu, A. Hazra and T. K. Maji, *Chem. Commun*, 2014, **50**, 13567.

18. B. J. Zhu, X. Y. Yu, Y. Jia, F. M. Peng, B. Sun, M. Y. Zhang, T. Luo, J. H. Liu and X. J. Huang, *J. Phys. Chem. C*, 2012, **116**, 8601.

19. J. He, K. K. Yee, Z. Xu, M. Zeller, A. D. Hunter, S. S. Y. Chui and C. M. Che, *Chem. Mater.*, 2011, **23**, 2940.

20. S. B. Maity, S. Banerjee, K. Sunwoo, Jong Seung Kim and P. K. Bharadwaj, *Inorg. Chem.*, 2015, 54, 3929.

21. K. K. Yee, N. Reimer, J. Liu, S. Y. Cheng, S. M. Yiu, J. Weber, N. Stock and Z. Xu, *J. Am. Chem. Soc.*, 2013, **135**, 7795.

22. X. P. Zhou, Z. T. Xu, M. Zeller and A. D. Hunter, *Chem. Commun.*, 2009, 5439.

23. T. Liu, J.-X. Che, Y.-Z. Hu, X.-W. Dong, X.-Y. Liu and C.-M. Che, *Chem. Eur. J.*, 2014, **20**, 14090.

24. B. Chen, M. Eddaoudi, T. M. Reineke, J. Kampf, M. O'Keeffe and O. M. Yaghi, *J. Am. Chem. Soc.,* 2000, **122**, 11559.

25. B. Chen, N. W. Ockwig, A. R. Millward, D. S. Contreras, O. M. Yaghi, *Angew. Chem. Int. Ed.* 2005, 44, 4745.

26. A. Hazra, P. Kanoo and T. K. Maji, *Chem. Commun.*, 2011, **47**, 538.

27. S. R. Caskey, A. G. Wong-Foy and A. J. Matzger, *J. Am. Chem. Soc.*, 2008, **130**, 10870.

28. X.-L. Yang, C. Zou, Y. He, M. Zhao, B. Chen, S. Xiang, O'Keeffe and C-D. Wu, *Chem. Eur.J.*, 2014, **20**, 1447.

29. Y. Bai, J. Lu, Z. Shi and B. Yang, *Synlett.,* 2001, 544.

30. D. G. O. Sullivan and A. K. Wallis, *J. Med. Chem.*, 1972, **15**, 103.

31. P. W. Erhardt, *J. Med. Chem.*, 1987, **30**, 231.

32. G. L. Gravatt, B. C. Baguley, W. R. Wilson and W. A. Denny, *J. Med. Chem.* 1994, **37**, 4338.

33. N. Zheng, K.W. Anderson, X. H. Huang, H. N. Nguyen and S. L. Buchwald, *Angew. Chem.* 2007, **119**, 7653.

34. M. Shen and T. G. Driver, *Org. Lett.* 2008, **10**, 3367.

35. L. C. R. Carvalho, E. Fernandes, M. M. B. Marques, *Chem. Eur. J.* 2011, **17**, 12544.

36. A. Dutta, J. Mondal, A. K. Patra and A. K. Bhaumik, *Chem. Eur. J.*, 2012, **18**, 13372.

37. SMART (V 5.628), S. V. a., XPREP, SHELXTL; Bruker AXS Inc. Madison, Wisconsin, USA, 2004.

38. G. M. Sheldrick, *SADABS, Empirical Absorption Correction Program, University of Göttingen, Göttingen* **1997**.

39. A. Altomare, G. Cascarano, C. Giacovazzo and A. Guagliardi, *J. Appl. Crystallogr.* 1993, 26, 343.

40. G. M. Sheldrick, *SHELXL 97, Program for the Solution of Crystal Structure, University of Göttingen, Germany* 1997.

41. A. Spek, *J. Appl. Crystallogr.* 2003, **36**, 7.
42. L. Farrugia, *J. Appl. Crystallogr.* 1999, **32**, 837.

Chapter 4B

Mechanochemical Synthesis of Halide Perovskite Quantum Dot-MOF Composite by Post-synthetic Metalation
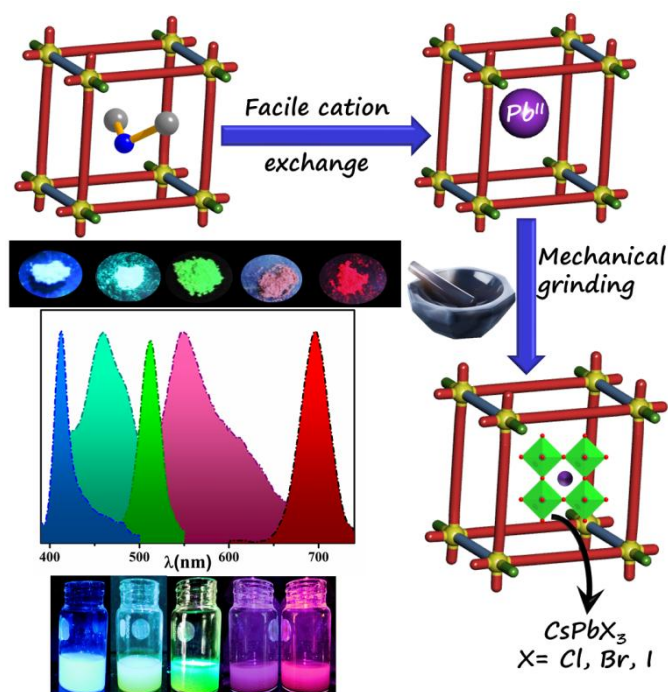
Abstract

Perovskite quantum dots (PQDs) are some of the most sought after materials for optoelectronic and photovoltaic applications. This chapter contains the mechanochemical, solvent-free synthesis of **PQD@MOF** composite using a post-synthetically Pb^{II} metalated anionic MOF **AMOF-1** {[(NH$_2$Me$_2$)$_2$][Zn$_3$(L)$_2$].9H$_2$O} (L=5,5′-(1,4-phenylenebis(methylene))bis(oxy)diisophthalate) as a template. CsPbX$_3$ PQDs are formed on the **AMOF-1** template just by grinding **Pb^{II}@AMOF-1** with CsX (X=Cl, Br and I). The size of the PQDs thus formed is restricted by the structure of **AMOF-1** thereby manifesting quantum confinement effect. PXRD pattern confirms the formation of the PQDs on the MOF template. The composites show the typical narrow emission bands of the CsPbX$_3$ PQDs with bright blue, green and red luminescence for X= Cl, Br and I, respectively. In a first, the luminescent **AMOF** is exploited for Försters Resonance Energy Transfer (FRET) from the framework to the stabilized CsPbBr$_3$ PQDs. **AMOF-1** also imparts superior solvent stability and processability to the PQDs compared to untemplated mechanochemically synthesized PQDs. The processibility of the composite is further manifested by fabricating a colour-tunable ink using the composite.

4B.1 Introduction

Over the past decade, colloidal nanocrystal halide perovskite quantum dots (PQDs) have emerged as supremely important materials for photovoltaic and optoelectronic applications.[1-4] The miniscule sizes of PQDs endow them with a variety of interesting features[5-7] involving an intriguing surface chemistry, which are otherwise not observed in their bulk counterparts.[8] Among these, cesium lead halide ($CsPbX_3$) perovskite nanocrystals (NCs) have gathered the attention of scientists because of excellent photovoltaic efficiency.[5,9] Their high emission intensities and quantum yield, narrow emission bands and tunable band gaps by composition, size or morphology have made them perfect candidates for optoelectronic devices, e.g., LEDs, lasers or specific detection.[10-11] However, the use of these materials in practical applications is hindered by their poor stability when exposed to variable atmospheric conditions e.g., humidity, temperature or light.[12] This instability can be majorly attributed to the ionic character of $CsPbX_3$ NCs along with their labile surfaces and metastable structures.[13-14] In order to address this issue, besides the conventional method of synthesizing these NCs like hot injection and various liquid phase methods,[15-17] attempts have also been made to immobilise them in silica or polymer matrices.[18-21] The size and spatial control of such PQD NCs by confining them within the nanospaces of a porous Metal-organic framework (MOFs)[22-24] is an intriguing technique to tune their optical band gap while enhancing their stability.[20,25-30] MOFs, well known for their porosity, tunability and high surface area, surpass contemporary porous materials in their flexibility and easy functionalization.[23] The definite size of the MOF pores is particularly advantageous in quantum confinement of such NCs, thereby enhancing their optoelectronic properties, and providing extra stability for better performance in devices.[25-30] There are only a handful of reports of PQD@MOF composites and the synthetic methods all involve harsh conditions concerning expensive and precarious organic solvents, capping agents and organometallic complexes.[26-27] In a recent report, Zhang, *et al.* have derived PQDs from a Pb^{II}-based MOF,[25] however, the MOF template cannot sustain the harsh synthetic procedure and is broken down in the process. In contrast, a mechanochemical method would be simple, fast, efficient and environmentally benign for synthesizing such PQD@MOF composites.[31-34] However, attaining PQDs by such mechanochemical

156
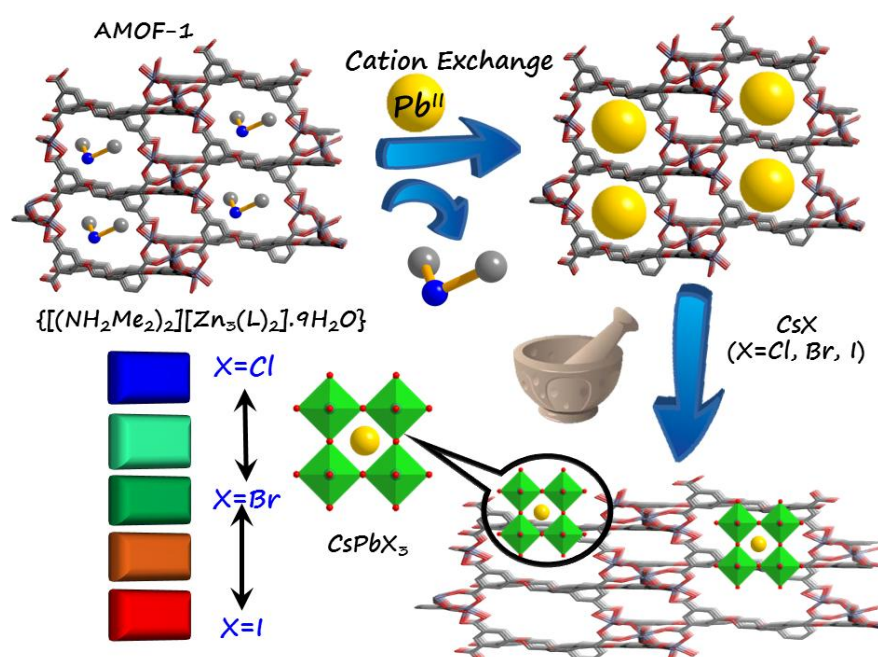
Scheme 1. Mechanochemical synthesis of **QD@MOF** composite mediated by cation exchange in **AMOF-1**.

methods is a highly challenging task owing to the lack of control over crystal growth. Moreover, the instability of the PQDs also demands synthesis in controlled and inert atmosphere.[5,31-34] A porous template like MOF can alleviate this issue by restricting the size of the NCs by the nanochannels and also by providing extra stability. This chapter demonstrates the synthesis and characterization of unique **CsPbX$_3$@AMOF** composites by a simple mechanochemical grinding method involving a post-synthetically Pb^{II} metalated anionic MOF (AMOF) (**Scheme 1**). This process ensures the stabilization of PQD on the MOF surface, thus restricting their size and dictating their optical properties based on quantum confinement effect. The **CsPbX$_3$@AMOF** composites show intense luminescence, enhanced stability, processibility and also manifests energy transfer from the framework to the PQDs when X=Br. This is also the first instance of Förster Resonance Energy Transfer (FRET) from the host luminescent framework to the stabilized CsPbBr$_3$ PQDs.

4B.2 Experimental Section

4B.2.1 Materials

Zn(NO$_3$)$_2$.6H$_2$O, dimethyl-5-hydroxy isophthalate, α,α' dibromo paraxylene,

dibenzo-18-crown-6 and K_2CO_3 were all obtained from Sigma Aldrich Co. and were used as procured without further purification. All the solvents were obtained from Spectrochem Co.

4B.2.2 Synthesis of Pb^{II}@AMOF-1

AMOF-1 was degassed overnight at 120°C under vacuum. 150 mg of the degassed sample is then immersed in 5 ml 10^{-2} M solution of $Pb(NO_3)_2$ for a week and the solution is changed every alternate day. After a week, the residue was centrifuged and washed several times with water to yield **Pb^{II}@AMOF-1**. ICP-OES reveals that 18 wt% Pb is present in **Pb^{II}@AMOF-1**, which is equivalent to 0.8 molecules of Pb^{II} per formula unit of **AMOF-1**.

4B.2.3 Synthesis of CsPbX$_3$@AMOF-1

3 equivalents of CsX are taken for 1 equivalent of Pb^{II} present in **Pb^{II}@AMOF-1**. Accordingly, 40 mg of **Pb^{II}@AMOF-1** was taken and 0.104 mmol of CsX was taken and grinded with **Pb^{II}@AMOF-1** in a mortar and pestle for 15-20 mins. The sample was intermittently checked under UV lamp for the appearance of characteristic perovskite emission (**Fig. 1**).
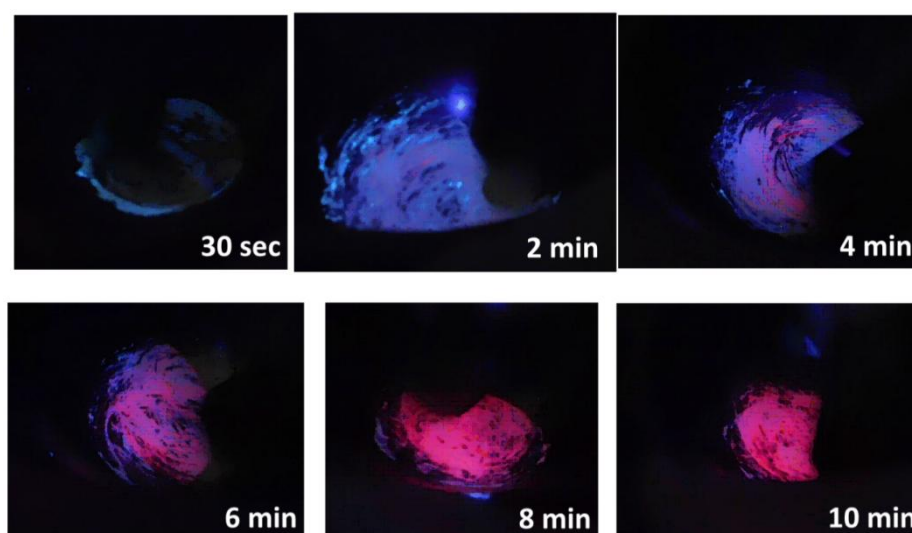
Fig. 1 Images captured during various stages during mechanochemical synthesis of **CsPbI$_3$@AMOF-1** by mechanical grinding under UV light showing change from the blue emission of **AMOF-1** to the red emission of CsPbI$_3$.

4B.2.4 Synthesis of CsPbBr$_3$_mc

1 mmol each of PbBr$_2$ and CsBr were taken in a mortar and pestle and grinded for

15 mins in open atmosphere. A yellow solid was formed which was characterized by different techniques.

4B.2.5 Preparation of Colour-tunable Ink

~50 mg of **Pb^{II}@AMOF-1** was dispersed in 10 ml toluene and put inside the ink chamber of a roller ball pen. After writing with this pen, the writing portion was sprayed with CsBr solution in water to prepare **CsPbBr$_3$@AMOF-1**. The formation of this composite was easily realized by the green emission under UV lamp.

4B.2.6 Physical Measurements

The elemental analysis was carried out using a Thermo Fischer Flash 2000 Elemental Analyzer. Thermogravimetric analysis (TGA) was carried out using a Mettler-Toledo instrument in nitrogen atmosphere (flow rate = 50 ml min^{-1}) in the temperature range from 30 – 550 °C (heating rate: 3°C min^{-1}). Powder X-ray diffraction (PXRD) was recorded by using Cu-Kα radiation (Bruker D8 Discover; 40 kV, 30 mA). IR spectra of the compounds were recorded with a Bruker IFS 66v/S spectrophotometer using the KBr pellets in the region 4000−400 cm^{-1}. The scanning electron microscopy images were obtained using a Nova Nanosem 600 FEI field emission scanning electron microscope (FESEM).Transmission electron microscopy (TEM) analysis has been performed using a JEOL JEM-3010 with an accelerating voltage at 300 kV or a FEI TECNAI G2 20 STWIN TEM operating at 200 kV. One drop of the samples dispersed in ethanol solution was taken in a holey carbon coated Cu grid for TEM imaging. Inductively Coupled Plasma-Optical Emission Spectroscopy (ICP-OES) measurements were recorded on a Perkin Elmer Optima 7000dv ICP-OES instrument. UV−Vis spectra were recorded on a Perkin Elmer Model Lambda 900 spectrophotometer. Fluorescence studies were accomplished using Perkin Elmer Ls 55 Luminescence spectrometer. Time-resolved decay experiments were recorded on a Horiba Delta Flex time-correlated single-photon-counting (TCSPC) instrument. A 442-nm nano-LED with a pulse repetition rate of 1 MHz was used as the light source. The instrument response function (IRF) was collected by using a scatterer (Ludox AS40 colloidal silica, Sigma-Aldrich). For the 442-nm LED light source, the instrumental full width at half maximum including detector response was 0.2 ns. The excited state decay of the sample was collected by fixing the emission wavelength at a particular wavelength. The decay was fitted using IBH software (DAS6).

4B.2.7 Preparation of Sample for Adsorption

Adsorption isotherm of CO_2 at 195 K was recorded with the dehydrated sample using QUANTACHROME QUADRASORB-SI analyzer. To prepare the dehydrated sample of **AMOF-1** and **CsPbBr$_3$@AMOF-1**, approximately 100 mg of sample was taken in a sample holder and degassed at 150ºC at 10^{-1} pa vacuum for about 8 h prior to measurements. The dead volume of the sample cell was measured using He of 99.999% purity. The amount of adsorbed gas was calculated from the pressure difference $(P_{cal} - P_e)$, where P_{cal} is the calculated pressure with no gas adsorption and P_e is the observed equilibrium pressure. All operations were computer-controlled and automatic.

4B.3 Results and Discussions

4B.3.1 Characterization of CsPbX$_3$@AMOF-1
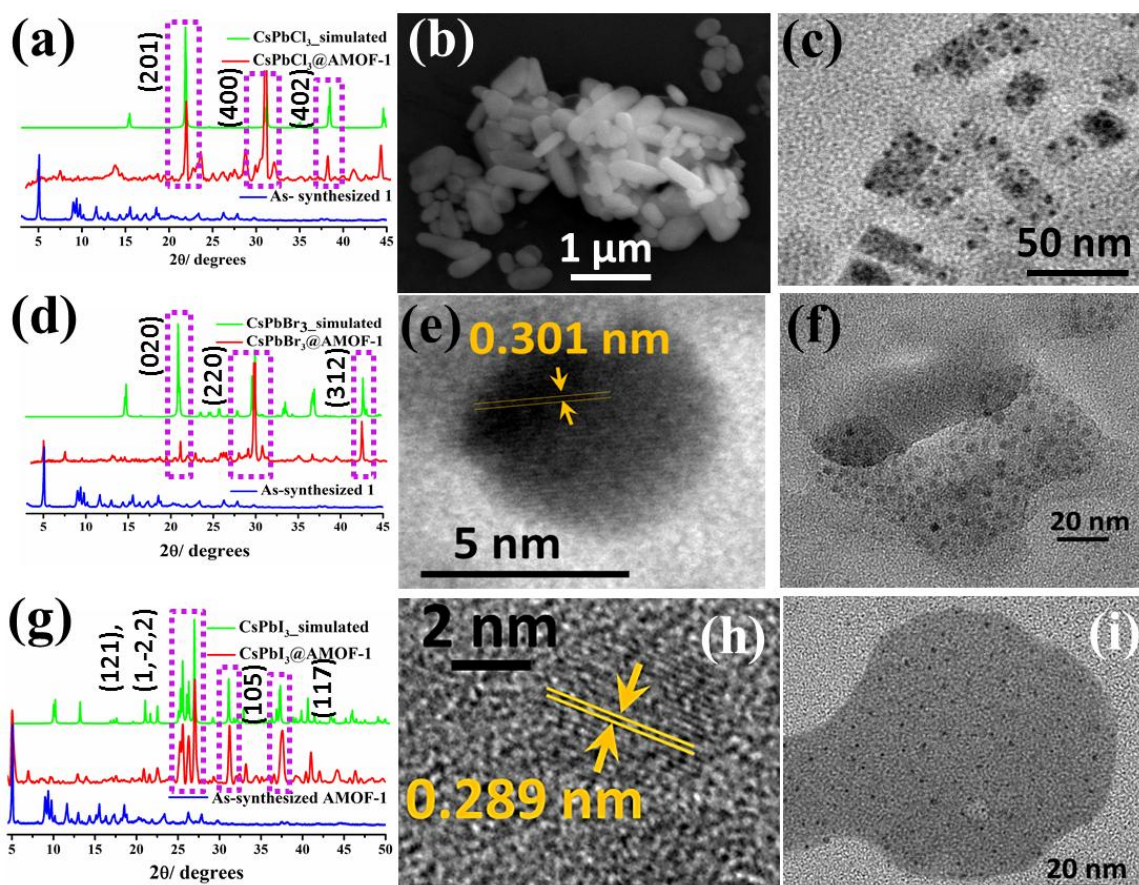
Fig. 2 (a) PXRD pattern of **CsPbCl$_3$@AMOF-1** along with **AMOF-1**. **(b)** FESEM images of as-synthesized **AMOF-1**. **(c)** TEM image of **CsPbCl$_3$@AMOF-1**. **(d)** PXRD pattern of **CsPbBr$_3$@AMOF-1** along with **AMOF-1**. **(e)** HRTEM of **CsPbCl$_3$@AMOF-1**. **(f)** TEM of **CsPbBr$_3$@AMOF-1**. **(g)** PXRD pattern of **CsPbI$_3$@AMOF-1** along with **AMOF-1**. **(h)** HRTEM of **CsPbBr$_3$@AMOF-1**. **(i)** TEM of **CsPbI$_3$@AMOF-1**.

AMOF-1 {[(NH$_2$Me$_2$)$_2$][Zn$_3$(L)$_2$].9H$_2$O} (L=5, 5′- (1,4-phenylenebis(methylene))bis--(oxy)diisophthalate), is used in this study which is a 3D flexible AMOF,[35-40] with dimethyl ammonium (DMA) guest cations maintaining its charge neutrality. In **AMOF-1**, a trinuclear [Zn$_3$(CO$_2$)$_8$] secondary building is connected by tetracarboxylate L linker to form the 3D network. As mentioned in the previous chapter, **AMOF-1** manifested excellent water stability, along with high affinity towards heavy metal cations like Pb^{II} by exchange with the guest DMA cation.[40] We seek to transform the Pb^{II} encapsulated AMOF (**Pb^{II}@AMOF-1**) into a value-added PQD@MOF composite by simple solvent-free means which will be ideal for several optoelectronic applications. The Pb-exchanged sample is washed with water several times to yield **Pb^{II}@AMOF-1**, which contains 18 wt% Pb, as determined by ICP-OES. Accordingly, 3 molar equivalents of CsX (X= Cl, Br, I) are taken and grinded with **Pb^{II}@AMOF-1** in a mortar and pestle without any solvent for 15mins in the open atmosphere. When observed under UV lamp, the bright emission (blue when X=Cl, green when X=Br and red when X=I) starts appearing immediately with the grinding (**Fig. 1**). The samples thus synthesized are characterized initially using powder X-ray diffraction (PXRD) where we clearly see the presence of perovskite peaks in addition to the peaks for **AMOF-1** (**Fig. 2 (a,d,g)**). In each case, the low angle peak of **AMOF-1** is present at 2θ = 5°. Since **AMOF-1** is a flexible MOF, the mechanical grinding
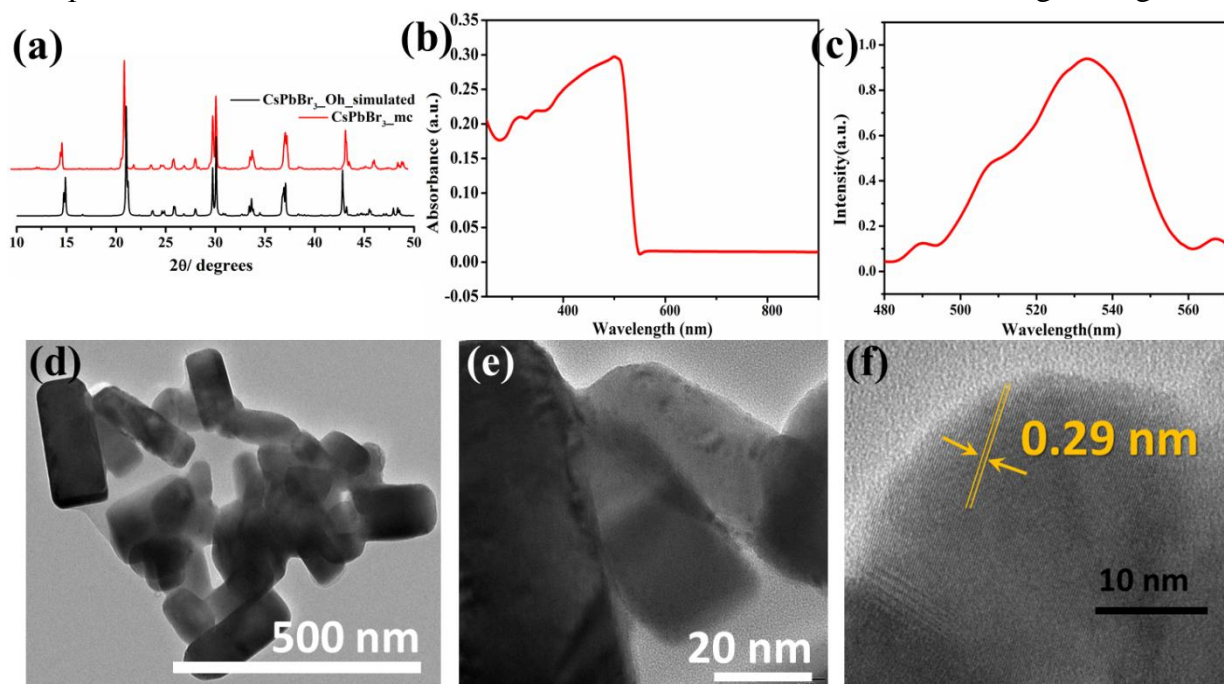
Fig. 3 (a) PXRD, **(b)** Absorption spectrum **(c)** PL spectrum, **(d, e)** TEM and **(f)** HRTEM of **CsPbBr$_3$_mc**.

may bring about orientational changes which are reflected by the appearances of some new peaks and change in intensities of the peaks in PXRD. These perovskite peaks have been matched with orthorhombic *Pbnm* phase in all three cases, which indicates that during mechanical synthesis, all of the $CsPbX_3$ PQDs crystallize in the orthorhombic phase. The sharp intensity of the PXRD peaks leads us to believe that surface attached Pb^{II} cations upon grinding give rise to a small percentage of bulk $CsPbX_3$ microcrystallites in addition to the $CsPbX_3$ PQDs, which show strong diffraction. For comparison, we have mechanochemically synthesized $CsPbBr_3$ (**CsPbBr₃_mc**) without a template by grinding $PbBr_2$ and CsBr in the open atmosphere which also crystallized in the orthorhombic phase (**Fig. 3(a)**). A previous report on the mechanochemical synthesis of $CsPbX_3$ has also recorded the formation of the perovskites in the orthorhombic phase.[31] Thermogravimetric analysis (TGA) of **CsPbX₃@AMOF-1** composites show high thermal stability by remaining unharmed till 280°C (**Fig. 4(a)**). The incorporation of these PQDs within the MOF structure is also evidenced by the adsorption isotherm for CO_2 at 195 K, where **CsPbBr₃@AMOF-1** shows a marked decrease in the total adsorption amount from **AMOF-1** (**Fig. 4(b)**). Under FESEM, **AMOF-1** shows
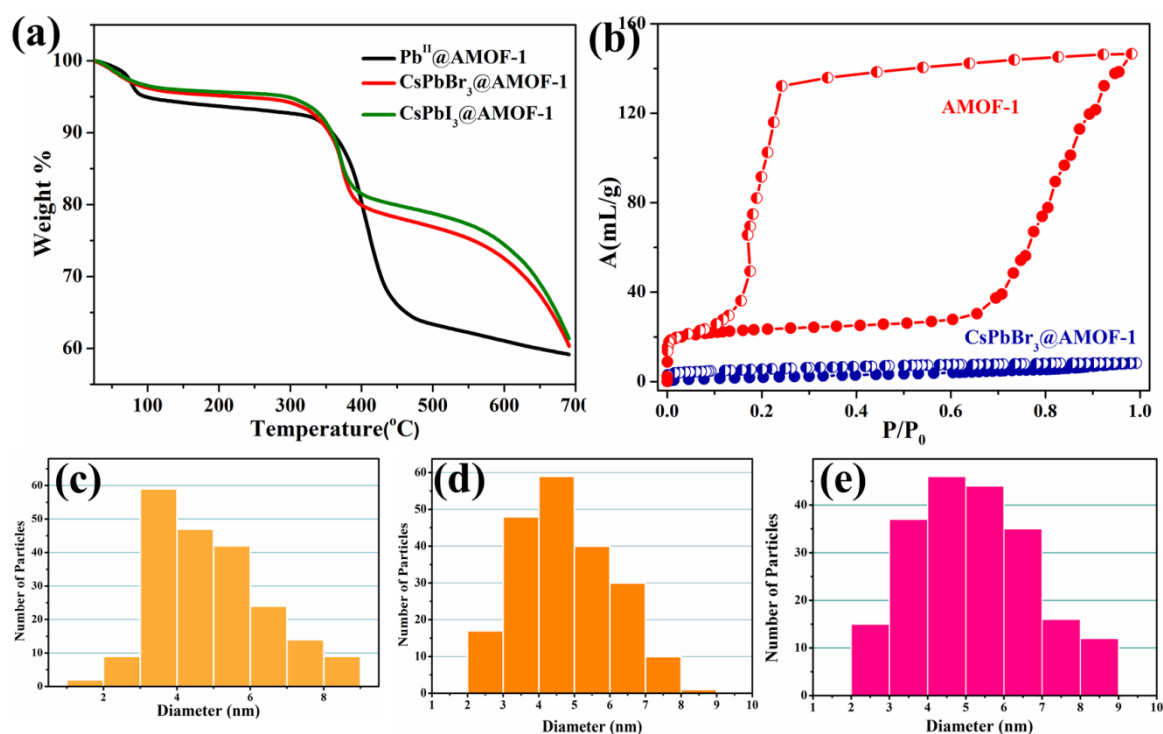
Fig. 4 (a) Thermal stability of **Pb^II@AMOF-1** and **CsPbX₃@AMOF-1** (X= Cl, Br and I) **(b)** CO_2 adsorption isotherms at 195 K for **AMOF-1** and **CsPbBr₃@AMOF-1**. Particle size distribution in **(c) CsPbCl₃@AMOF-1**, **(d) CsPbBr₃@AMOF-1**, **(e) CsPbI₃@AMOF-1**.
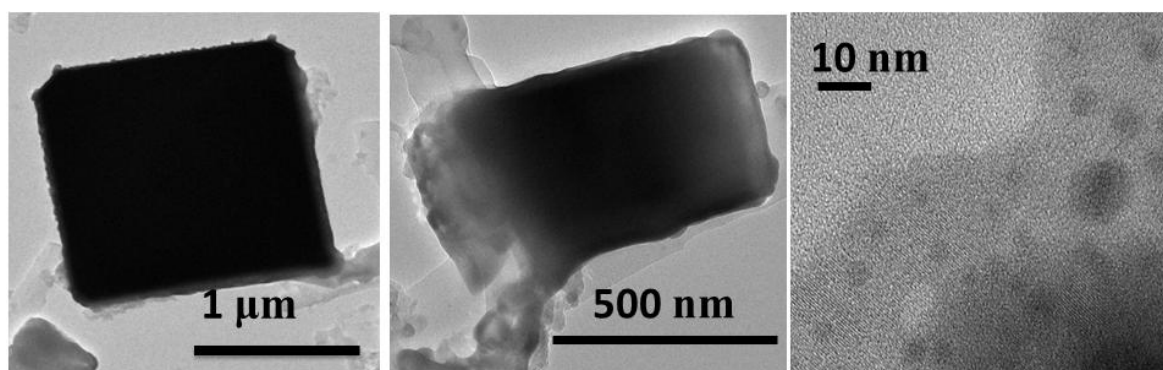
Fig. 5 TEM images of **CsPbBr$_3$_L** shows a mixture of bulk and quantum dot states.

cuboidal microcrystallites which are 500-700 nm in length (**Fig. 2(b)**). The PQDs encapsulated in the MOF matrix were visualized using TEM, where well- defined quantum dots, 2-9 nm in diameter were observed uniformly distributed on rectangular MOF microcrystallites for **CsPbCl$_3$@AMOF-1** (**Fig. 2(c)**). HRTEM of a single PQD shows a lattice spacing of 0.301 nm, corresponding to (110) plane typical in orthorhombic CsPbCl$_3$ (**Fig. 2(e)**). In case of **CsPbBr$_3$@AMOF-1**, the size distribution is similar and the PQDs show a lattice spacing of 0.298 nm, which corresponds to the (200) plane in orthorhombic CsPbBr$_3$ (**Fig. 2(f,h)**).[41] Similar morphology is also observed in case of **CsPbI$_3$@AMOF-1**, where a uniform distribution of PQDs of 5-8 nm dimensions is seen over the AMOF matrix (**Fig. 2(i)**). In the absence of any template, **CsPbBr$_3$_mc** grows to large cuboidal nanocrystals, 100-200 nm in dimension without any uniformity in size (**Fig. 3(d)**).[31] However, in case of **CsPbX$_3$@AMOF-1**, confinement effect by the **AMOF-1** structure supported by the post-synthetic cation exchange restricts the size of the PQDs to lower ranges of the nanoscale. NC growth is restricted by the AMOF, thereby controlling its size and it could be a prominent method to produce a library of CsPbX$_3$ PQDs. In order to demonstrate that the sized of CsPbX$_3$ is indeed restricted by the AMOF and not merely due to capping by the MOF ligand, we have prepared another batch of sample by grinding PbBr$_2$ and CsBr with the ligand L (**CsPbBr$_3$_L**). Under TEM, for **CsPbBr$_3$_L**, we observe large rectangular chunks of bulk perovskite along with a few dots which have a non-uniform size distribution. This is a clear indication that the intact AMOF template restricts the size of CsPbX$_3$ and provided extra stability and the PQDs are not formed due to capping by the ligand leached from the framework.

4B.3.2 Optical Properties of CsPbX$_3$@AMOF-1

The optical properties of the **CsPbX$_3$@AMOF-1** have been studied extensively. The solid-state UV spectrum of **AMOF-1** shows absorption maximum at 316 nm and a blue emission with a broad emission peak centred at 420 nm (as shown in Chapter 4A). The optical properties of **Pb^{II}@AMOF-1** are identical to that of **AMOF-1**. However, in case of all the **CsPbX$_3$@AMOF-1** samples, the individual absorption bands of the respective PQDs also appear with maxima at 401 nm when X = Cl, at 508 nm when X = Br and at 670 nm when X = I, in addition to the 316 nm band for **AMOF-1** (**Fig. 5(a)**). **CsPbCl$_3$@AMOF-1** shows intense blue emission with emission maxima at 412 nm (λ_{ex}=320 nm) whereas **CsPbBr$_3$@AMOF-1** shows a bright green emission with emission maxima at 515 nm when excited at 365 nm. The **CsPbI$_3$@AMOF-1** shows red emission with emission maxima at 695 nm, when excited at 500 nm (**Fig. 5(b,c)**). The emission bands are extremely narrow which indicates towards the narrow size distribution owing to quantum confinement.[8] All the samples show typical intense luminescence under UV lamp in both solid states as well as when dispersed in ethanol (**Fig. 5(b,d)**). When excited at 365 nm, **CsPbBr$_3$_mc** shows an emission peak with a maximum at 530 nm, which is very broad due to the heterogeneity in
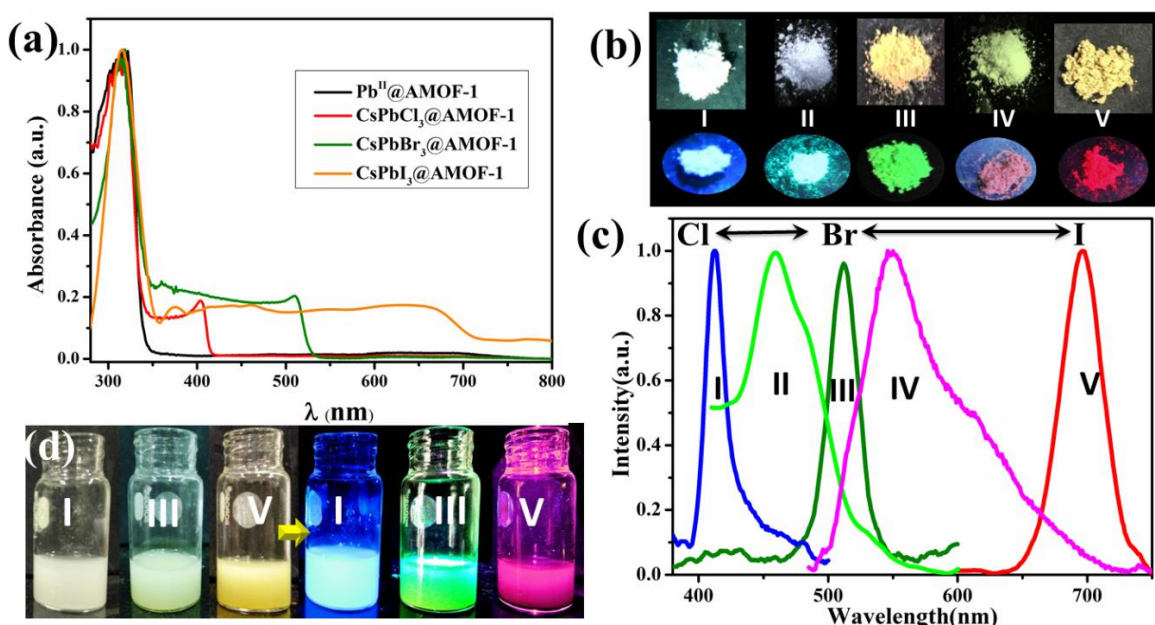
Fig. 5 (a) UV-Vis spectra of **CsPbX$_3$@AMOF-1** and **AMOF-1**. **(b)** Photographs of solid samples of **CsPbX$_3$@AMOF-1** under ambient and UV light. **I: CsPbCl$_3$@AMOF-1**; **II: CsPbCl$_x$Br$_{3-x}$@AMOF-1**; **III: CsPbBr$_3$@AMOF-1**; **IV: CsPbBr$_x$I$_{3-x}$@AMOF-1**; **V: CsPbI$_3$@AMOF-1**. **(c)** Emission spectra of **I-V**. **(d)** Dispersions of **CsPbX$_3$@AMOF-1** in acetonitrile under room light and UV light.

size (**Fig. 3(c)**). Owing to stabilization of the PQDs on the AMOF template, quantum confinement effect is at play in the composites.[42-43] This is established by the blue-shift in the emission maximum of **CsPbBr₃@AMOF-1** from that in **CsPbBr₃_mc** and the uniformity in size also ensures a sharp narrow peak.[31] According to a calculation by Protesescu, *et al*., the exciton Bohr diameter of the $CsPbCl_3$, $CsPbBr_3$ and $CsPbI_3$ are 5, 7 and 12 nm, respectively.[8] In order to behave like a PQD, the semiconductor NCs should have diameters lower than their exciton Bohr diameter.[8] Hence clearly, in case of **CsPbX₃@AMOF-1**, the nanocrystals which are 2-9 nm in diameter are indeed highly luminescent PQDs formed by the confinement effect of the MOF structure.

4B.3.3 Energy Transfer in CsPbBr₃@AMOF-1

The emission peak of **AMOF-1** is a broad band with a maximum at 420 nm whose tail extends till 580 nm (**Fig. 6(a)**). Hence it finds an overlap with the absorbance of $CsPbBr_3$, giving rise to the possibility of energy transfer from donor **AMOF-1** host to PQD. True to our conjecture, upon exciting **CsPbBr₃@AMOF-1** at 320 nm (absorbance MOF), the emission of the pristine **AMOF-1** at 420 nm is almost quenched (**Fig. 6(a)**), however it yields very high intensity emission peak with a maximum at 515 nm corresponding to $CsPbBr_3$. In addition, the direct excitation at
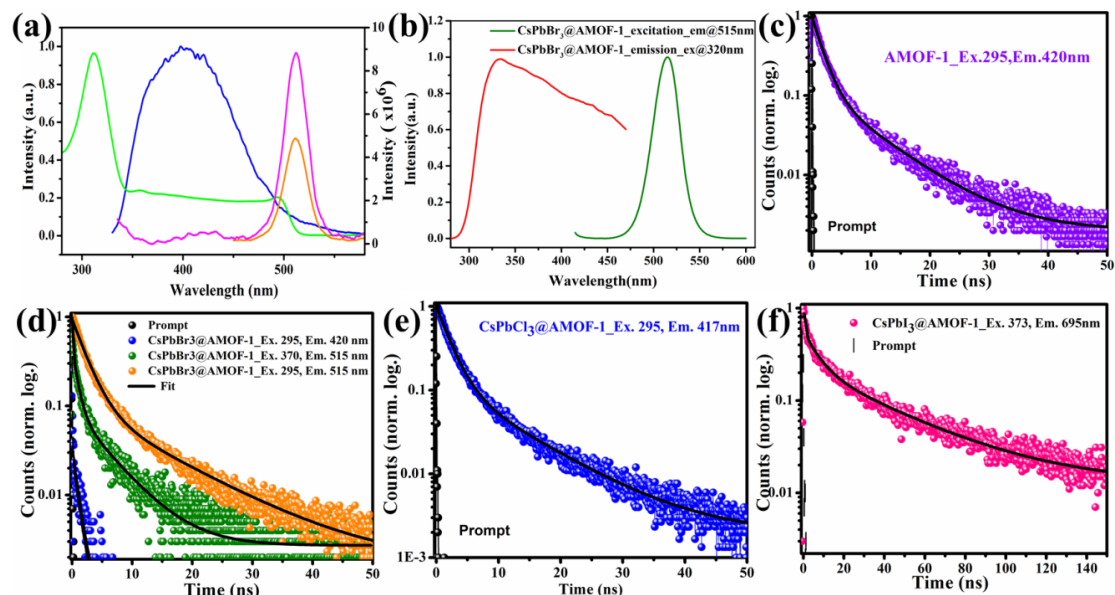
Fig. 6 (a) Energy transfer process in **CsPbBr₃@AMOF-1**. **Green:** Absorbance spectrum of **CsPbBr₃@AMOF-1**, **Blue:** Emission spectrum of **AMOF-1**; **Pink and orange:** Emission spectra of **CsPbBr₃@AMOF-1** excited at 320 and 400 nm, respectively. **(b)** Excitation spectrum of **CsPbBr₃@AMOF-1**. Fluorescence decay profiles for **(c) AMOF-1, (d) CsPbBr₃@AMOF-1, (d) CsPbCl₃@AMOF-1, (d) CsPbI₃@AMOF-1.**

400 nm shows less intensity of the 515 nm peak compared to indirect excitation at 320 nm, clearly indicating a light harvesting phenomenon through FRET mechanism (**Fig. 6(a)**). This is further supported by the excitation spectrum of the 515 nm peak of **CsPbBr$_3$@AMOF-1** which shows a maximum at ~320 nm, clearly suggesting the contribution of MOF to the observed PQD emission (**Fig. 6(b)**). The transfer of energy from the framework to encapsulated CsPbBr$_3$ is also evident from the time-resolved photoluminescence decays of **CsPbBr$_3$@AMOF-1**. The original **AMOF-1** emission at 420 nm shows a lifetime of 4.25 ns, which is reduced to 0.01 ns in **CsPbBr$_3$@AMOF-1** (**Fig. 6(c)**). Moreover, the 515 nm peak corresponding to acceptor CsPbBr$_3$ shows a lifetime of 7.97 ns when excited at 295 nm (**Fig. 6(d)**). However, when excited directly at 370 nm, a shortening emission lifetime (3.3 ns) is observed, as compared to indirect excitation (**Fig. 6(d)**). When excited at wavelength 295 nm, the 417 nm peak of **CsPbCl$_3$@AMOF-1** shows an average lifetime of 6.11 ns (**Fig. 6(e)**) and the 695 nm emission peak of **CsPbI$_3$@AMOF-1** show a lifetime of 30.3 ns, when excited at 370 nm (**Fig. 6(f)**). **CsPbBr$_3$@AMOF-1** records a quantum yield of 14%. In addition to **CsPbX$_3$@AMOF-1**, we have been also able to synthesize two intermediates **CsPbCl$_x$Br$_{3-x}$@AMOF-1** and **CsPbBr$_x$I$_{3-x}$@AMOF-1** which show emission maxima at 458 nm and 548 nm, respectively (**Fig. 5(b,c)**). **CsPbCl$_x$Br$_{3-x}$@AMOF-1** is synthesized by grinding **CsPbCl$_3$@AMOF-1** and **CsPbBr$_3$@AMOF-1** together, whereas **CsPbBr$_x$I$_{3-x}$@AMOF-1** is synthesized by grinding **CsPbBr$_3$@AMOF-1** and **CsPbI$_3$@AMOF-1** together. We observed an interesting anion exchange feature as well, where **CsPbBr$_3$@AMOF-1** upon grinding with CsI completely converts to **CsPbI$_3$@AMOF-1**, as evident from the complete conversion of the emission colour from green to red (**Fig. 7**). This indicates towards a facile anion exchange in case of the perovskite nanocrystals, assisting in easy inter-conversion and hence, colour-tuning.
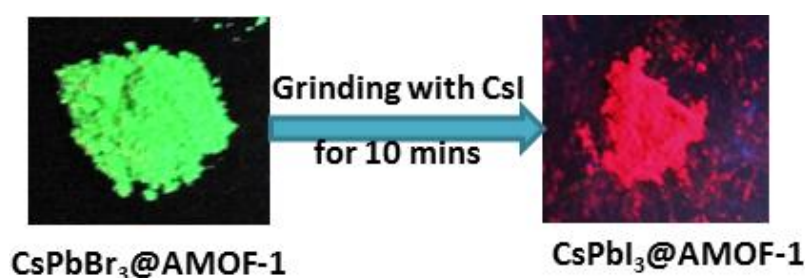
Fig. 7 Conversion of **CsPbBr$_3$@AMOF-1** to **CsPbI$_3$@AMOF-1** by facile anion exchange.

4B.3.4 Stability and Processibility of CsPbX₃@AMOF-1

One of the most important features of the **CsPbX₃@AMOF-1** composites is their exceptional robustness owing to caging by the framework which makes them lucrative for several applications. The solvent stability of the composite material was tested by immersing the solid **CsPbBr₃@AMOF-1** in different solvents over long periods of time while checking the emission intermittently. The emission intensity is found to be same in acetonitrile, toluene and dimethylformamide even after two weeks (**Fig. 8(a,b)**). However, **CsPbBr₃_mc** loses its emission even when exposed to air for more than 24 hrs and its stability in the different solvents is only for a few hours (**Fig. 8(c)**). This clearly elucidates that the AMOF template strengthens the perovskite QDs with superior stability in different medium and thus they can be easily processable for a variety of applications. Although the emission is quenched immediately when **CsPbBr₃@AMOF-1** is immersed in water, the
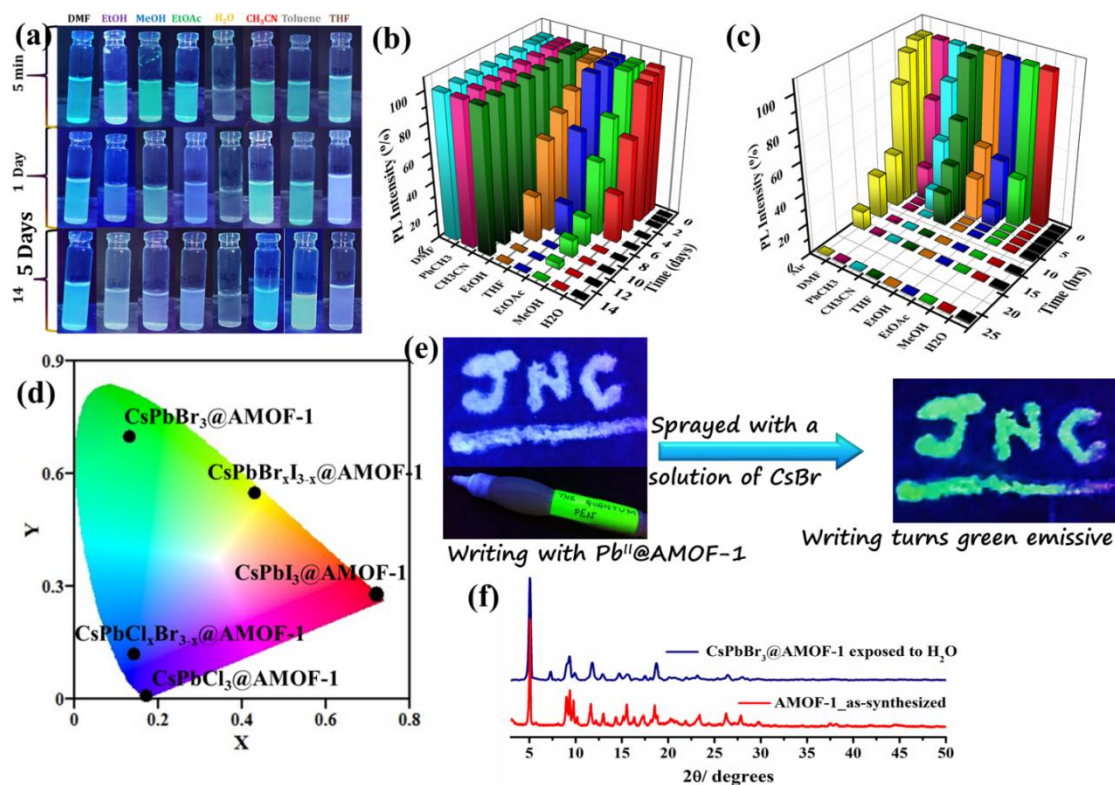
Fig. 8(a) Photograph of dispersion of **CsPbBr₃@AMOF-1** in different solvents under a UV light over several days. **(b)** Stability of emission of **CsPbBr₃@AMOF-1** dispersed in different solvent over 14 days. **(c)** Stability of emission of **CsPbBr₃_mc** dispersed in different solvent over 14 days. **(d)** Emission of the **CsPbX₃@AMOF-1** samples plotted on a CIE chromaticity coordinates. **(e)** Colour tunability and easy processiblity in this composite material displayed by writing with a pen containing **Pbᴵᴵ@AMOF-1** and then spraying it with CsBr. **(f)** PXRD pattern of **CsPbBr₃@AMOF-1** after being immersed in water, which shows that the **AMOF-1** framework is intact and can be reused.

framework remains intact and can be reused, as is evident from the PXRD pattern obtained after exposure to water (**Fig. 8(f)**). This is also an evidence that the formation of the PQDs do not disrupt the structural integrity of the framework.

In order to illustrate the processibility and application of **CsPbBr₃@AMOF-1**, we attempted the development of a colour changing security ink exploiting the simple synthetic technique of the PQD@MOF composite and its supreme stability. We dispersed **Pb**^{II}**@AMOF-1** in toluene and inserted it into the ink chamber of a roller ball pen (**Fig. 8(e)**) and wrote with it on a piece of paper. This writing shows a pale blue emission under UV lamp. As soon as the writing is sprayed with a CsBr solution, the writing turns green emissive and conspicuous owing to the formation of CsPbBr₃. Hence this is a highly processable material which can be used for easy colour tunability and can find applications in security ink. The emission of the **CsPbX₃@AMOF-1** samples and the intermediates when plotted on CIE chromaticity covers a wide colour gamut (**Fig. 8(d)**).[5,8]

4B.4 Conclusion

In conclusion, in this work, we have demonstrated a simplistic green approach for the sustainable solvent-free synthesis of PQDs confined on the MOF template with high stability and exciting optoelectronic properties. The AMOF structure restricts the size of the QDs and determines their luminescent properties. Energy transfer is also observed from the framework to the encapsulated CsPbBr₃ QDs. The AMOF template also renders supreme stability to the PQDs, making stable dispersion in a variety of solvents, thereby enhancing their processability. This work is remarkable since it does not involve the several environmentally hazardous organic reagents traditionally used for the synthesis of halide perovskite quantum dots. Thus this method can be further used for the synthesis of a library of such composites for various specific applications owing to their intense luminescence and solvent stability.

4B.5 References

1. A. Kojima, K. Teshima, Y. Shirai and T. Miyasaka, *J. Am. Chem. Soc.* 2009, **131**, 6050.

2. Y. Dong, T. Qiao, D. Kim, D. Parobek, D. Rossi and D. H. Son, *Nano Lett.*, 2018, **18**, 3716.

3. M. Leng, Z. Chen, Y. Yang, Z. Li, K. Zeng, K. Li, G. Niu, Y. He, Q. Zhou and J. Tang, *Angew. Chem. Int. Ed.* 2016, **55**, 15012.

4. V. K. Ravi, N. Singhal and A. Nag, *J. Mater. Chem. A* 2018, **6**, 21666.

5. M. V. Kovalenko, L. Protesescu and M. I. Bodnarchuk, *Science* 2017, **358**, 745.

6. T. Chiba, K. Hoshi, Y.-J. Pu, Y. Takeda, Y. Hayashi, S. Ohisa, S. Kawata and J. Kido, *ACS Appl. Mater. Interfaces* 2017, **9**, 18054.

7. F. Locardi, M. Cirignano, D. Baranov, Z. Dang, M. Prato, F. Drago, M. Ferretti, V. Pinchetti, M. Fanciulli, S. Brovelli, L. De Trizio and L. Manna, *J. Am. Chem. Soc.* 2018, **140**, 12989.

8. L. Protesescu, S. Yakunin, M. I. Bodnarchuk, F. Krieg, R. Caputo, C. H. Hendon, R. X. Yang, A. Walsh and M. V. Kovalenko, *Nano Lett.* 2015, **15,** 3692.

9. X. Sheng, Y. Liu, Y. Wang, Y. Li, X. Wang, X. Wang, Z. Dai, J. Bao and X. Xu, *Adv. Mater.* 2017, **29**, 1700150.

10. J. Y. Woo, Y. Kim, J. Bae, T. G. Kim, J. W. Kim, D. C. Lee and S. Jeong, *Chem. Mater.* 2017, **29**, 7088.

11. H-Ch. Wang, S-Y. Lin, A-C. Tang, B. P. Singh, H-C. Tong, C-Y. Chen, Y-C. Lee, T-L. Tsai and R-S. Liu, *Angew. Chem. Int. Ed.* 2016, **55**, 7924.

12. Y. Dong, Y. Zhao, S. Zhang, Y. Dai, L. Liu, Y. Li and Q. Chen, *J. Mater. Chem. A***,** 2018, **6**, 21729.

13. H. Huang, M. I. Bodnarchuk, S. V. Kershaw, M. V. Kovalenko, and A. L. Rogach, *ACS Energy Lett.* 2017, **2**, 2071.

14. F. Krieg, S. T. Ochsenbein, S. Yakunin, S. t. Brinck, P. Aellen, A. Süess, B. Clerc, D. Guggisberg, O. Nazarenko, Y. Shynkarenko, S. Kumar, C-J. Shih, I. Infante and M. Kovalenko, *ACS Energy Lett.* 2018, **3**, 641.

15. S. Bai, Z. Yuan and F. Gao, *J. Mater. Chem. C*, 2016, **4**, 3898.

16. M. Yarema, O. Yarema, W. M. M. Lin, S. Volk, N. Yazdani, D. Bozyigit and V. Wood, *Chem. Mater.* 2017, **29**, 796.

17. V. K. Ravi, R. A. Scheidt, J. DuBose and P. V. Kamat, *J. Am. Chem. Soc.* 2018, **140**, 8887.

18. H. Parala, H. Winkler, M. Kolbe, A. Wohlfart, R. A. Fischer, R. Schmechel, H. von Seggern, *Adv. Mater.* 2000, **12**, 1050.

19. V. Malgras, S. Tominaka, J. W. Ryan, J. Henzie, T. Takei, K. Ohara and Y. Yamauchi, *J. Am. Chem. Soc.* 2016, **138**, 13874.

20. J. Aguilera-Sigalat and D. Bradshaw, *Coord. Chem. Rev.* 2016, **307**, 267.

21. S. Huang, Z. Li, L. Kong, N. Zhu, A. Shan and L. Li, *J. Am. Chem. Soc.* 2016, **138**, 5749.

22. S. Roy, A. Chakraborty and T. K. Maji, *Coord. Chem. Rev.* 2014, **273-274**, 139.

23. S. Kitagawa, R. Kitaura and S.-i. Noro, *Angew. Chem. Int. Ed.* 2014, **43**, 2334.

24. S. Bhattacharyya, C. Das and T. K. Maji, *RSC Adv.* 2018, **8**, 26728.

25. C. Zhang, B. Wang, W. Li, S. Huang, L. Kong, Z. Li and L. Li, *Nat. Commun.* 2017, **8**, 1138.

26. S. Jin, H-J. Son, O. K. Farha, G. P. Wiederrecht and J. T. Hupp, *J. Am. Chem. Soc.* **2013**, *135*, 955.

27. Z. Chen, Z-G. Gu, W-Q. Fu, F. Wang and J. A. Zhang, *ACS Appl. Mater. Interfaces*, 2016, **8**, 28737.

28. H. He, Y. Cui, B. Li, B. Wang, C. Jin, J. Yu, L. Yao, Y. Yang, B. Chen and G. Qian, *Adv. Mater.* 2018, 1806897.

29. D. Zhang, Y. Xu, Q. Liu and Z. Xia, *Inorg. Chem.* 2018, **57**, 4613.

30. K. Mandel, T. Granath, T. Wehner, M. Rey, W. Stracke, N. Vogel, G. Sextl and K. Muller-Buschbaum, *ACS Nano*, 2017, **11**, 779.

31. P. Pal, S. Saha, A. Banik, A. Sarkar and K. Biswas, *Chem. Eur. J.* 2018, **24**, 1811.

32. C. C. Stoumpos, C. D. Malliakas and M. G. Kanatzidis, *Inorg. Chem.* 2013, **52**, 9019.

33. D. Prochowicz, M. Franckevičius, A. M. Cieślak, S. M. Zakeeruddin, M. Grätzel and J. Lewiński, *J. Mater. Chem. A*, 2015, **3**, 20772.

34. A. D. Jodlowski, A. Ypez, R. Luque, L. Camacho and G. de Miguel, *Angew. Chem. Int. Ed.* 2016, **55**, 14972.

35. L. Liu, X.-N. Zhang, Z.-B. Han, M.-L. Gao, X.-M. Cao and S.-M. Wang, *J. Mater. Chem. A*, 2015, **3**, 14157.

36. X.-X. Jia, R.-X. Yao, F.-Q. Zhang and X.-M. Zhang, *Inorg. Chem.* 2017, **56**, 2690.

37. J. Li, H.-R. Fu, J. Zhang, L.-S. Zheng and J. Tao, *Inorg. Chem.* 2015, **54**, 3093.

38. J. Yu, Y. Cui, C. Wu, Y. Yang, Z. Wang, M. OKeeffe, B. Chen and G. Qian, *Angew. Chem. Int. Ed.* 2012, **51**, 10542.

39. S. Bhattacharyya, A. Chakraborty, K. Jayaramulu, A. Hazra and T. K. Maji, *Chem. Commun.* 2014, **50**, 13567.

40. A. Chakraborty, S. Bhattacharyya, A. Hazra, A.C. Ghosh and T. K. Maji, *Chem. Commun.* **2016**, *52*, 2831.

41. S. Wei, Y. Yang, X. Kang, L. Wang, L. Huang and D. Pan, *Chem. Commun.* 2016, **52**, 7265.

42. J. A. Sichert, Y. Tong, N. Mutz, M. Vollmer, S. Fischer, K. Z. Milowska, R. G. Cortadella, B. Nickel, C. Cardenas-Daw, J. K. Stolarczyk, A. S. Urban and J. Feldmann, *Nano Lett.* 2015, **15**, 6521.

43. L. Polavarapu, B. Nickel, J. Feldmann and A. S. Urban, *Adv. Energy Mater.* 2017, **7**, 1700267.

Chapter 4C

Facile Mechanochemical Synthesis of MAPbBr$_3$ Perovskite Quantum Dots from a Perovskite MOF
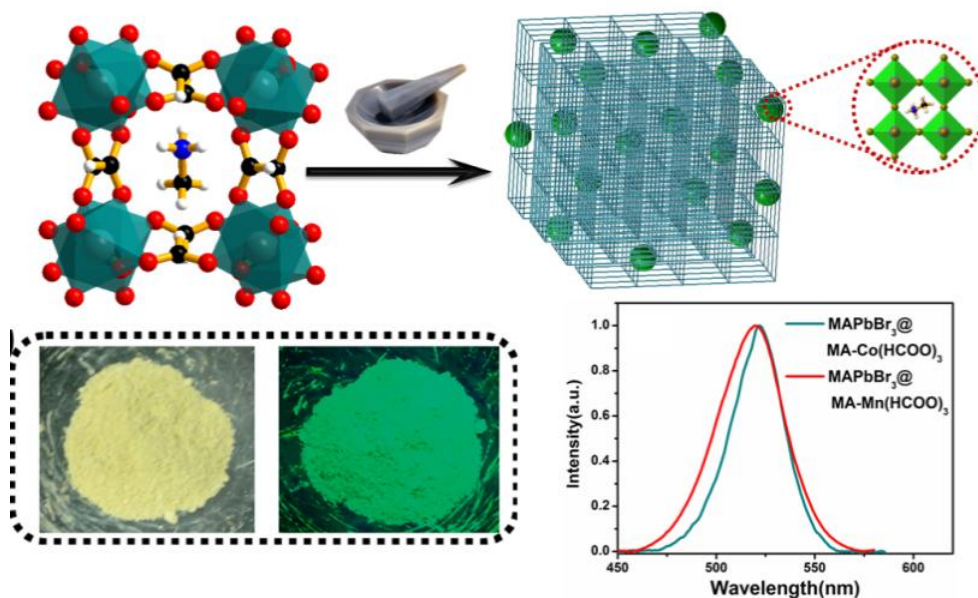
Abstract

T his chapter describes the one step mechanochemical stabilization of hybrid organic-inorganic lead halide (MAPbBr$_3$) perovskite quantum dots (PQDs) within a perovskite metal-organic framework (MOF) MA-M(HCOO$_3$) [M = Mn, Co; MA = methylammonium (CH$_3$NH$_3^+$)], without the use of any external reagents or solvents. The perovskite MOF template is the source of MA cations and hence this is a simple green approach towards the synthesis of PQD@MOF composite. MAPbBr$_3$@MA-Mn(HCOO)$_3$ composite shows high stability in several solvents as well as the signature of photoelectrochemical activity in the presence of light.

4C.1 Introduction

The recent times have seen burgeoning interest in the synthesis of lead halide perovskites[1] in the form of thin films, micro and nanocrystals is due to their potential applications in high efficiency photovoltaic cells,[2, 3] light emitting diodes,[3-5] lasers[6, 7] and photo-detectors.[8,9] Colloidal organic-inorganic hybrid lead halide perovskite ($CH_3NH_3PbX_3$) quantum dots (PQDs) have emerged as one of the most promising opto-electronic materials for incorporation in various opto-electronic devices because of their intriguing electronic properties and intense luminescence.[8, 10-21] Recent research work has also been able to increase the quantum yields of MAPbBr$_3$ perovskite quantum dots such that they are approaching unity.[22-24] Quantum confinement of such semiconductor quantum dots offers interesting behaviour, such as bandgap expansion, increased paired charges, coulombic attraction, energy level quantization, and slower electron-phonon relaxation, when the nanocrystal radius is less than the exciton Bohr radius.[16] Usually, PQDs are highly unstable in most of polar organic solvents and water, which is a major impediment towards their processibility and applications.[1] Traditionally, these methyl ammonium (MA, $CH_3NH_3^+$) lead bromide (MAPbBr$_3$) PQDs are synthesized using various methods like hot injection technique,[25] template based method,[16, 26] ligand assisted reprecipitation technique,[27] non-aqueous emulsion synthesis,[28] etc. The synthetic conditions demanded by these methods are not only very harsh, involving high temperatures on hazardous organic reagents, but also are extremely expensive. Hence, efficient, cost-effective methods for the synthesis of processable MAPbBr$_3$ QDs are highly sought after. In this context, mechanochemical synthesis seems to be extremely advantageous as it is very simple, and does not involve extreme reaction conditions or organic solvents and is also economically viable.[29] In spite of the simplistic nature of the mechanochemical process, attaining homogeneous nanocrystals with a uniform phase using this method is a rather daunting task owing to the lack of control nanocrystals growth. This hurdle can be overcome by utilizing a perovskite MOF as a template in which MA cations are already well distributed within the pores,[30] having weak non-covalent interactions with the MOF.[30] Upon grinding with PbBr$_2$, these non-covalent interactions weaken owing to the stronger interaction of MA with PbBr$_2$. Moreover, the competitive interactions between MOF or PbBr$_2$ and MA might assist the formation of quantum dots. Of late, organic-ammonium metal formate based perovskite MOFs have emerged as a relatively small, but unique class of MOFs and garnered great interest due to
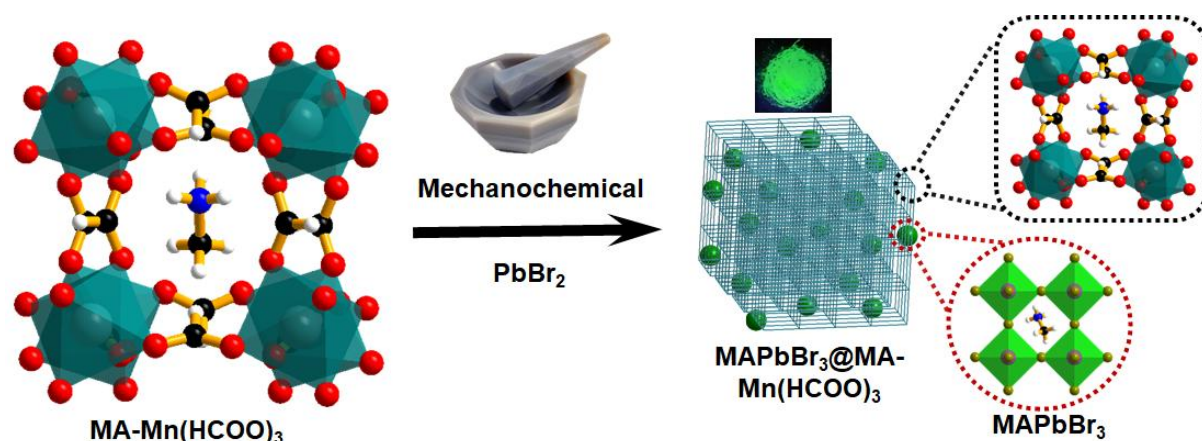
Scheme 1. Synthetic strategy for the synthesis of MAPbBr$_3$ QDs on perovskite MOF (MAPbBr$_3$@MA-Mn(HCOO)$_3$) via solvent free mechanochemical grinding.

their electric and magnetic properties.[31-41] Keeping in view of these considerations, we have focused on the synthesis of MAPbBr$_3$ PQDs on a perovskite metal-organic framework (MOF) *via* solid state mechanochemical grinding process.

In this chapter, a single step mechanochemical synthesis of MAPbBr$_3$ QDs on perovskite MOFs in the presence of PbBr$_2$ *via* a single step solid state mechanochemical grinding process towards the synthesis of PQDs@MOF nanocomposites has been described. Here, we have utilized MA-M(HCOO)$_3$, (M = Mn and Co) perovskite MOFs as template as well as the source for MA for stabilization of MAPbBr$_3$ QDs on the MA-M(HCOO)$_3$. To the best of our knowledge, mechanochemical synthesis of MAPbBr$_3$ QDs is yet to be documented. Perovskite-MOF composites containing MAPbBr$_3$ QDs are found to be stable in most of the solvents except water. Also, ion exchange of MAPbBr$_3$@MA-Mn(HCOO)$_3$ with iodide ion and gram scale synthesis of MAPbBr$_3$@MA-Mn(HCOO)$_3$ was achieved. Therefore, MAPbBr$_3$@MA-Mn(HCOO)$_3$ composite is prominent material containing superior stability compare to MAPbBr$_3$ QDs and the mechanochemical approach and its results are unprecedented.

4C.2 Experimental Section

4C.2.1 Materials

All the materials used were obtained from Sigma Aldrich Co. and were used as procured without further purification. All the solvents were obtained from Spectrochem Co.

4C.2.3 Synthesis of Methylammonium metal formates [MA-M(HCOO)₃]

We followed a previously reported strategy for the preparation of the perovskite MOF[1] [MA-M(HCOO)₃] (methylammonium metal formate, M= Mn and Co). Methanolic solutions of formic acid (0.5 M, 5 mL) and methylamine (0.5M, 5 mL) were mixed in a glass vial. To this, methanol (2 mL) followed by methanolic solution of $MnCl_2$ or $Co(NO_3)_2$ (0.1 M, 8 mL) was carefully added. The vial was kept undisturbed for a few days for crystallization. The solid MOF obtained was later filtered, washed with methanol and dried at 60 °C.

MA-Mn(HCOO)₃ : Anal. Calcd. C, 21.64; H, 4.09; N, 6.31%. Found: C, 21. 58; H, 4.06, N, 6.31%. FTIR (KBr pellet, 4000−400 cm^{-1}): 3117 (b), 3034 (sh), 2967 (sh), 2880 (m), 2607 (w), 2484 (w), 1645 (sh), 1596 (s), 1519 (sh), 1459 (w), 1422 (w) 1385 (sh), 1361 (s), 997 (w), 971(w), 797 (s).

MA-Co(HCOO)₃ : Anal. Calcd. C, 21.25; H, 4.01; N, 6.20%. Found: C, 20.80; H, 3.90, N, 5.83%. FTIR (KBr pellet, 4000−400 cm^{-1}): 3135 (b), 3038 (sh), 2970 (sh), 2881 (m), 2782 (w), 2615 (w), 1647 (sh), 1591 (s), 1523 (sh), 1460 (w), 1376 (sh), 1356 (s), 972 (w), 810 (s), 763 (w), 734 (w), 571 (w).

4C.2.4 Mechanochemical synthesis of perovskite-MOF composite (MAPbBr₃ QDs@MA-M(HCOO)₃)

50 mg of the obtained MOF was grinded with 5 mg of $PbBr_2$ using pestle and mortar. Change in colour to yellow was observed immediately within 2 minutes of grinding indicating the formation of $MAPbBr_3$. The mixture was grinded for 10 minutes to ensure uniform distribution. Green emission was observed from the mixture when subjected to UV light. The sample was then washed with ethanol. The resulting composites have been characterized by PXRD and by different spectroscopic and microscopic imaging techniques.

4C.2.5 Synthesis of MAPbBr₃ Quantum Dots

MAPbBr₃ QDs were synthesized by adopting ligand assisted reprecipitation technique (LARP) method.[2] A mixture of 0.16 mmol CH_3NH_3Br and 0.2 mmol $PbBr_2$ was dissolved in 5 mL of DMF with 20 μL of n-octylamine and 0.5 mL of oleic acid to form a precursor solution. 2 mL of this precursor solution was dropped into 10 mL of

vigorously stirring Toluene to obtain the colloidal solution of quantum dots. It was immediately centrifuged under 7000 rpm for 10 minutes to separate the quantum dots from the bulk. The quantum dots have been characterized using PXRD and different spectroscopic techniques.

4C.2.6 Gram Scale synthesis of MAPbBr$_3$@MA-Mn(HCOO)$_3$

Since the strategy to prepare MAPbBr$_3$@MA-Mn(HCOO)$_3$ on a small scale was successful, we aimed at synthesis of MAPbBr$_3$@MA-Mn(HCOO)$_3$ on a large scale. 1.5 g of the MOF was prepared by scaling up the above mentioned reaction procedure by 10 folds. 1 g of MOF was grinded with 50 mg of PbBr$_2$. Within minutes, appearance of emission was observed and was thoroughly grinded for nearly an hour and washed with Ethanol. The synthesized sample has been characterized using PXRD and other spectroscopic techniques.

4C.2.7 Ion exchange of MAPbBr$_3$@MA-Mn(HCOO)$_3$ with Iodide ion

55 mg of previously obtained MAPbBr$_3$@MA-Mn(HCOO)$_3$ was grinded with 5 mg of potassium iodide (KI). Again, there was a change in colour which when subjected to UV light gave pink colour indicating exchange of bromide ions in the perovskite with iodide ions to form methylammonium iodide PQDs.

4C.2.8 Physical Measurements

The elemental analysis was carried out using a Thermo Fischer Flash 2000 Elemental Analyzer. Powder X-ray diffraction (PXRD) was recorded by using Cu-Kα radiation (Bruker D8 Discover; 40 kV, 30 mA). IR spectra of the compounds were recorded with a Bruker IFS 66v/S spectrophotometer using the KBr pellets in the region 4000−400 cm^{-1}. Transmission electron microscopy (TEM) analysis has been performed using a JEOL JEM-3010 with an accelerating voltage at 300 kV or a FEI TECNAI G2 20 STWIN TEM operating at 200 kV. One drop of the samples dispersed in ethanol solution was taken in a holey carbon coated Cu grid for TEM imaging.

4C.2.9 Photoelectrochemical (PEC) Performance

5 mg of MAPbBr$_3$@MA-M(HCOO)$_3$ in 70 µl IPA (isopropyl alcohol) was dispersed via sonication (5 min) and vortexer (5 min) then 4 µl of binder (nafion) was

added and vortexed for 10 min followed by 3 min sonication. We have used 20 µl mixture to dropcast it on ITO (1.0 cm × 0.6 cm) and dried at room temperature. MAPbBr$_3$@MA-M(HCOO)$_3$ on ITO used as electrode to perform the PEC (photoelectrochemical) performance in the presence of light/dark and electrolyte is 0.1 M tetrabutylammonium hexafluorophosphate in ACN.

4C.3 Results and Discussions

4C.3.1 Characterization of MAPbBr$_3$@MA-M(HCOO)$_3$

The perovskite MOF MA-M(HCOO)$_3$ was synthesized by a reported procedure. The MOFs have the general formula of $[A^I][M^{II}(HCOO)_3]$ where A= methylammonium (MA), whereas M^{II} can be either Mn or Co, which have been used for the construction of the perovskite MOF. For this purpose, we have first prepared the perovskite MOF MA-M(HCOO)$_3$ (M= Mn or Co) by layering a methanolic solution of Mn^{II} or Co^{II} salt over a mixture of methylamine and formic acid in methanol.[30,41] MA-Mn(HCOO)$_3$ crystalizes in *Pnma* space group, where each Mn^{II} centre is octahedrally connected with six formate ligands which further bridge six Mn^{II} ions in all the directions to form a 3D framework.[30] MA cations are located within the cavities of this NaCl type framework formed by the extension of Mn-formate octahedral (**Fig. 1(a)**).[30] The MA cations are further stabilized by the weak non-covalent hydrogen bonds (N–H···O and C–H···O) between its N–H and C–H groups and the oxygen atoms from the formate linkers of the framework. MA-Co(HCOO)$_3$ is also iso-structural to MA-Mn(HCOO)$_3$ as is proven by the identical PXRD pattern (**Fig. 1(b)**). The phase purity and structural integrity of these frameworks were ensured by matching its PXRD pattern with the simulated one from the previous reports. The MA cations of these frameworks are used to grow MAPbX$_3$ PQDS by simply grinding the framework with PbBr$_2$ (**Scheme 1**) at room temperature and open atmosphere to yield the PQD@MOF composites MAPbBr$_3$@MA-M(HCOO)$_3$. The formation of the MAPbBr$_3$ PQDs is marked by the appearance of a bright green luminescence that is observed under the UV light immediately upon grinding the framework with PbBr$_2$. The formation of MAPbBr$_3$ within the MOF is ascertained by the PXRD pattern where both the peaks for the MOFs as well as MAPbBr$_3$ peaks are observed (**Fig. 1(b)**). Most remarkably, the peaks observed at 2θ= 30.1, 33.7 and 43.08° in the PXRD pattern of the composite corresponds to the (200), (210), (220) planes of
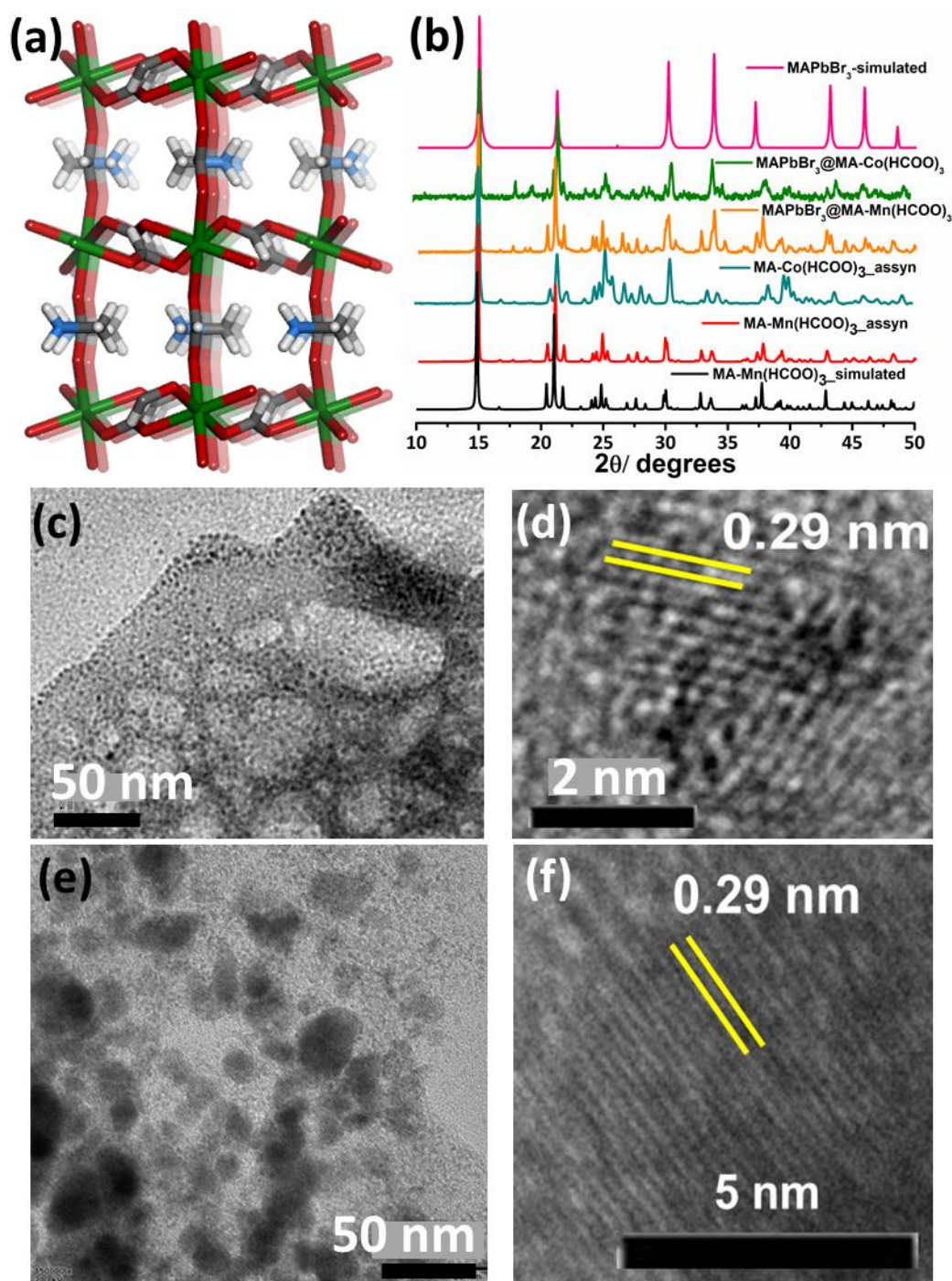
Fig. 1(a) Structure of MA-M(HCOO)$_3$ MOF. **(b)** PXRD patterns of MA-M(HCOO)$_3$ and MAPbBr$_3$@MA-M(HCOO)$_3$ samples. **(c)** TEM and **(d)** HRTEM images of MAPbBr$_3$@MA-Mn(HCOO)$_3$. **(e)** TEM and **(f)** HRTEM images of MAPbBr$_3$@MA-Co(HCOO)$_3$.

pristine orthorhombic MAPbBr$_3$. The synthesized MAPbBr$_3$@MA-Mn(HCOO)$_3$ composite is observed using various microscopic techniques like FESEM and TEM. Under TEM, we observe the MAPbBr$_3$ PQDs are strewn uniformly over the layers of the MA-Mn(HCOO)$_3$ with diameters between 3-4 nm (**Fig. 1(c)**), whereas those in MA-Co(HCOO)$_3$ have diameters of 8-15 nm (**Fig. 1(e)**). HRTEM of a single PQD in both

cases, show a lattice spacing of 0.29 nm which corresponds to the (200) plane in MAPbBr$_3$ (**Fig. 1(d, f)**). Since in this case, the size of the unit cell of MAPbBr$_3$ is larger than the pore size of the perovskite MOF, the PQDs are stabilized on the surface of the MOF.

4C.3.2 Optical Properties of MAPbBr$_3$@MA-M(HCOO)$_3$

The optical properties of the composite thus synthesized are extensively studied. The absorbance maximum of MAPbBr$_3$@MA-Mn(HCOO)$_3$ suffers a hypsochromic shift from bulk MAPbBr$_3$ sample synthesized in a similar fashion, indicating towards the quantum confinement effect in the composite (**Fig. 2(a)**).[16, 26] Accordingly, a blue shift is also observed in the emission spectrum of the composite where a band is observed at 520 nm upon excitation at 365 nm (**Fig. 2(b)**). Excitation of MAPbBr$_3$@MA-Co(HCOO)$_3$ composite at 365 nm yields emission band having a maximum at 522 nm (**Fig. 2(b)**). The
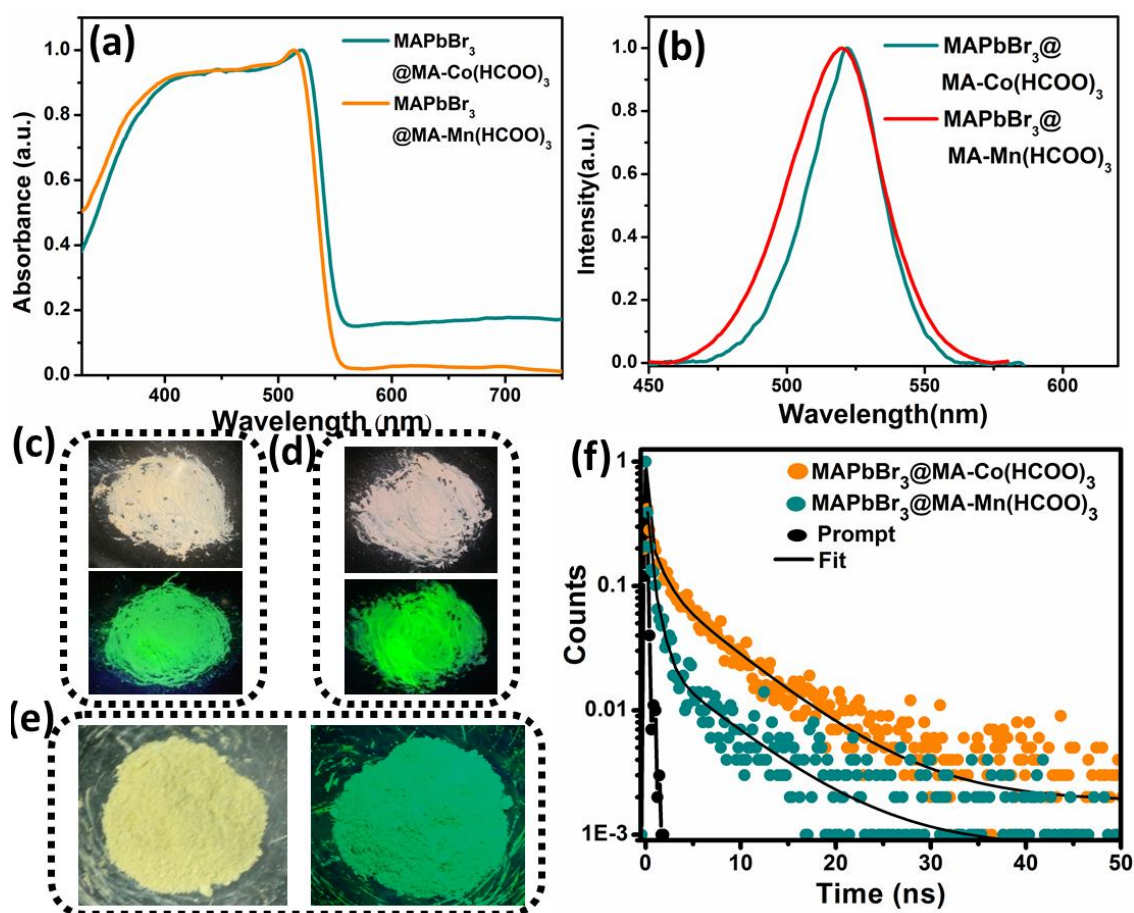
Fig. 2(a) Solid state UV-vis spectra of the MAPbBr$_3$@MA-M(HCOO)$_3$ samples. **(b)** Emission spectra of MAPbBr$_3$@MA-M(HCOO)$_3$ samples. Photographs of **(c)** MAPbBr$_3$@MA-Mn(HCOO)$_3$ and **(d)** MAPbBr$_3$@MA-Co(HCOO)$_3$ under vis and UV light. **(e)** Photograph of gram scale synthesis of MAPbBr$_3$@MA-Mn(HCOO)$_3$. **(f)** Lifetime decays for MAPbBr$_3$@MA-M(HCOO)$_3$ [M = Mn and Co].
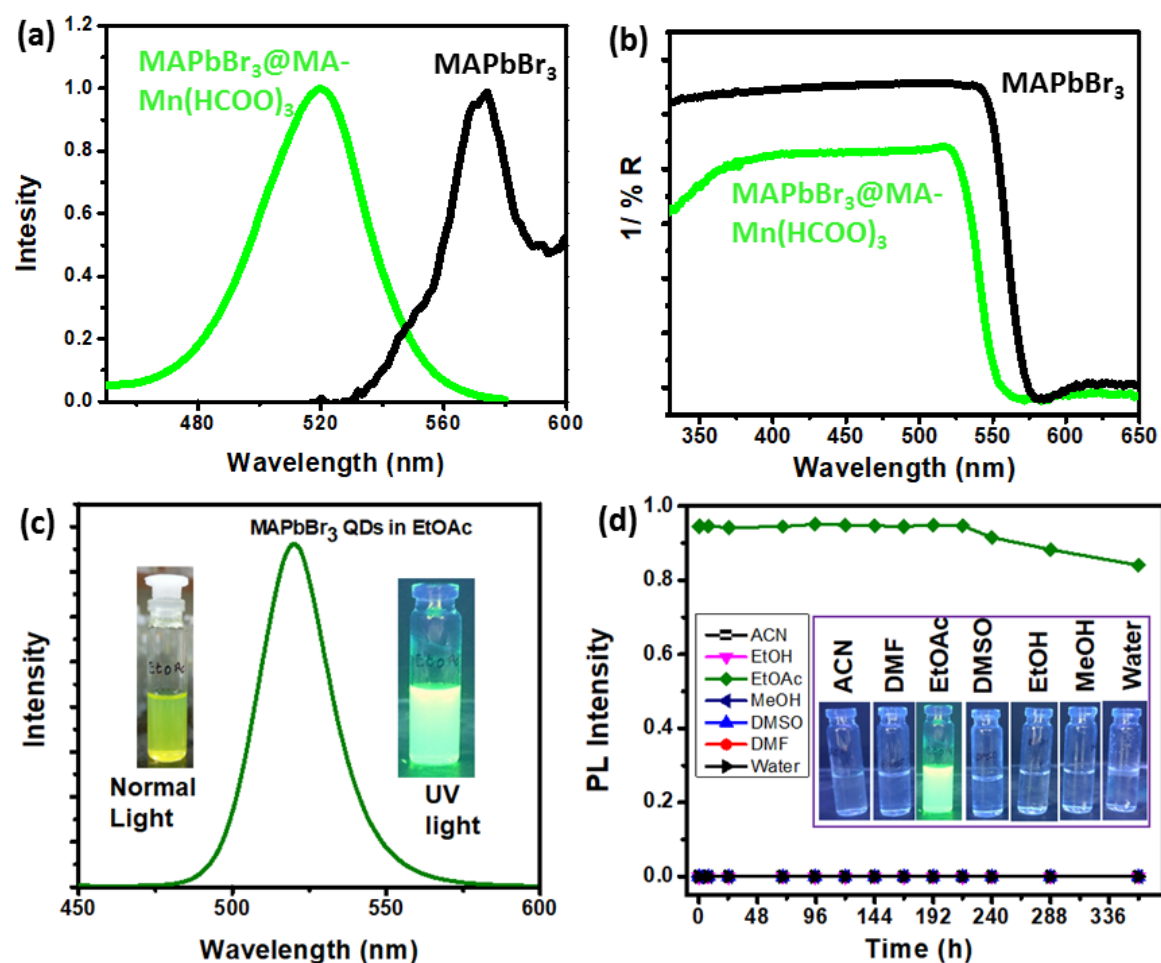
Fig. 3 (a) PL and **(b)** UV-vis spectra of MAPbBr$_3$@MA-Mn(HCOO)$_3$ and MAPbBr$_3$ bulk. **(c)** PL spectrum of MAPbBr$_3$ QDs in EtOAc upon excitation of 365 nm. **(d)** PL intensity changes of MAPbBr$_3$ QDs in different solvents with respect to time. **(inset)** showing photographs of same under UV light.

smaller size of the PQDs in MAPbBr$_3$@MA-Mn(HCOO)$_3$ is reflected in the blue shift of its emission maximum from those of MAPbBr$_3$@MA-Co(HCOO)$_3$. The previous reports of confined MAPbBr$_3$ QDs in mesoporous silica or MOF all show emission maxima between 473 nm to 527 nm. [16, 26, 42, 43] We also employed a solvent mediated method to synthesize pristine MAPbBr$_3$ PQDs with an average diameter of 3.3 nm, a dispersion of which showed the emission at 520 nm in ethylacetate upon excitation of 365 nm (**Fig. 3(a,b)**). This is in accordance with the emission maximum shown by MAPbBr$_3$@MA-Mn(HCOO)$_3$. The time resolved PL spectra of MAPbBr$_3$@M(HCOO)$_3$ manifest a tri-exponential decay where MAPbBr$_3$@MA-Co(HCOO)$_3$ and MAPbBr$_3$@MA-Mn(HCOO)$_3$ have average emission lifetimes of 2.89 ns and 5.22 ns, respectively (**Fig. 2(f)**). It is well known that the emission lifetimes decreases with decreasing size of PQD as a consequence of dominant surface trapping.[7] Accordingly, MAPbBr$_3$@Mn(HCOO)$_3$

shows a shorter lifetime as compared to the MAPbBr$_3$@MA-Co(HCOO)$_3$ (**Table 1**). The absolute Quantum yield (QY) is observed to be 1.4% and 2.6% for MAPbBr$_3$@MA-Co(HCOO)$_3$ and MAPbBr$_3$@MA-Mn(HCOO)$_3$, respectively. This implies that in these composites, the non-radiative decay pathway takes precedence over the radiative pathway, which causes the lower quantum efficiency (**Table 2**).

Table 1. PL lifetime details for MAPbBr$_3$@MA-M(HCOO)$_3$ [M = Mn and Co]

Name	A1(%)	τ_1(ns)	A_2(%)	τ_2 (ns)	A_3(%)	τ_3 (ns)	τ_{avg} (ns)
MAPbBr$_3$@MA-Co(HCOO)$_3$	19.2	0.81	78.9	0.114	1.9	7.15	2.89
MAPbBr$_3$@MA-Mn(HCOO)$_3$	21.5	1.25	11.4	7.1	67.1	0.136	5.22

$$\tau_{avg} \text{ (ns)} = (\Sigma A_i \tau_i^2 / \Sigma A_i \tau_i)$$

Table 2. Excited state features of MAPbBr$_3$@MA-M(HCOO)$_3$ [M = Mn and Co]

Name	Quantum Yield (Φ)	τ_{avg}^{a} (ns)	k_r 10^7 s^{-1}	k_{nr} 10^7 s^{-1}
MAPbBr$_3$@MA-Co(HCOO)$_3$	1.4	2.89	0.48	34.1
MAPbBr$_3$@MA-Mn(HCOO)$_3$	2.6	5.22	0.5	18.7

$^{a}\tau_{avg} = 1/(k_r + k_{nr})$ and $k_r = \Phi/\tau_{avg}$)

4C.3.3 Stability of MAPbBr$_3$@MA-M(HCOO)$_3$

In order to demonstrate the practical synthetic applicability of our approach, we have also performed the gram scale mechanochemical synthesis of MAPbBr$_3$@MA-Mn(HCOO)$_3$. For this purpose, 1 gram of MA-Mn(HCOO)$_3$ MOF is grinded with PbBr$_2$ in the open atmosphere and at room temperature (**Fig. 2(e)**). The mixture emits a bright green luminescence under UV light within 5 mins of grinding indicating towards the formation of MAPbBr$_3$@MA-Mn(HCOO)$_3$. In order to ensure uniformity in size and phase purity, the grinding is continued for an hour and thoroughly washed with ethanol. Hence the simplistic nature of this synthetic strategy underlines the fact that this is ideal for large industrial scale production, without the use of any hazardous organic solvents. The production costs and environmental risks for the bulk scale production of such PQDs *via* a solvent mediated method will be several folds higher owing to the use of a large amount of organic solvents and capping agents used. The use of PQDs are limited by their surface lability and instability in most solvents.[44] While oleic acid stabilized MAPbBr$_3$ PQDs[27] are stable in ethylacetate (EtOAc), they are highly unstable in other solvents such
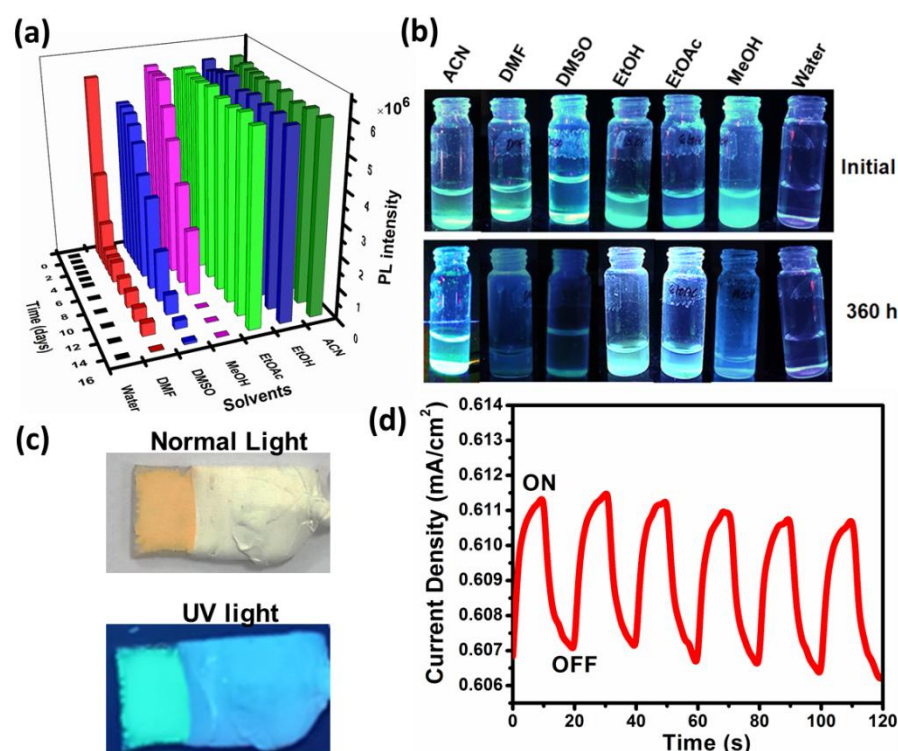
Fig. 4(a) PL intensity changes of MAPbBr$_3$@MA-Mn(HCOO)$_3$ in different solvents with respect to time. **(b)** Photographs of MAPbBr$_3$@MA-Mn(HCOO)$_3$ in various solvents under UV light. **(c)** Photograph of MAPbBr$_3$@MA-M(HCOO)$_3$ photoelectrode under normal light and UV light. **(d)** Amperometric $I-t$ curves plotted at -0.35 V$_{Ag/Ag+}$ under light and dark.

as acetonitrile (ACN), EtOH, DMSO, DMF, MeOH and H$_2$O (**Fig. 3(b,c)**). We checked the stability of MAPbBr$_3$@MA-Mn(HCOO)$_3$ by keeping it immersed in a series of solvents (ACN, EtOAc, EtOH, DMSO, DMF, MeOH and water) over 15 days and the emission spectra were recorded intermittently. It is found that even after 15 days, the emission of MAPbBr$_3$@MA-Mn(HCOO)$_3$ remains unchanged in ACN, EtOAc and EtOH. The emission of the composite also persists in DMSO and MeOH for few days.
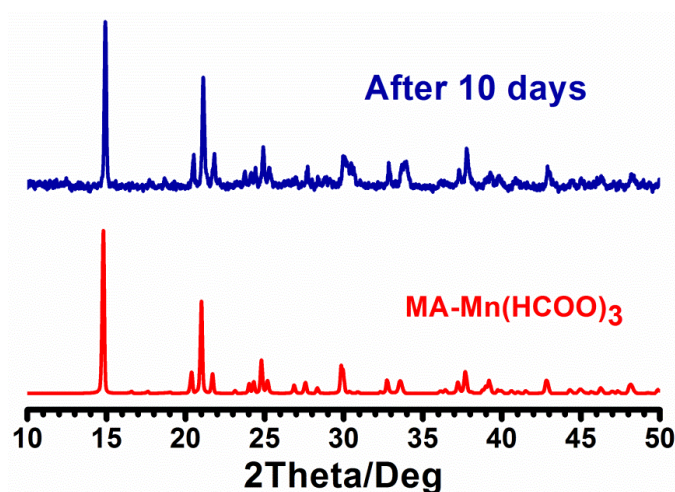
Fig. 5 PXRD pattern of MAPbBr$_3$@MA-Mn(HCOO)$_3$ after keeping it immersed in MeOH for 10 days.
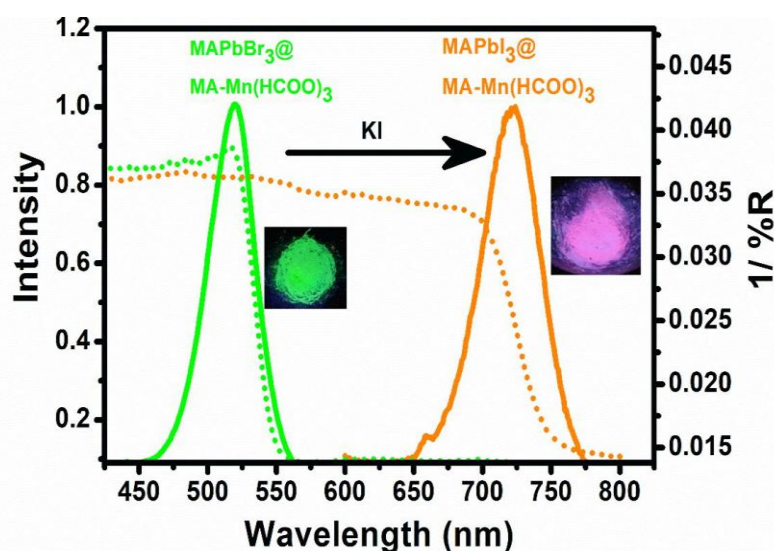
Fig. 6 UV-vis (dotted line) and PL (solid line) spectra of MAPbBr$_3$@MA-Mn(HCOO)$_3$ and MAPbI$_3$@MA-Mn(HCOO)$_3$ [before and after iodide exchange], inset showing corresponding photographs under UV light.

Interestingly, the PXRD pattern of the sample obtained from methanol solution even after 10 days showed the peaks corresponding to MA-Mn(HCOO)$_3$ suggesting the robustness and stability of the MOF structure and also suggests that the MOF can be further used for the stabilization of PQD. (**Fig. 5**). The pristine MAPbBr$_3$ sample does not retain its emission in any solvent for more than a few hours. Its emission is lost even upon exposure to air after a day. Although the direct mechanochemical synthesis of MAPbI$_3$@MA-Mn(HCOO)$_3$ by grinding PbI$_2$ and MA-Mn(HCOO)$_3$ is unsuccessful, we were able to yield MAPbI$_3$@MA-Mn(HCOO)$_3$ by ion exchange. Upon grinding MAPbBr$_3$@MA-Mn(HCOO)$_3$ with a suitable amount of KI, the emission colour changes from green to pink under UV light, which is indicative of the replacement of the bromide ion with iodide ion to form MAPbI$_3$@MA-Mn(HCOO)$_3$ (**Fig. 6**). MAPbI$_3$@MA-Mn(HCOO)$_3$ shows an emission maximum at 720 nm, when excited at 480 nm.

To show the practical applicability of the PQD@MOF composite, we examined the photoelectrochemical (PEC) performances with the help of a photoelectrochemical cell. For this, we prepared a photoelectrode by coating MAPbBr$_3$@MA-M(HCOO)$_3$ on ITO which shows the typical green luminescence of the PQD under UV lamp (**Fig. 4(c)**). The amperometric I–t curves were plotted at -0.35 V$_{Ag/Ag+}$ and it proved that the photocurrent is produced upon switching light on and off (**Fig. 4(d)**). The photocurrent response was observed to be 0.6115 μA cm^{-2}.

4C.4 Conclusion

In conclusion, we have demonstrated a facile green and fast approach to synthesize MAPbBr$_3$@MOF composites using the perovskite MOF MA-M(HCOO)$_3$ (M=Mn and Co) at ambient conditions by simply grinding it with PbBr$_2$, without the use of any other reagents. This simplistic approach is also useful for the bulk production of the composites industrially which was demonstrated by a gram scale synthesis of MAPbBr$_3$@MA-Mn(HCOO)$_3$. By doing away with other solvents, reagents and capping agents, we are not only able to reduce the cost of our synthesis, but we are also able to formulate an environmentally benign green synthetic approach. The MOF template also imparts extra stability to the MAPbBr$_3$ PQDs which is evident in the superior solvent stability of MAPbBr$_3$@MA-Mn(HCOO)$_3$ over oleic acid stabilized MAPbBr$_3$ QDs. Thus this synthetic approach is a sustainable environmental friendly method for the synthesis of solvent stable and processable MAPbBr$_3$ composites for a several applications.

4C.5 References

1. M. V. Kovalenko, L. Protesescu and M. I. Bodnarchuk, *Science*, 2017, **358**, 745.

2. I. Chung, B. Lee, J. He, R. P. H. Chang and M. G. Kanatzidis, *Nature*, 2012, **485**, 486.

3. M. Grätzel, *Nat. Mater.*, 2014, **13**, 838.

4. T. Chiba and J. Kido, *J. Mater. Chem. C*, 2018, **6**, 11868.

5. H.-C. Wang, S.-Y. Lin, A.-C. Tang, B. P. Singh, H.-C. Tong, C.-Y. Chen, Y.-C. Lee, T.-L. Tsai and R.-S. Liu, *Angew. Chem. Int. Ed.*, 2016, **55**, 7924.

6. C.-Y. Huang, C. Zou, C. Mao, K. L. Corp, Y.-C. Yao, Y.-J. Lee, C. W. Schlenker, A. K. Y. Jen and L. Y. Lin, *ACS Photonics*, 2017, **4**, 2281.

7. L.-J. Chen, J.-H. Dai, J.-D. Lin, T.-S. Mo, H.-P. Lin, H.-C. Yeh, Y.-C. Chuang, S.-A. Jiang and C.-R. Lee, *ACS Appl.Mater. Interfaces*, 2018, **10**, 33307.

8. R. Pan, H. Li, J. Wang, X. Jin, Q. Li, Z. Wu, J. Gou, Y. Jiang and Y. Song, *Part. Part. Syst. Charact.*, 2018, **35**, 1700304.

9. C. C. Stoumpos and M. G. Kanatzidis, *Adv. Mater.*, 2016, **28**, 5778.

10. J. Cho, Y.-H. Choi, T. E. O'Loughlin, L. D. Jesus and S. Banerjee, *Chem. Mater.*, 2016, **28**, 6909.

11. J. A. Sichert, Y. Tong, N. Mutz, M. Vollmer, S. Fischer, K. Z. Milowska, R. G. Cortadella, B. Nickel, C. Cardenas-Daw, J. K. Stolarczyk, A. S. Urban and J. Feldmann, *Nano Lett.*, 2015, **15**, 6521.

12. J. Choi, H. C. Woo, X. Huang, W.-G. Jung, B.-J. Kim, S.-W. Jeon, S.-Y. Yim, J.-S. Lee and C.-L. Lee, *Nanoscale*, 2018, **10**, 13356.

13. W. Deng, H. Fang, X. Jin, X. Zhang, X. Zhang and J. Jie, *J. Mater. Chem. C*, 2018 **6**, 4831.

14. Y. Hassan, Y. Song, R. D. Pensack, A. I. Abdelrahman, Y. Kobayashi, M. A. Winnik and G. D. Scholes, *Adv. Mater.*, 2016, **28**, 566.

15. A. Kojima, K. Teshima, Y. Shirai and T. Miyasaka, *J. Am. Chem. Soc.*, 2009, **131**, 6050.

16. V. Malgras, S. Tominaka, J. W. Ryan, J. Henzie, T. Takei, K. Ohara and Y. Yamauchi, *J. Am. Chem. Soc.*, 2016, **138**, 13874.

17. G. Li, F. W. R. Rivarola, N. J. L. K. Davis, S. Bai, T. C. Jellicoe, F. d. l. Peña, S. Hou, C. Ducati, F. Gao, R. H. Friend, N. C. Greenham and Z.-K. Tan, *Adv. Mater.*, 2016, **28**, 3528.

18. J. Burschka, N. Pellet, S.-J. Moon, R. Humphry-Baker, P. Gao, M. K. Nazeeruddin and M. Gra¨tzel, *Nature*, 2013, **499**, 316.

19. L. Polavarapu, B. Nickel, J. Feldmann and A. S. Urban, *Adv. Energy Mater.*, 2017, **7**, 1700267.

20. H.-S. Kim, C.-R. Lee, J.-H. Im, K.-B. Lee, h. Moehl, A. Marchioro, S.-J. Moon, R. Humphry-Baker, J.-H. Yum, J. E. Moser, M. Gra¨tzel and N.-G. Park, *Sci. Rep.*, 2012, **2**, 591.

21. Y. Wei, X. Deng, Z. Xie, X. Cai, S. Liang, P. a. Ma, Z. Hou, Z. Cheng and J. Lin, *Adv. Funct. Mater.*, 2017, **27**, 1703535.

22. N. Droseros, G. Longo, J. C. Brauer, M. Sessolo, H. J. Bolink and N. Banerji, *ACS Energy Letters*, 2018, **3**, 1458.

23. M.-R. Ahmadian-Yazdi and M. Eslamian, *Nanoscale Res. Lett.*, 2018, **13**, 6.

24. D. W. deQuilettes, S. Koch, S. Burke, R. K. Paranji, A. J. Shropshire, M. E. Ziffer and D. S. Ginger, *ACS Energy Lett.*, 2016, **1**, 438.

25. M. C. Weidman, A. J. Goodman and W. A. Tisdale, *Chem. Mater.*, 2017, **29**, 5019.

26. V. Malgras, J. Henzie, T. Takeia and Y. Yamauchi, *Chem. Commun.*, 2017, **53**, 2359.

27. J. Zhang, Z. Zhao, Z. Xia and L. Dai, *Nat. Nanotech.*, 2015, **10**, 444.

28. H. Huang, F. Zhao, L. Liu, F. Zhang, X.-g. Wu, L. Shi, B. Zou, Q. Pei and H. Zhong, *ACS Appl. Mater. Interfaces*, 2015, **7**, 28128.

29. C. C. Stoumpos, C. D. Malliakas and M. G. Kanatzidis, *Inorg. Chem.*, 2013, **52**, 9019.

30. Z. Wang, B. Zhang, T. Otsuka, K. Inoue, H. Kobayashi and M. Kurmoo, *Dalton Trans.*, 2004, 2209.

31. G. Kieslich, A. C. Forse, S. Sun, K. T. Butler, S. Kumagai, Y. Wu, M. R. Warren, A. Walsh, C. P. Grey and A. K. Cheetham, *Chem. Mater.*, 2016, **28**, 312.

32. M. Šimėnas, S. Balčiunas, M. Trzebiatowska, M. Ptak, M. Maˌczka, G. Vo¨lkel, A. Po¨pplc and J. Banysa, *J. Mater. Chem. C*, 2017, **5**, 4526.

33. D.-W. Fu, W. Zhang, H.-L. Cai, Y. Zhang, J.-Z. Ge, R.-G. Xiong, S. D. Huang and T. Nakamura, *Angew. Chem. Int. Ed.*, 2011, **50**, 11947.

34. B. Liu, R. Shang, K.-L. Hu, Z.-M. Wang and S. Gao, *Inorg. Chem.*, 2012, **51**, 13363.

35. Z. Wang, B. Zhang, K. Inoue, H. Fujiwara, T. Otsuka, H. Kobayashi and M. Kurmoo, *Inorg. Chem.*, 2007, **46**, 437.

36. G.-C. Xu, X.-M. Ma, L. Zhang, Z.-M. Wang and S. Gao, *J. Am. Chem. Soc.*, 2010, **132**, 9588.

37. G.-C. Xu, W. Zhang, X.-M. Ma, Y.-H. Chen, L. Zhang, H.-L. Cai, Z.-M. Wang, R.-G. Xiong and S. Gao, *J. Am. Chem. Soc.* , 2011, **133**, 14948.

38. R. Shang, G.-C. Xu, Z.-M. Wang and S. Gao, *Chem. Eur. J.*, 2014, **20**, 1146.

39. Z. Wang, K. Hu, S. Gao and H. Kobayashi, *Adv. Mater.*, 2010, **22**, 1526.

40. T.-M. Zhao, S. Chen, R. Shang, B.-W. Wang, Z.-M. Wang and S. Gao, *Inorg. Chem.*, 2016, **55**, 10075.

41. I. E. Collings, J. A. Hill, A. B. Cairns, R. I. Cooper, A. L. Thompson, J. E. Parker, C. C. Tangc and A. L. Goodwin, *Dalton Trans.*, 2016, **45**, 4169.

42. C. Zhang, B. Wang, W. Li, S. Huang, L. Kong, Z. Li and L. Li, *Nat. Commun.*, 2017, **8**, 1138.

43. D. Zhang, Y. Xu, Q. Liu and Z. Xia, *Inorg. Chem.*, 2018, **57**, 4613.

44. H. Huang, M. I. Bodnarchuk, S. V. Kershaw, M. V. Kovalenko and A. L. Rogach, *ACS Energy Lett.*, 2017, **2**, 2071.

Chapter 5

Summary and Future Outlook

This thesis attempts to investigate the role of flexible and anionic metal-organic frameworks (MOFs) in energy and environmental applications. MOFs are widely celebrated in materials science because of their unique salient features e.g., very high surface areas, ultra-low density, tunable porosity and easily functionalizable structures. Since these structures house accessible nanospaces within their confines which can be exploited for a variety of applications like separation and storage of gases, catalysis, drug delivery and sensing. In this thesis, two major types of MOFs, namely flexible and anionic, have been explored. While in the first part of the thesis, the structure-property relationships in flexible MOFs for gas separation have been extensively discussed, the second part deals with the role of anionic MOFs in non-traditional applications like sensing and water purification.

Gas separation is one of the most important techniques of the current world, which is extremely relevant both from industrial as well as environmental point of view. The separation of CO_2 from N_2 from industrial effluent flue gas is of supreme importance in order to prevent the release of CO_2 in the atmosphere and thereby in curtailing global warming. Moreover, the separated CO_2 can be converted to value-added products like methanol, methane or formic acid for energy applications. Similarly, different hydrocarbons are produced as a mixture by the steam cracking of petroleum and need to be separated for their individual use in industries. Even 1% acetylene present as an impurity in ethylene acts as a catalyst poison during the latter's polymerization. In contrast to conventional gas separation techniques, MOF based gas separation is inexpensive, highly selective and also energy efficient. In order to explore the role of MOFs in such practical gas separation, we have developed several novel dynamic MOF systems. These MOFs have structural flexibility that has been well corroborated by their single crystal structures as well as their adsorption behaviours. The unique structural features of these structures have been discussed in details. In order to establish their practical applicability in gas separation, a breakthrough setup, based on a mass-flow controller and gas chromatography, has been developed. Both the MOFs show excellent ability to separate C_2H_2 from a mixture of C_2H_2/C_2H_4 (v/v, 1:99), C_2H_6 from a mixture of CH_4/C_2H_6 (v/v, 50:50)and CO_2 from a mixture of CO_2/N_2 (v/v, 15:85). The efficiency of these MOFs in the breakthrough separation shows their true potential as an excellent adsorptive separator for gases.

The second part of the thesis delves deep into the structures and applications of

anionic MOFs. While neutral MOFs are widely studied, the facile applications of ionic MOFs are much less explored. The careful consideration of stoichiometry leads to the formation of anionic MOFs (AMOFs) where a guest counter cation resides within the framework to maintain the overall charge neutrality. This guest species can be exchanged with other extra-framework cationic species to get specific applications. We have designed and synthesized two such anionic frameworks, one with Zn^{II} and the other with Mg^{II} nodes, both containing dimethylammonium (DMA) cation as a guest. In case of the Mg^{II} MOF, this DMA cation has been replaced by Cu^{II} cations to show selective Cu^{II} sequestration among all transition metal cations and also show turn-off Cu^{II} sensing. This framework also shows a unique specific sensitization of Eu^{III} which results in a red luminescence *via* antenna effect. The facile synthesis of MOF derived materials using AMOFs has also been exhibited using this framework, where the DMA cation acts as a pre-bonded C-N-C moiety for the formation of carbon nitride materials. This AMOF has been pyrolyzed at two different temperatures without any external precursor to generate a very high surface area nanoporous carbon and carbon nitride dots. The carbon nitride dots were found to be an active electrocatalyst for oxygen reduction reaction (ORR) and its performance was further enhanced by doping Co traces. Another water-stable Zn^{II} based AMOF has been used for the capture of Cu^{II} to use it as a heterogeneous catalyst for the synthesis of benzimidazole derivatives. Moreover, this AMOF is extremely efficient in the removal of heavy metal cations like Hg^{II}, Pb^{II} and Cd^{II} from water even at concentrations as low as 1 ppm. This AMOF has also been exploited for the facile mechanochemical synthesis of $CsPbX_3$ perovskite quantum dot-MOF composites with superior stability and processibility by a cation exchange pathway. This strategy has been further extended to synthesize organic-inorganic lead perovskites namely methylammonium lead halide ($MAPbX_3$) perovskite quantum dots in a perovskite AMOF.

The overall findings of this thesis address the following issues:

1. The role of dynamic and flexible MOFs in practical application of absorptive separation. This encompasses both the separation of CO_2/N_2 as well as small hydrocarbons e.g., C_2H_2/C_2H_4 and CH_4/C_2H_6.

2. The multifarious applications of AMOFs, e.g., sensing, catalysis, sensitization and water purification.

3. The conversion of AMOFs to carbon derivatives and perovskite quantum dot composites by facile cost-effective methods.

The careful selection of linkers and metal nodes to construct different MOFs suited for specific applications have led to the formation of high-performance novel structures. The work in this thesis also upholds several proof-of-concepts, which can be used for the development of protocols for the synthesis of such systems which can open up a vista of new possibilities. The advancement of the synthesis and applications of such materials has the potential to solve many of the industrial and environmental crises of the modern world.
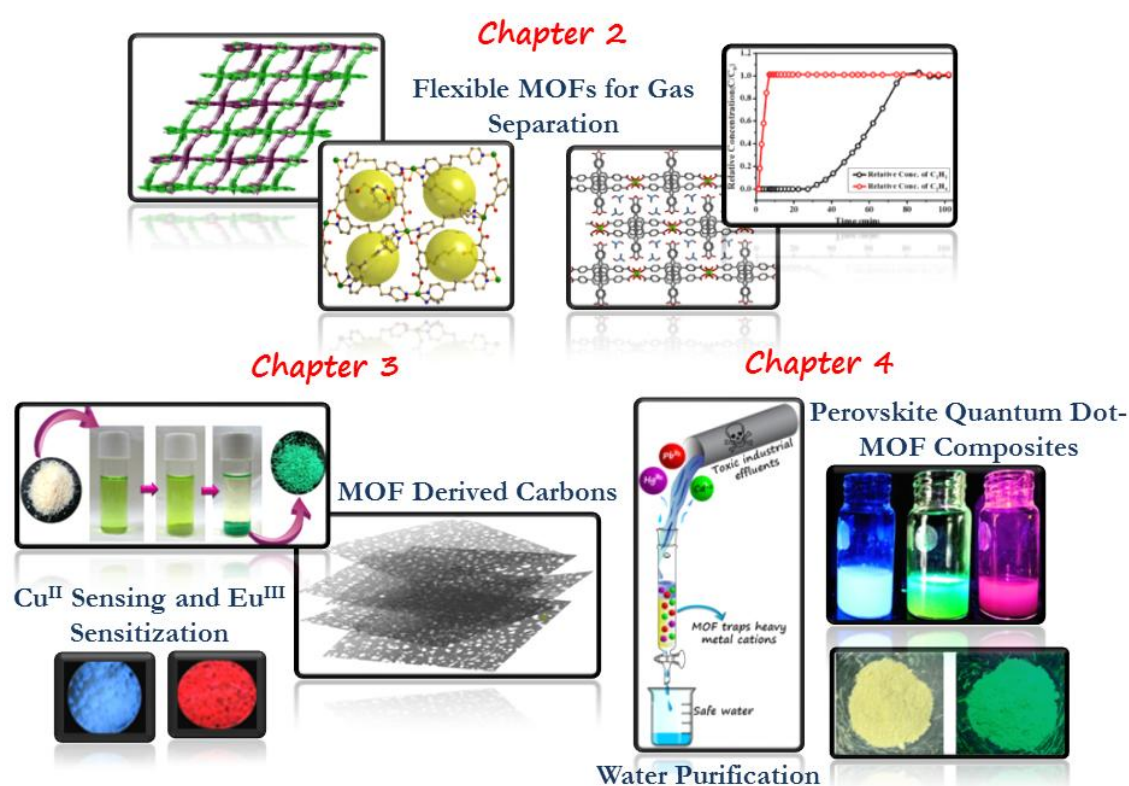
Scheme 1. Schematic summarizing the overall work of the thesis.

The exploration of the role of the perovskite quantum dot-MOF composites in photovoltaic devices lie beyond the scope of this thesis and has not been done. This is one of the major applications that need to be investigated in the future. Perovskite quantum dots are well known for their excellent photovoltaic efficiencies and small band gaps. However, their widespread commercial application is hindered by their poor stability and tedious synthetic techniques. Being incorporated into the MOF composite enhances their stability several folds and thereby increases their processibility to a great extent. Moreover, the synthesis of these composites are extremely simple and inexpensive and do

not require any hazardous chemical reagents. Thus such composite based devices can help in the commercialization and extensive use of perovskite quantum dot based devices for application in green renewable energy.

The role of the MOF based carbons as bi and trifunctional electrocatalysts also remain to be explored in this thesis. The combined electrocatalytic activity of such carbon materials in oxygen reduction (ORR), oxygen evolution (OER) and hydrogen evolution reactions can prove their potential to be used in total water splitting and metal-air batteries. Achieving such materials with superior efficiency is the absolute crowning glory for electrochemists as they hold the key to solve the energy crises of the world. In this context, the role of AMOFs as efficient photocatalysts, by encapsulating the suitable cationic species, has also not been explored in this thesis and can be done in the future. The well planned synthesis of such MOFs and their derivatives can pave the way for the development of several clean energy techniques which will lead the world towards a better future.

Biography

Sohini Bhattacharyya obtained her bachelors' degree in Chemistry from Presidency College, Kolkata in 2012. She completed MS in Materials Sciences from Chemistry and Physics of Materials Unit, Jawaharlal Nehru Centre for Advanced Scientific Research (JNCASR), Bangalore in 2015 under the supervision of Prof. Tapas K. Maji. She is currently pursuing her PhD under the guidance of Prof. Tapas K. Maji at JNCASR, Bangalore. Her research work is focused on flexible MOFs and post-synthetic modification of MOFs. She has been and INSPIRE scholar since 2012 and received the Post Graduate Indira Gandhi Fellowship during 2012-2014. Currently, she receives the INSPIRE Fellowship for PhD. She has received International Travel Support (2016), Jawaharlal Nehru Centre for Advanced Scientific Research (JNCASR), to attend the International Fall School on Organic Electronics held at Moscow, Russia and and International Travel Support (2018), Science and Research Board, Department of Science and Technology (DST), Government of India, to attend the 6th International Conference on Metal-organic Frameworks and Open Framework Compounds, Auckland, New Zealand. She also received Students' Travel Grant to attend International Workshop on Advanced Materials, Ras al Khaimah, United Arab Emirates.

List of Publications

1. **S. Bhattacharyya**, D. Rambabu, Chakravarthy M.L., T. Singh, T. K. Maji, Facile Mechanochemical Synthesis of MAPbBr$_3$ Perovskite Quantum Dots from a Perovskite MOF, *Manuscript under preparation*.

2. **S. Bhattacharyya**, D. Rambabu, T. K. Maji, Mechanochemical Synthesis of Processable Halide Perovskite Quantum Dot-MOF Composite by Post-synthetic Metalation, *J. Mater. Chem. A*, **2019**, DOI: 10.1039/C9TA05977F.

3. **S. Bhattacharyya**, A. Hazra, Nimish D., S. Pal Chowdhury, S. Balasubramanian, T. K. Maji, A Dynamic Supramolecular Framework for Gas Separation, *Manuscript under preparation*.

4. **S. Bhattacharyya**, S. Sobczak, A. Półrolniczak, S. Roy, D. Samanta, Andrzej Katrusiak, T. K. Maji, Dynamic Resolution of Piezosensitivity in a Single Crystal of π-Conjugated Molecules, *Chem. Eur. J.*, **2019**, *25*, 6092-6097.

5. D. Samanta, A. Singh, P. Verma, **S. Bhattacharyya**, S. Roy, T. K. Maji, Photoswitchable J-aggregated Processable Organogel by Integrating a Photochromic Acceptor, *J. Org. Chem.*, **2019**, DOI: 10.1021/acs.joc.9b01555.

6. **S. Bhattacharyya**, D. Samanta, S.Roy, V. P. H. Radhakantha, T. K. Maji, In situ Stabilization of Au and Co Nanoparticles in a Redox-Active Conjugated Microporous Polymer Matrix: Facile Heterogeneous Catalysis and Electrocatalytic Oxygen Reduction Reaction Activity, *ACS Appl. Mater. Interfaces*, **2019**, *19*, 5455-5461.

7. S. Roy, D. Samanta, **S. Bhattacharyya**, P. Kumar, A. Hazra, T. K. Maji, Tunable Physical States and Optical Properties of Bola-Amphiphilic OPE Based Supramolecular Networks Assisted by Functional Group Modulation, *J. Phys. Chem. C*, **2018**, *122*, 21598-21606.

8. **S. Bhattacharyya**, C. Das, T. K. Maji, MOF derived carbon based nanocomposite materials as efficient electrocatalysts for oxygen reduction and oxygen and hydrogen evolution reactions, *RSC Adv.*, **2018**, *8*, 26728-26754.

9. **S. Bhattacharyya**, A. Chakraborty, A. Hazra, T. K. Maji, Tetracarboxylate Linker Based flexible Cu^{II} Frameworks: Efficient Separation of CO_2 from CO_2/N_2 and C_2H_2 from C_2H_2/C_2H_4 Mixtures, *ACS Omega*, **2018**, *3*, 2018-2026.

10. **S. Bhattacharyya**, B. Konkena, K. Jayaramulu, W. Schuhmann, T. K. Maji, Synthesis of nano-porous carbon and nitrogen doped carbon dots from an anionic MOF: a trace cobalt metal residue in carbon dots promotes electrocatalytic ORR activity, *J. Mater. Chem. A*, **2017**, *5*, 13573-13580.

11. **S. Bhattacharyya**, A. Chakraborty, A. Hazra, A. C. Ghosh, T. K. Maji, Post-synthetic metalation in an anionic MOF for efficient catalytic activity and removal of heavy metal ions from aqueous solution, *Chem. Commun.*, **2016**, *52*, 2831-2834.

12. **S. Bhattacharyya**, A.Chakraborty, K. Jayaramulu, A. Hazra, T. K. Maji, A bimodal anionic MOF: turn-off sensing of Cu^{II} and specific sensitization of Eu^{III}, *Chem. Commun.*, **2014**, *50*, 13567-13570.